biomass  coreh₂o  premier

→ REPORT FOR MISSION SELECTION

An Earth Explorer to observe snow and ice

biomass  **coreh₂o**  premier

→ **REPORT FOR MISSION SELECTION**

**An Earth Explorer to observe snow and ice**

This report is based on contributions from the following members of the CoReH$_2$O Mission Advisory Group (MAG):

    Helmut Rott – MAG Chairman (University of Innsbruck, AT)
    Claude Duguay (University of Waterloo, Ontario, CA)
    Pierre Etchevers (Météo-France, FR)
    Richard Essery (University of Edinburgh, GB)
    Irena Hajnsek (DLR, DE, and ETH, CH)
    Giovanni Macelloni (Institute for Applied Physics- CNR, IT)
    Eirik Malnes (Northern Research Institute, NO)
    Jouni Pulliainen (Finnish Meteorological Institute, FI)

They were supported by two observers:

    Donald Cline (NOAA, NWS, US)
    Simon Yueh (JPL, US)

The scientific content of the report was compiled by Michael Kern (Scientific Coordinator) with additional contributions, in particular, from Anthony Freeman (JPL, US), Markus Heidinger (ENVEO, AT), Juha Lemmetyinen (FMI, FI), Thomas Nagler (ENVEO, AT), Karl Voglmeier (ENVEO, AT) and from ESA, Nicolas Floury, Andrea Perrera and Dirk Schüttemeyer.

The technical content of the report was compiled by Arnaud Lecuyot (Technical Coordinator) with contributions from Antonio Gabriele, Nicolas Gebert, Patrick Grimont, Florence Hélière and David Patterson (all from ESA), based on inputs derived from industrial Phase-A system and technical activities.

Recommended citation: ESA (2012). Report for Mission Selection: CoReH$_2$O, ESA SP-1324/2 (3 volume series), European Space Agency, Noordwijk, The Netherlands.

Cover image: ESA/AOES Medialab

# Contents

# → EXECUTIVE SUMMARY

# Executive Summary

The Earth Explorer Cold Regions Hydrology high-resolution Observatory (CoReH$_2$O) will be the first satellite mission dedicated to making global measurements of freshwater stored in snow on land surfaces and snow accumulated on glaciers and ice caps. It will provide repeated observations of snow and ice properties at fine spatial scales for modelling and validating surface–atmosphere exchange processes, climate research and hydrological applications. This measurement dataset cannot be obtained adequately from ground-based or airborne sensors, nor is it delivered by any other existing or planned spaceborne sensor.

Snow and glaciers are vital resources of freshwater in high-latitude regions and many densely populated areas in mid and low latitudes. Covering up to 50 million km$^2$ of Earth's land surface, snow is a key component in the global water cycle, influencing atmospheric circulation and the climate from regional to global scales. As climate change threatens access to freshwater resources, there is a call for immediate action to quantify the amount and variability of water stored as snow, reduce uncertainties in these terms, and improve the prediction of climatic effects on the water cycle and associated feedbacks. There is also the need to address the effects of snow distribution on the carbon cycle and greenhouse-gas exchange, the effects of lake ice on heat exchange between the surface and the atmosphere, and the role of snow in ice formation for sea-ice thermodynamics and mass balance.

The importance of improved snow and ice observations for climate research and modelling, for numerical weather prediction, for water management and ecology, and for supporting the adaptation to climate change has been highlighted in several reports such as the Intergovernmental Panel on Climate Change Report on Climate Change and the Integrated Global Observing Strategy Cryosphere Theme Report. The hydrological modelling and forecasting community requests high-resolution snow information, particularly over areas of moderate to complex topography where the snowpack can be very heterogeneous. The climate modelling and numerical weather prediction user community is well-prepared to handle the observations and to exploit the unique dataset that CoReH$_2$O will provide. The mission objectives are directly linked to specific challenges in ESA's Living Planet Programme and address four of the five components of the Earth system; namely, the cryosphere (including water budgets), the land surface, the ocean and the atmosphere (through surface-atmosphere exchange processes).

CoReH$_2$O will provide observations from a Synthetic Aperture Radar (SAR) at X- and Ku-band, transmitting signals with vertical linear polarisation and receiving backscattered signals from Earth's surface with vertical and horizontal linear polarisations. Signals at Ku-band are more sensitive to shallow dry snow, while X-band signals provide better penetration of deep snow layers and provide information about the underlying ground. Multiple science objectives that require high spatial- and temporal-resolution and extended coverage will be achieved through two mission phases each with different orbit repeat intervals.

CoReH$_2$O will deliver unique information on extent and mass of seasonal snow-cover, and snow accumulation on glaciers at a resolution of a few hundred metres. Links can then be made to the topographic changes observed by altimetry missions such as CryoSat and relevant process parameterisations in climate models. CoReH$_2$O will also complement microwave and scatterometer missions that provide snow information at very coarse spatial resolutions (>20 km), thus enabling studies of downscaling options and contributing to improvement and validation of low-resolution

products. CoReH$_2$O is also highly complementary to lower-frequency SARs that are not sensitive to dry snow, providing a unique testbed for experimental studies on radar signal interactions, as well as for testing and advancing bio- and geophysical parameter retrievals in various research fields. Finally, the scientific advancements in observation and modelling of snow and ice resources triggered by CoReH$_2$O will find additional applications and be of environmental and socio-economic benefit.

The CoReH$_2$O space segment comprises a single satellite carrying the SAR, which uses signals at two frequencies (9.65 GHz in X-band and 17.25 GHz in Ku-band) with dual polarisation (VV and VH). The SAR, operating in ScanSAR mode, observes a ground swath of about 100 km.

The mission includes two distinct operational phases. Phase-1 aims to make observations over dedicated test sites and key snow-covered regions with a revisit period of 3 days. Phase-2 provides observations of snow- and ice-covered areas with a revisit period of 15 days. In both phases, the satellite operates in a near-polar Sun-synchronous orbit with the descending node at 06:00 local time. The altitudes are 666 km for Phase-1 and 645 km for Phase-2. The satellite will be injected into the Phase-1 orbit by a Vega launcher, but is designed for compatibility with the Polar Satellite Launch Vehicle as backup.

The Sun-synchronous orbit is needed to provide repeatable and favourable observing conditions throughout the mission's life. Given the high power needs and high thermal dissipation of the SAR payload, the illumination conditions provided by the selected dusk/dawn orbits reduce the need for complex power generation and thermal-control subsystems.

The CoReH$_2$O satellite makes extensive reuse of flight-proven solutions for the platform subsystems, but features a specific structural concept driven by the accommodation of the SAR instrument and by the geometrical constraints imposed by the viewing geometry between the reflector and the antenna feed system. The SAR concept is based on a single deployable parabolic reflector measuring up to 4.3 × 1.8 m, illuminated by two feed-arrays that generate the multiple beams required to cover the ground swath with the ScanSAR operation mode. The SAR is operated with an incidence angle range constrained to 30–45°.

The CoReH$_2$O satellite has a launch mass of ~1225 kg, versus a launcher nominal capability of 1390 kg, and a power generation capability of ~2.5–3.0 kW at end of life. The instantaneous instrument data rate of 170–180 Mbit/s requires, for the different communication architecture under consideration, an onboard mass memory of ~1000 Gbit and a data downlink capacity in the range of 470–520 Mbit/s.

The data acquired by the SAR instrument are sent to the ground via a high-rate radio downlink in X-band. Communication for satellite monitoring and control is supported via a two-way S-band link.

The ground segment uses the generic Earth Explorer ground segment infrastructure. This comprises the Flight Operations Segment and the Payload Data Ground Segment. The science data, processed up to Level-1 and Level-2, are made available to users, including climate modelling and research centres.

During Phase-A, supporting scientific studies and campaigns were performed to answer all critical scientific issues that had been identified for the mission including those set out by the Earth Science Advisory Committee at the mission down-selection following Phase-0.

By means of the available campaign data, further advances have been made in the understanding of the physics underlying the microwave interactions at X- and Ku-band. A baseline retrieval algorithm has been developed and thoroughly tested using simulated data that reproduces the threshold performance of the designed system concepts. The algorithm has been used successfully on campaign data covering a variety of snow conditions. With the development of a new airborne sensor during Phase-A, spatially-distributed, coincident and collocated Ku- and X-band backscatter image data were

obtained, which enables further testing and potential enhancement of the retrieval algorithms over different snow regimes. The main areas influencing the retrieval performance have been recognised. Additional experiments with the end-to-end performance simulator are in progress, targeted risk reduction measures have been identified and additional campaigns have been initiated.

No critical elements have been identified for the development of the CoReH$_2$O satellite platform. The proposed baseline design presents adequate margins at this stage of the mission definition with some capacity for growth.

For the critical items identified in the SAR, the design and test results show that the proposed equipment can meet the requirements. This is also true of the high-power amplifier technologies (travelling wave tube and Klystron), for which analyses of designs based on heritage equipment, breadboarding and tests have demonstrated feasibility. The limiting factor is only the number of on/off cycles for the tube, which constrains the system and operation concept.

Assuming the expected successful outcome of ongoing pre-developments, the maturity of critical technologies will reach the required level prior to the start of the implementation phase. The development schedule is compatible with a launch in 2019.

# → INTRODUCTION

# 1. Introduction

The changing Earth system poses significant scientific challenges and opportunities for Earth observations from the vantage point of space. As part of its Earth Observation Envelope Programme, the European Space Agency's (ESA's) series of Earth Explorer missions offers new observational capabilities to explore and understand different aspects of the Earth system.

These missions are developed in response to priorities identified by the scientific community. They address and fulfil ESA's Living Planet Programme strategic objectives (SP-1304, 2006) and comprise a critical component of the global Earth observing system.

The fundamental principle of defining, developing and operating Earth Explorer missions in close cooperation with the scientific community provides an efficient tool to address pressing Earth-science questions as effectively as possible. Coupled with an ability to develop and embark novel sensing technologies, this gives the possibility to substantially advance the frontier of our scientific knowledge of the Earth system and the human impact on natural processes.

Since the science and research elements of the Living Planet Programme were established in the mid-1990s, this user-driven strategy has resulted in the selection of six Earth Explorer missions for implementation. Together, they cover a broad range of scientific topics. Importantly, the complementarity between the selected missions also offers new opportunities for exploiting mission synergies, thereby establishing a stimulus for the development of new applications of Earth observation data.

Earth Explorer missions are split into two categories: Core and Opportunity. Core Earth Explorers are larger missions addressing complex issues of scientific interest and which require substantial elements of new technology. By contrast, Opportunity missions are smaller and have more focused scientific goals that are normally achieved by novel uses of existing lower-risk technologies. Through a process of peer review and selection, both types are implemented in separate cycles to ensure a steady flow of missions to address key Earth-science questions.

The first cycle for Core missions resulted in the Gravity field and steady-state Ocean Circulation Explorer, GOCE, which was launched in March 2009, and the Atmospheric Dynamics Mission ADM-Aeolus, scheduled for launch in 2014. The second cycle, initiated in 2000, resulted in the Earth Clouds Aerosols and Radiation Explorer, EarthCARE, due for launch in 2015. The first cycle for Opportunity missions resulted in the ice mission CryoSat, which was rebuilt and launched in April 2010 following a launch failure in 2005, and the Soil Moisture and Ocean Salinity, SMOS, mission, also launched in 2009. The second cycle resulted in the magnetic field mission, Swarm, which is scheduled to be launched in 2012.

A third cycle of Earth Explorer Core missions was initiated by a Call for Ideas released in 2005. In May 2006, six of the candidate missions were selected for Assessment Study following a peer review of 24 proposed mission ideas. Upon completion of Pre Feasibility Study (Phase-0), a User Consultation Meeting was held in January 2009 in Lisbon, Portugal, at which the six candidates were presented to the scientific community together with their accompanying Reports for Assessment, (SP-1313, 2008).

In February 2009, three out of the six candidates were selected for Feasibility Study (Phase-A): Biomass, Cold Regions Hydrology high-resolution Observatory (CoReH$_2$O) and Process Exploration through Measurement of infrared and millimetre-wave Emitted Radiation (PREMIER).

— Biomass aims to observe global forest biomass for a better understanding of the carbon cycle.

— CoReH$_2$O aims to observe snow and ice for a better understanding of the water cycle.

— PREMIER aims to observe atmospheric composition for a better understanding of chemistry–climate interactions.

The Report for Mission Selection for each candidate captures the status of the respective mission concept at the end of Phase-A activities. The three reports are provided to the Earth observation research community prior to the User Consultation Meeting to be held in 2013 and subsequent selection of a single Earth Explorer 7 mission.

The three reports follow a common structure comprising this introductory first chapter and eight subsequent chapters as follows:

— Chapter 2 – identifies the background and scientific issues to be addressed by the mission, considering the contribution of past and present activities in the field. It provides the justification for the mission, set within the post-2018 time frame, and includes a review of the current scientific understanding of the issue in question while identifying the potential 'delta' that the mission could provide.

— Chapter 3 – drawing on arguments presented in Chapter 1 and Chapter 2, this chapter summarises the specific research objectives of the mission.

— Chapter 4 – outlines the mission requirements, including required geophysical data products and observational parameters, the need for observations from space and aspects of timeliness and timing of the mission.

— Chapter 5 – provides an overview of the system elements, including the space and ground segments; and of the operations, calibration and data processing up to Level-1b.

— Chapter 6 – describes the advances in scientific algorithms and processing, validation and assimilation techniques which may be required to meet the data product requirements.

— Chapter 7 – makes a comparison of expected versus required performance and ability to fulfil the research/observational objectives based upon the documented system concept.

— Chapter 8 – documents the maturity of the scientific user community in respect to planned use of the anticipated scientific products, the global context in terms of complementary missions as well as the operational or applications potential of the data products.

— Chapter 9 – outlines a programme of implementation. It also addresses scientific and technical maturity, the development status of key technologies, risks, logistics and schedules.

This Report for Selection covers the CoReH$_2$O mission.

# → BACKGROUND AND SCIENTIFIC JUSTIFICATION

# 2. Background and Scientific Justification

## 2.1 Introduction

As a major component of the water budget in many parts of the world, snow cover constitutes the dominating element of the cryosphere in terms of spatial extent and temporal variability. Therefore, the understanding of the global water cycle demands accurate high-resolution observations of freshwater stored as snow. The impact of climate change on this resource, including feedbacks and amplifications, can only be assessed and predicted if the coupling between the dynamic processes of snow and ice with other main components of the Earth system can be quantified and modelled. This requires a holistic approach, as stressed in *The Changing Earth: New Scientific Challenges for ESA's Living Planet Programme* (ESA SP-1304, 2006).

The CoReH$_2$O mission directly addresses the challenges of the programme's themes related to the cryosphere and hydrosphere, and provides important information on feedbacks relevant to key processes in the boundary layer of the atmosphere and in the biosphere. Measurements supplied by CoReH$_2$O are particularly important for advancing our knowledge on:

— The role of snow and glaciers in influencing the global water cycle and regional water resources.

— Parameterisation and downscaling of snow and ice processes in atmospheric circulation and climate models.

— Effects of snow regimes on boundary conditions for carbon exchange, trace-gas exchange and preservation of biodiversity.

— Processes in high-latitude ocean circulation and thermodynamics related to sea-ice formation and freshwater fluxes from high-latitude rivers.

The importance of improved snow and ice observations for climate research and modelling, for numerical weather prediction, for water management and ecology, and for supporting the adaptation to climate change has been highlighted in the Intergovernmental Panel on Climate Change (IPCC) *Report on Climate Change* (IPCC, 2007; Lemke et al., 2007), in the United Nations Environment Programme (UNEP) *Outlook for Global Ice and Snow* (UNEP, 2007) and in the *Arctic Climate Impact Assessment* (ACIA, 2005). These initiatives clearly point out present deficits in snow and ice observations and in their integration in climate models and environmental process models. This gave rise to new, upcoming international programmes such as the Global Cryosphere Watch of the World Meteorological Organization (WMO) which was approved at the World Meteorological Congress session in May 2011, and the Cryosphere Theme of the Integrated Global Observing Strategy (IGOS), now Group on Earth Observations; (IGOS, 2007).

## 2.2 Critical Role of Snow and Ice in the Climate System and Water Cycle

The cryosphere includes terrestrial snow cover, glaciers, ice caps, ice sheets, permafrost, seasonally frozen ground, sea ice, lake and river ice, and solid precipitation. Of these, seasonal snow cover and frozen ground dominate in spatial extent and temporal variability, covering up to about 50% of the land in the northern hemisphere (Zhang et al., 2003). Improving quantification

of the interactions between the cryosphere and the atmosphere is a crucial and challenging research issue in climate analysis and modelling. Meeting this challenge requires more accurate observations and modelling of the energy budget and mass exchange of snow and ice, including snow and ice contributions to freshwater runoff.

Snow and ice masses are important components of the global climate system (Fig. 2.1). While known to have a strong impact on surface energy, moisture and gas fluxes at the interface of Earth's surface and atmosphere, the magnitudes of these feedbacks remain very uncertain in current climate predictions (e.g. Hall and Qu, 2006; Wang and Zeng, 2010). The extent of snow and ice cover affects the meridional temperature gradients and transport processes, both in the atmosphere and oceans (Dutra et al., 2011). Global circulation model (GCM) experiments show that the presence of snow on large land surfaces not only reduces surface temperatures locally, but may also influence remote climate phenomena through teleconnections (Peings & Douville, 2010; Lin and Wu, 2011; Sobolowski et al., 2011).

## 2.2.1 Snow and Glaciers: Critical Sources of Water

Seasonal snowpacks and glaciers store large amounts of freshwater and are critical components of the water cycle. Snow is a major, or even dominating source, of runoff in many regions of the world (Fig. 2.2). More than one-sixth of Earth's population rely on seasonal snowpacks and glaciers for their water supply (Barnett et al., 2005; UNEP, 2007).

Since the 1970s, there has been a clear trend in accelerating retreat of terrestrial snow cover, which is very pronounced in spring and summer (Lemke, et al., 2007; Brown and Robinson, 2011). Changes are particularly evident in northern high-latitudes, where warming at almost double the average global rate has been reported over the last 30 years (ACIA, 2005; Trenberth et al., 2007; Brown et al., 2010). Also in mid-latitude mountainous regions, snow retreat has exceeded prediction based on rising temperatures (Abatzoglou, 2011).
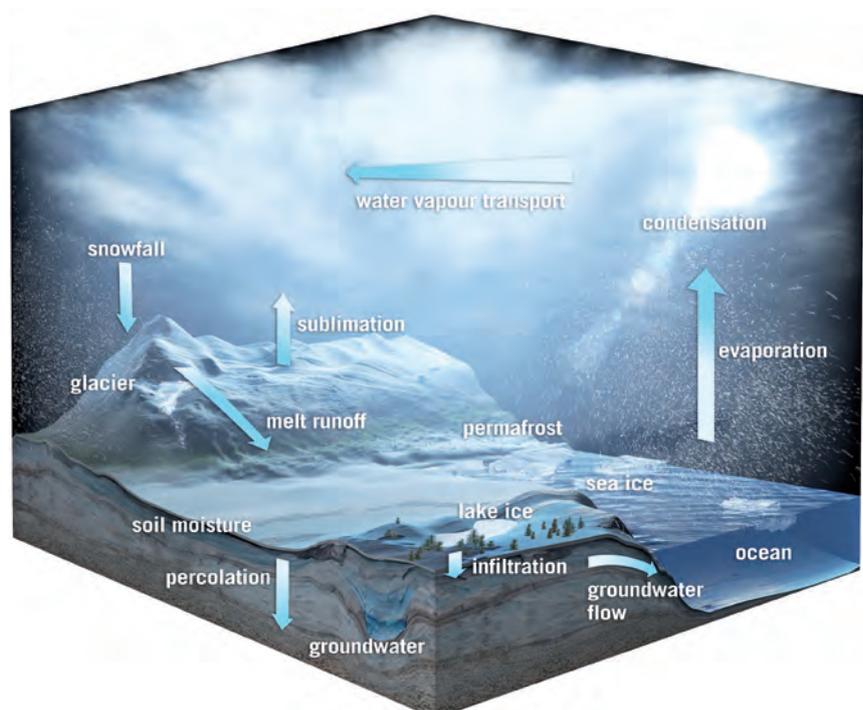


Figure 2.1. CoReH$_2$O addresses major uncertainties in the role that snow, glaciers, lake ice and sea ice play in global climate and in the water cycle. (ESA/AOES Medialab)
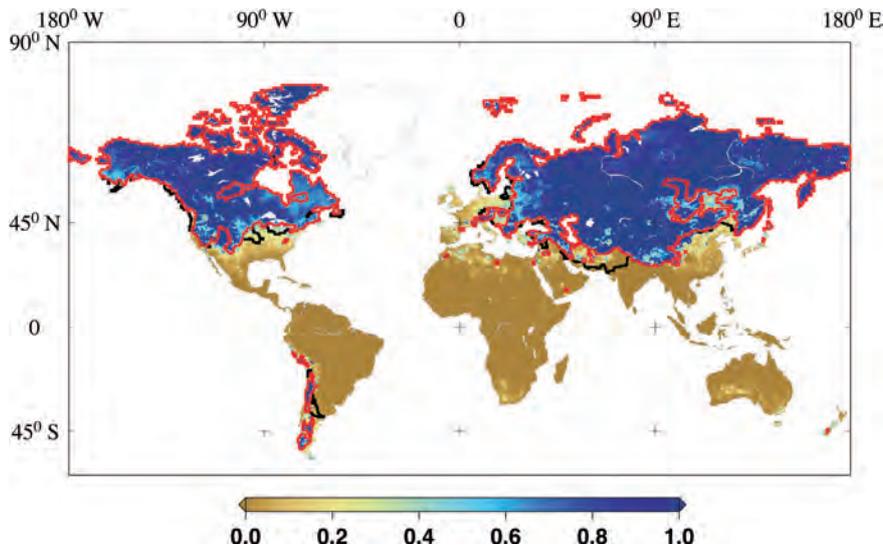
Figure 2.2. Streamflow is dominated by snowmelt within areas outlined in red. The black lines delineate additional areas where water availability is strongly influenced by snowmelt generated upstream. The colour scale indicates the ratio of accumulated annual snowfall divided by annual runoff. (Adapted from Barnett et al., 2005)

If the climate continues to warm, reduced snow and ice will affect freshwater flows, resulting in serious consequences for human health, regional food security and biodiversity (IPCC, 2007). Changes in the amount and distribution of terrestrial snow cover will directly impact the timing of spring and annual runoffs. This affects the environment and occurrence of floods and droughts, irrigation for agriculture, civilian water supply, groundwater recharge, and moisture for spring planting. In addition to the socio-economic impacts, there will be direct effects on the functioning of ecosystems in these regions (Omann et al., 2009; Kreyling et al., 2011). Winter climate-change and retreat of snow can have long-term implications on the structure of ecosystems and biodiversity.

Changes in the timing and amount of runoff from mountain snowpacks and glaciers are of particular concern for dry climates such as that of southwest US, northwest China, central Asia and the Andean countries (Kundzewicz et al., 2007), but will also affect more humid regions such as the European Alps (Bavey et al., 2009). In the mid-west and western US, snow that accumulates in the mountains provides much of the water used to irrigate crops during the growing season. Widespread and regionally coherent trends towards earlier onset of spring snowmelt and streamflow have been reported for the period 1948–2002 (Stewart et al., 2005) and will further shift in a changing climate. Glaciers and snowmelt also have an important regulatory function for water supply in parts of Europe. Climate projections for strong (A2) and moderate (B2) carbon dioxide ($CO_2$) increase indicate a temporal shift in streamflow and increased peak flow for the Dischma basin (43 km$^2$) in Switzerland, which may cause more frequent floods (Fig. 2.3).

In the greater Himalayas-Hindu Kush-Tien Shan region and in the Andes, snow cover and glaciers provide headwaters to major rivers, which supply water to some of the most densely populated regions in the world. These resources are particularly important for maintaining river flow in the dry season and recharging aquifers. The recent controversy regarding the expected shortage of water in Asia, owing to the retreat of glaciers and snowpack, stresses the need for more and consistent observational data (Cogley et al., 2010). In order to obtain reasonable estimates on the vulnerability of water supplies resulting from the retreat of snow and glaciers, it is necessary to collect spatially-detailed data on these parameters, especially because regional differences are large (Malone, 2010).

Rapid snowmelt events resulting from warm spring temperatures or rain on snow are often preconditions for floods. Consequently, the measurement of the water stored in the snowpack, called Snow Water Equivalent (SWE), is

Figure 2.3. Daily values of discharge for the Dischma catchment, Switzerland, reference scenario (average for 2001–2006) and simulations for the period 2071–2100, for two common climate change scenarios (IPCC A2 and B2; IPCC, 2007). (Bavay et al., 2009)
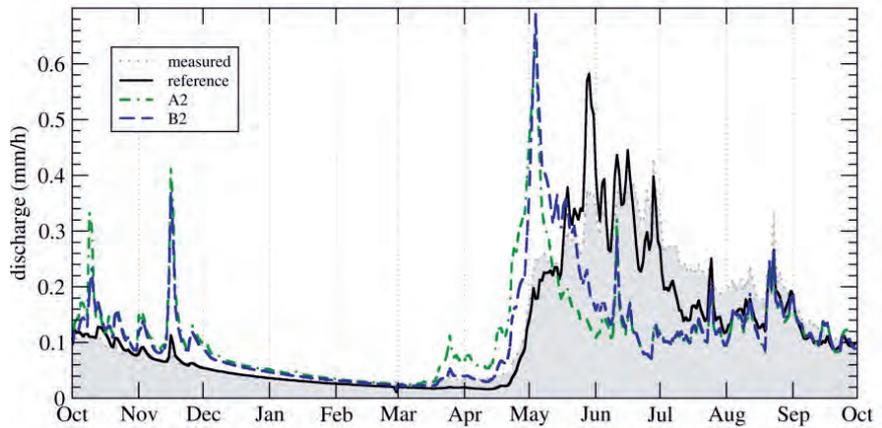
extremely useful for predicting spring and summer water supplies as well as flood potential. SWE is snow depth × snow density, expressed in either kg m$^{-2}$ or in metres (water equivalent).

Uncertainties in the magnitude of snow-water storage are very high owing to inadequate coverage and lack of snow observations. For example, estimates of snow-water storage for one day over continental USA, derived from modelling and assimilation of ground observations of SWE, can be more than twice the magnitude observed from passive microwave-remote sensing (personal communication, NOAA, 2007, Fig. 2.4). Major differences for SWE have also been found for Siberia between the Special Sensor Microwave Imager, European Centre for Medium-range Weather Forecasts (ECMWF) 40-year reanalysis data (ERA40), and snow climatology from HadCM3 (Clifford, 2010). Poor correlation was also found between NASA's Advanced Microwave Scanning Radiometer-E (AMSR-E) SWE and SWE/snow-depth of NOAA's Snow Data Assimilation System product for the US (Tedesco & Narvekar, 2010). Coarse-resolution passive-microwave radiometers provide a critical climate record of terrestrial snow characteristics, but these data must be better calibrated and downscaled to solve open questions.
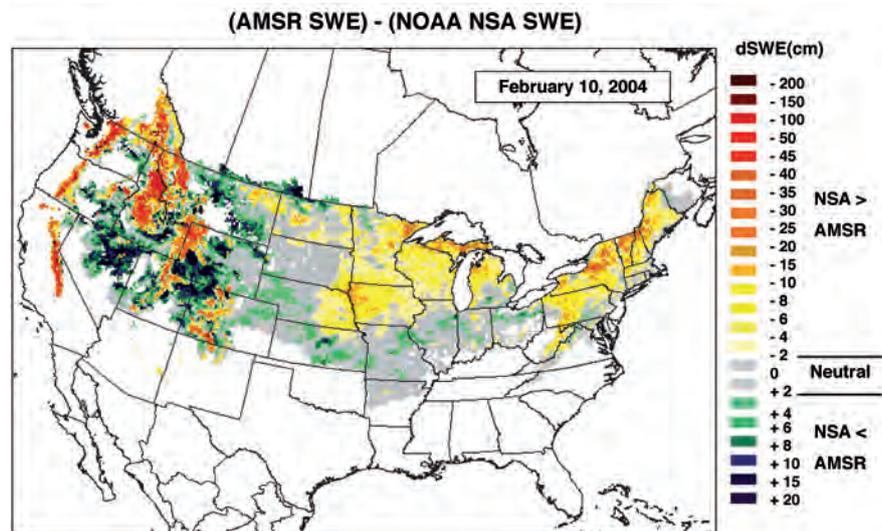
Figure 2.4. Differences between SWE observed by the AMSR-E instrument and SWE analysed by operational modelling and data assimilation by NOAA's National Snow Analyses for 10 February 2004 show widespread discrepancies, and thus uncertainties, especially in mountainous areas. (NOAA)

## 2.2.2 Terrestrial Snow: Feedbacks to the Climate System, Permafrost and Carbon Cycle

The presence of snow cover during the cold season has a significant influence on the ground thermal regime. Snow is a strong insulator, limiting the transfer of heat between the atmosphere and the ground. Where there is snow cover in the winter, the mean annual ground-surface temperature is warmer than the mean annual air temperature because of the insulating effect of snow. The timing, rate of accumulation, duration, density, and depth of snow cover during the winter play an important role in determining how the air temperature signal propagates into the ground (Stieglitz et al., 2003). Warming of permafrost in the late 1980s and early 1990s in Alaska, for example, has been attributed to deeper snow cover in the winters (Osterkamp, 2008). Increases in snow depth can cause a rise in the mean annual ground and permafrost surface temperature by several degrees. In regions of discontinuous and sporadic permafrost, the absence of seasonal snow cover may be a key factor for permafrost development. In regions where the ground freezes seasonally, snow cover can substantially reduce the freezing depth. The influence of snow cover on seasonally frozen ground has received relatively little attention, and further study is needed (Zhang, 2005).

Snow-climate interactions are complex (Brown, 2000), and in turn, snowpack response to climate forcing has a major influence on ecosystem function (Fig. 2.5). In particular, at high latitudes vulnerability of ecosystems to climate change is high owing to positive snow-atmosphere feedback and degrading permafrost (Denman et al., 2007; Hollesen et al., 2011; Kittel et al., 2011). For example, snow has an important impact on winter respiration and net carbon-exchange, and hence, determines whether an ecosystem is a source or sink for atmospheric carbon (Morgner et al., 2010; Natali et al., 2011). The timing, condition and duration of regional snow-cover controls the surface energy balance and the severity of soil frost. As described by Jarvis and Linder (2000), Picard et al. (2005), Rogers et al. (2011) and others, there is much to learn about net carbon-exchange in northern regions, but it is now well established that snow:

— directly controls the timing of carbon uptake by vegetation.

— directly controls the magnitude of winter $CO_2$ efflux from soil.

— indirectly controls rates of carbon uptake through freeze-thaw regulation to soil decomposition, respiration and nitrogen availability.

To reduce the uncertainty of predictions on environmental and ecological impacts of climate change, a much better understanding of the role of snow and ice in the climate system is required. Because of the intrinsic role snow has in climate response and ecosystem forcing, this cannot be achieved without accurate quantification of snow cover/atmosphere/hydrosphere interaction processes.

Detailed observations of snow properties, affecting permafrost and wetlands, are required to establish boundary conditions of surface/atmospheric exchange processes to estimate fluxes of trace gases from northern ecosystems. These fluxes represent a highly uncertain component of future global change (Davidson & Janssens, 2006; Dolman et al., 2010). The wet lowlands of Arctic permafrost are natural sources of the climate-relevant trace-gas methane. The contribution this area makes in the global methane budget is poorly quantified (Walter et al., 2006; McGuire et al., 2009). Accelerated thawing of Siberian bogs could unleash billions of tonnes of methane (Pearce, 2005). Thus, the decrease of snow cover and retreat of permafrost in high-latitude areas may switch

Figure 2.5. The links between snow, climate, and ecosystems, including the positive ice/snow albedo feedback, terrestrial snow and vegetation feedbacks and the negative cloud/radiation feedback. Warming at low and high latitudes (brown boxes) results in terrestrial and marine responses. On land, less snow mass and higher temperatures result in earlier snowmelt and decreased albedo, increased net radiation, and atmospheric heating, supporting further warming. (UNEP)

tundra from a sink to a source of atmospheric carbon. This would generate positive climate feedback, accelerating the rate of global warming in the future.

## 2.2.3 Mass Balance of Glaciers, Ice Caps and Ice Sheets

Glaciers and glacial environments are sensitive indicators of climate change and important elements of the hydrological cycle. The response of glaciers to climate is governed by the surface mass balance, which is determined by accumulation from snowfall and the ablation of snow and ice. There are an estimated 160 000 mountain glaciers and ice caps (Meier & Bahr, 1996), covering a total area of about 785 000 km$^2$ (Dyurgerov & Meier, 2005). Globally, glaciers and ice caps only make up a small proportion of land ice, but they are more sensitive to climate variability and change than large ice sheets because they lie in warmer climates and have larger relative mass turnover. Glacier melt dominated eustatic sea-level rise in the last century, and this contribution has increased over the last decade (Meier et al., 2007; Radic and Hock, 2011). Change in ice volume varies considerably in different glacial regions, so predictions of future mass depletion are highly uncertain.

Globally, glaciers have retreated since the 19th century. Downwasting has accelerated in recent years (Fig. 2.6). The global average for glacier mass balance is estimated at –356 kg m$^{-2}$ yr$^{-1}$ for the period 1990/91–2003/04, twice the estimated annual mass deficit for the period 1960/61–1989/90 (Lemke et al., 2007). Only a very few glaciers have their mass balance measured directly, so these are large error bars in regional and global mass balance numbers (Braithwaite, 2009). Models are applied to estimate glacier mass balance in response to atmospheric forcing (Oerlemans, 2001), but these models suffer from a lack of observational data for initialisation and validation.

Mass balance estimates for the Greenland and Antarctic ice sheets also have large error bars (Shepherd & Wingham, 2007; Thomas et al., 2008). Mass balance estimates for the Antarctic ice sheet lie between approximately +50 Gt yr$^{-1}$ to –250 Gt yr$^{-1}$ for 1992–2009 (Zwally & Giovinetto, 2011). For Greenland, the mass balance has clearly been negative for about 15 years. The average annual mass balance is estimated at –50 Gt yr$^{-1}$ to –100 Gt yr$^{-1}$ for 1993–2003 (Lemke, et al., 2007), contributing to a sea-level rise of 0.13–0.26 mm yr$^{-1}$. Recent observations show significant acceleration of

Figure 2.6. Five-year average mass balance of the world's glaciers and ice caps. Mean specific mass balance (left axis) is converted to total mass balance and to sea-level equivalent (right axis) using the total ice surface area. C05a is an arithmetic mean over all annual measurements within each pentad. The grey envelope is the 90% confidence level of the C05a data and represents the spatial variability of the measured mass balances. C05i is obtained by spatial interpolation (Cogley, 2005), while DM05 (Dyurgerov and Meier, 2005) and O04 (Ohmura, 2004) are area-weighted global numbers. MB is the arithmetic mean of C05i, DM05 and O04, with its uncertainty (red shading). (From Lemke et al., 2007)

downwasting. For 2003–07, the mass balance is estimated at –171 Gt yr$^{-1}$, contributing to a sea-level rise of 0.5 mm yr$^{-1}$ (Zwally et al., 2011). Complementary to observations from low-resolution sensors made over the main parts of the ice sheets, spatially-detailed data on snow accumulation in the boundary zones of ice sheets are required for relating mass changes to atmospheric forcing.

## 2.2.4 Lake and River Ice Processes

There is strong evidence that shows the robustness of using freshwater ice as a proxy indicator of climate variability and change (e.g. Magnuson et al., 2000; Lacroix et al., 2005; Duguay et al., 2006). Although, globally, the duration of ice-cover on rivers and lakes in the northern hemisphere has significantly reduced in response to an increasingly warmer climate during the 20th century, the response has been shown to vary regionally. This response is also strongly related to the variability and regime shifts in large-scale atmospheric and oceanic oscillations (Bonsal et al., 2006; Duguay et al., 2006; Lemke et al., 2007; Prowse et al., 2007; Benson et al., 2011). With continued climate warming, lake-ice models forced with climate-model data indicate that ice-cover duration and winter ice-thickness will be further reduced in some regions in the northern hemisphere (Brown & Duguay, 2011a). However, the problem in using lake-ice models to predict future conditions (timing of break-up, ice thickness and composition) is that they poorly represent the amount and density of snow that accumulates on the ice surface, the patterns of which tend to be quite different than over land owing to redistribution by the wind (Brown & Duguay, 2011b).

Lakes are not only influenced by climate, but they also influence local and regional weather and climate (thermal moderation, enhanced evaporation, lake-effect snowfall) (Brown & Duguay, 2010). For this reason, there is growing interest in coupling regional climate models and Numerical Weather Prediction (NWP) models to lake models, as well as assimilating lake surface-temperature and ice-cover (fraction, thickness and snow on ice) observations derived from remote sensing in NWP (Kourzeneva et al., 2008; Eerola et al., 2010; Samuelsson et al., 2010). Figure 2.7 clearly illustrates the importance of accounting for the effects of lakes in atmospheric models. A comparison
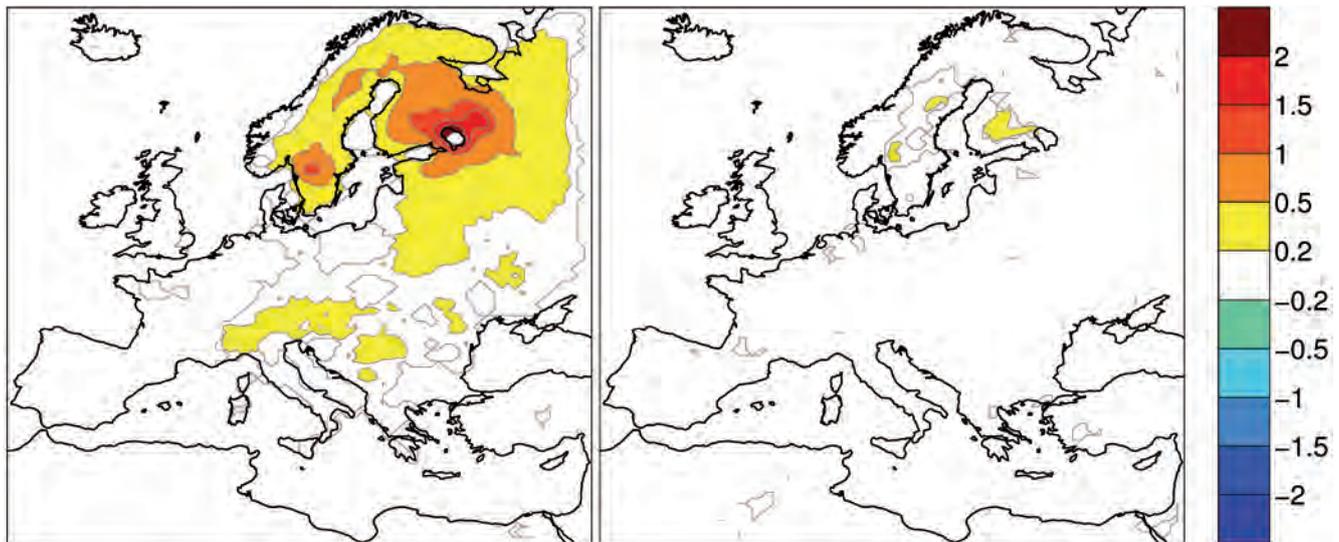
Figure 2.7. Differences in simulated air temperature (°C) at 2 m from the RCA model with lakes (coupled with FLake lake model) and without lakes (open land) for winter (left) and spring (right) 1961–90. The grey lines indicate areas for which p=0.05 (t-test). The null hypothesis is rejected and mean differences for areas within grey lines do not contain 0 at a 95% confidence interval level. Note that p ≤0.05 for all coloured areas. (Swedish Meteorological and Hydrological Institute)

of the Rossby Centre Atmospheric (RCA) model runs (1961–1990) with lakes (RCA and FLake lake model flux coupled) and without lakes, where all lakes in the RCA domain are replaced by land, shows that lakes induce a warming effect on European air temperatures 2 m above open land. This is particularly evident over northern Europe where there are many lakes covering a large area. Particularly interesting is the warming effect lakes have in the winter when ice cover is prevalent. One contributing factor to this winter warming is the heat transfer through the ice and overlying snow to the atmosphere, which can be on the order of 10 W m$^{-2}$ higher than the heat flux from the surrounding land (Jeffries et al., 1999). Although Regional Climate Models (RCMs) and NWP models are increasingly being coupled to lake models, the representation of snow-cover properties and processes in the latter is either done simplistically or not at all. As a result, there is a significant degree of uncertainty in the magnitude of heat transfer to the atmosphere predicted by atmospheric-lake models.

River-ice also affects an extensive portion of the global hydrologic system, particularly in the northern hemisphere where major ice-cover develops on 29% of the total river length and seasonal ice affects 58% (Prowse et al., 2007). It is also an important modifier of numerous biological, chemical, and hydrologic processes, and is capable of causing extensive and costly damage to infrastructure (ice jams, flooding). Scientific concern has been expressed about how future changes in climate might affect river-ice regimes (e.g. Anisimov et al., 2001; Walsh et al., 2005). In the context of regional hydrological studies, the coupling of atmospheric and river-ice hydraulic/thermodynamic/mechanical models is very much an area of research.

To improve our understanding of lake and river ice processes and the prediction of ice-cover regimes with climate warming, observations of ice thickness and snow on ice, and further refinement of models of lake-ice growth and river-ice dynamics are needed.

### 2.2.5 Sea-ice Thermodynamics and Mass Balance

Sea ice has an impact on Earth's radiation balance, the exchange of heat and momentum between the ocean and the atmosphere, deep-water formation

and other important ocean processes. It has a strong influence on regional climate, on marine and coastal habitats in the Arctic and Antarctic, and on maritime traffic and operations in polar regions. The high albedo, low thermal conductivity, and freshwater content of snow on sea ice, amplify the importance of sea ice in the atmosphere-ice-ocean system (Warren et al., 1999). Land-surface snow seems to respond to sea-ice loss; increased snow cover in Siberia during autumn and early winter is correlated with decreased Arctic sea-ice in September (Gathak et al., 2010).

Satellite data have shown a decline of 2.7±0.6% per decade in the annual mean of Arctic sea-ice extent since 1978 (Lemke et al., 2007). The decline of summer extent is larger than in winter, with the summer minimum declining at a rate of 7.4±2.4% per decade from 1979–2006, which is faster than climate models predict (Stroeve et al., 2007). In the summer of 2007, Arctic sea-ice extent reached a record minimum. There is no sign that this long-term trend is reversing as the 2011 summer minimum was similar to the 2007 record (National Snow and Ice Data Center (NSIDC) 2011). In contrast, sea-ice extent in the Southern Ocean has remained constant or has slightly increased, which is partially down to the importance of relatively thick snow-cover for the mass balance of Antarctic sea-ice through snow ice and superimposed ice formation (Massom et al., 2001; Haas et al., 2001; Screen, 2011).

The thickness of Arctic sea-ice has also decreased in recent years, with Arctic-wide reductions estimated at 10–15%, and up to 40% regionally between the 1960s and 1990s (ACIA, 2005), and a 53% reduction between 2001 and 2007 around the North Pole (Haas et al., 2008). The low sea-ice coverage in 2007 led to a net ocean-atmosphere heat output about three times greater than observed in previous years, suggesting that sea-ice losses are now playing a role in increasing surface air temperatures in the Arctic (Kurtz et al., 2011). Stratification of the Arctic Ocean and the presence of sea ice depend strongly on the input of freshwater from river runoff. Although the Arctic Ocean comprises only 1.5% of the world's ocean waters, it receives 10% of the global river runoff. This is dominated by the melting of snow in Siberia and North America. Sea ice break-up and melting in spring are strongly affected by thermal forcing owing to river runoff.

Snow that covers sea ice has important implications for the formation and mass balance of the ice. Most ice forms in leads and polynyas, regions of open water and thin ice (ice thickness <50 cm), with little snow cover. These are also the regions with the largest ocean-atmosphere heat flux (Fig. 2.8), which is strongly dependent on the thickness of new ice and snow
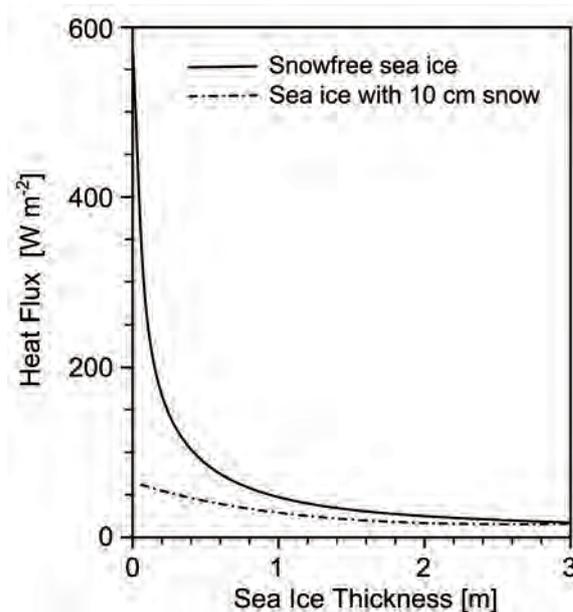


Figure 2.8. Dependence of the ocean-atmosphere heat flux on sea-ice thickness for snow-free and snow-covered sea ice for typical Arctic winter conditions. Input parameters: air temperature −25°C, cloud fraction 0.5, wind speed 6 m/s, relative humidity 0.9, and no shortwave flux. (Adapted from Kurtz et al., 2011)

(Kurtz et al., 2011). These parameters are not observed by any available satellite sensor. Information on snow cover is also necessary to support ice-thickness retrievals from altimeter data, as provided by missions such as CryoSat. Advancing our understanding of sea-ice processes and the fate of sea ice in a warming Earth requires improved observations of snow mass and melt processes, as well as of polynya processes and new ice formation.

## 2.3 The Need for Improved Snow and Ice Observations

### 2.3.1 Observation Needs: Terrestrial Snow

#### 2.3.1.1 Representation of snow in climate, meteorological and hydrological models

An accurate description of the land surface, including terrestrial snow cover, is of fundamental importance for advancing numerical weather forecasting, and the assessment and prediction of climate change. To obtain an accurate estimate of initial conditions, advanced data assimilation systems and observations are needed. ECMWF applies a four-dimensional variational data assimilation system (4D-Var) for their GCM, which uses more than 5 000 000 observations every 12 hours from satellites, radiosondes, synoptic stations, etc. A new snow scheme was introduced in the ECMWF forecasting system in 2009. This includes a new parameterisation of snow density, and revised formulations for the sub-grid snow-cover fraction and snow albedo (Dutra et al., 2010). Snow-depth data at approximately 1500 stations are used for the global snow-depth analysis applying Optimum Interpolation, but the stations are very unevenly distributed and lack information about the mass of water, which is crucial for model validation. Consistent, spatially-distributed data on snow mass are needed to perform proper model initialisation and validation. However, there is generally insufficient confidence in remotely-sensed SWE data and representativness of *in situ* SWE measurements to back up the models.

As snow cover is heterogeneous on scales smaller than GCM grids, parameterisations are used to calculate snow-cover fraction from gridbox-average snow masses and surface characteristics (Liston, 2004; Clark et al., 2011; Liston & Hiemstra, 2011). Owing to the shortage of reliable high-resolution measurements of snow extent and mass, these parameterisations have, so far, been mostly empirical and highly generalised, limiting the diagnostic power of the models to infer impacts of changing snow distributions on weather and climate and impairing the estimate of snow/atmosphere energy exchange (Fig. 2.9). This is even more critical for mesoscale numerical models, where
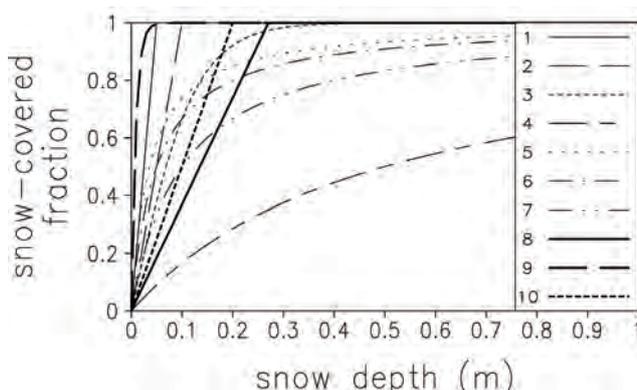


Figure 2.9. Snow-fraction parameterisations used within 14 land surface and large-scale atmospheric models (Liston, 2004; Liston and Hiemstra, 2011). The parameterisation has a large impact on the modelled surface-atmosphere heat transfer. (Liston, 2004)

resolutions are now approaching the 1 km scale (e.g. MeteoSwiss, 2011; ZAMG–Austrian Weather Service, 2011).

The spatial variability of snow accumulation and depletion is also very important for determining the timing and amount of snowmelt runoff (Luce et al., 1999). Physically based, distributed or semi-distributed runoff models provide a good basis for investigating hydrological processes and studying the response of the water cycle to climate change. These models are also useful for water-resource management and flood forecasting, because they can be calibrated better for a range of different boundary conditions than empirical models (Blöschl, 1999; Maurer et al., 2010). The climate research and hydrological communities stress the need for high-quality distributed snow-extent and snow-mass data to initialise and validate models of snow accumulation and melt to advance the parameterisation of the energy and water cycle of cold regions in water, weather and climate models.

In addition, to reduce the uncertainty of energy balance and trace-gas fluxes in northern latitudes, spatially-detailed snow measurements, as to be delivered by CoReH$_2$O, are required. Key factors for surface energy partitioning and trace-gas exchange in these regions are snow cover, cloud cover, and the temperature gradient in the soil. Because of the small-scale heterogeneity of surface cover and snowpacks in tundra regions, the spatial variability of energy and mass fluxes is high (Langer et al., 2011), so that spatially-detailed data are needed to improve the parameterisations of these processes.

### 2.3.1.2 Shortcomings in current snow observations

A comprehensive overview on the status and deficits of current snow observations has been published (IGOS, 2007). The main snow parameters for meteorology, hydrology and climate monitoring are snow extent and SWE. SWE and snow-depth data are typically based on *in situ* measurements that are carried out at fixed points. However, snowpacks are spatially heterogeneous and cannot be described reliably by point measurements as the snow-cover patterns are governed by effects of topography, land cover, wind redistribution, solar irradiance, and air temperature (Anderton et al., 2004; Trujillo et al., 2009). Moreover, worldwide, many surface-based snow observation networks have been abandoned in the last few decades. Whereas snow depth is reported in the WMO synoptic code, SWE is largely based on very limited special station networks or snow courses with large differences in quality and density of observations.

There are significant deficiencies in current satellite-based snow observations. Optical sensors operating at visible and near-infrared wavelengths supply information on the areal extent and albedo of snow cover. Medium-resolution optical sensors are widely used such as the Advanced Very High Resolution Radiometer (AVHRR) on NOAA and MetOp satellites, the Moderate Resolution Imaging Spectroradiometer (MODIS) on the Terra and Aqua satellites, and the Advanced Along Track Scanning Radiometer (AATSR) on Envisat. Optical sensors suffer from cloud obscuration and deliver no information on SWE. C-band imaging radar sensors, on Radarsat, Envisat and the upcoming Sentinel-1, can be applied for mapping the extent of melting snow, using a change-detection algorithm (Nagler & Rott, 2000). However, C-band radar is not sensitive to dry snow or to SWE.

ESA's Data User Element (DUE) GlobSnow project (*www.globsnow.info*) delivers long-term datasets (15–30 years) on snow extent based on optical AATSR data at a resolution of 1 km and daily maps of SWE based on microwave radiometry (SSM/I, AMSR-E) at 25 km resolution for climate research purposes. As an example, Fig. 2.10 presents the snow extent and SWE estimated for the northern hemisphere for March 2003. The SWE product on a 25 km grid is produced through the assimilation of coarse-resolution microwave radiometer data with discrete weather station observations of snow depth

Figure 2.10. The ESA GlobSnow SWE product of the northern nemisphere in March 2003 based on satellite microwave radiometer data. Mountain regions with high topographic variability within the pixels of 25 km resolution are masked off. (FMI)
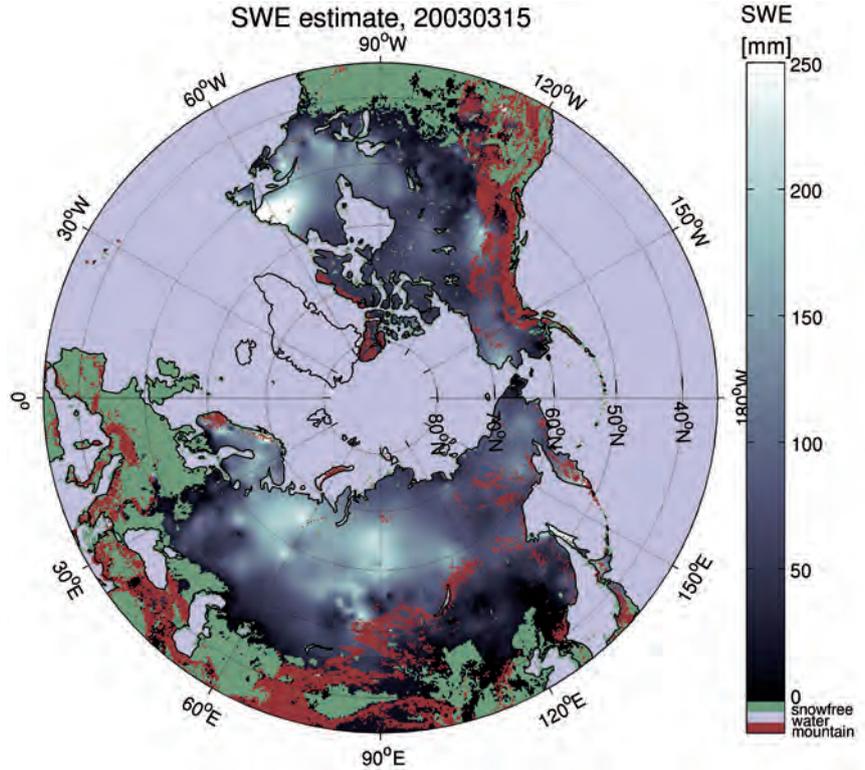
(Takala et al., 2011). Mountains are masked owing to saturation of the signal and heterogeneity of snow and land cover within a pixel.

With regard to SWE and snow depth, satellite microwave-radiometry is presently the only option for mapping these parameters over large areas. Owing to the coarse resolution, these retrievals are suitable for extended regions with homogenous snowpack and land cover, but miss the requirements in mountainous terrains. Even in areas with moderate topography, the snowpack can be quite heterogeneous owing to snow drift or complex land-cover (Berezovskaya et al., 2010), which affects the quality of the derived snow-cover product.

Presently, even point models reveal significant differences in simulating snow mass and properties, as the Snow Model Intercomparison Projects SnowMIP-1 and SnowMIP-2 show (Fig. 2.11) (Etchevers et al., 2004; Rutter et al., 2009). These difficulties extend from point models to regional and global models. The second phase of the Atmospheric Model Intercomparison Project (AMIP-2) found that GCM simulations of snow extent show large differences between individual models (Frei et al., 2003). Even SWE mean values of the models over several years show large regional biases (Fig. 2.12).
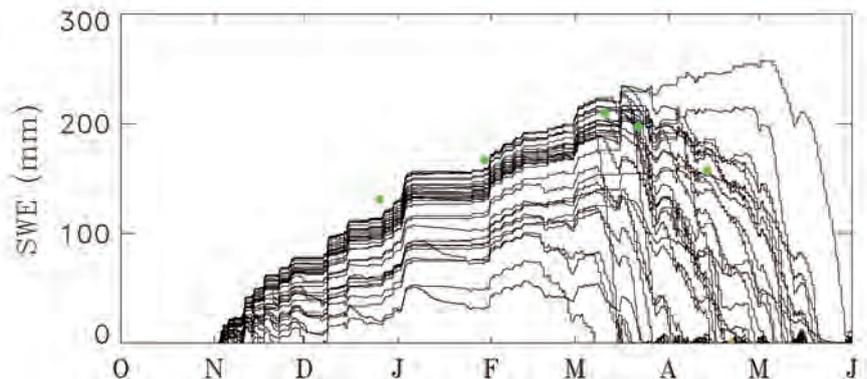


Figure 2.11. Uncertainty in snow process modelling is illustrated by comparison of 33 point models (lines) and SWE measured in snow pits (green dots) at Fraser, Colorado, US in winter 2003–2004 (Rutter et al., 2009). (University of Edinburgh)
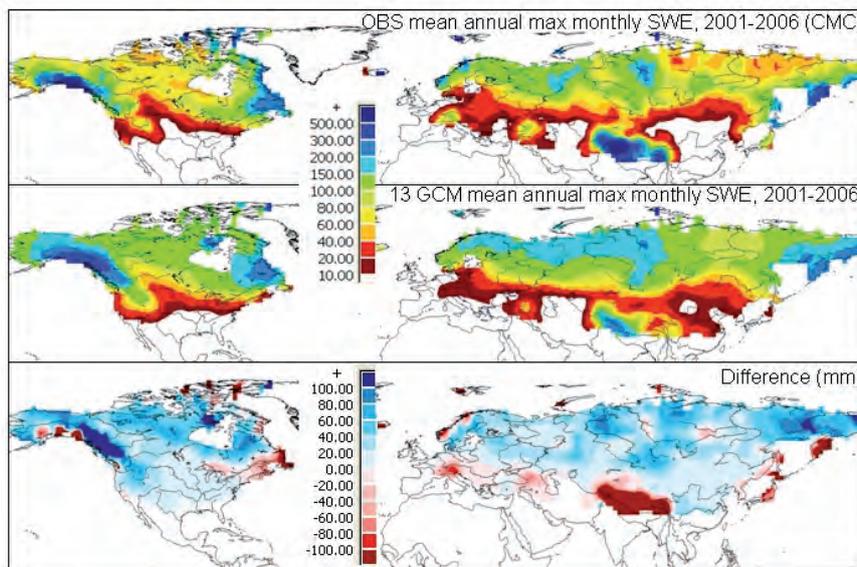
Figure 2.12. Comparison of SWE max (mm) estimated from Canadian Meteorological Center daily global snow-depth analyses for 2001–06 based on *in situ* data with 13 GCM mean SWE max and mean model bias. (Adapted from Brown & Mote, 2009)

Since there is a lack of suitable datasets on SWE, the representation and validation of snow in GCMs and mesoscale models remains unsatisfactory, both in the accumulation and the snow-melt period (e.g. Navascués et al., 2003). This is attributed largely to inconsistencies in the various snow-cover datasets (Ge & Gong, 2007). Assimilation of spatially distributed SWE measurements would be able to improve the cryosphere component of mesoscale models significantly (Jin & Miller, 2007). One of CoReH$_2$O's primary objectives is to provide SWE measurements for this purpose.

### 2.3.2 Observation Needs: Glacier Mass Balance and Runoff

The mass balance of glaciers, ice caps and ice sheets is an important parameter for climate research and hydrology (Oerlemans, 2001). Motivations for mass balance studies are to:

— Derive past climate signals from historic glacier fluctuations by means of inverse modelling.

— Quantify and model the water supply from glaciers and predict the impact of climate change.

— Discover how glaciers respond to climate signals and contribute to sea-level rise.

Most information about volume changes in large ice masses comes from satellite altimetry (Shepherd & Wingham, 2007). Over mountain glaciers, temporal changes in surface topography, mapped by airborne or satellite-borne imaging sensors, are used to determine volume changes (Cogley, 2009; Fischer, 2011). These geodetic measurements have been used to estimate total mass changes for selected glaciers at annual or multiyear intervals. The measurements cannot be directly related to atmospheric forcing. To model the glacier response to climate change and quantify glacier-melt contributions to the water balance, it is necessary to know the individual components of the surface mass-balance at comparatively high-spatial resolution. These data are highly complementary to measurements of topographic change by CryoSat, IceSat and other altimetry missions.

The annual mass-balance of mountain glaciers has been determined traditionally by the glaciological method (Kuhn et al., 1999), using labour-

Figure 2.13. Map of snow accumulation in mm water equivalent (end of winter 2003–04) on Vernagtferner (glacier), Ötztal Alps, Austria, based on field measurements. (Bavarian Academy of Sciences, Munich & ENVEO)
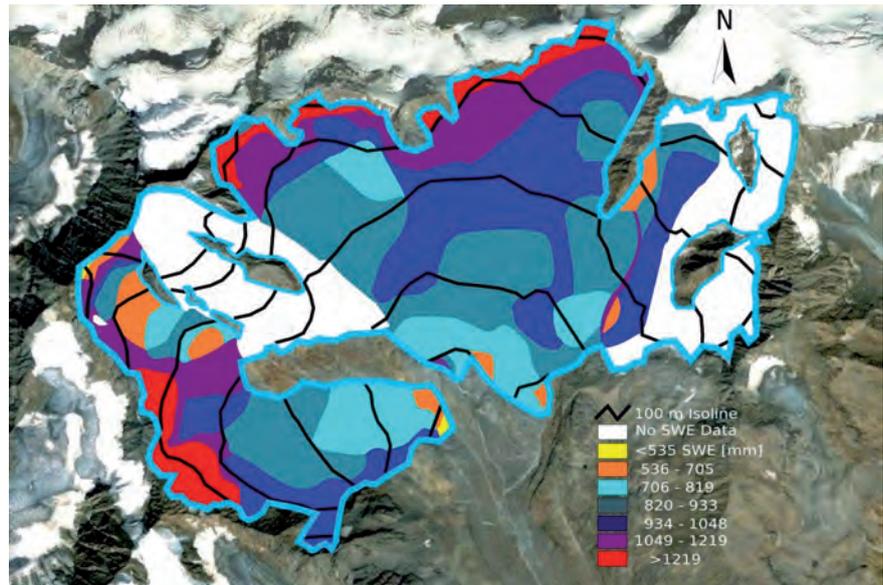
intensive point measurements of ablation and accumulation at representative points over a glacier. There are only about 50 glaciers worldwide with annual mass-balance measurements over relatively long periods (>20 years). These tend to cluster in a few regions and are biased towards small glaciers (Dyurgerov & Meier, 2002). This results in large uncertainties for regional and global assessments (Key et al., 2007; Braithwaite, 2009).

In order to augment the mass-balance database, various types of models are used to calculate mass balance as a function of meteorological and physiographic data (Oerlemans, 2001, Rott et al., 2008). The models range from simple correlations with climate data to spatially-distributed models that consider the physical processes determining the exchange of energy and mass between the glacier surface and atmosphere. Calibration of the models is supported by mass-balance field measurements available only for very few glaciers (Braithwaite, 2009). A main input parameter for the models is snow accumulation. Figure 2.13 shows a map of snow accumulation at the end of winter in 2003–04 on Vernagt glacier, Austria, based on a dense network of *in situ* point measurements (Escher-Vetter et al., 2009).

Snow accumulation is a main error source for mass-balance modelling, as this parameter is often governed by small-scale orographic effects. Even if a high-resolution meteorological model were available, large corrections are needed on snowfall to adjust model-predictions to field-measured accumulation. Gerbaux et al. (2005), for example, report a typical adjustment factor of 1.5 for winter accumulation on French glaciers. Mass-balance models need high-quality precipitation input to be extended to unsurveyed glaciers. This emphasises the need for improved remote-sensing tools to measure snow accumulation, as to be provided by CoReH₂O.

### 2.3.3 Observation Needs: Lake and River Ice

Surface-based observations were once the most important source of information regarding lake-ice and river-ice conditions. Their analysis has provided much of the evidence on the impact of climate warming on ice conditions at regional and global scales. The declining state of the surface-based networks since the mid-1980s in many northern countries has led to serious geographical and temporal gaps for several ice parameters (e.g. freeze-up and break-up dates, ice thickness and on-ice snow-depth) used both to monitor the impact of climate and to validate numerical freshwater ice models. Observations of area, dates of ice formation and melt, ice types, snow

accumulation on ice, and ice thickness from high-frequency SARs are needed to validate and improve the representation of snow and ice processes in lake and river hydrologic/hydraulic models.

With improvement in the resolution of climate and weather-forecasting models, and the realisation that lakes have an important influence on local and regional climates (e.g. Rouse et al., 2005; Rouse et al., 2008a), work is ongoing to develop ways of better representing lakes and their effect in atmospheric models (Kourzeneva et al., 2008; Eerola et al., 2010; Samuelsson et al., 2010). Observations of ice-covered areas are particularly useful for validating and improving lake-model schemes coupled to RCMs and NWP models. In northern latitudes, the performance of atmospheric models is strongly affected by the accuracy of initial conditions and the representation of lake ice and on-ice snow properties and processes.

One parameter that causes a high degree of uncertainty in lake model estimates of ice break-up dates, ice type and composition (including clear-ice and snow-ice), ice growth (thickness) and the resulting energy exchange with the atmosphere is snow accumulation (depth and density) on the ice surface. Currently, snow depth information used in lake models comes from measurements taken at weather stations on land or from atmospheric reanalysis. Snow can be strongly redistributed over open areas such that actual snow depth on ice tends to represent only a fraction of the amount measured over land (Duguay et al., 2003; Brown and Duguay, 2011a,b). The impact of various scenarios of snow depth (100–0%) on simulated total ice-thickness and the fraction representing snow-ice formation owing to slushing events (i.e. refrozen snow at the snow-ice interface) is illustrated in Fig. 2.14. Lake-ice model simulations conducted over two winters at a lake near Churchill, Canada, show that a small change in snow accumulation on the ice surface can have a substantial effect on the rate of ice growth, ice composition, the timing of ice melt, and consequently energy exchange with the atmosphere. This experiment clearly illustrates the need for quality observations of snow-accumulation depth on ice as to be provided by CoReH$_2$O.

Figure 2.14 is also relevant for hydrological models. Some of the current models that represent river ice include relatively simple 1D thermodynamic

Figure 2.14. Canadian Lake-Ice Model simulations of snow on ice (red), depths of snow ice (green) and total ice thickness (blue) for various snow-cover scenarios (0, 5, 10, 25, 50 and 100% accumulation from amount measured at a nearby weather station on land) to represent potential snow redistribution on the ice surface at Malcolm Ramsay Lake, Churchill, Canada. (Brown & Duguay, 2011b)
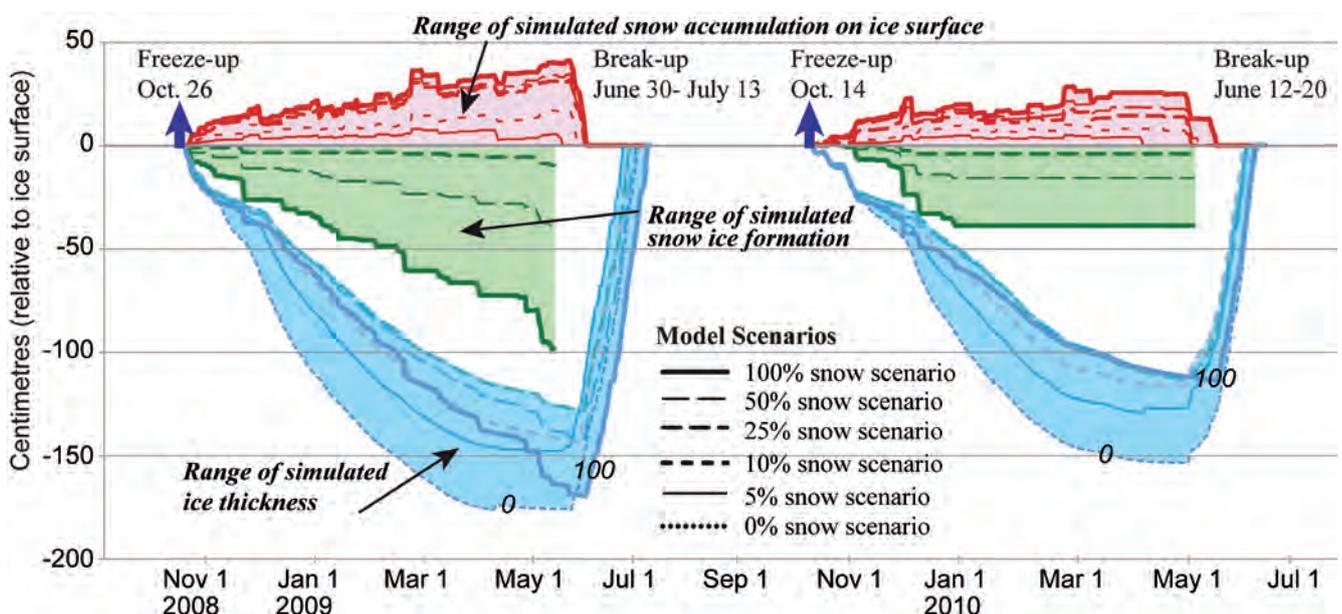
ice-growth models to simulate the timing of ice formation, development of ice thickness, snow on ice and melting of the ice (Vehviläinen et al., 2005). For rivers, 1D models are applied as small lakes along river segments. Observations of ice and snow lying on ice acquired by high-frequency SAR systems are necessary to verify and improve ice models used in hydrological/hydraulic models.

## 2.3.4 Observation Needs: Sea Ice

To date, observations of sea-ice produced routinely for climate monitoring comprise measurements of ice extent and concentration from low-resolution passive-microwave radiometry, and sea-ice surface temperatures from passive microwave and infrared radiometry. In addition, C-band radar is applied to monitor sea-ice extent, type, roughness, drift, melt, and other processes, both in high-resolution SAR and low-resolution scatterometer mode. However, there are various properties and processes that need to be better observed (Key et al., 2007). These include:

— Snow accumulation and melting processes on sea ice. These are also of great relevance to the freshwater balance of the Arctic Ocean.

— Ice formation and ice thickness in polynyas and leads, and their temporal evolution.

High-frequency SARs (Ku- and X-band), complementing existing C-band radar sensors, are promising tools to measure important observables required for studying and modelling these processes. The backscattering response at X-band is mainly caused by volume inhomogeneities in the upper part of the ice (Dierking et al., 1999). The relevance of Ku-band observations for sea-ice studies (extent, melt onset, and area balance) has been demonstrated with satellite scatterometry (Yueh & Kwok, 1998; Nghiem et al., 2005). However, the observation of snow burden and thin ice-thickness requires dual-frequency and dual-polarisation capabilities.

Because there are no operational snow-thickness data available, most modelling and remote-sensing studies (including ice-thickness retrievals by CryoSat) rely on snow thicknesses from a climatology derived from *in situ* measurements (Warren et al., 1999). In the Arctic, snow thickness varies seasonally and regionally, measuring 0.0–0.4 m. Therefore, estimates with an accuracy of better than 0.1 m are required. A snow layer of 0.1 m reduces the heat flux from the ocean to the atmosphere by 40% in 0.8 m-thick ice. The snow on Antarctic sea-ice cover is generally thicker, typically measuring 0.2–1.2 m in thickness (Massom et al., 2001).

Some experimental work has been performed to determine the thickness of thin ice and to classify different thickness classes in polynyas and leads using radar data. These are the regions of largest ice production and deep-water formation, and polynyas are frequently referred to as ice factories (Busche et al., 2011; Fig. 2.15). Models based on air temperature and the prevailing wind direction and velocity (e.g. Haarpaintner et al., 2001) calculate the ice production in polynyas. They always rely on the assumption of a certain, initial consolidated ice-thickness, which is generally unknown. Low-resolution Ku-band satellite data indicate considerable sensitivity of backscatter to the properties of thin ice and snow burden (e.g. Howell et al., 2005; Kern et al., 2011; Nihashi et al., 2011; Walker et al., 2006; Willmes et al., 2011). However, high-spatial resolution is required to deliver robust and accurate estimates of thin ice-thickness in the regions of polynyas and to delineate individual bands and gradients therein.

Leads are other important areas of high ice-production. Regions of increased lead activities, 'linear kinematic features', extend    hundreds
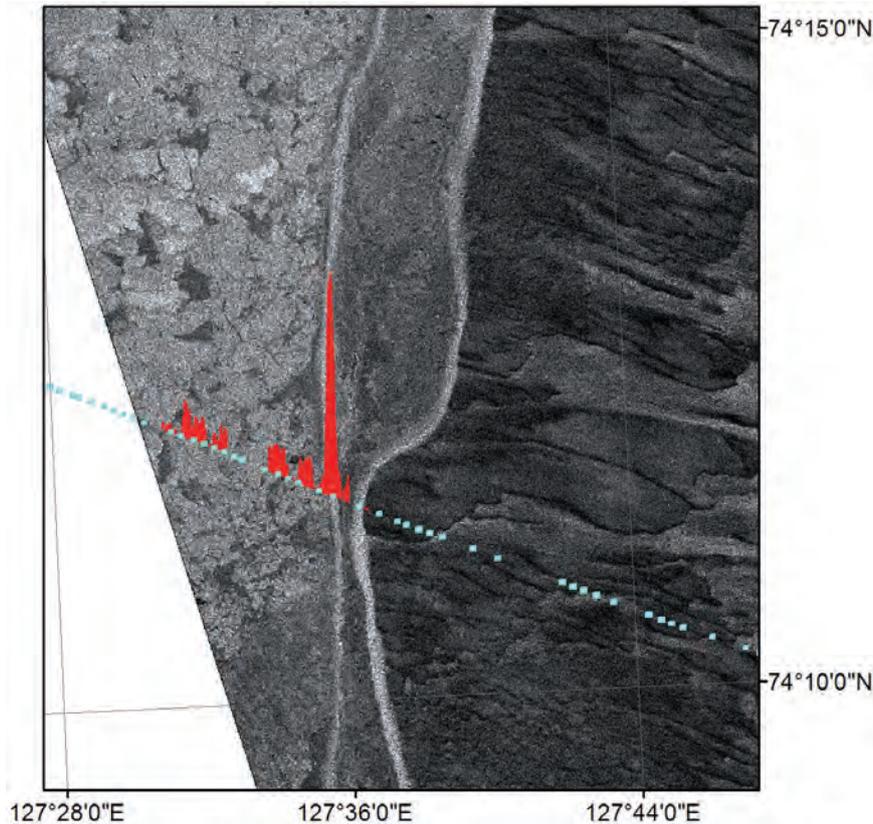
Figure 2.15. Costal polynya, Laptev Sea. Subset of the TerraSAR-X stripmap scene, X-band, HH, 28 April 2008, with thickness profile overlay. The dark grey area in the right of the image is the new ice with a fraction of open water. Light grey bands represent the border where the young ice hits the consolidated pack ice. The left part of the image is the consolidated ice zone, with bigger floes. (Adapted from Busche et al., 2009)

of kilometres across the Arctic and Southern Oceans. Estimates of ice formation in these leads still relies on simple freezing-degree-day models. Estimation of lead ice-thickness using high-frequency SAR sensors such as CoReH$_2$O would improve the understanding of the contribution of lead opening and deformation to the sea-ice mass balance, and would enable the parameterisation of these processes in sea-ice and climate models. As Fig. 2.8 demonstrates, the thickness of ice cover and snow burden on ice strongly determine the magnitude of the ocean-atmosphere heat flux. NWP and climate models require better parameterisations of heat fluxes from leads, polynyas, and the marginal ice zones.

## 2.4   Scientific Questions

CoReH$_2$O will deliver observations on key parameters of the cryosphere, helping to close gaps in the knowledge of the Earth system related to the following scientific questions:

— Q1. How much freshwater is stored in snow and ice masses, and how can we improve the representation of these resources in hydrologic models?

As reduced runoff from snow and dwindling glacial reserves becomes a reality, the availability of freshwater for human consumption, agriculture, energy production and transportation in many regions of the world is at risk. Significant spatial and seasonal changes in local, regional and global snow-water storage are anticipated because of global warming (Kundzewicz et al., 2007). Predicting the impact of climate change on the future availability of snow and glacial meltwater is crucial for preparedness and timely actions (Parry et al., 2007). Advanced observations are needed to evaluate freshwater

storage at multiple scales, quantify uncertainty in these estimates, and provide improved initial conditions for hydrologic predictions.

— Q2. How can we represent snow and ice feedbacks more accurately in models of the climate system and reduce cryosphere-related uncertainties in climate predictions?

Substantial uncertainty remains in the magnitude of cryospheric feedbacks, impairing the predictability of climate variability and change (IPCC, 2007; Randall et al., 2007). Evaluations of cryospheric effects in models consistently point to the need for sub-grid scale representation of snow and ice, and for observations at commensurate scales to validate and improve weather and climate models and predictions.

— Q3. How can we improve downscaling of climate models to estimate regional- and local-scale climate change?

One of the greatest challenges lies in predicting effects of regional and local changes in the climate. To accomplish this, climate models must be downscaled. This requires accurate representation of snow and ice processes, which are known to have a very strong impact on the climate from the global down to regional and local scales (Randall et al., 2007). Due to the shortage of reliable measurements of snow mass at high resolutions, parameterisations of snow processes have, so far, been highly generalised, limiting the diagnostic power of the models with regard to snow distributions and snow/atmosphere interactions.

— Q4. How does cryospheric change affect permafrost, the carbon cycle and greenhouse-gas exchange?

Major feedbacks from changes in high-latitude ecosystems are expected to enhance climate change, as trace-gas fluxes and net-carbon exchange respond to variations in tundra vegetation and permafrost. The carbon cycle and greenhouse-gas exchange are two of the most uncertain components in high-latitude climate change; both intrinsically involve snow and ice through surface-atmosphere exchange processes, which are strongly affected by spatially variable snow distributions. High-resolution snowpack observations are necessary to resolve and quantify these distributions, and assess changes over time.

— Q5. How can we better understand historical and current changes in climate by quantifying processes governing the mass balance of glaciers and ice sheets?

Glaciers and ice sheets are among the most responsive indicators of climate change, but very poorly represented in climate models. Relating observed changes of mountain glaciers to climate parameters is critical for understanding the factors governing the present downwasting of glaciers, and for improving parameterisations for glacier response to climate change to reconstruct climate history from records of past glacier extent. The annual and seasonal surface mass-balance are needed for glaciers worldwide. This would provide a comprehensive view of glacier response, and separate signals of local and regional climate forcing from large-scale factors. Numerical mass-balance models, used for studying glacier-climate relations, require winter snow-accumulation as a key input. This is presently not available with the accuracy needed. Better snow accumulation data are required to quantify glacier-climate relations.

— Q6. How do changes in the properties of lake ice affect regional weather and climate?

The greatest terrestrial source of water vapour in high latitudes is evaporation from lakes (Rouse et al., 2008b), strongly influencing landscape-scale evaporative and sensible heat inputs to the atmosphere, and therefore local and regional meteorological processes (Rouse et al., 2005). The duration of lake ice is dominant in the control of the seasonal heat budget of lake systems, determining the magnitude and timing of evaporation. In addition, during the winter, lakes conduct heat through the ice to the atmosphere and the magnitude of this flux is strongly influenced by snow and ice thickness. Consequently, predictive weather and climate models for high latitudes must represent lake-ice processes accurately. Advanced observations of properties of lake ice and snow burden are needed to validate and improve these models.

— Q7. What is the role of snow and thin ice for sea-ice thermodynamics and mass balance?

The fate of sea ice depends not only on changes in thermodynamics and dynamic boundary conditions, but also on changes in precipitation and snow accumulation. The competing effects of insulation and snow-ice formation on sea-ice mass balance are important, but poorly known at appropriate spatial and temporal scales. Improved predictions of sea-ice mass balance can only be gained with better estimates of properties of the snow burden. Also the occurrence of leads and polynyas and the thickness of their ice cover are key factors for the magnitude of the ocean-atmosphere heat flux in high latitudes, but comprehensive information on relevant physical properties of thin ice is not available.

## 2.5  Overview of the Mission Concept

The scientific questions emphasise the requirement for spatially-detailed observations of the physical properties of seasonal snow-cover, glaciers and ice sheets, freshwater ice, and sea ice. The primary geophysical parameters to be measured by CoReH$_2$O are the extent and water equivalent of seasonal snow-cover and winter snow-accumulation on glaciers. The mission's capabilities are also of great interest for observing ice type (with the emphasis on thin ice) and snow depth on sea ice and freshwater ice. These observational requirements can be achieved by a dual-frequency (X- and Ku-band), dual-polarised SAR. The high frequencies are particularly sensitive to the physical properties of snow and ice volumes. The dual-frequency, dual-polarisation (co- and cross-polarisations) capability provides different sensitivities to surface and volume scattering contributions, as required for snow parameter retrieval. Measurements at both frequencies need to be near simultaneous to avoid ambiguities that could result from temporal changes in snow and ice properties driven by meteorological forcing.

The spatial and temporal scales of the various scientific topics suggest the operation of the mission in two different temporal observation phases. A three-day repeat cycle would provide observations for a subset of the global snow and ice areas at a timescale compatible with meteorological forcing in high- and mid-latitudes. In particular, this addresses cryosphere-atmosphere exchange and the parameterisation of snow and ice processes in hydrological and meteorological models. The second mission phase would provide comprehensive observations of the global cryosphere in roughly a two-week repeat cycle to study the global distribution and the seasonal changes of snow and ice masses, and to validate and downscale continental-scale hydrological and land-surface process models.

## 2.6    Unique Contributions of the Mission – the 'Delta'

The CoReH$_2$O mission concept is scientifically and technically unique. It will observe key parts of the water cycle and cryosphere that have not been addressed effectively by any other mission. The mission concept is a unique dual-frequency (X- and Ku-band), dual-polarisation SAR system to be operated in an innovative fashion to achieve the mission objectives.

### 2.6.1 Science Innovation

CoReH$_2$O is the first satellite mission dedicated specifically to measuring freshwater stored in snow on land surfaces and snow accumulation on glaciers and ice caps. It will provide spatially-detailed repeat observations of snow and ice properties for modelling and validating surface/atmosphere exchange processes, climate research, and hydrological applications from regional to global scales. This information cannot be obtained from conventional observation systems and not from any satellite mission presently in space.

CoReH$_2$O will provide a unique database for developing and testing downscaling techniques for cryospheric elements and processes to be applied in meteorological, hydrological and climate models.

Multiple science objectives requiring both high-spatial and temporal resolution and broad-spatial coverage are achieved through two mission phases. Studies of synoptic-scale processes of snow and ice with high-spatial and temporal detail are enabled during Phase-1, and thus contribute to improving the parameterisation of the cyrosphere component in land-surface process models and atmospheric-circulation models. Phase-2 will provide near-complete coverage of the cyrosphere over 2–3 annual cycles, delivering new, spatially-detailed information on global snow and ice masses for process studies and model validation.

CoReH$_2$O will deliver unique snow and ice products that are synergistic to altimetry missions such as CryoSat and the Sentinel-3 SAR altimeter. By addressing, in detail, the surface-atmosphere exchange processes and atmospheric forcing that drive snow and ice mass balance, CoReH$_2$O will provide the link between the topographic changes observed by altimetry missions and the relevant process parameterisations in climate models.

CoReH$_2$O will provide the database for calibrating and downscaling snow-cover products from coarse-resolution microwave radiometers and scatterometers.

By means of its dual-frequency, dual-polarisation capability and high-spatial resolution, CoReH$_2$O will enable better derivations of the thickness of thin sea-ice and of the snow burden to improve observations of key variables for the sea-ice mass balance and ocean-ice-atmosphere interactions.

The dual-frequency, X- and Ku-band, sensor capability, complementary and in synergy with the C-band of Sentinel-1, will provide a unique testbed for experimental studies on radar signal interactions, as well as for testing and advancing multifrequency electromagnetic forward and inversion models for bio- and geophysical parameters in various research fields.

### 2.6.2 Technical Innovation

The CoReH$_2$O payload is a unique, dual-frequency, dual-polarisation (X- and Ku-band) SAR system that exploits the sensitivity of these radar frequencies to physical properties of snow and ice under a wide range of target conditions. CoReH$_2$O will deploy the first Ku-band (17.2 GHz) SAR sensor in space, pushing satellite radar observations of Earth into a high-frequency band.

# → RESEARCH OBJECTIVES

# 3. Research Objectives

The CoReH$_2$O mission addresses urgent needs for improved information on the cryosphere component of the Earth system. Cryospheric processes, to be studied by the mission from regional to global scales, are coupled with other main components of the Earth system, in particular, the atmosphere and hydrosphere. The complex feedbacks and interactions of these dynamic processes are not well understood. Events at regional-scales may have global effects, and forcings by the global climate system may trigger widely diverse responses at regional scales.

## 3.1 Mission Objectives

In order to tackle the scientific questions highlighted in Section 2.4, a set of key scientific objectives has been defined. Based on the scientific priorities addressed in Chapter 2, the mission objectives can be grouped into primary objectives that will receive principal focus, and secondary objectives that are opportunities for the mission to help address important questions and challenges (Table 3.1). The objectives are directly linked to specific challenges in ESA's Living Planet Programme (SP-1304, 2006). The mission addresses directly four of the five components of the Earth system highlighted, namely the cryosphere (including water budgets), the land surface, the ocean, and the atmosphere (through surface/atmosphere exchange processes).

Table 3.1. CoReH$_2$O scientific objectives.

| CoReH$_2$O Scientific Objectives | Primary (P) or Secondary (S) Objective | CoReH$_2$O Science Questions Addressed | ESA's Living Planet Programme Challenges |
|---|---|---|---|
| 1. Quantify the amount and variability of freshwater stored in terrestrial snowpacks and snow accumulation on glaciers. | P | Q1 | Cryosphere challenge 3 |
| 2. Validate and improve predictive hydrology models to reduce uncertainties in streamflow forecasts. | P | Q1 | Cryosphere challenge 3 |
| 3. Validate and improve the representation of snow and ice processes and feedbacks in regional and global climate models to reduce uncertainty in predictions. | P | Q2 | Cryosphere challenge 3, Atmosphere challenge 1 |
| 4. Evaluate high-resolution snow distributions and assess their relationship to climate model grid scales to support development of improved downscaling techniques for local-regional climate models. | P | Q3 | Cryosphere challenge 3, Atmosphere challenge 1 |
| 5. Explore the distribution of snow properties in high-latitudes with focus on the implications for terrestrial carbon cycling, trace-gas exchanges and permafrost. | P | Q4 | Cryosphere challenge 5, Land Surface challenges 1 & 4 |
| 6. Evaluate the mass balance of a broad sampling of glaciers and ice caps worldwide to understand current changes and place them in historical context. | P | Q5 | Cryosphere challenge 2 |
| 7. Validate and improve lake-ice process models with observations of ice properties to reduce model uncertainty and assess effects of lake ice on surface energy exchanges. | S | Q6 | Cryosphere Challenges 3 and 5 |
| 8. Explore properties and distribution of snow on sea ice and of thin sea-ice to help understand their role in sea-ice thermodynamics and mass balance. | S | Q7 | Cryosphere Challenge 1 and 4, Ocean Challenge 2 |

CoReH$_2$O will contribute to these objectives through the following observations:

— Objective 1: Observations from CoReH$_2$O will be used fundamentally to estimate SWE and snow extent on land, and snow accumulation on glaciers, and to observe the variability of these parameters in time (Phase-1) and space (Phase-2). These quantities will be used to assess total freshwater storage in snow across multiple spatial and temporal scales. Improved accuracy, coverage and detail from CoReH$_2$O observations are expected to reduce uncertainties in current estimates of snow-water storage that are based on modelling and assimilation of limited datasets. CoReH$_2$O SWE and snow extent observations will be compared to estimates from relevant models and water budget assessments to evaluate their skill and determine uncertainty.

— Objective 2: Various physically-based snow models are used in hydrology forecasting. These models, forced by meteorological variables, are applied to simulate and predict the mass and energy fluxes of snowpacks. CoReH$_2$O observations of SWE, total snow-extent, and the extent of areas of melting snow will be used to evaluate the representation of snow processes in these models. The CoReH$_2$O time series observations in Phase-1 (three-day repeat) will be important for examining the ability of the models to respond to rapid meteorological forcings. The extensive coverage of CoReH$_2$O observations in Phase-2 (15-day repeat) will be used to evaluate the ability of the models (and their forcings) to represent spatial variability. These results will guide future investments in model improvement.

— Objective 3: Climate models can represent several snow and ice processes that are manifest by SWE, extent of snowmelt areas, and snow accumulation on glaciers. CoReH$_2$O observations of these variables will be used to evaluate the skill of regional and global climate models in representing cryosphere processes and interactions. These evaluations will support improvements in tools for simulating and predicting the magnitude, rate and timing of snow and ice masses in climate models.

— Objective 4: Spatially-detailed observations of SWE, snow extent, and snow depth delivered by CoReH$_2$O will be compared to corresponding climate model grid cells to assess overall model performance and representation of non-linear processes that result in spatially-variable snowpacks. Spatial aggregation of the high-resolution observations to larger grid scales will provide robust estimates of relevant spatial means and variance, and will help to determine improved strategies for downscaling cryospheric processes to local and regional scales. Furthermore, the high-resolution SWE observations from CoReH$_2$O will also help to validate SWE products of low-resolution microwave sensors and will support the development of improved snow-retrieval algorithms for these sensors.

— Objective 5: CoReH$_2$O observations of snow extent and SWE will provide information on the spatial and temporal distribution of snow-influenced boundary conditions for soil thermal regimes and permafrost at high latitudes to support inference about effects on net-carbon exchange and trace-gas exchanges. The spatial and temporal repeat coverage at high latitudes will enable high-resolution mapping of the seasonal evolution of these influences.

— Objective 6: The CoReH$_2$O winter-snow accumulation and glacier-facies observations will be used to estimate the mass balance of glaciers and their response to atmospheric forcing in glacier regions worldwide. This comprehensive and consistent view of glacier mass-balance and the driving

processes will help to better quantify the glacier volume and water supply response to climate change and to establish realistic future scenarios.

— Objective 7: Consistent $CoReH_2O$ observations of lake-ice extent and properties (including snow on ice and ice thickness) will be used to assess the performance and timing of lake ice processes in relevant models. These observations will be complementary to those from C-band SAR sensors, which cannot provide estimates of snow depth on ice necessary to calculate rates of ice growth and conductive heat fluxes with models. Results will be used to guide model improvements. A broad sampling of high-latitude lakes will be studied to evaluate snow on ice and ice effects on surface energy exchanges and associated uncertainties.

— Objective 8: Thin sea-ice types in polynyas and leads and their temporal evolution will be mapped for heat flux estimations, and for studying regional ice kinematics and dynamics in marginal ice zones. Also, $CoReH_2O$ observations of snow burden, snowmelt onset date, and snowmelt area will be used to study the effects of snow on surface heat fluxes and sea-ice mass balance. These observations are complementary to low-resolution sea-ice products of microwave radiometers and to sea-ice monitoring by C-band SAR, and have the potential to support the retrieval of sea-ice thickness by altimeters.

## 3.2 Potential Additional Research Contributions of $CoReH_2O$

The $CoReH_2O$ mission has great potential for contributing to the advancement of additional scientific topics for which snow cover information is of relevance. In addition, spare operating time (in particular during the northern hemisphere summer) will allow experimental use of the system for Earth observation tasks in other domains.

— Spatially detailed studies of rainfall: The dual-frequency backscatter measurements by $CoReH_2O$ offer interesting opportunities for spatially-detailed studies of rainfall over land and ocean (Marzano et al., 2008; Weinman et al., 2009). The relatively high-spatial resolution of $CoReH_2O$ data can provide new insight into the structure of precipitating clouds and, thus, will be highly complementary to measurements of rainfall rate by microwave radiometry. The sensor can potentially measure the slant-path integrated scattering and attenuation of precipitation in oblique directions. The dual-frequency, dual-polarisation approach should be useful for separating the backscattering and attenuation effects of the rainfall areas and background target, which would help to reduce the uncertainty in retrieved rainfall parameters. A prototype algorithm for retrieval of rainfall rates from SAR measurements, addressing the C- to Ku-band range, has been developed (Marzano et al., 2008; Weinmann et al., 2008).

— Studies on multifrequency microwave interactions with natural targets: $CoReH_2O$ will extend the overall frequency range of spaceborne SAR systems to the upper Ku-band. Occasions of overlapping swathes, e.g. with the Sentinel-1 C-band SAR will offer the opportunity to test and advance models of microwave interaction for a wide range of natural targets beyond snow and ice such as soil, vegetation, and water. This is of interest for the improvement of SAR bio-geophysical retrieval techniques and would provide important information for soil-vegetation-atmosphere transfer models.

# → OBSERVATIONAL REQUIREMENTS

# 4　Observational Requirements

The CoReH$_2$O mission will provide observations of snow and ice for applications in climate research, hydrology and meteorology. The definition of observational requirements builds on the needs defined in international planning documents, in particular, the IGOS *Cryosphere Theme Report* (IGOS, 2007) and the *Report on Satellite-based Products of the Global Observing System for Climate* (GCOS, 2006), as well as on input supplied by the scientific community at dedicated workshops. This chapter specifies the observational requirements and explains the measurement principle.

## 4.1　Geophysical Observation Requirements

The observations must provide spatially-detailed information on snow and ice with sufficient accuracy and resolution to meet the scientific objectives specified in Chapter 3. Observations from space are pivotal to obtaining the sampling density and coverage required for observing process-scale variability. The specifications of spatial scale address the needs of various terrain types, including areas of complex topography and heterogeneous land cover. Also, for the purpose of integrating the mission observations with ground measurements at study sites and for validation through field experiments, comparatively high-spatial resolution is required. At the same time, the mission observations must be made over space and timescales large enough to be representative of the areas and processes for which models need to be assessed and improved. This also requires appropriate temporal sampling. Finally, the accuracy and overall fidelity of the observations must be sufficient to improve skill of models, resolve process-related changes in snow conditions, and assess water balance in different regions and under various conditions.

### 4.1.1 Geophysical Parameters

The science objectives drive the specific requirements for observation of snow and ice parameters. The snow extent and SWE of seasonal snow cover and the snow accumulation on glaciers have been identified as main geophysical parameters for the mission, which will be delivered as primary Level-2 products (Table 4.1). The mission will also have the capability to measure a number of other important snow and ice parameters, listed in Table 4.1, as secondary parameters. These parameters are not system drivers, but nevertheless are very relevant for advancing the understanding and modelling of geophysical processes of the main elements of the cryosphere: seasonal snow cover, glaciers and ice sheets, freshwater ice, and sea ice.

The mass of snow on ground (SWE, in kg m$^{-2}$ or metre water equivalent) and snow extent are the main snow parameters for the hydrological cycle and for assessing climate impact on seasonal snow cover. SWE is related to snow depth (SD) by the relation SWE=SD·$\varrho$, where $\varrho$ is the mean density of the snowpack in kg m$^{-3}$. The backscatter data of CoReH$_2$O will be inverted with regard to SWE as a basic Level-2 product. SD can be estimated from SWE data by using a model for the evolution of snow density with time that is driven by meteorological input data (from numerical analysis or predictions) (e.g. Kazama, 1998; Douville et al., 1995). Separating dry and melting snow area extent is important for hydrological applications and climate studies. In the retrieval processing line the separation in dry snow, wet snow and snow-free surfaces is performed in the initial stage dealing with segmentation of surface types, based on multitemporal backscatter ratios (Nagler & Rott, 2000; Rott et al., 2011).

| Variable | | Spatial resolution (m) | | Temporal Sampling (days) | Accuracy (RMS) |
| --- | --- | --- | --- | --- | --- |
| | | Global | Regional | | |
| Primary Parameters | | | | | |
| Snow | Snow water equivalent | 500 | 200 | 3–15 | 3 cm for SWE ≤30 cm 10% for SWE >30 cm |
| | Snow extent (dry, melting) | 500 | 200 | 3–15 | 5% |
| Glaciers | Winter snow accumulation | 500 | 200 | ≤15 | 10% of maximum |
| Secondary Parameters | | | | | |
| Snow | Snow depth | 500 | 200 | 3–15 | 10% |
| Glaciers | Facies type | 200 | 200 | ≤15 | 5% of glacier area |
| | Terminus position, glacier lakes | 50 | 50 | ≤15 | 50 m |
| Lake and river ice | Ice area | 50 | 50 | 3–15 | 5% of ice area |
| | Freeze-up and melt onset | 50 | 50 | 3 | Date ±3 days |
| | Snow depth on ice | 200 | 200 | 3–15 | 3 cm |
| | Type and thickness of ice | 200 | 200 | 3–15 | 5% classification error; ±5 cm |
| Sea ice | Snow water equivalent | 200 | 200 | 3–15 | 3 cm |
| | Snowmelt onset date | 200 | 200 | 3 | Date ±3 days |
| | Snowmelt area | 200 | 200 | 3–15 | 5% of sea ice area |
| | Type and thickness of thin ice | 200 | 100 | 3–15 | 5% classification error; ±5 cm thickness |

Table 4.1. Key geophysical observation parameters and measurement requirements.

An essential measurement parameter for glacier mass balance studies is the winter snow accumulation: the SWE deposited on glacier surfaces. In addition, the area extent of diagenetic glacier facies is key information for studying mass balance trends and climate response of glaciers. Glacier facies are distinct zones in the top layers of glaciers and ice sheets that are related to accumulation, ablation and metamorphic state of snow and ice. The main facies types retrievable from SAR data are the dry-snow facies, the percolation facies, the wet-snow facies, the ice facies, transient melt areas, and surface moraines (Partington, 1998). In support of mass balance studies and for the assessment of glacier-related hazards, the regular repeat observation of glacier fronts and glacier lakes is also very important.

Key lake and river-ice parameters, such as snow depth (or snow mass) on ice, ice thickness and ice types are currently not available from other satellite mission operational products (e.g. MODIS Snow Cover of NOAA's Interactive Mapping System). CoReH₂O addresses this need with high-spatial resolution observations. The benefit here also includes the introduction of channels above the C-band which are more sensitive to the above parameters.

In order to meet IGOS sea-ice observation requirements (IGOS, 2007), CoReH₂O is able to provide measurements that are complementary to other satellite missions. CoReH₂O addresses, in particular, observations of new ice and its temporal dynamics including ice formation, thin-ice thickness and melt processes in polynyas and marginal ice zones, information which is crucial for quantifying thermodynamic processes. Knowledge of freshwater flux from rivers into the Arctic basin is essential for modelling ocean circulation. Also, snow accumulation and melting processes on sea-ice cover are of great relevance to the sea-ice mass balance and oceanic freshwater fluxes.

## 4.1.2 Temporal and Spatial Sampling Requirements and Coverage

The spatial resolution requirements in Table 4.1 meet the needs of distributed snow and ice process models and of climate models from regional to global scales. The regional products (50–200 m depending on the variable) account for heterogeneity of complex terrain and land cover. For global datasets the spatial resolution requirements are relaxed (up to 500 m); this can be matched by upscaling of swath products if required.

The geographic coverage includes all snow, land ice, and sea-ice areas. Acquisition masks have been elaborated for northern hemisphere winter/ southern hemisphere summer and for northern hemisphere summer/ southern hemisphere winter (Fig. 4.1). These maps represent the upper limit of coverage and are derived from mean (years 2000–10) monthly fractional snow-cover of more than 5% for January (derived from Hall et. al., 2006) and the mean (years 1979–2007) monthly fractional sea-ice extent greater than 5% for February (derived from Maslanik & Stroeve, 1999). During the summer, the proposed acquisitions include high mountains with glaciers and lasting seasonal snow, and high-latitude zones to provide the necessary snow-free background for regions with an early snow season. In the winter, the coverage is extended to include seasonal snow and sea-ice areas. For low relief terrain, single-view (descending) acquisitions are suggested. In addition, a mountain mask has been produced. This is based on global digital-elevation data, which covers the regions for dual view (ascending and descending orbit) SAR acquisition comprising 16% of the land areas. Through this acquisition strategy, favourable radar look-angles are obtained over all mountain areas. Zones of layover and foreshortening, which are not favourable for snow retrievals, can be omitted.
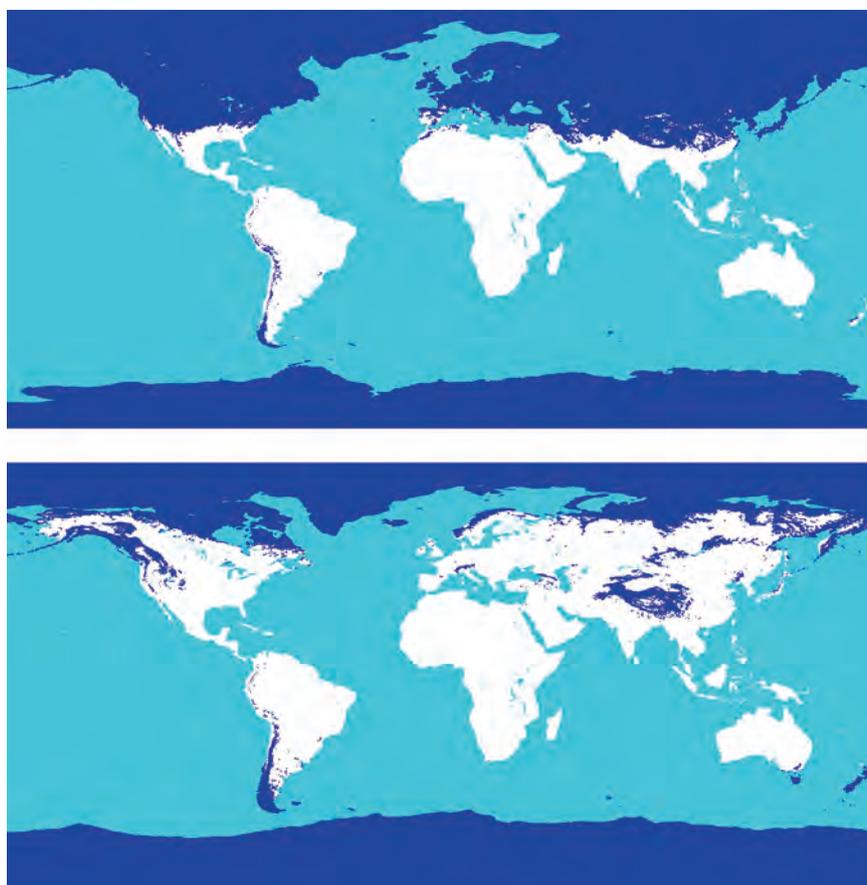


Figure 4.1. Masks for data acquisition during northern hemisphere winter/ southern hemisphere summer (top) and northern hemisphere summer/southern hemisphere winter (bottom) covering snow, land-ice and sea-ice areas (dark blue). (ENVEO)

The scientific objectives described in Chapter 3 address snow and ice processes over a range of temporal and spatial scales. Mission objectives call for observations resolving synoptic scale processes over different snow regimes, and on the other hand for observations of intraseasonal and inter-annual changes in snow accumulation and depletion at near-global coverage. For this reason two specific mission phases are proposed with emphasis on either temporal or spatial coverage:

— Phase-1 (Year 1 and 2) has a three-day revisit for snow and ice observations at timescales of typical mid- and high-latitude synoptic meteorological systems. During this phase, the emphasis is on advancing parameterisations of snow and ice processes in response to rapid meteorological forcing, in order to improve mesoscale atmospheric models, hydrological models, and land-surface process models. These observations will also support studies on effects of temporal sampling in different snow regions to prepare for possible aliasing effects of the longer repeat intervals in Phase-2 of the mission. Two snow seasons are required, starting with implementation and testing of the new data assimilation and parameterisation schemes in the first winter and validating the impact of satellite data and model improvements during the second winter. The spatial coverage of the three-day cycle is limited but suitable for the objective of model development and validation. It allows for the observation of a significant number of test sites in different geographic regions to cover the main snow regimes and glacier zones. Activities will include validation of data products at sites equipped with hydro-meteorological measurement systems, and the improvement and validation of regional-scale snow process models and hydrological models. A three-day revisit cycle is also appropriate for the observation of sea-ice processes in polynyas and marginal ice zones. In the first phase, the satellite should provide data products for at least 80% of the masks (as covered by a three-day orbit) provided in Fig. 4.1. Over some high-latitude areas, snow-cover changes are expected at a slower rate and, therefore, products with a 15-day revisit are sufficient.

— Phase-2 (Year 3+) addresses global patterns of snow accumulation within a single winter and variability between individual years. Near complete (> 85%) coverage of global snow and ice areas at a revisit period of 15 days is proposed. Data assimilation studies, performed in Nordic and Alpine snow regimes indicate that increasing the revisit time from three to 15 days would not significantly reduce the performance of snow process modelling owing to the long correlation time for accumulation (Essery et al., 2011). This behaviour will be further checked in Phase-1 for different geographic zones. The main motivations for having Phase-2 are the improvement and validation of continental-scale hydrological models and climate models, and the development and verification of techniques for the downscaling of snow-cover products from other sources such as coarse-resolution satellite snow measurements. This mission phase will enable spatially-detailed hydrological process studies for large basins. The data will also be very relevant for advancing and validating snow-cover parameterisations in land-surface components of atmospheric circulation models and for downscaling cryosphere processes in climate models.

Near-realtime data delivery, addressed in ESA's *The Changing Earth* (ESA SP-1304), is also of great relevance for the CoReH$_2$O mission. Objectives are the advancement and validation of data assimilation methods for snow products (snow area and SWE) to test the impact of innovative snow products for the improvement of snow-cover and streamflow forecasts. Significant interest has been expressed by hydrological and meteorological agencies in Europe and North America to obtain CoReH$_2$O snow-cover products within 24 hours

for both mission phases to improve and validate data assimilation and downscaling procedures in regional-scale nowcasting and forecasting models.

For the orbits in Phase-1 and Phase-2, a dawn/dusk orbit is proposed with morning acquisitions (06:00 ±30 minutes) for the descending orbit to minimise effects of surface melt on the snow surface. All repeating acquisitions should be obtained with the same acquisition geometry and the respective swaths should largely overlap (collocated to 1 km or less at 1 RMS). It is further expected that the images are co-registered in radar geometry to within 20 m. A swath width of larger than, or equal to, 100 km is suitable to cover large hydrological units and to provide sufficient spatial coverage in the second phase of the mission. Furthermore, a minimum image size of at least 100 km × 100 km is required to cover medium-sized basins.

Ongoing and new international research initiatives, such as the World Climate Research Programme (WCRP)-CliC (Climate and Cryosphere) programme and the recently approved Global Cryosphere Watch of WMO, emphasise the urgency of consistent, spatially distributed snow and ice observations. These can only be provided by improved satellite observations. Also in hydrology and water management, the community is longing for better snow observations to advance distributed hydrological modelling. This emphasises the timeliness of the CoReH$_2$O mission.

## 4.2 Geophysical Products

The Level-2 (geophysical) products will be swath-based maps in cartographic projection (Universal Transverse Mercator) matching the observational requirements specified in Table 4.1. The baseline concept foresees generation of the primary products: snow extent (separated in wet and dry snow), snow mass on land, and snow accumulation on glaciers. The repeat interval for a given location will be 3 or 15 days, depending on the mission phase. The standard products will be supplied in 200 m raster (corresponding to regional-scale products in Table 4.1), with the exception of snow in forested areas and snow accumulation on glaciers where the spatial resolution of the global product (500 m) is adopted. This adjustment accounts for the reduced dynamic range of the backscatter signal for snow in forests and winter snow on glaciers, as explained in Section 4.3.

## 4.3 Measurement Principle

In order to fulfil the geophysical observation requirements a sensor is needed that is sensitive to the physical properties of the snow volume and provides comparatively high-spatial resolution. This can be achieved by an imaging radar that operates at relatively high radar frequencies. The use of X-band (9.6 GHz) and Ku-band (17.2 GHz) frequencies is proposed to obtain proper sensitivity to SWE, both for shallow and deep snowpacks. These two frequencies show different sensitivities to the snow volume and the background medium below the snowpack.

### 4.3.1 Radar Interaction with Snow

The retrieval of SWE and depth is based on the interaction of the backscattered radar signal with the snow volume. For SWE retrieval, the snowpack has to be dry. In wet snow, dielectric losses are high and the typical penetration depth is in the order of only a few centimetres (e.g. Mätzler, 1987). This enables clear detection of melting snow due to the strong drop of the backscatter coefficient and has been applied for mapping areas of melting snow using C-band and X-band SAR data (Nagler & Rott, 2000; Floricioiu and Rott, 2001). For dry snow,

Figure 4.2. Observed one-way penetration depth in dry snow for ▲ Alps (Mätzler, 1987) and ● ■ Antarctica (Rott et al., 1993). The vertical dotted lines show the CoReH$_2$O frequencies at X-band (9.6 GHz) and Ku-band (17.2 GHz). (ENVEO)
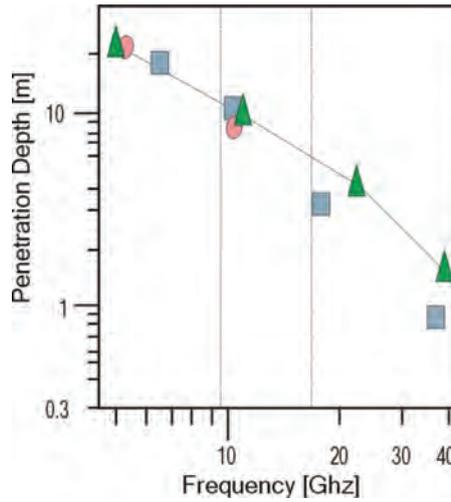
the penetration depth in the X- to Ku-band range is in the order of several metres, increasing from values of 3–4 m at 17.2 GHz to about 10 m at 9.6 GHz (Fig. 4.2).

For the retrieval of SWE, it is necessary to separate the backscatter contributions of the snow volume and the background medium (soil surface on land, or frozen firn and ice on glaciers) and to compensate for impact of grain size on scattering in the snow volume. The total backscatter, $\sigma^t$, from snow-covered ground at transmit and receive polarisation combination, pq, is made up from the following main contributions:

$$\sigma_{pq}^{t} = \sigma_{pq}^{as} + \sigma_{pq}^{v} + \sigma_{pq}^{gv} + \sigma_{pq}^{g'} \qquad (4.1)$$

where $\sigma^{as}$ represents scattering at the air/snow interface, $\sigma^{v}$ represents the direct volume scattering term, $\sigma^{gv}$ the contributions by ground surface/volume and volume/ground surface interactions, and $\sigma^{g'}$ the backscatter of the ground surface after transmission through the snowpack (Fig. 4.3). The magnitude of the individual contributions depends on the scattering and absorption properties of the snow volume and on the backscatter signal of the background medium. The main backscattering contributions of dry snow on the ground come from the snow volume (direct contribution) and the ground surface below the snowpack. Scattering at the air/snow interface amounts to a few percent at most. The retrieval of SWE is based on the backscatter contribution from the snow volume.

For the definition of sensor specifications and the development of retrieval algorithms it is useful to examine the magnitude of the various backscatter
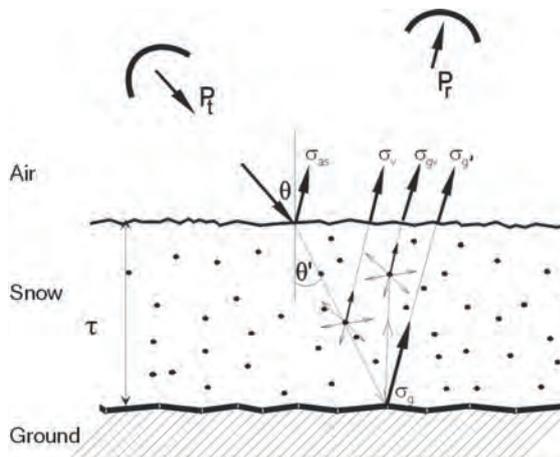


Figure 4.3. Main contributions to radar scattering from snow-covered ground. P$_t$ is the transmitted power signal and P$_r$ is the signal that is received by the radar antenna. The angle θ' is the angle of refraction in the snowpack. (ENVEO)
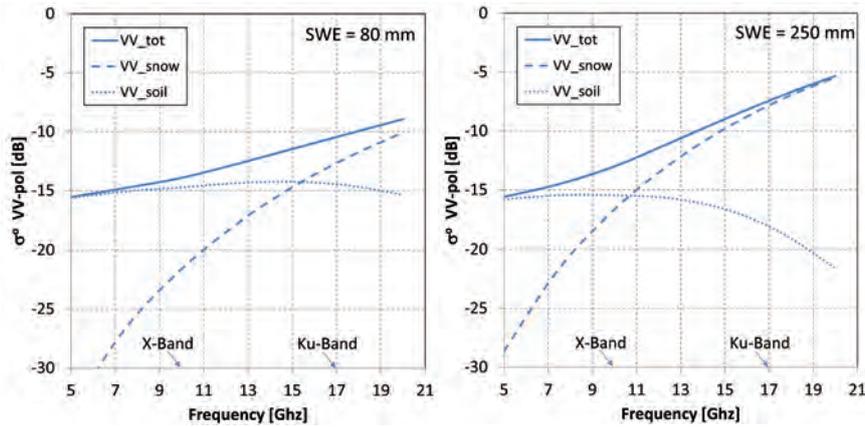
Figure 4.4. Backscatter coefficients at VV polarisation (40° incidence angle) for shallow (SWE=80 mm, left) and deep snow (SWE=250 mm, right) over a moderately rough soil background. Solid line=total backscattering, dashed line=snow volume contribution, dotted line=soil contribution attenuated by snow. (IFAC)

contributions at different frequencies. Ku- and X-band frequencies show distinctly different sensitivities to the snow medium and soil background (Figs. 4.4 and 4.5). Because of the impact of meteorological events on snow backscatter, the Ku- and X-band backscatter data need to be acquired nearly simultaneously (time lag of <1 hour). From Fig. 4.4, it is obvious that at X-band the backscatter contribution of soil below the snowpack is more important than at Ku-band, providing information on the state of the snow/soil interface. C-band SAR data (5.3 GHz) are almost exclusively determined by backscatter at the snow/soil interface, as dry snow is quite transparent at these frequencies.

Cross-polarised channels are proposed to complement co-polarised channels (a) owing to the differences in the relative contributions of various backscattering mechanisms of snow-covered terrain and (b) owing to differences in sensitivities to properties of vegetation and ground surfaces. In the cross-polarised signal, the relative volume to surface backscatter contribution is higher than in the co-polarised channels (e.g. Fig. 4.5, in particular at Ku-band). SWE retrieval benefits from observations that show distinct sensitivities to different target characteristics as provided by the inclusion of both co- and cross-polarised measurements.

The backscatter simulations in Fig. 4.5 have been computed with a semi-empirical radiative transfer model (sRT). This model is also used in the inversion procedure for SWE (Chapter 6, and Rott et al., 2010; 2011). The backscatter simulations illustrate the angular dependence of total backscatter, as well as the individual contributions by backscatter of the soil attenuated by the snowpack and by the volume. The specifications for this case correspond to typical values for seasonal snow: SWE=150 mm, snow density=250 kg/m$^{-3}$
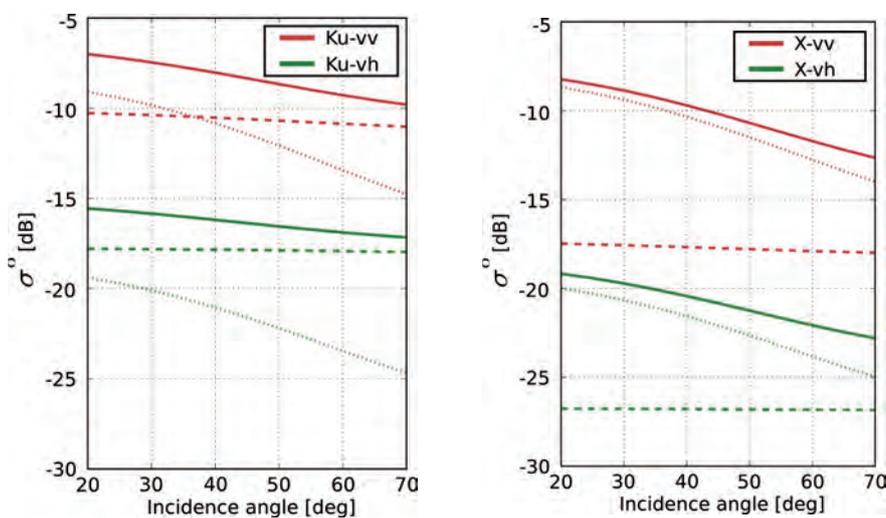


Figure 4.5. Model calculations of the total backscatter (solid line) dependent on incidence angle, and contributions of the snow volume (dashed) and rough soil surface (dotted). For seasonal snow with SWE=150 mm at 17.2 GHz (Ku-band) and 9.6 GHz (X-band); co-polarisation (VV), cross-polarisation (VH). (ENVEO)

(corresponding to snow depth of 0.6 m), and effective snow grain radius Re=0.5 mm. The effective grain radius is commonly used in the radiative transfer approach as a parameter to characterise the scattering efficiency of the snow volume (e.g. Chen et al., 2003). Re corresponds approximately to the observed mean radius of the grains in a snowpack, as defined by the international classification for seasonal snow (Colbeck et al., 1990).

In seasonal snowpacks of shallow and medium depth the ground-surface scattering contribution dominates at X-band, both for co- and cross-polarisations. X-band backscatter of the snow volume becomes more important for larger snow grains and for deeper snowpacks, as well as for smoother background targets. The ratio of volume to ground backscatter increases with the incidence angle. Model calculations and studies with experimental data show that at Ku-band, co- and cross-polarisation volume scattering in snow is important at incidence angles above 20° even for comparatively shallow snowpacks (Rott et al., 2011; see also Figs. 4.4 and 4.5). This points out that local incidence angles of ≥20° are well-suited for SWE retrieval. An incidence angle range of about 30–45° is suggested for the sensor referring to flat surfaces. The retrieval on sloping terrain can then be extended to include local incidence angles ranging 20–70°.

The different sensitivities to SWE at Ku- and X-band are evident in Fig. 4.6 where data from NoSREx field campaigns and model calculations of radar backscatter are shown for the incidence angle of 40°. The observations were performed at Sodankylä, northern Finland, in two winters, employing a scatterometer (SnowScat) operating in the frequency range of CoReH₂O. Backscatter data for dry snow over frozen ground in relation to SWE measured in snow pits are shown. The background medium is mineral soil (clearing in forest land). The forward calculations on backscatter dependence of SWE in Fig. 4.6 apply grain size values according to observations (mean value of two winters and ±1 standard deviation, respectively, for the three curves) for estimating the volume scattering coefficient. The grain size values of the three curves correspond to effective grain radius of the sRT model of 0.5 mm (mean), 0.4 mm (lower curve) and 0.6 mm (upper curve), showing increase of backscatter sensitivity to SWE with increasing grain size.

The obtained data indicate strong sensitivity of Ku-band backscatter to increase in SWE. At X-band, the sensitivity is much smaller. At the incidence angle of 40°, Ku-band shows for shallow snow a sensitivity of about 30 mm/dB at VV and slightly higher at VH polarisations, dropping gradually towards higher SWE values (~40 mm/dB).

The comparison of observed backscatter coefficients with *in situ* measurements of SWE shows relations that can be well approximated by the radiative transfer model at Ku-band applying the two-winter average snow grain size (middle line Fig. 4.6). This is because the mean (effective) grain size vertically averaged over the snowpack, which is relevant for the
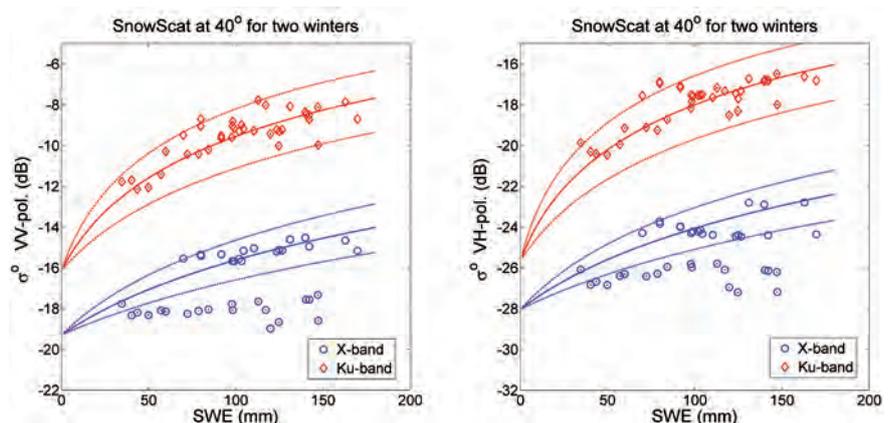


Figure 4.6. Backscatter coefficients as function of observed SWE at Ku-band (16.7 GHz) and X-band (10.2 GHz), 40° incidence angle, from observations at Sodankylä, northern Finland, and forward model calculations (lines) for boreal snow conditions. The points correspond to tower-based SnowScat measurements for the winters of 2009–10 (open symbols) and 2010–11 (dotted symbols). (FMI)

backscatter signal, was quite stable throughout the two winters, even though the snowpack structure showed significant differences in vertical stratigraphy. On the other hand, for this dataset of rather shallow snow the X-band signal differs considerably between the two years. This can be attributed to different conditions at the snow/soil interface, which were caused by different sequences of melt-refreeze events in early winter.

Relations between SWE and total radar backscatter show variations, related to the metamorphic state and grain size of the snowpack and to the scattering properties of the background target. Measurements at a tundra site near Churchill, Canada, show higher sensitivity to SWE than the observations at Sodankylä. The site represents typical wet tundra with a peat soil and shallow snowpack. Sensitivities are about 5 mm/dB for the Ku-band co-polarisation and 6 mm/dB for the cross polarisation when SWE ranges from 0–40 mm (Fig. 4.7). The sensitivity at X-band is weaker, but clearly detectable: 9 mm/dB for the co-polarisation and 17 mm/dB for the cross-polarisation. The higher sensitivity at Churchill compared to Sodankylä can be explained by the different metamorphic state of the snowpack, with larger grain size at Churchill caused by temperature gradient metamorphism. Differences in the backscatter behaviour of background medium also play a role, but are not decisive. At Ku-band, the backscatter levels of the background (SWE=0 mm) are similar at both sites.

Backscatter simulations and experimental data (Rott et al., 2011) suggest the dynamic range for the CoReH$_2$O sensor to be equal to, or greater than, 30 dB, considering that the dynamic range applied for normalised radar cross-section ($\sigma^0$) values measurable by the system is within one Level-1b image. Table 4.2 summarises the dynamic range estimates for different surfaces.

The required noise equivalent $\sigma^0$ (X-band: ≤−23 dB for VV; ≤−27 dB for VH, Ku-band: ≤−20 dB for VV; ≤−25 dB for VH) has been defined based on Ku- and X-band campaign data measured with airborne and *in situ* scatterometer systems over snow, glaciers and other target types, including the Cold Land Process Experiment, SARAlps2007, and HeliSnow2008 campaigns. In addition, spaceborne sensors offer large archives of backscatter data, including X-band data from X-SAR (which operated on two Space Shuttle missions in 1994), TerraSAR-X and COSMO-Skymed (both in orbit since June 2007), and Ku-band data from scatterometer missions.

The radiometric requirements have been derived from sensitivity analysis of the statistical retrieval method superimposing random noise to field campaign backscatter data (Nagler et al., 2008) and with synthetic backscatter data computed with the synthetic scene generator (Rott et al., 2011). The results show that better than the benchmark values for SWE retrieval accuracy (Table 4.1) can be obtained by 0.5 dB radiometric stability,
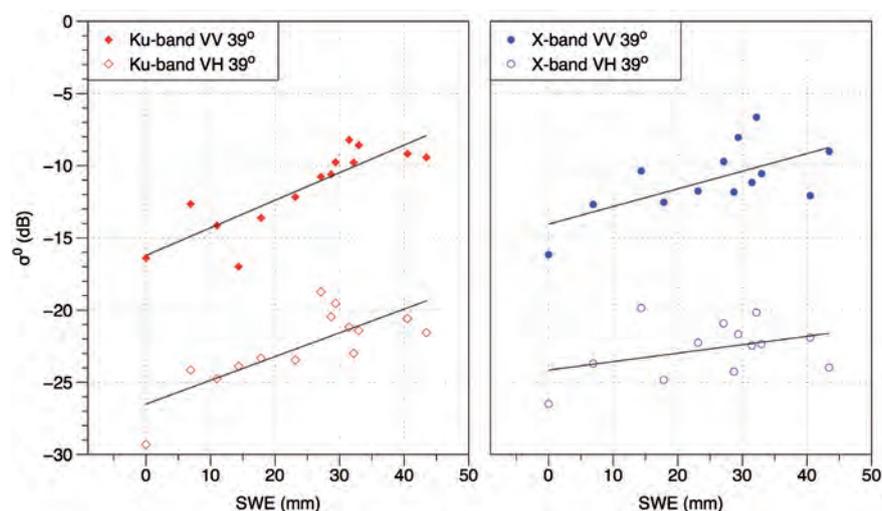


Figure 4.7. Behaviour of backscatter (normalised radar cross-section) as a function of SWE for the wet tundra site of Churchill, at X- and Ku-bands. The results show a strong correlation between the radar observations and SWE. (University of Waterloo)

Table 4.2: Radiometric backscatter range for main targets.

| Target | Polarisation | Ku-band dynamic range (dB) | X-band dynamic range (dB) |
|---|---|---|---|
| Dry snow on land | VV | −18 to 0 | −22 to 0 |
| | VH | −25 to −3 | −28 to −5 |
| Melting snow | VV | −20 to −10 | −23 to −10 |
| | VH | −25 to −15 | −28 to −15 |
| Dry snow on glaciers | VV | −15 to 0 | −15 to 0 |
| | VH | −20 to −5 | −22 to −5 |
| Land background targets | VV | −20 to 0 | −22 to 0 |
| | VH | −25 to −5 | −28 to −10 |

0.51 dB speckle noise, and −20 dB total ambiguity ratio. 0.51 dB is the speckle related uncertainty (standard deviation of backscattered power) for $\sigma^0$ at 64 independent looks (effective number of looks) corresponding to the 200 m size of the SWE product. The absolute radiometric bias should be equal to, or lower than, 1 dB. Additional results on retrieval performance using simulated data with various numbers of looks are shown in Chapter 7.

The 50 m spatial resolution is needed to comply with the maximum geometric requirement stated in Table 4.1. In addition, high-spatial resolution is required for accurate terrain-corrected geocoding.

## 4.3.2 Effects of Vegetation

Studies on the effects of vegetation for snow retrievals show that during the winter the presence of dormant herbaceous or short vegetation has a small influence on the background level of backscattering, but does not affect the sensitivity to SWE (Rott et al., 2011). The main impact for CoReH₂O snow retrieval comes from conifer species in the boreal forests and strongly depends on forest density and fractional cover. Model calculations show that in the case of low biomass or low fractional cover (i.e. vegetation biomass lower than 110 m³/ha and fractional cover lower than 25%) the backscatter of snow dominates the time-varying part of the radar signal. When density or fractional cover increases, the signal from the ground is almost completely masked by the trees and consequently the sensitivity to SWE decreases at both X- and Ku-band (Fig. 4.8).

Because trees attenuate the snow-cover signal, SWE retrieval can only be carried out for open forests. In the CoReH₂O retrieval procedure, dense forests are masked out and corrections for attenuation are applied for open forests in dependence of cover density, as described in Chapter 6.
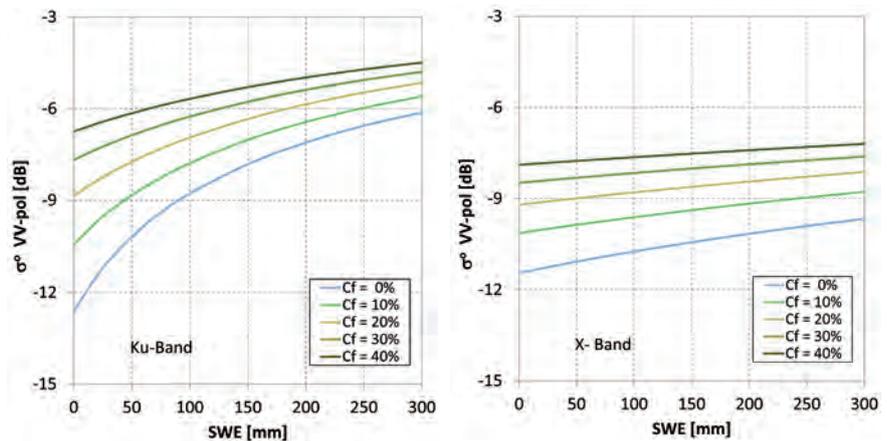


Figure 4.8. Simulated backscattering coefficients for forest canopy (coniferous forest) and snow-covered ground as a function of SWE at 17.2 GHz (left) and 9.6 GHz (right), VV polarisation, incidence angle 40°, for forest Cover Fraction (CF) from 0% (non-vegetated surface) to 40%. Woody volume of the forested area ranges 0–350 m³/ha. (IFAC)
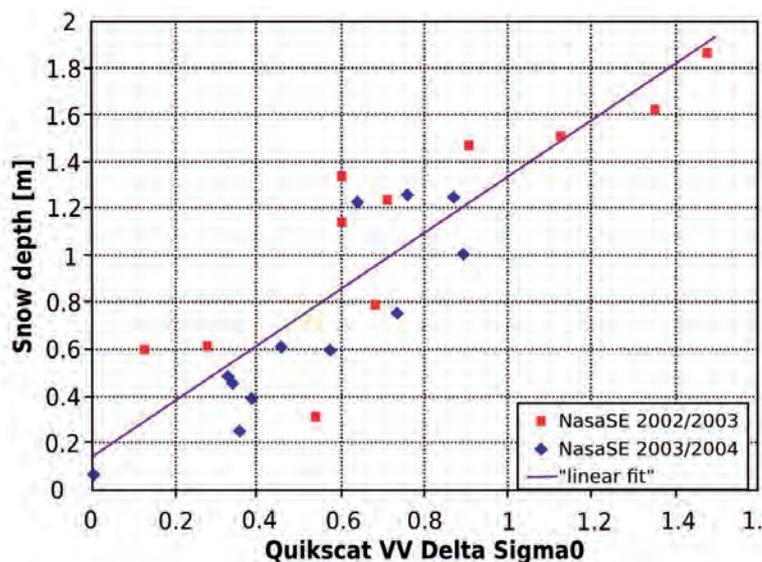
Figure 4.9. Ku-band backscatter difference ($\Delta\sigma^0=\sigma^0$ autumn$-\sigma^0$ winter) in dB derived from QuikSCAT data vs. snow depth at the station NASA-SE at 20-day intervals, during accumulation periods 2002–03 and 2003–04. (ENVEO).

### 4.3.3 Snow Accumulation on Glaciers and Ice Sheets

The retrieval of winter snow accumulation on glaciers and ice sheets is based on the backscatter contrast of winter snow vs. the background target. The retrieval of SWE is performed in the glacier ice and firn zones (refrozen snow from previous years, also called the percolation zone), which are characterised by high backscatter values whereas winter snow has lower scattering albedo. Nghiem et al. (2005) demonstrated the feasibility of this concept for mapping snow accumulation in southern Greenland at low-spatial resolution, based on Ku-band backscatter measurements by QuikSCAT. The higher spatial resolution of CoReH$_2$O will also enable measurements of snow accumulation on mountain glaciers and small ice caps.

The characteristic of backscatter utilised in the retrieval procedure is illustrated in Fig. 4.9, showing high correlation between snow accumulation in the percolation zone of Greenland and the seasonal decrease of Ku-band backscatter intensity measured by QuickSCAT. The abscissa scale represents the difference in backscatter coefficient $\Delta\sigma^0$ in dB at the beginning of the accumulation period (autumn) minus $\sigma^0$ measured at a given date in winter. The strong scattering signal by frozen snow and ice is attenuated by snow accumulating in winter. The relationship between the depth of the snow layer in linear scale and decrease in total backscatter due to attenuation in dB agrees with radiative transfer theory.

### 4.3.4 Radar Interactions with Lake Ice

Freshwater ice (lake ice and river ice) is probably the component of the cryosphere that has been the least studied with radar remote-sensing. Very few studies have investigated the backscatter signature of lake ice and on-ice snow cover, especially at Ku- and X-band frequencies. The studies to date suggest that radar backscatter is affected by the presence of inclusions (bubbles) in congelation ice (C- and X-band investigations). It is reasonable to expect that the presence of snow-ice (with densely packed air bubbles) in the top layer of the ice will also have an influence on backscatter, at least at the lower radar frequencies. Measurements at 9 GHz and 17 GHz by Onstott et al. (1982) show that the presence of snow cover on relatively bubble-free lake-ice can increase the backscatter significantly. Further research is needed to assess to the potential for retrieving snow depth on ice by the CoReH$_2$O sensor.

Figure 4.10. Temporal evolution of QuikSCAT $\sigma^0$ (left axis, black curve) over a test site on Great Bear Lake (2000–03). The first solid vertical black line represents melt onset, the second vertical dashed line represents ice-off, the third vertical dashed line represents freeze onset (ice-on), and the red time series is Extended AVHRR Polar Pathfinder surface air temperature (right axis). (University of Waterloo)
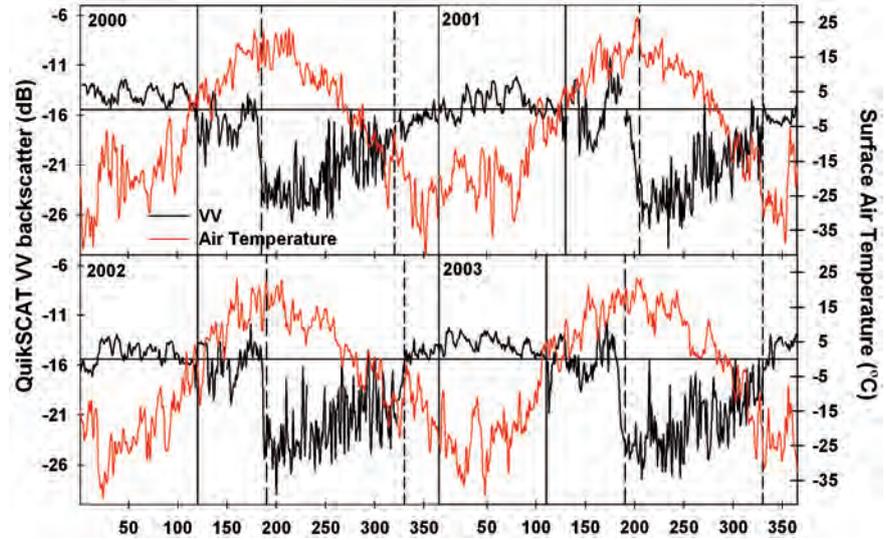
The sensitivity of Ku-band backscatter to the seasonal evolution of ice cover on Great Bear Lake (66°N, 121°W), Canada, is illustrated in Fig. 4.10. It shows the temporal evolution of the QuikSCAT $\sigma^0$ compared to the surface air temperature from the extended AVHRR Polar Pathfinder from 2000–03 (Wang & Key, 2005). The figure shows that Ku-band backscatter coefficients $\sigma^0$ (VV) from QuikSCAT can be used to detect melt onset, ice-off and freeze onset (ice-on) dates. In winter, $\sigma^0$ exhibits relatively high returns, whereas melt onset is marked by a strong decrease in $\sigma^0$. Following the first significant downturn in the QuikSCAT $\sigma^0$ temporal evolution, the $\sigma^0$ begins a series of up and downturn oscillations. The first oscillation (i.e. upturn and downturn) is related to freeze-thaw processes. The sharp drop in QuikSCAT $\sigma^0$ after this period marks the date when the lake becomes clear of ice (ice-off). The QuikSCAT $\sigma^0$ then increases sharply from the relatively low open-water $\sigma^0$ values to higher $\sigma^0$ values to indicate freeze onset (ice-on). From this analysis, it is anticipated that CoReH$_2$O measurements will clearly be successful at distinguishing ice-covered from ice-free areas, which will be facilitated by acquisitions at VH polarisation. During the ice growth period, it may also be possible to derive snow depth and ice thickness, but this needs to be confirmed by experimental data. The development of any retrieval algorithm prior to the CoReH$_2$O mission will require field measurement campaigns supported by radar observations and backscatter models.

## 4.3.5 Radar Interactions with Sea Ice

The backscatter signal of sea ice at high radar frequencies is controlled by interactions with the ice surface and volume, as well as by the snow layer. Experimental data indicate that Ku-band is sensitive to ice thickness up to 10 cm ice, whereas at X-band the range extends to 30 cm (Beaven et al., 1995). After ice reaches a certain thickness, snow tends to accumulate on top. Whereas for thin ice the backscatter signal comes directly from the ice layer, for thicker ice covered by snow the radar signal has to penetrate the snow before information about the sea ice can be obtained.

This points out that Ku- and X-band SAR would provide sea-ice observations, complementing measurements at longer wavelengths. In polynyas and leads, where new ice is being formed, properties of thin ice can be observed. Due to the different penetration characteristics, the combination of X- and Ku-band backscatter is particularly sensitive to thickness variations of new ice. New ice of varying development history and age appears as banded structures in SAR imagery (see example for X-band data in Fig. 2.15). An example of the high
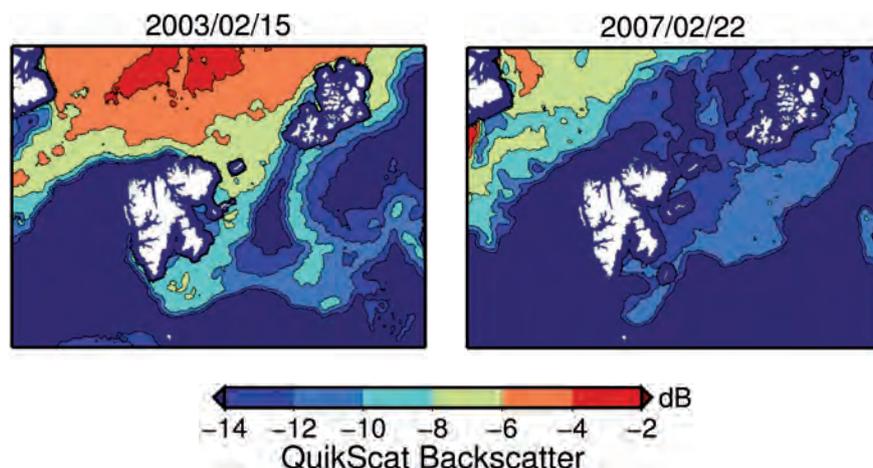
Figure 4.11. Ku-band (QuikSCAT) backscatter maps of the Barents Sea for two dates in February 2003 and 2007, showing large differences related to sea-ice type. High backscatter (red) coincides with rough multiyear ice, low backscatter (blue) with smooth first-year sea ice. (Adapted from Hendricks et al., 2011)

dynamic range of Ku-band backscatter for different ice types, including new ice, is shown in Fig. 4.11.

For thicker ice, the signal contribution of the snow layer on top becomes increasingly important. Interaction between snow on sea ice and microwaves is subject to the same physical principles as for snow on land, and therefore snow mass may also be obtained, in principle, over sea ice. However, snow on first-year ice can be saline, increasing absorption and limiting penetration depth. In addition, snow on sea ice can be highly metamorphic owing to the proximity to the underlying warm water. This may significantly increase the volume scattering component. Like soil, the underlying sea ice contributes to the total backscatter signal, which varies as function of ice type and surface roughness (e.g. Onstott et al., 1979; Kim et al., 1984). First-year ice is mostly saline at the surface and relatively smooth, leading to low backscatter. Multiyear ice is desalinated and highly porous, causing strong volume scattering. Radiative transfer simulations show that the backscatter signal at Ku-band and X-band is sensitive to the accumulated SWE on sea ice as long as the snow layer is dry. As with any snowpack, radar penetration depth and backscatter decrease strongly with increases in snow wetness. This enables the detection of melt onset and mapping of melt extent. The interannual variability of melt areas is an important application of radar measurements of sea ice for climate research (Willmes et al., 2006; Perovich et al., 2007).

### 4.3.6 Atmospheric Effects

Effects of the atmosphere have been studied, using a radiative transfer model of atmosphere and experimental data (Rott et al., 2011). The main atmospheric propagation losses are caused by absorption owing to water vapour and liquid water (Ulaby et al., 1981). At X- and Ku-band, the absorption losses clearly exceed the scattering losses, not only in clouds but also in precipitation. For snow and ice applications these effects are weak, because the non-precipitating liquid and vaporous water content of the atmosphere is rather low in cold environments, in particular over non-melting snow and ice surfaces, which is a precondition for retrieving SWE.

The effects of variations of atmospheric transmittance on X- and Ku-band backscattering measurements were estimated from the ECMWF ERA40 atmosphere data for various locations in the snowy season (for a 10-year period), using the atmospheric propagation model of Ulaby et al. (1981) and Ulaby (1986). Corrections for transmissivity can be obtained by using numerical atmospheric circulation model data as input to radiative transfer models for atmospheric propagation. These corrections amount to no more than 0.2 dB at Ku-band in winter atmospheres (Fig. 4.12).

Figure 4.12. Correction to the backscattering coefficient measured at satellite, to compensate for atmospheric effects for selected coastal regions in March. The average absolute correction and upper/lower limits of correction owing to monthly variability in atmospheric conditions are shown. Incidence angle $\theta$=30°. (FMI)
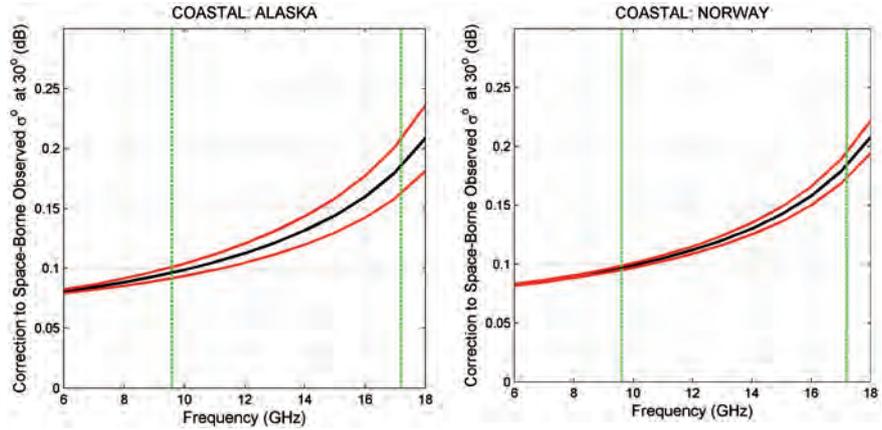


## 4.4 Summary of Observation Requirements

The theoretical and experimental studies point out that a dual-frequency SAR operating at Ku- and X-band frequencies with comparatively high-spatial resolution is a promising solution for retrieval of physical properties of snow and ice, including snow mass. The frequency difference between the Ku- and X-band channels should be large enough to exploit the different sensitivities to volume scattering for retrieving SWE, suggesting the use of the 17.2 and 9.6 GHz frequency bands. Co- and cross-polarisations show different sensitivities to surface and volume scattering, which supports the retrieval of physical properties of the snow volume. Therefore, the SAR should feature both co- and cross-polarised channels. Experimental data and theory only show small differences between VV and HH polarisations for snow-covered areas at the Ku- and X-band frequencies. Therefore, only single co- and cross-polarisations (VV and VH) are selected. Because of the dynamic nature of snow and ice, the Ku- and X-band backscatter data need to be acquired nearly simultaneously (time lag of <1 hour).

System stability and calibration are important because the retrievals are based on backscatter intensity. The radiometric requirements (Table 4.3) are based on backscatter signatures and retrievals of primary Level-2 products with simulated and experimental data (Rott et al., 2011, and examples in this chapter). The 50 m spatial-resolution refers to the maximum geometric resolution in observational requirements (Table 4.1) and is also needed to support accurate terrain-corrected geocoding. The preferred incidence angle range is 30–45° on a horizontal surface. This enables the application over

Table 4.3. The main instrument and radiometric requirements for the CoReH$_2$O sensor.

| Parameter | Requirement |
|---|---|
| SAR frequency | 9.6 GHz and 17.2 GHz bands |
| Polarisations | VV and VH |
| Incidence angle (at horizontal surface) | 30–45° (swath within this range) |
| Spatial resolution | ≤50 m × 50 m (≥4 equivalent number of looks) |
| Swath width | ≥100 km |
| Noise equivalent $\sigma^0$ | X-band: ≤–23 dB for VV; ≤–27 dB for VH<br>Ku-band: ≤–20 dB for VV; ≤–25 dB for VH |
| Radiometric stability | ≤0.5 dB |
| Absolute radiometric bias | ≤1.0 dB |
| Dynamic range | ≥30 dB |
| Total ambiguity ratio | ≤–20 dB |

sloping and mountainous terrain. Results of model computations show that SWE retrievals are possible over local incidence angles from about 20–70°. A fixed swath width of at least 100 km is proposed to enable the observations of extended hydrological units in one image. Combined with the 15-day repeating ground track of the orbit this provides the required near global coverage (>85%) in Phase-2. Repeating orbit coverage is needed for consistent observations, so that all repeating swaths should be collocated within less or equal 1 km (1 RMS).

# → SYSTEM CONCEPT

# 5 System Concept

## 5.1 Introduction

This chapter provides the technical description of the CoReH$_2$O mission, as derived from the preparatory activities at Phase-A level, for implementation as an Earth Explorer in the frame of ESA's Living Planet Programme. It shows how candidate implementation concepts can respond to the scientific mission requirements defined in the previous chapters.

The system description is based mainly on the results of the work performed during parallel Phase-A system studies by two industrial consortia (EADS Astrium DE, 2012 and Thales Alenia Space IT, 2012). Whenever relevant, two implementation concepts (Concepts A and B) are described to present different implementation options capable of meeting the mission requirements.

After an overview of the mission architecture and the proposed orbit (Sections 5.2 and 5.3), the space segment is described in detail (Section 5.4) followed by the launcher, ground segment and operations concepts (Sections 5.5, 5.6 and 5.7). The overall mission performance is summarised in Chapter 7.

## 5.2 Mission Architecture Overview

The main architectural elements of the mission are shown in Fig. 5.1. The space segment comprises a single spacecraft carrying a SAR payload that uses signals at two frequencies (9.6 GHz in X-band and 17.2 GHz in Ku-band) with dual polarisation (VV and VH). The SAR, operating in ScanSAR mode, observes a ground swath of about 100 km.

The mission includes two distinct operational phases. Phase-1 aims to make observations over dedicated test sites and key snow-covered regions with a repeat period of 3 days. Phase-2 provides observations of snow- and ice-covered areas with a repeat period of 15 days. In both phases the satellite operates in a near-polar Sun-synchronous orbit with the descending node at 06:00 local time. The reference altitude of these orbits is 666 km for Phase-1 and 645 km for Phase-2.



Figure 5.1. CoReH$_2$O mission and system architecture.

The Sun-synchronous configuration is needed to provide repeatable and favourable observing conditions throughout the mission's life. Given the high-power needs and high-thermal dissipation of the SAR payload, the relatively stable illumination conditions provided by the selected dusk/dawn orbits reduces the need for complex power generation and thermal-control subsystems.

The CoReH$_2$O satellite makes extensive reuse of flight-proven solutions for the platform subsystems, but features a specific structural concept driven by the accommodation of the SAR instrument and by the geometrical constraints imposed by the viewing geometry between the reflector and the antenna feed system.

The satellite is injected into the Phase-1 orbit by a Vega launcher and is designed for compatibility with a backup launcher (PSLV).

The scientific data acquired by the SAR instrument are sent to the ground via a high-rate radio downlink in X-band. Communication for satellite monitoring and control is supported via a two-way S-band link.

The ground segment is based on the ESA Earth Explorer ground segment infrastructure and comprises:

— The Flight Operation Segment (FOS), which includes the Telemetry, Tracking and Command (TT&C) ground station and the Flight Operation Control Centre (FOCC).

— The Payload Data Ground Segment (PDGS), which includes the Payload Data Acquisition Station (PDAS), the processing and archiving elements and the mission planning and monitoring elements.

The science data, processed up to Level-1b by the PDGS, are made available to users, including climate modelling and research centres.

## 5.3   Mission Analysis and Orbit Selection

### 5.3.1 Orbit Selection

The orbit selection has been driven by revisit and coverage requirements, payload performance, observation geometry, delta-V needs (i.e. propellant use) and operations simplicity. The result of this trade-off is summarised in Table 5.1.

The mission comprises two sequential nominal operational phases with different requirements in terms of revisit and coverage. This led to the selection of two different orbits for these two phases. During the first phase, the system must provide data products with a repeat period of three days, with no specific requirements on coverage. In the second phase, observations must be made of at least 85% of the snow and ice areas with a repeat period of 12–15 days. A repeat cycle of 15 days is preferred on the basis of favourable coverage, average duty-cycle and overall delta-V budget. In both phases, Sun-synchronous orbits with a local time descending node of 06:00 ±30 minutes have been selected so that observations of snow and icepack conditions are made at the same local time.

|  | Phase-1 | Phase-2 |
|---|---|---|
| Repeat cycle | 3 days | 15 days |
| Orbits per day | 14+2/3 | 14+11/15 |
| Mean altitude | 666 km | 645 km |
| Local time descending node | 06:00 ±30 min | |

Table 5.1. CoReH$_2$O orbit characteristics.
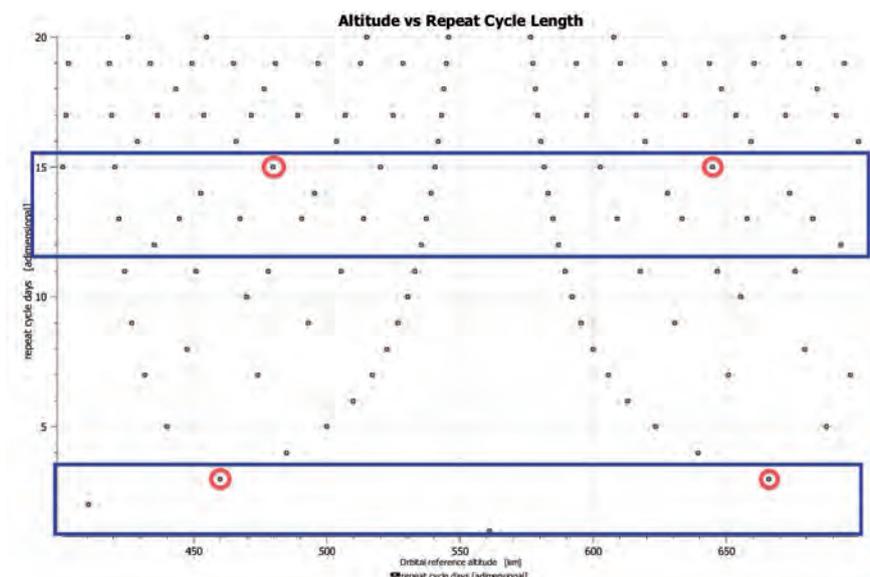
The difference between the orbit altitudes of the two nominal operational phases must be as small as possible to minimise the delta-V needed for the orbit transfer. This and the repeat requirement limits the orbit selection to only two possible orbit pairs: one with altitudes at 645 km and 666 km, and the other at 460 km and 480 km, as illustrated in Fig. 5.2. The two possible solutions have been traded off and the higher orbit pair has been selected on the basis of a longer contact time with the ground stations and of a significant reduction of the frequency of orbit-correction manoeuvres compared to the lower orbit pair.

The ground track patterns of the selected orbits repeat exactly according to the phase requirements (every 3 or 15 days), allowing regular revisit of the acquired scenes under almost identical geometric conditions. Orbit control manoeuvres are executed regularly to compensate for orbit decay, caused by atmospheric drag, and to ensure accuracy of where the repeating ground tracks meet the collocation requirements between successive acquisitions of the same area. Manoeuvres are needed every 9–60 days throughout the mission, depending on the atmospheric density, which varies with solar activity. They have limited impact on the overall mission availability. Figure 5.3 presents a summary of the frequency of these in-plane correction manoeuvres throughout the mission.

Eclipse seasons are concentrated in May–August. The maximum eclipse duration (19 minutes) occurs at the summer solstice, which is beneficial to the sizing of the power subsystems.

### 5.3.2 Mission Profile

The whole mission profile is shown in Fig. 5.4. The satellite will be injected by the Vega launcher into the Phase-1 orbit at an altitude of 666 km. The same orbit is also used for the Early Operations Phase (EOP) and for the Commissioning (COM) Phase. At the end of the latter, the system will start Phase-1 operations, which lasts for two years. A short transition phase is foreseen for the transfer to the 645-km orbit for Phase-2. This second phase lasts three years. Finally, the end-of-life (EOL) operations will start and the satellite will be manoeuvred to lower its perigee to an altitude that allows it to reenter the atmosphere within 25 years.

The acquisition strategy to observe snow and ice areas is optimised to reduce the volume of data and the duty cycle of the SAR. To this end, each visited area is imaged once during the repeat period to avoid duplicates of data. Observations are made during the descending path, i.e. in the local morning,

Figure 5.3. Frequency of in-plane orbit control manoeuvres during nominal mission phases.
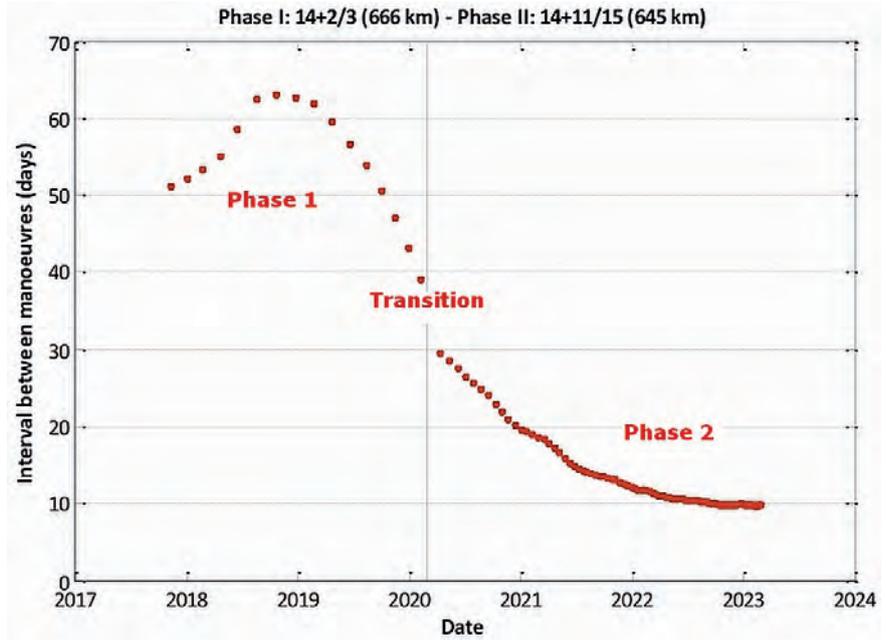


to minimise the effects of melt on the snow surface. Mountainous areas are observed during both ascending and descending paths to compensate for radar layover and shadowing effects.

### 5.3.2.1 Phase-1 orbit coverage

The main objective of Phase-1 is to observe specific areas of snow and ice with a short revisit, at the expense of a limited coverage. The coverage pattern is shown in Fig. 5.5, where blue areas are observed with a 3-day repeat, while red ones need only to be observed once every 15 days, thanks to the lower variability of snow and ice cover at those latitudes. This reduces the orbit acquisition duty-cycle to an average of 15%, which is beneficial for the system design.
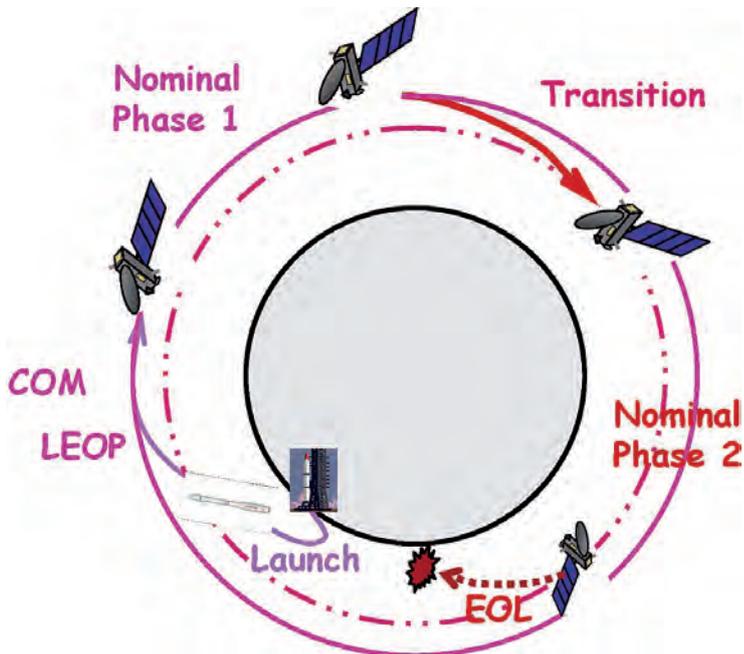


Figure 5.4. CoReH$_2$O mission profile.

### 5.3.2.2 Phase-2 orbit coverage

During the second operational phase, which lasts three years, the satellite will be in a Sun-synchronous orbit at a reference altitude of 645 km and 15-day repeat cycle. The main focus of Phase-2 is to provide systematic quasi-global coverage (more than 85%) of snow and ice areas. An example of the typical coverage provided in northern hemisphere winter is illustrated in Fig. 5.6. To perform the data acquisition over the coverage areas the SAR average orbit duty-cycle is in the range 15–18%.

## 5.4  Space Segment

### 5.4.1 Overview

The CoReH$_2$O space segment consists of a single satellite carrying the X-/Ku-band SAR payload. The physical configuration of the satellite is driven by the largest items to be accommodated, namely the SAR antenna assembly (reflector and feed) and the solar array. After trading possible design solutions, the resulting configuration is similar for both Concepts A and B. The functional configuration is driven by the requirements on the interface between the
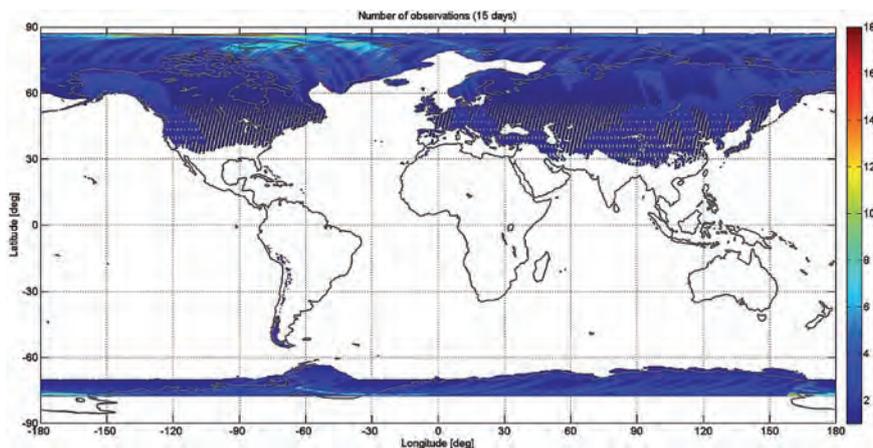


Figure 5.6. Typical coverage pattern in Phase-2 during northern-hemisphere winter.

payload and the platform in terms of data and power. Here as well, after trading various options the resulting functional (and electrical) design is similar for both concepts.

The SAR concepts are based on a single deployable parabolic reflector up to 4.3 m × 1.8 m in size, illuminated by two feed-arrays that generate the multiple beams required to cover the ground swath with the selected ScanSAR operation mode. The main differences between the concepts reside in the design of the feed system, in the detailed architecture of the SAR electronics, and in the technology selected for the high power amplification stage.

This overall similarity of the two (independently developed) concepts increases the confidence that mature design solutions are available for the implementation of the platform and for most elements of the payload. Following the satellite description in Subsection 5.4.2, the payload concept will be described in Subsection 5.4.3, and complemented by the description of the platform subsystems and the satellite budgets in Subsections 5.4.4 and 5.4.5.

## 5.4.2 Satellite Configuration

The configuration of the two satellite concepts is shown in Figs. 5.7 and 5.8. Both concepts are driven by the need to accommodate the reflector in the stowed configuration and to guarantee the relative viewing geometry between the deployed reflector and the feed subsystem. At the same time, the resulting configuration must be compatible with the baseline and backup launchers in terms of performance to orbit, fairing volume constraints and dynamic loads. Given the dimension of the antenna and focal length, an elongated satellite design is required, with the reflector stowed on the velocity side and hinged at the bottom of the satellite (i.e. close to the launcher interface plane), and the feed system accommodated at the top. The single-wing solar array is stowed on the anti-velocity side. After deployment, it is orientated at a fixed cant angle to optimise the incident solar flux, considering the seasonal variability of the Sun aspect angle and the attitude of the satellite.

In flight, the longitudinal axis of the satellite is also canted across-track with respect to the nadir direction in order to provide the incidence angle needed by the SAR viewing geometry. This cant angle depends on the concept and – due to the altitude variation along the orbit – it can be either fixed or variable.
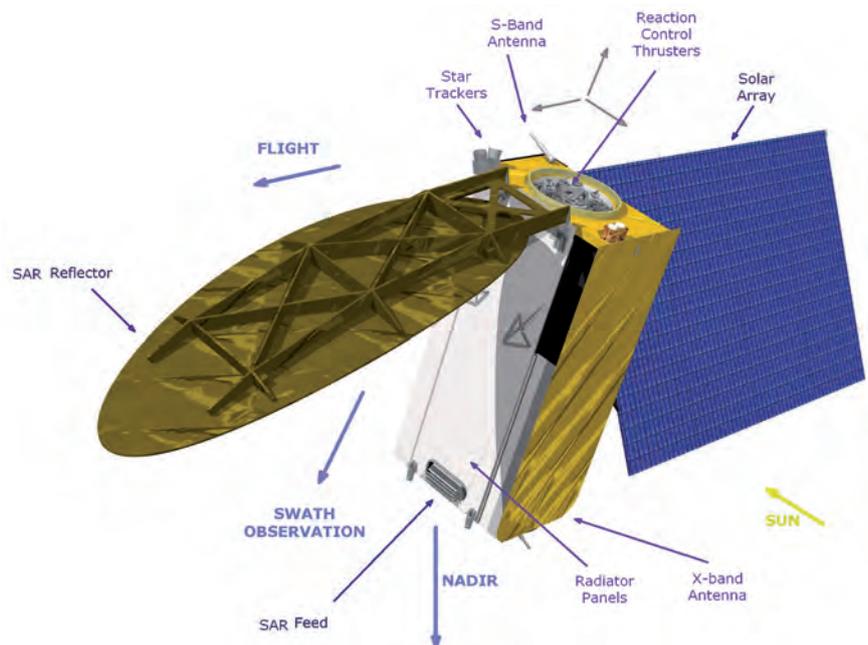


Figure 5.7. Concept A configuration.
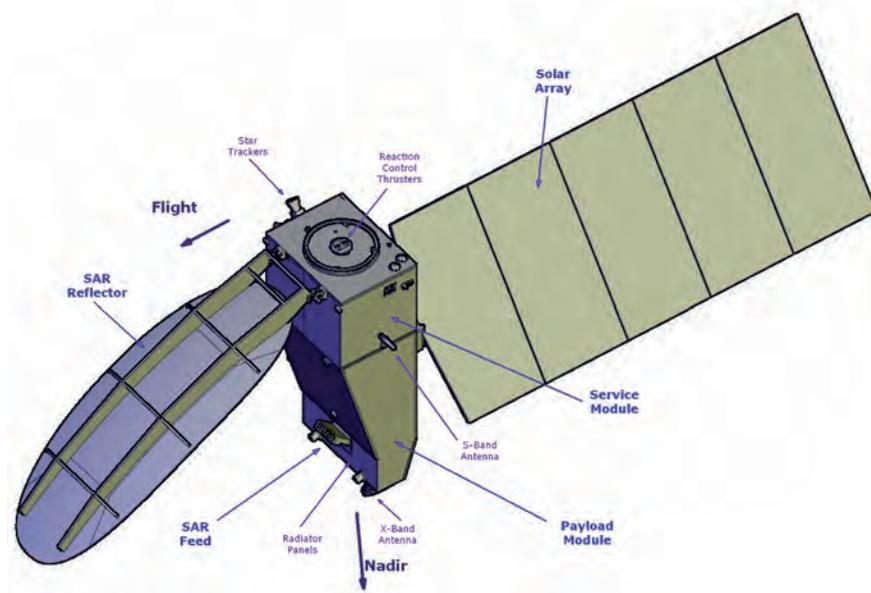
Figure 5.8. Concept B configuration.

The satellite panel facing deep space provides accommodation for the radiating surfaces of the units with high-thermal dissipation (SAR amplifiers and electronics). The velocity and anti-velocity side panels, as well as part of the sunlit panel, are used to accommodate the radiators for the platform subsystems and for other SAR equipment.

Other drivers for the configuration are related to the accommodation of the Attitude and Orbit Control (AOCS) sensors and actuators and to the positioning of the communication antennas (X- and S-band), to provide the required fields of view in all relevant operating conditions.

The AOCS startrackers are positioned close to the reflector hinge plane to minimise the impact of the relative thermoelastic distortions. Depending on the concept, the number and location of the Reaction Control Thrusters (RCTs) vary. The number is constrained by the need to provide the required thrust as well as the required torque control authority in the case where the RCT are also used for attitude control in safe/acquisition modes. For both concepts the thrusters are located in a group on the bottom face of the satellite (launch vehicle interface). Therefore, for each orbit manoeuvre a slew manoeuvre is necessary to orient the thrusters along the flight direction.

The accommodation of the X-band downlink antenna has to fulfil not only fields of view constraints, but also radio frequency (RF) interference constraints with respect to the SAR X-band payload in order to guarantee the required RF isolation. This aspect has been considered in both conceptual designs of the satellite.

Two different approaches have been considered for the overall satellite architecture, i.e. an integrated platform/payload approach for Concept A as opposed to a modular design with separate Platform and Service Modules (PLM and SVM) for Concept B. Both approaches have their pros and cons, mainly in relation to programmatic and assembly, verification and integration aspects. These two options provide, at this stage, additional flexibility for future implementation scenarios. They are both equally valid from a technical feasibility standpoint.

### 5.4.3 Payload

#### 5.4.3.1 Overview

The CoReH$_2$O payload is a dual-frequency X-band and Ku-band SAR operated with an incidence angle range constrained to 30–45°. It transmits single linearly-polarised (V) signals and acquires data in both polarisations (VV and VH). The combination of requirements for high resolution (50 m × 50 m) with at least four Effective Number of Looks (ENL) and for a wide swath (≥100 km) led to the choice of ScanSAR operation to allow using an elliptical reflector-based antenna with a convenient aspect ratio. Additionally, the following high-level trade-offs have been performed:

— Dual antenna vs. single antenna.

— Synchronised operation vs. non-synchronised operation of the two frequencies.

A single-reflector antenna illuminated by two adjacently placed feed subsystems with synchronised transmission pulses has been chosen for both concepts on the grounds of performance, power demand and launcher compatibility. Further trade-offs at lower levels involved:

— Antenna size and number of ScanSAR beams needed to cover the swath.
— Multi-look strategy in range and azimuth for both frequencies.
— Available technology and use of heritage.

These led to different implementation choices, which are detailed hereafter. This subsection starts with the description of the observation principle. Then, based on the ScanSAR mode defined, the functional architecture of the instrument is described including the detailed design and technology for the various subsystems. The subsection ends with considerations on the instrument characterisation and a description of the calibration approach.

#### 5.4.3.2 Observation principle

The SAR payload will operate in ScanSAR mode. Multiple sub-swaths (six or seven depending on the concept) are used to cover the 100 km swath with a resolution of 50 m × 50 m for the Level-1 product (after multi-looking). The swath is located at the far end of the possible incidence angle range; this is preferred to minimise the required RF power and data rate and to optimise the antenna length. In order to minimise the radiometric variations, the ScanSAR cycle has been defined such that each area is revisited multiple times during imaging, meaning that from each target multiple bursts are recorded. This approach is used to mitigate the scalloping effect and was already used for the Advanced Synthetic Aperture Radar (ASAR) on Envisat. The observation principles of both concepts are illustrated in Fig. 5.9.

Concept A uses a ScanSAR cycle with seven sub-swaths. Roll steering of the satellite is foreseen to mitigate slant range variations, which occur owing to the varying altitude along the orbit. This leads to a variable access range with incidence angles of 36–42° during Phase-1 (for 666 km altitude, in red in Fig. 5.9) and 39–45° during Phase-2 (for 645 km altitude, in black in Fig. 5.9). The ScanSAR timeline and illumination times are driven by the multi-look approach. In X-band there are five bursts for each target, each corresponding to one natural azimuth look. In Ku-band there are three bursts, each one being further processed to three overlapping azimuth looks. At processing level,
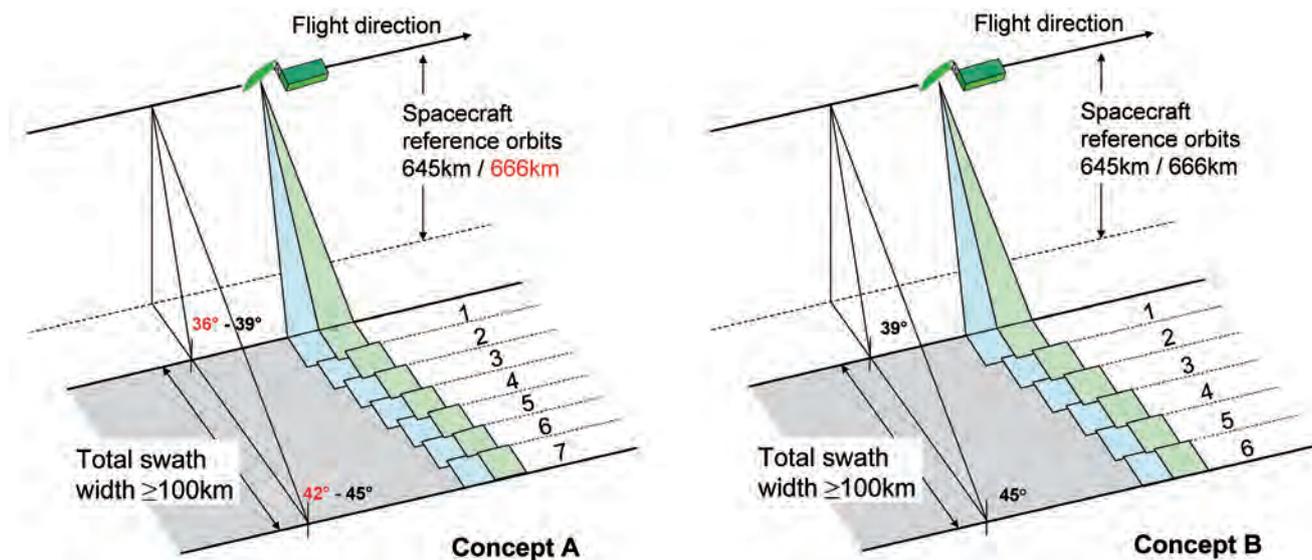
Figure 5.9. Observation principle of the two concepts: ScanSAR acquisition with seven sub-swaths, incidence angles in red for Phase-1 and in black for Phase-2 (left) and ScanSAR acquisition with six sub-swaths, constant incidence angle (right).

specific weighting is applied to each look to achieve ENL ≥4 in azimuth. Hence, only one look in range is necessary.

Concept B uses a ScanSAR cycle with six sub-swaths and constant access range located between the incidence angles of 39–45° (Fig. 5.9). The Pulse Repetition Frequency (PRF) is adapted along the orbit to compensate for the variations in slant range. With regard to the multi-look approach, the ScanSAR timeline is adapted for acquisition of four bursts in X-band (each corresponding to one natural azimuth look) and two bursts in Ku-band (each further processed to two overlapping looks). At processing level, the looks in azimuth are weighted such that the azimuth pattern is compensated. In Ku-band, this is complemented by additional multi-looking in range, ensuring ENL ≥4.

To generate the beams, both concepts are based on a single reflector illuminated by two multiple-beam feed systems located side-by-side in the focal plane. This use of a combined aperture leads to two sets of footprints (one for each frequency), which are separated by a few seconds in the along-track direction (coloured in light blue and green in Fig. 5.9) requiring co-registration during ground processing. The main advantage of the use of a single reflector is the possibility to optimise its size to minimise the required RF power. Additionally, both concepts need two transmission chains: one for X-band, one for Ku-band, and four reception chains for the co- and cross-polarised signals at both frequencies, which are operated in a synchronised way. The synchronisation of both frequencies simplifies the SAR operations as it enables a common timing, which ensures that reception in one of the bands does not coincide with emission in the other band. However, such synchronisation leads to different azimuth resolutions for both bands, as it imposes identical burst illumination times. A complex multi-look strategy adapted to dual-frequency operation allows meeting the spatial-resolution performance for both bands via dedicated processing on the ground.

### 5.4.3.3 Functional architecture

The functional architecture of the payload is based on a conventional SAR concept. The main blocks are depicted in Fig. 5.10. In transmission (purple

path), the same scheme applies at each frequency: the linearly Frequency Modulated (FM) chirp signal is generated at baseband and up-converted to the desired transmit frequency by means of a local oscillator locked to a stable and coherent frequency reference. This reference is used for both frequencies to ensure perfect synchronisation of the two emitted channels . Then, the signal is amplified by the High Power Amplifier (HPA) and distributed to the feed array. A subset of horns switched electronically radiates to the reflector, which then illuminates the area to be imaged on the ground.

On reception (green path in Fig. 5.10), the backscattered signal is collected through the reflector antenna and focused onto the feed subsystem. The separation between polarisations is performed at antenna level through the use of Ortho-Mode Transducers (OMTs) to generate the four receiver channels. These have an identical architecture: After power combination in the switch matrix and Low Noise Amplification (LNA), including limiters, the signal is down-converted and digitised. After digital signal-processing and formatting, the data is sent to the platform.

Figure 5.11 presents further details on the implementation at subsystem-level. The detailed description of this equipment for the two concepts is presented in the following subsections, addressing:

— Reflector antenna and feed
— Switch matrix and distribution network
— Active front-end (LNA and HPA)
— Radar central electronics

### 5.4.3.4  Instrument subsystems: reflector antenna and feed

Two adjacent feed subsystems illuminate a single parabolic offset reflector, as shown in Fig 5.12. The reflector size is optimised for both bands. In azimuth, the antenna length is tuned to optimise the performance linked to the multi-looking approach, including ambiguities and radiometry. In elevation, the reflector illumination is adjusted to ensure identical swaths for both frequencies. The reflector is under-illuminated in Ku-band, to cope with the higher frequency.

For Concept A, the projected aperture is 4.2 m × 1.7 m with elliptical rim; the focal length to the feed is 3.2 m. For Concept B, the projected aperture is 4.3 m × 1.8 m with super-elliptical rim; the focal length to the feed is 3 m. In both cases, the reflector is built in Carbon Fibre Reinforced Plastic (CFRP) sandwich with aluminium core, to provide low mass, high stiffness, and
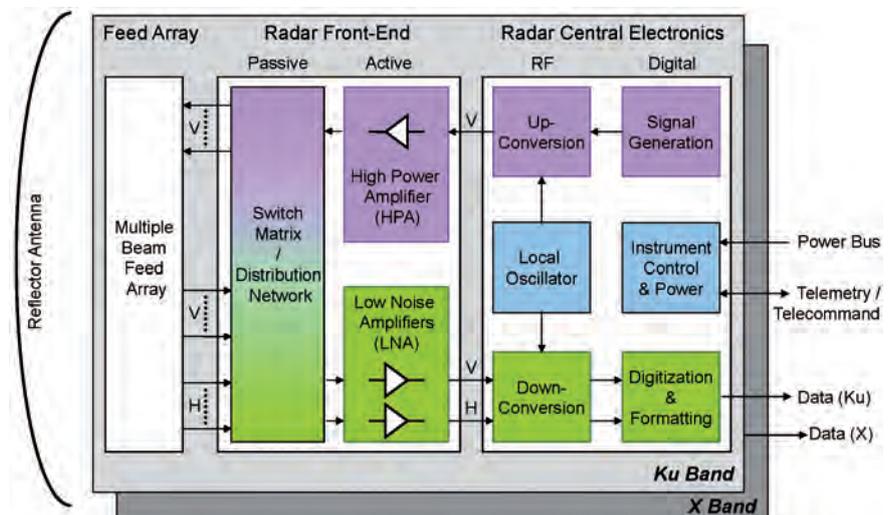


Figure 5.10. Payload functional architecture.
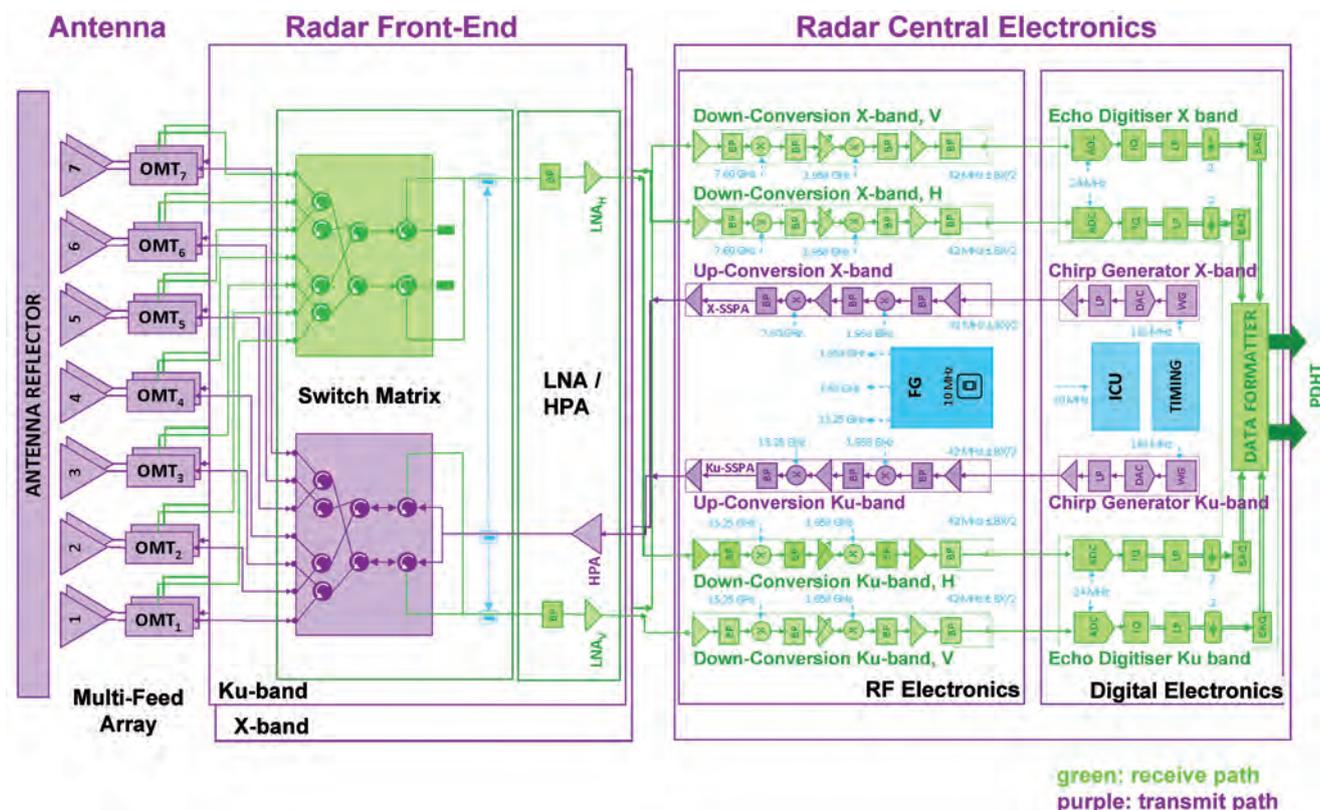
Figure 5.11. SAR detailed functional architecture implementation, Concept B.

thermal stability. Heritage for this technology is available in Europe, as shown in Fig. 5.13.

The design of the feeds in both frequencies is driven by the following requirements:

— Alignment of the beams in azimuth.

— Optimisation of the secondary antenna pattern side lobe levels for achieving the required ambiguity performance.

— Improvement of the directivity and beam overlap between adjacent beam to minimise the RF power.

— Cross-polarisation performance $\leq-25$ dB.

As already outlined, the feed subsystem of both concepts is based on an array of multiple horns. The horns are activated individually via the switch network, which controls the direction of the generated antenna beam and thus the illuminated area on the ground. Each of the various beams required for ScanSAR (six or seven depending on the concept) is generated by combining two adjacent horns. In addition, neighbouring beams on the ground are generated by overlapping horns. As an example, beam 1 is generated by horns 1 and 2, while beam 2 relies on horns 2 and 3, and so on (see Fig. 5.14). This ensures a larger overlap between adjacent beams and creates the desired crossover gain level to limit the radiometric performance variation over the swath. The position of the horn is given by the focal distance of the reflector antenna and the required beam separation. The same horns are used for reception of both polarisations, which are then separated by OMTs providing high cross-polar isolation.

Figure 5.12. Geometry of the feeds and reflector configuration.
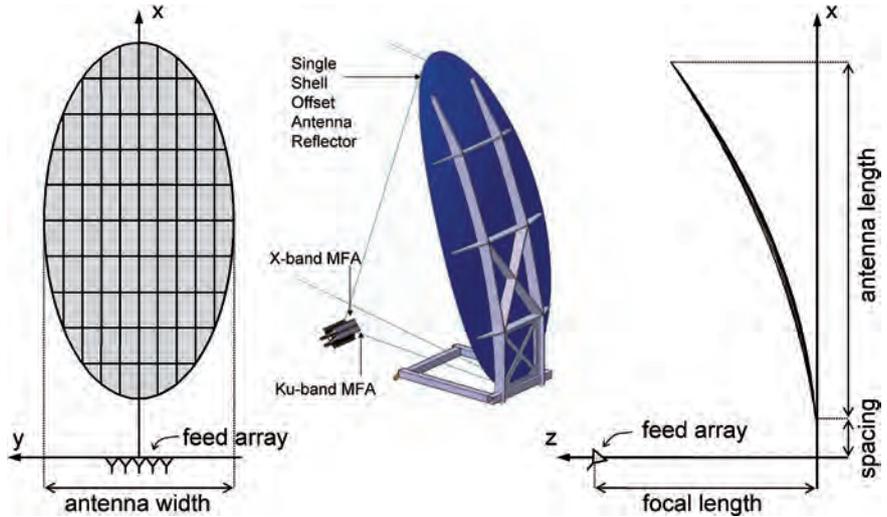
To implement this technique and fulfil the necessary requirements, different technologies are possible. For Concept A, the technology is based on split horns. The patented design (Heer et al., 2004), called Multi-Feed Array (MFA), has been demonstrated through an X-band breadboard prototype (Koch et al., 2007, Heer & Grafmüller, 2004) and more recently a Ku-band one (Fügen et al., 2011, 2012). This MFA consists of eight split horns that form seven beams. An X-band split horn is composed of two split-horn elements while at Ku-band four elements per split horn are required, because of the frequency ratio. Each element is built by a sector horn flared in the azimuth plane only (i.e. along-track) and with constant width in the elevation plane. The azimuth plane walls are corrugated to obtain identical illumination of the reflector for vertical and horizontal polarisations. The two-feed systems at both frequencies have been successfully built and tested (Figs. 5.15 and 5.16). Test results show that the return loss within the frequency range is lower than –24 dB for both vertical and horizontal polarisations (Fig. 5.17), providing a global isolation between the two polarisations higher than 54 dB. The cross coupling within the same



Figure 5.13. Astra-1K CFRP reflector (3.5 m × 2.6 m). (Astrium)
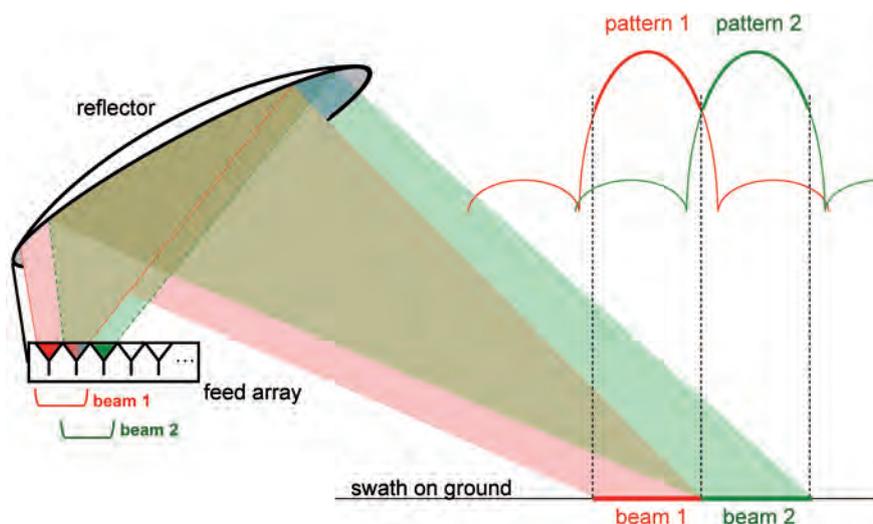
polarisation has been measured to be below −41 dB. All these measurements are well in line with the SAR performance requirements.

For Concept B, the technology is based on multimodal horns (Cecchini et al., 2011, 2012). Similar technology has already been used for telecommunication programmes, e.g. Astra. Each horn is composed of a flared phasing section and a mode launcher. The effect introduced by the pyramidal section is a square law phase error on the modes that provides a broadening of the beam pattern, depending on the flare angle (or equivalently on the length) of the horn section. The general approach to generate and select the antenna beams is very similar to Concept A, but the baseline design is based on seven horns, as only six beams are foreseen. For each frequency the combination of two horns is used to form one beam and adjacent beams on the ground are formed by partly overlapping horns in the feed. The separation of the polarisations is done by OMTs providing the necessary isolation of 50 dB. The Ku-band feed has already been successfully built and tested (Fig. 5.18), while an X-band feed breadboard is about to be completed. Figure 5.19 shows the good agreement between measurements and simulation for the primary patterns. The cross-polarisation level represented in red is in line with the requirements.

### 5.4.3.5 Instrument subsystems: switch matrix and distribution network

All channels of the antenna feed system consist of the radiating elements, which are activated electrically via a distribution network also called 'switch matrix'. Its purpose is to ensure the radiation of selected horns, thereby controlling the different antenna beams. The switch matrix is adapted to



Figure 5.15. Concept A Ku-band MFA breadboard applicable for CoReH$_2$O. (EADS Astrium GmbH)

Figure 5.16. Concept A X-band MFA breadboard applicable for CoReH$_2$O. (EADS Astrium GmbH)
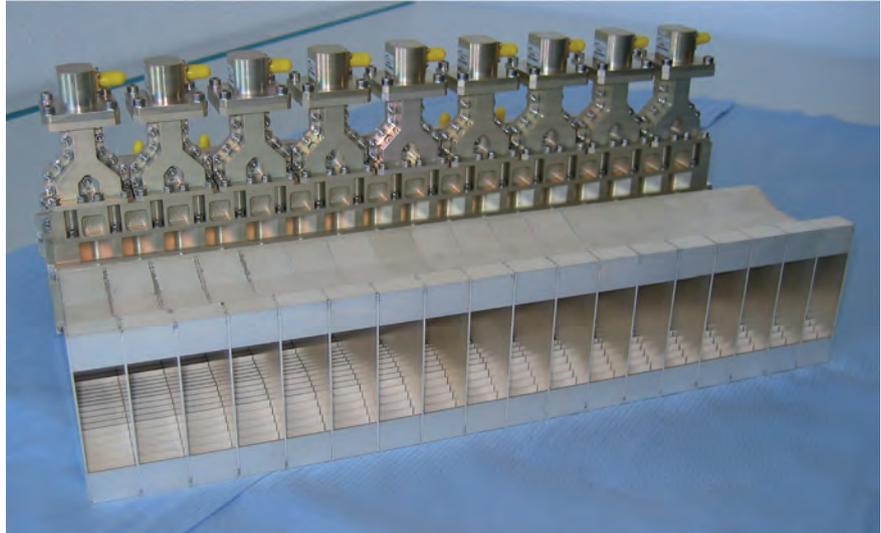
the specific feed implementation and is used in transmission as well as in reception. Hence, in total, four switch matrices are required, one for each of the four different channels (two frequency bands and two polarisations).

To illustrate the functional block diagram, the feed system and the X-band distribution network for the VV channel (highlighted by the blue box) of Concept A are shown in Fig. 5.20. The overall design of these networks for both concepts are identical, but they have a different number of split horn elements for X- and Ku-band.

This distribution network relies on the use of power combiners/splitters and high-power switches. Depending on the respective concept, the switch matrix can be either based on latching circulators or phase shifter switches (Khairuddin et al., 2009). The basic requirements for these two technologies are summarised in Table 5.2.

The latching circulator-type switches are based on three-port waveguide circulator technology. This ferrite component (Fig. 5.21 left) is based on the heritage of Sentinel-3 for both the microwave radiometer and the altimeter, but with a frequency range adapted to 17.2 GHz and increased power handling capability. A complete model of the switch has already been built and successfully tested. Measurements have shown transmission loss ≤0.17 dB.

The phase shifter switch is a ferrite component that has some heritage from telecommunication programmes such as ARTES. The bandwidth required for

Figure 5.17. Measured return loss for the Concept A Ku-band MFA.
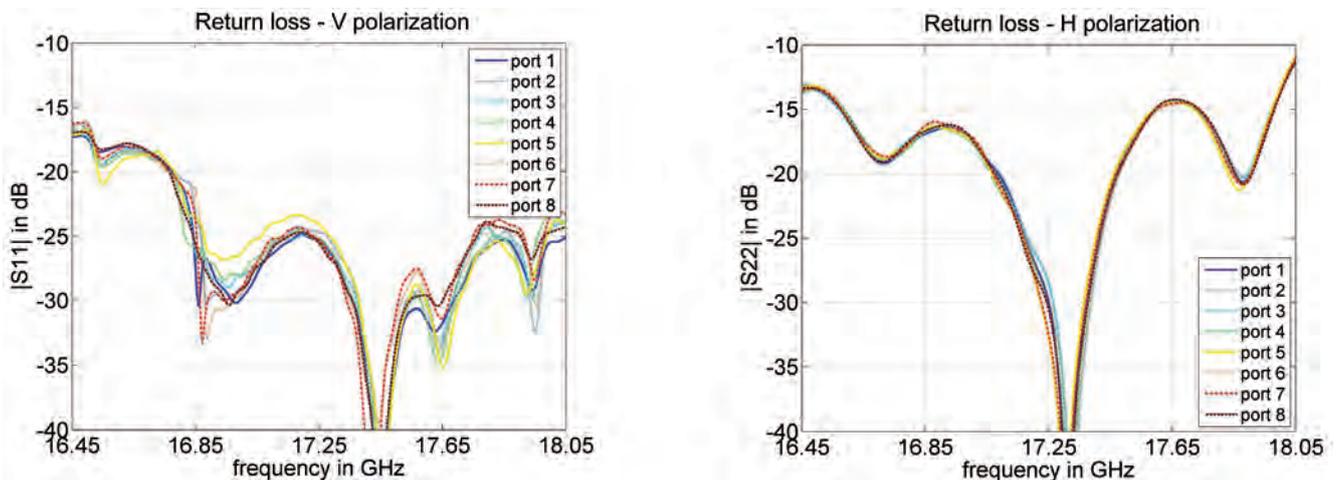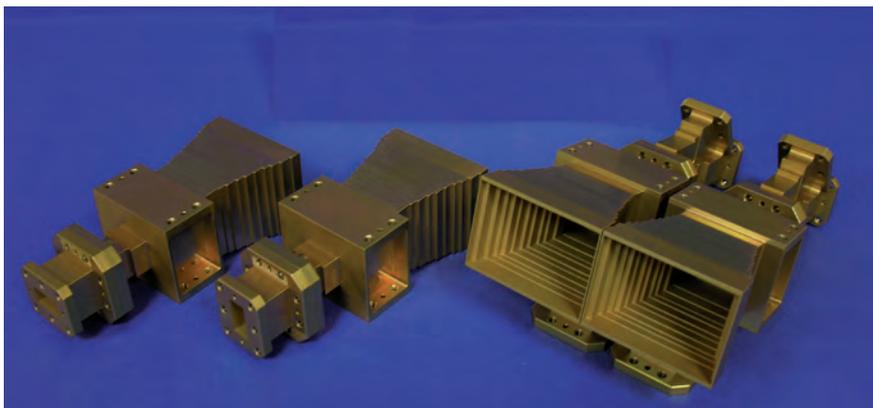
Figure 5.18. Ku-band feed horn element breadboard applicable for CoReH$_2$O for Concept B. (Thales Alenia Space IT)
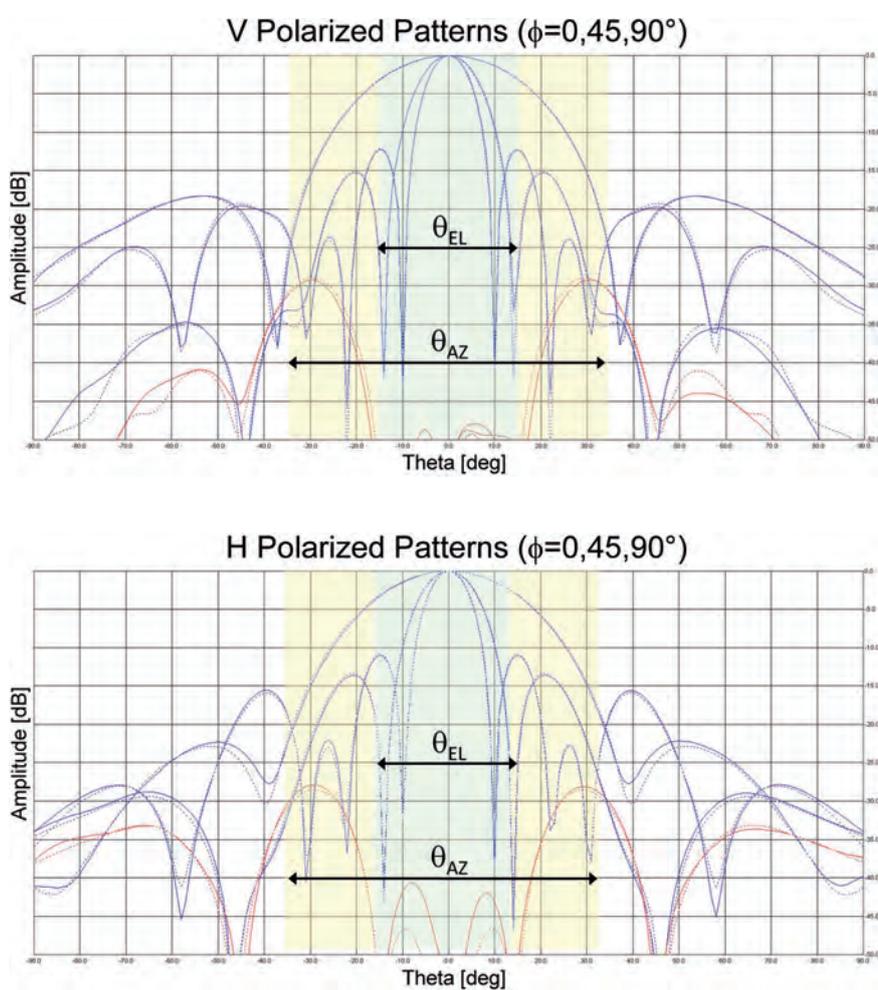


Figure 5.19. Comparison between measured and simulated primary patterns at feed level (simulated dotted line, measured continuous line) for Concept B feed breadboard.

|  |  | Latching Circulator | Phase Shifter Switch |
|---|---|---|---|
| RF Power | W | 1400 peak<br>140 average | 2500 peak<br>400 average |
| Isolation | dB | ≥25 threshold over total temperature range | ≥25 threshold over total temperature range |
| Transmission Loss | dB | ≤0.25 dB | ≤0.35 dB |

Table 5.2. Requirements for high-power switch element.

Figure 5.20. X-band distribution for feed system architecture for Concept A.
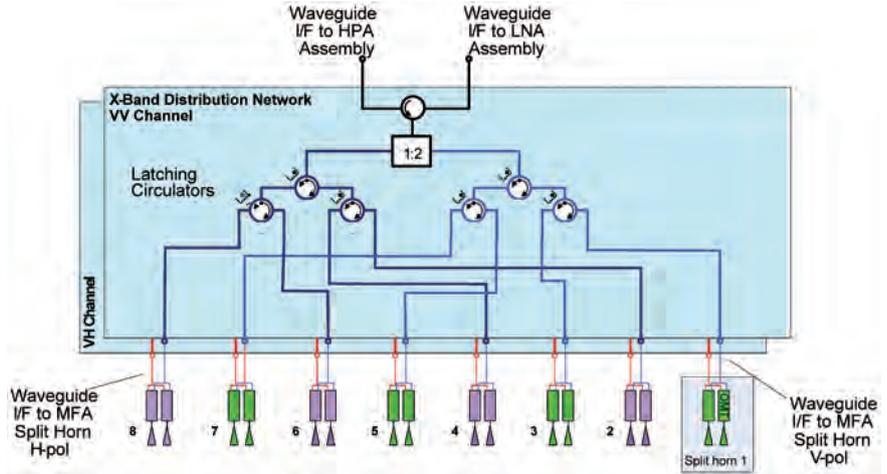


Figure 5.21. The Ku-band latching circulator (left) and phase shifter (right) breadboards applicable for CoReH₂O. (ComDev GB)
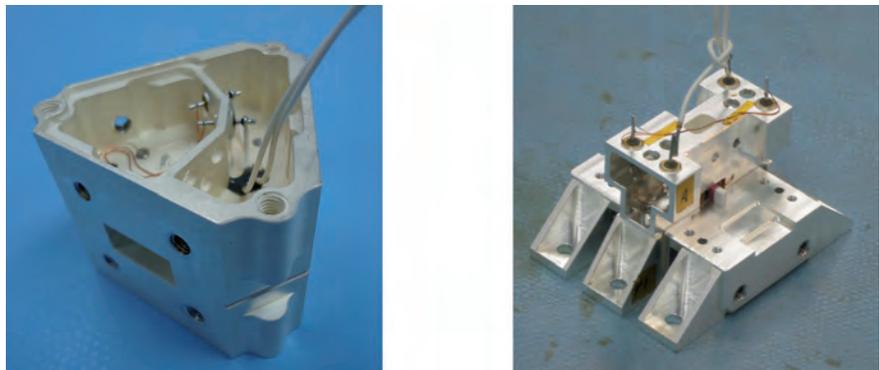


CoReH$_2$O is smaller, but the power has to be increased. A model of the phase shifter has already been built and successfully tested (Fig. 5.21 right).

### 5.4.3.6 Instrument subsystem: active front-end

The active front-end is made of the LNA and HPA which both amplify the signal at different points in the RF receive and transmit chains, respectively. The LNA is the first amplification stage of the received signal and its noise figure has significant impact on the required power. The HPA is the main amplification stage of the transmit signal and the key parameters are the power levels and number of on/off cycles.

The LNA assemblies form a dedicated sub-unit located close to the switch matrix. Each of the four receive channels requires an LNA stage, leading to a total of four LNAs, each backed up by a cold redundant unit. Depending on the technology chosen for implementation and on the frequency, noise figures below 2 dB in X-band and below 2.5 dB in Ku-band are achieved. These values are taken into account to ensure compliance with the Noise Equivalent Sigma Zero requirements for the four channels.

The HPA subsystem includes the vacuum tubes, the redundancy switches and the Electronics Power Conditioners (EPCs). This equipment, required for both frequencies, is considered a separate subsystem because of the high power consumption and dissipation (Fig. 5.22). Two HPA technologies are available: Travelling Wave Tube (TWT) and Klystron. Each concept favours either one or the other option in view of their different power requirements (Table 5.3), but is compatible with the alternative technology.

For Concept A, the baseline is based on a TWT initially developed for the X-band (Fig. 5.23). The proposed TWT are based on a qualified design,
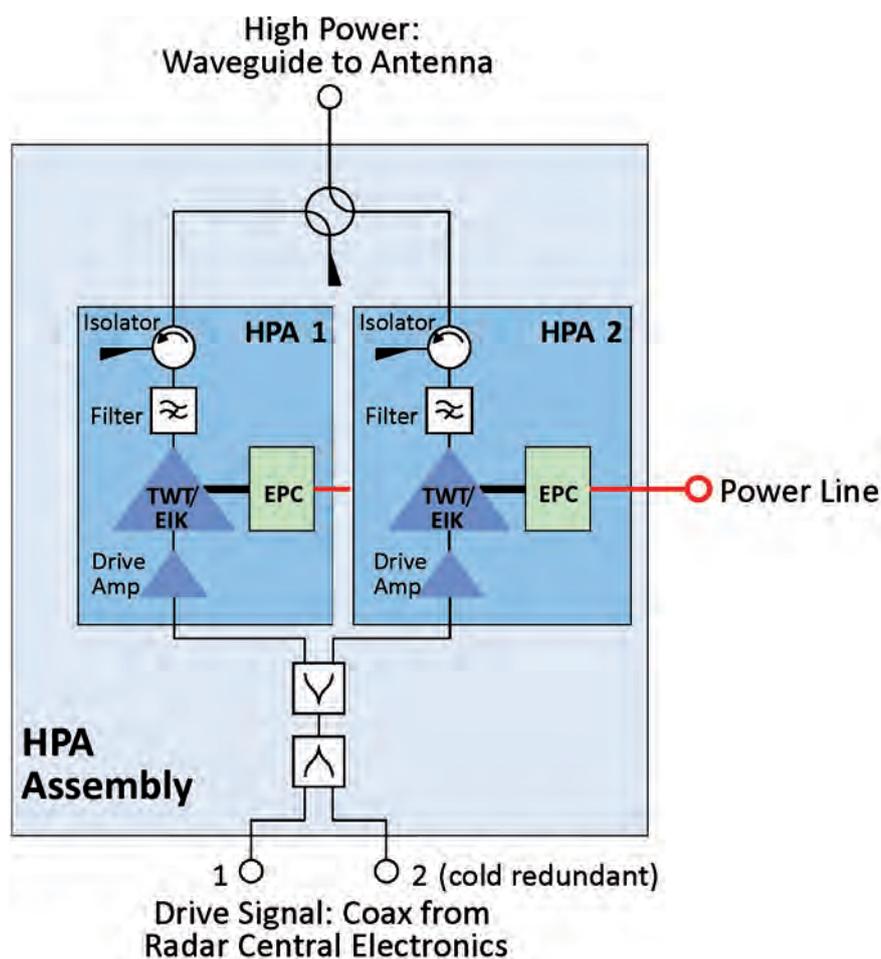
Figure 5.22. Functional block diagram of HPA assembly (per frequency band).

| Frequency | 17.2 GHz | 9.6 GHz |
|---|---|---|
| Bandwidth | 20 MHz | |
| PRF | 5400–7100 Hz | |
| Pulse Duty Cycle | 10% for Concept A 16.3% for Concept B | |
| RF Peak Power | 2.2 kW for Concept A 2.5 kW for Concept B | 2.6 kW for Concept A 2 kW for Concept B |
| Average RF Power | 220 W for Concept A 410 W for Concept B | 260 W for Concept A 340 W for Concept B |
| Efficiency | ≥40% | |
| Time of operation | 30 minutes per orbit | |
| On/off cycles | >120 000 | |
| Life | 5.5 years | |

Table 5.3. Requirements for the HPA for both concepts.

successfully operating in orbit at X-band (up to 2.5 kW peak power with 10% instrument duty-cycle). For use at Ku-band, the TWT design has to be adapted with modification of the gun and of the collector. The pre-development of Ku-band tube sub-assemblies has already started. Test results and simulations have confirmed the capability to operate up to 16% instrument duty-cycle with 2.5 kW peak power in Ku-band and 3 kW peak power in X-band with such a modified design.

The TWT efficiency is higher than 35% depending on the peak-power setting. The possible limitation on the number of on/off cycles (50 000 were

Figure 5.23. Electron gun TWT in X-band. (Thales Electron Devices GmbH)
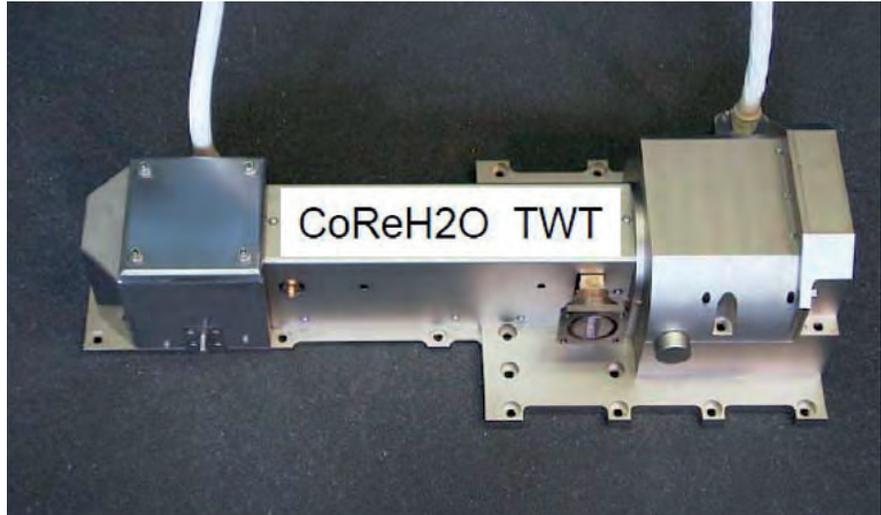


confirmed by testing) imposes some constraints, which have been taken into account in the mission operation plan for Concept A. As an alternative, Concept A has the possibility to accommodate the Klystron tube technology. The lower power demand leads to a slightly reduced efficiency of the HPA, though all the requirements of Table 5.3 are still met.

For Concept B, the Klystron technology has been selected as a baseline. It is a linear beam vacuum electron device that uses conventional space-qualified materials and assembly techniques. It utilises multiple interaction gaps in each resonator cavity, thereby improving the efficiency at higher RF operating frequencies. A similar 94 GHz Klystron has been in orbit since 2006 as part of NASA's CloudSat mission and has been further improved for ESA's EarthCARE mission. A comparable 35 GHz Klystron is also being developed for NASA's SWOT mission.

A Ku-band CoReH$_2$O Klystron first Engineering Model (EM) was built (Fig. 5.24), with the same assembly methodology and materials as used for the existing space-qualified Klystrons, including magnets and gun support ceramics. A lower temperature (larger diameter) cathode was used to achieve a longer life. The collector has been slightly adapted to handle higher power. The enclosure design includes two cold plate interfaces to dissipate the higher power. A new RF circuit was developed to meet the Ku-band frequency requirements while conforming to the total length permitted by the existing baseline gun/magnet design. This Ku-band EM has been successfully tested with performance beyond the requirements (Horoyski et al., 2011). The output power reached up to 3.5 kW peak power with up to 20% instrument duty-cycle with a measured efficiency greater than 43%. The number of on/off cycles is estimated to meet the requirements.

The X-band Klystron design is a slight modification of the Ku-band design, apart from new windows and adapted RF circuitry to account for the lower operating frequency. Similar performance as for Ku-band has been assessed by simulation. As an alternative, Concept B has the possibility to accommodate the TWT technology. The limitation on the number of on/off cycles, as discussed for Concept A, will induce similar constraints on the mission operation plan.

### 5.4.3.7 Instrument subsystems: radar central electronics

As shown in Fig. 5.11, the radar central electronics is split between the RF Electronics and the Digital Electronics. For both concepts, the synchronisation of the two emission chains is based on the use of the same Intermediate Frequency (IF) for both X- and Ku-band. The local oscillators are generated starting from a common reference from the Ultra-Stable Oscillator (USO) at
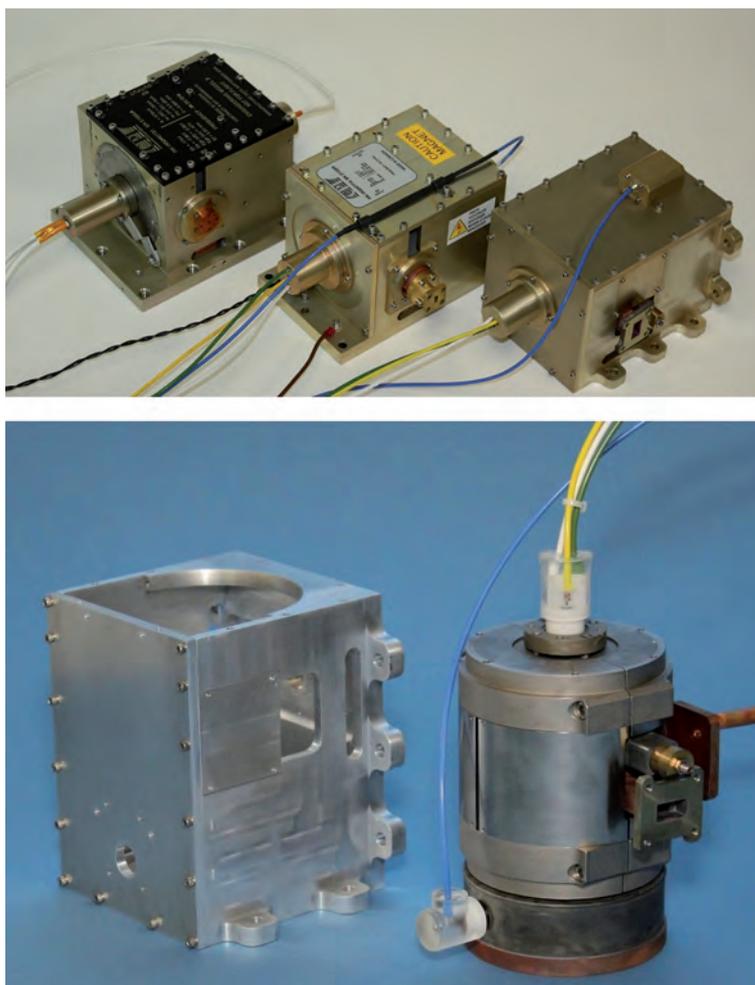
Figure 5.24. Klystron models. Top left to right in decreasing order of operating frequency: EarthCARE model (94 GHz), SWOT model (35 GHz), first Ku-band EM for CoReH$_2$O (17.2 GHz). Bottom: Ku-band EM before enclosure. (CPI Inc.)

10 MHz. For Concept A, the central electronics is based on a single stage up- and down-conversion using a common chirp generator for X- and Ku-band at 900 MHz. For Concept B, the up- and down-conversions are done in two stages integrating additional filtering, the IF being 42 MHz (Fig. 5.11).

The RF electronics (Germani et al., 2011) provides the following main functions:

— The frequency up-conversion of the waveforms (in purple in Fig. 5.11) increases the centre frequency from IF at output of the Digital Electronics up to X-band or Ku-band. The IF of the signal is mixed with a local oscillator. This multiplication stage moves the centre frequency up to 9.6 GHz for X-band and to 17.2 GHz for Ku-band. Band-pass filters suppress the harmonics at each stage.

— The frequency down-conversion (in green in Fig. 5.11) decreases the centre frequency from X-band or Ku-band down to IF. The signal is mixed with the same local oscillator and shifted down to IF. Additional filtering and amplification of received signals are also included at each stage.

— The Frequency Generator (FG) produces all the reference frequencies necessary for assuring the coherency among all channels. The different frequencies needed to implement the frequency plan are derived from an Ultra-Stable Oscillator at 10 MHz (Fig. 5.11).

The Digital Electronics implements the functions of signal generation, echo sampling, compression and formatting. In addition, it implements also the functions of instrument control and timing generation. As shown in Fig. 5.11:

— Two Chirp Generators (in purple in Fig. 5.11) synthesise pass-band chirp waveforms at IF for the two emission chains in X- and Ku-band.

— The four Echo Digitisers (in green in Fig. 5.11) receive the down-converted signals at IF and perform the function of echo sampling (at 10 bit), phase detection, filtering, decimation, data quantisation and compression in the Block Adaptive Quantiser (BAQ), and formatting.

— The Instrument Control Unit (ICU) is dedicated to instrument control tasks and acquisition of telemetry, while the timing block manages timing signals of the SAR instrument. This unit ensures the interface and exchange of commands and telemetries from and to the platform.

To obtain a dynamic range of 30 dB, the signal is converted with a word length of 10 bits and then further compressed. The BAQ compression scheme has been carefully customised for both concepts, trading the data rate against signal quantisation loss. In particular, the latter requires careful attention, as the worst-case loss at the upper limit of the dynamic range must be considered as a contribution to the Noise Equivalent Sigma Zero.

Concept A includes a BAQ with ratio 10:9 for the cross-polarisation channel (VH) and 10:7 for the co-polarisation channel (VV) at both frequencies. This approach minimises the losses induced by the quantisation (losses ≤0.1 dB for VH and losses ≤0.6 dB for VV), thereby optimising the power need to fulfil the Noise Equivalent Sigma Zero requirements.

The approach taken for Concept B is to optimise the data rate by applying a BAQ of ratio 10:6 with an advanced compression scheme to all four channels. The quantisation losses impacting the Noise Equivalent Sigma Zero are then higher, inducing for VH a slightly higher need for power, which can be achieved thanks to the power capability of the Klystron tube.

### 5.4.3.8  Instrument characterisation and calibration

The objective of the instrument characterisation and calibration is to ensure stable measurements over the mission lifetime and, in particular, to guarantee the achievement of the radiometric requirements as defined in Chapter 4. It includes both on-ground measurements and in-orbit measurements through the internal and external calibration to eliminate errors, often due to instabilities, e.g. thermal drift, or to geometric dependence, e.g. swath position. The on-ground measurements during integration and testing are used prior to launch to characterise the complete transmit and receive chains over temperature and the antenna feed subsystem. The internal calibration is used to monitor and correct instrument internal amplitude and phase drifts and to derive the replica for processing. The external calibration is used for geometric and pointing calibration, antenna pattern verification and absolute radiometric calibration.

#### 5.4.3.8.1 Internal calibration

The internal calibration aims to measure the amplitude and phase stability of the instrument in flight to provide the required stability and relative accuracy of the SAR radiometric performance. Amplitude and phase drifts inside the instrument will be monitored by internal calibration loops, which are standard for SAR instruments and periodically included in the observation data acquisition sequence. The measurement of signal samples through

various paths of the instrument allows calibrating all active components and as many as possible of the passive components in three measurement steps, as illustrated in Fig. 5.25 for Concept A.

The three calibration loops, highlighted with three different colour codes, cover the following paths:

— Transmit path (Tx, green loop), encompassing the switch matrix, HPA, and radar electronics

— Receive path (Rx, blue loops), covering the switch matrix, LNA, and radar electronics

— Radar electronics short cut (RE, red loop), characterising the radar electronics only, enabling for compensation of its contribution to the Tx and Rx path.

These measurements allow acquiring loop-back signals, to be used with the twofold aim of generating replicas for improving the range compression stage of SAR processing and of measuring variations of transmitter power and gains in the receiver chains. The results of these measurements are combined on the ground to provide a value proportional to the system power gain product. In addition, internal calibration measurements allow evaluating gain and phase imbalances between channels at different polarisation and frequency. The accuracy of such internal calibration scheme has been assessed to be better than 0.25 dB for both concepts, which represents an important contribution to the radiometric stability and absolute radiometric bias budgets.
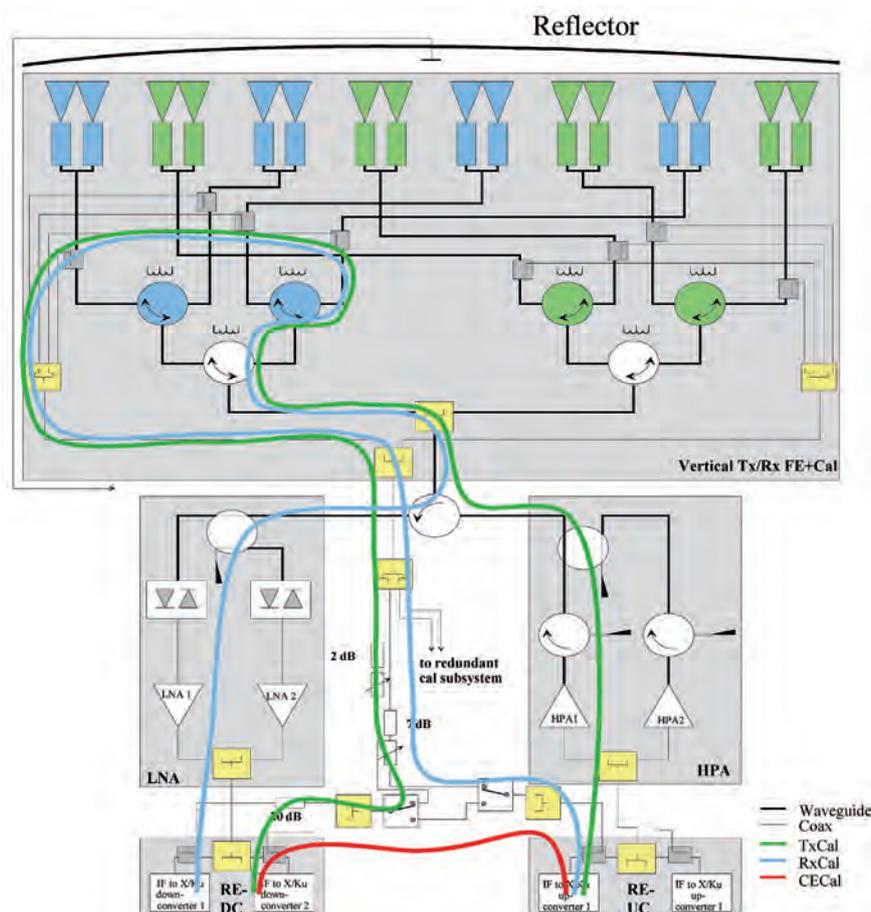


Figure 5.25. Front-end block diagram showing calibration loops for V path as defined for Concept A.

### 5.4.3.8.2 External calibration

As shown in Fig. 5.26, the external calibration is used for the geometric and pointing calibration, the antenna pattern verification and the absolute radiometric calibration. It exploits signals originating from, or scattered by, ground targets that can be either point targets with known radar cross-section (corner reflector, transponders) or distributed targets of known scattering characteristics.

To reach the required location accuracy (geometric calibration), each pixel in the SAR data product needs to be associated with its azimuth and range coordinates within the observed swath. For this purpose, the determination of systematic shifts in azimuth and range delay offsets caused by the internal electronic delay of the instrument is performed based on the use of known point targets on the ground and of the orbit and attitude data.

For the pointing calibration in azimuth, the Doppler information is used to determine the pointing of the antenna relative to ground receivers, whereas in elevation the rainforest is used. Since the Amazon rainforest is a large distributed target with quite homogeneous backscatterers, the radiated antenna pattern in elevation is clearly visible in the uncorrected images. After summing up the range lines in azimuth direction, the range profile can be extracted, yielding an estimate of the main beam shape in elevation. Then specific processing provides the pointing in elevation.

For the antenna pattern verification, since the dual-frequency CoReH$_2$O system is operated in ScanSAR mode, all beams must be measured, and this can be done simultaneously using the same calibration approach over the rainforest in one pass. This procedure allows the shape of all main beams to be derived. The beam-to-beam gain variation can then be verified.

After the correct alignment of the CoReH$_2$O SAR system, i.e. after the correct pointing of the antenna, the drift compensation of the instrument and the radiometric correction of the antenna patterns, the SAR data products are calibrated in terms of relative radiometry. As a final step, the measurement of the whole SAR system against reference targets, i.e. the absolute radiometric calibration, is performed, so that the calibration factor is determined and the cross-talk is verified. For this purpose, because of the dual-frequency SAR operation, two independent types of reference targets such as corner reflectors and transponders must be deployed.

The instrument monitoring, which enables drift effects to be compensated for, is performed by internal calibration. In principle, the amplitude and phase channel imbalances induced by the active components are then compensated. However, the internal calibration is unable to characterise the channel imbalances arising from the radiator, since this is outside of the internal calibration loop and in principle is unable to derive the cross-talk.
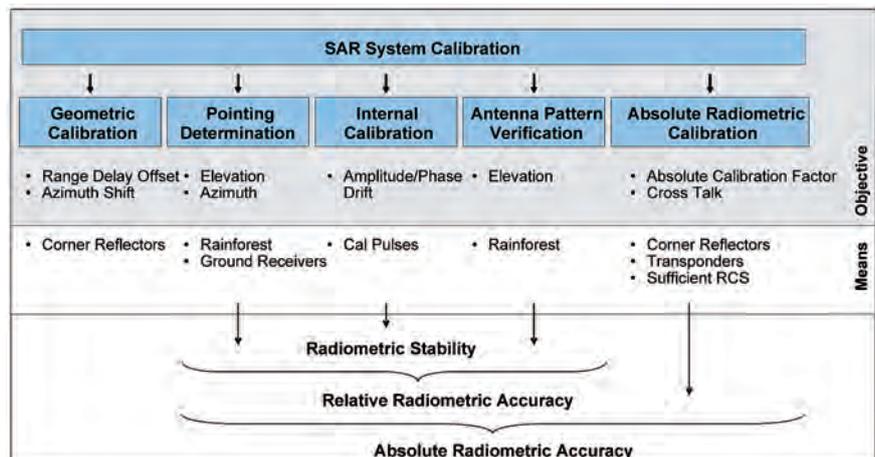


Figure 5.26. SAR system calibration procedures required for the absolute radiometric calibration of the SAR data products.

These characterisations can be performed by external measurements against reference targets such as active transponders, returning two polarisations simultaneously. Comparing the reference target in the SAR images of both polarisation channels provides the offsets caused by the system itself. This procedure is applicable to the absolute radiometric calibration to cover all the beams and to the geometric calibration to check the co-registration of pairs of dual-polarisation products.

After the absolute radiometric calibration, the image information can be transformed into physical units such as the Radar Cross Section (RCS) or the backscattering coefficients at each frequency band.

In summary, the external calibration relies on the systematic use of a calibration period over rainforest, but also on the use of ground targets. For both concepts, a combination of corner reflectors and active transponder has been recommended. The corner reflectors can be trihedrals less than 3 m wide, providing a RCS in the order of 55 dB·m$^2$ in X-band and 60 dB·m$^2$ in Ku-band (see Fig. 5.27). The active transponders with similar RCS will include X-band and Ku-band antennas in two polarisations to monitor channel imbalances and cross-talks. An example of preliminary design is shown in Fig. 5.27.

For the systematic calibration of the mission, the use of two calibration sites located at relatively high latitudes to ensure a frequent revisit is recommended. An example of location is provided in Section 5.7. These calibration sites will combine an active transponder and a passive target, e.g. corner reflectors. Ascending and descending passes will be used to calibrate at least four beams among the six or seven ScanSAR beams of the swath. The full antenna characterisation will be performed through dedicated calibration periods over the Amazon rainforest.

### 5.4.4 Platform

The platform subsystems provide all the functions for operating the spacecraft in the space environment as well as for the communications with the ground. These subsystems include the mechanical subsystems (structure, thermal and mechanisms), the electrical subsystems (payload data handling and transmission, TT&C, and electrical power), and the attitude and orbit control subsystem. The outstanding features of their design are addressed in the following sections.

### 5.4.4.1 Structure

The structure is designed to accommodate the SAR payload. The main elements driving this are the large reflector antenna and the feed assembly, which have

Figure 5.27. Calibration devices. Left: design of an active transponder for CoReH$_2$O (SEA). Right: a corner reflector. (University of Alaska)
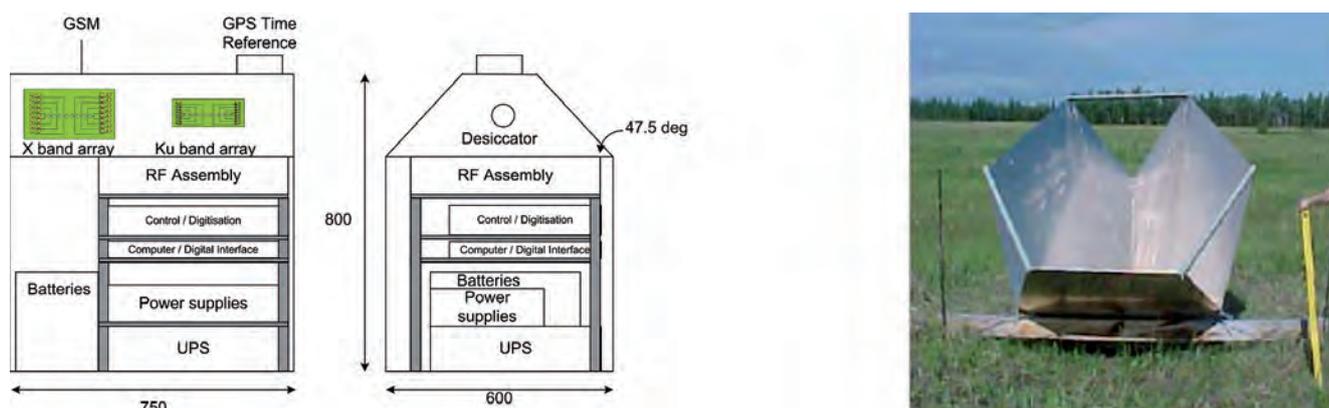
to be accommodated on the opposite ends of the satellite body. Because of this, a key requirement on the structure is to limit the in-orbit thermoelastic distortions affecting the assembly and interfaces with the attitude sensors. The other key requirement is the compatibility with the primary and back-up launchers (Section 5.5). This impacts the structure via the compliance with the minimum vibration frequency (i.e. stiffness) requirement, with the dimensional constraints to fit under the launcher fairing, and with the overall satellite mass and launch loads requirements. To ensure compatibility with both launchers, the structure is designed for a first longitudinal frequency above 60 Hz, which is well above typical values. The two structural concepts are depicted in Fig. 5.28.

The structural design of Concept A is based on an integrated solution supporting both the platform and the payload subsystem accommodation. The structure is shaped as an elongated box and consists of a base plate panel interfaced to the launcher adapter on one end and to the longitudinal corner struts on the other. The struts support the side panels, the internal transverse panel and the nadir panel on top. There is no sharp distinction between a primary and a secondary structure, the design being such that all structural elements contribute to the main load carrying capabilities, with the side panels supporting the loads from the platform and SAR equipment mounted on them. The base plate is reinforced to meet the lateral stiffness requirement imposed by the launcher. The panels are made of a composite sandwich with CFRP skins and aluminium honeycomb core, providing high stiffness with relatively low mass and minimising the thermoelastic distortions. The flight panel supports the SAR antenna in the stowed and deployed configuration and the MFA at the nadir side. The solar panel is mounted on the anti-flight side, with a dedicated panel on the central section supporting the Solar Array Deployment Mechanism (SADM).

For Concept B a modular architecture with separate SVM and PLM has been selected. The SVM provides the interface to the launcher and consists of a central CRFP cone, acting as primary structure and providing the main contribution to the overall stiffness of the SVM assembly. This cone
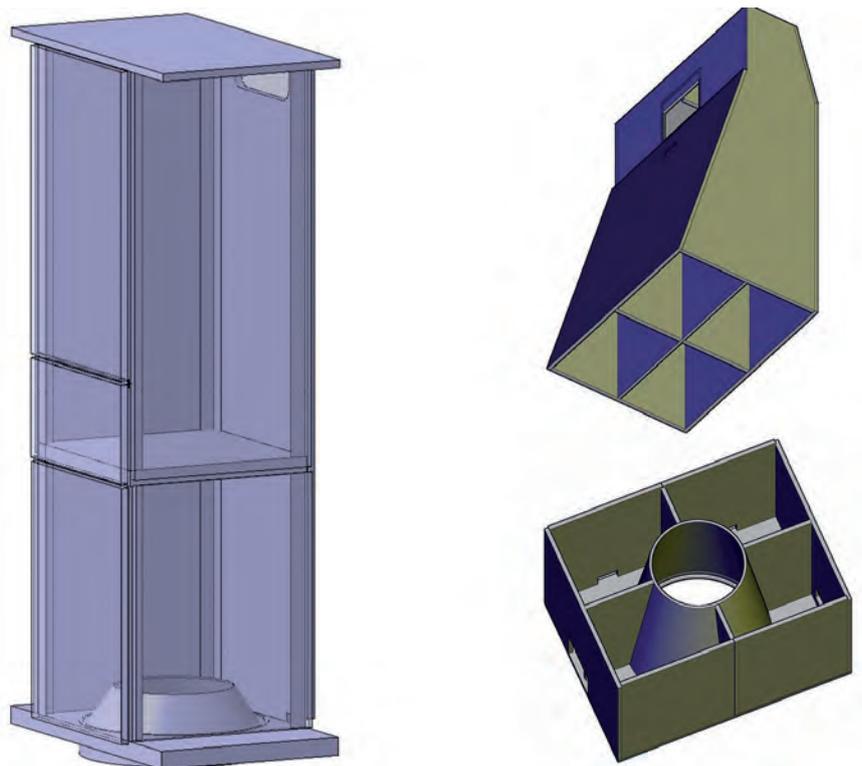


Figure 5.28. Panel-based structural concept (Concept A left, Concept B right).

| Case | Thermoelastic distortion Worst case | Stiffness Lateral worst case | Stiffness Axial worst case |
|---|---|---|---|
| Requirement | 0.007° | >18 Hz | >>55 Hz |
| Performance | 0.003° | 21 Hz 57% mass reacting | 91 Hz 41% mass reacting |

Table 5.4. Structural analysis results summary, worst cases.

is connected to a base plate and to four shear panels that support the lateral panels. The SVM provides accommodation for most platform subsystems and for the SAR reflector deployment mechanisms. The PLM has a tapered box shape and is made of side panels connected to four shear panels. It supports the accommodation of the SAR equipment and of the MFA as well as the SADM, the X-band antenna and one of the two TT&C antennas. In this case the overall structural performance of the satellite structure (stiffness and thermo-mechanical deformations) has required proper design of the mechanical interface between the SVM and the PLM.

Analysis of the structure shows that both concepts meet the requirements. Table 5.4 shows the detailed results of the modal and thermoelastic analyses and Fig. 5.29 shows the resulting mode shape and distorted shape. The strength analyses for the static loads also confirm the adequacy of the selected concepts. In conclusion, the structure subsystem is not critical and is based on mature concepts.

### 5.4.4.2 Thermal control

The thermal control design of the satellite is strongly affected by the need to maintain the highly dissipative SAR equipment (HPAs and to a lesser extent the RF and digital section of the SAR central electronics) within the allowable temperature limits under all operating conditions.

For both concepts, the thermal design is based on passive thermal control methods supplemented by electrical heaters to maintain the temperature of the equipment within the required limits under non-operating conditions.

The CoReH$_2$O dawn/dusk orbits provide favourable and relatively constant Sun illumination conditions on the satellite, with one side of the satellite always facing deep space and therefore providing an ideal accommodation for the most dissipative equipment and/or their radiators. In addition, the canted attitude of the satellite with respect to the nadir direction minimises the impinging infrared and albedo radiation from Earth on the deep-space panel, increasing the efficiency of the radiating surfaces on this side of the satellite, and also allows the use of radiators on parts of the Sun-illuminated surfaces.

The thermal control methods rely on traditional approaches. Most units and the internal surfaces of the panels are black to increase the radiation heat transfer internally towards the radiating surfaces. When needed, the



Figure 5.29. Structural analysis graphical results – thermoelastic distortion (left), lateral mode-shape (centre), axial mode shape (right) – deformations shown are exaggerated by orders of magnitude.

Figure 5.30. Example layout of heat pipes for Concept A showing embedded and externally-mounted pipes (main and redundant) with main heat dissipating payload equipment (TWT and EPC for both frequencies).
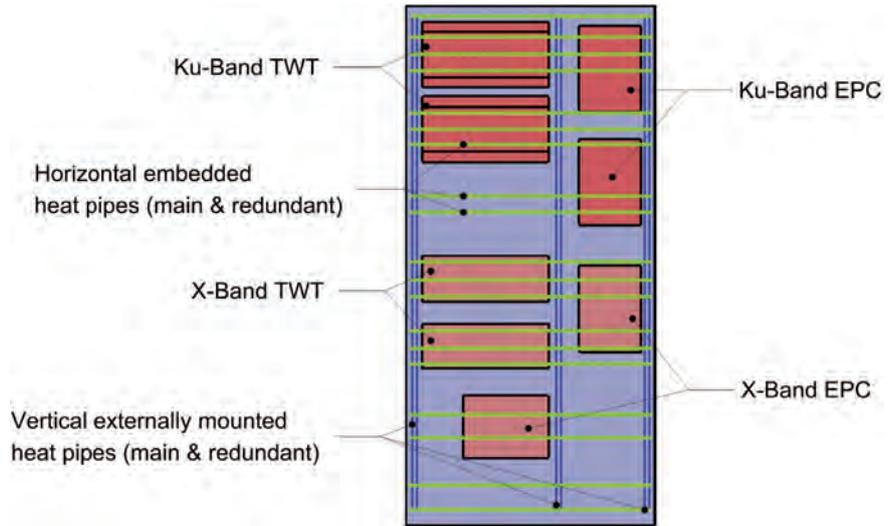


conductive heat transfer between the units and the supporting panels is increased with the use of thermal doublers and fillers. Thermal decoupling (e.g. for the batteries) is achieved with the use of multilayer insulation blankets and thermally insulating washers on the mounting brackets. The thermo-optical properties of the external surfaces of the satellite have been optimised with the use of specific materials such as black Kapton multilayer insulation blankets on the Sun-illuminated sides and optical surface reflectors (e.g. silver Teflon tapes) on the radiating surfaces.

The high dissipation of some SAR equipment and the constraints from the overall satellite configuration also impose the use of constant-conductance heat pipes to spread the concentrated heat loads of the units on the panel. Figure 5.30 shows an example for Concept A, which uses embedded as well as externally-mounted heat pipes. A similar design applies to Concept B.

A peculiar characteristic of Concept A is that the high-dissipation units accommodated on the deep-space panels as well as on the lower parts of the flight and anti-flight sunlit panels are mounted on the external surfaces and are not covered by radiating foils. This allows heat to be radiated directly to deep space.

Though requiring custom solutions, the thermal control is based on mature concepts and technologies and meets the relevant requirements with comfortable margins, as shown in Fig. 5.31 where the predicted temperatures of the SAR and platform equipment are shown to stay well within the allowable operating and non-operating ranges.

### 5.4.4.3 Mechanisms

The satellite and platform need four mechanisms, two for deploying the reflector antenna and two for deploying and/or rotating the solar array. This is illustrated in Fig. 5.32 (top). The Antenna Deployment Mechanism (ADM) is a one-axis rotating joint connected to the platform and to the base of the reflector. It uses one active and one passive hinge (Fig. 5.32, bottom left). The selected technology is based on a robust torque spring actuation with liquid dampeners. When stowed, the reflector is held by four Hold Down and Release Mechanisms (HDRMs). These use pyrotechnic or non-explosive devices for release after launch. The proposed technology is either cutter-based or makes use of the Frangibolt captive release concept (Fig. 5.32, bottom centre).

The solar array uses a SADM to ensure that all the panels are deployed to form a solar-array wing extending in the anti-flight direction, and then the orientation towards its final Sun-facing position. The SADM includes a
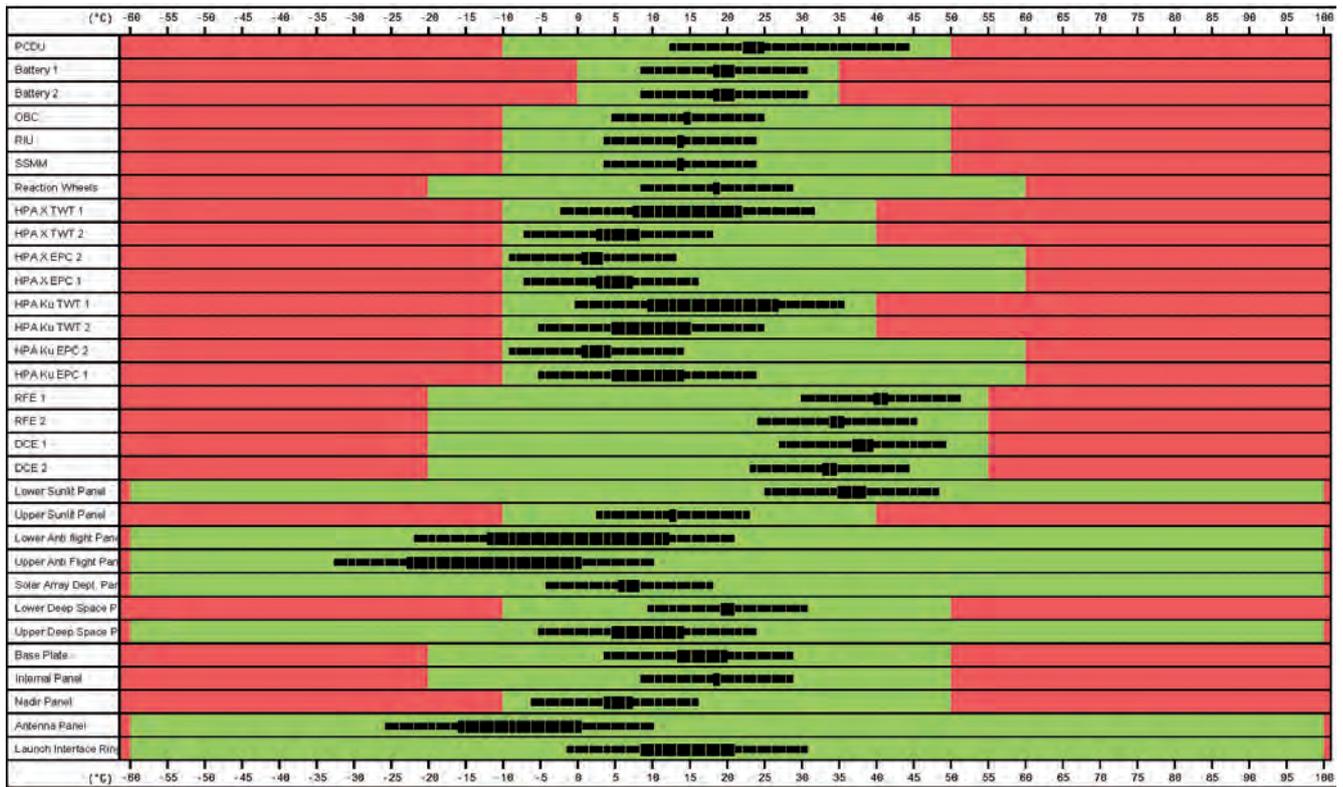
Figure 5.31. Temperature predictions for equipment for Concept A (predicted/operating range in black/green).

gear-based actuation and a twist capsule to transfer the power from the array to the Power Conditioning and Distribution Unit (PCDU) inside the platform (Fig. 5.32, bottom right). HDRMs, similar to those used for the antenna, maintain the array folded during launch and release it prior to the deployment.

Mature designs or existing equipment have been identified for all mechanisms. The proposed solutions are either based on off-the shelf equipment or custom implementations of existing flight-proven solutions.

### 5.4.4.4 Electrical architecture

The electrical architecture is designed to integrate the relevant platform subsystem so as to ensure:

— the command and control of the complete satellite in all relevant operating modes.

— the acquisition, storage and transmission to ground of the payload data and of the housekeeping telemetries.

— the power generation, storage and distribution to the platform and SAR equipment.

The electrical architecture of Concept A is depicted in Fig. 5.33. Heritage concepts and equipment have been considered and there are very few differences between the two concepts.

The command and control functions of the satellite are executed by the onboard software running on the On-Board Computer (OBC) and uses dedicated platform and payload command-and-control MIL-1553B data buses and Remote Interface Unit (RIU), catering for payload-specific interfaces and

**ADM**        **HDRM**        **SADM**
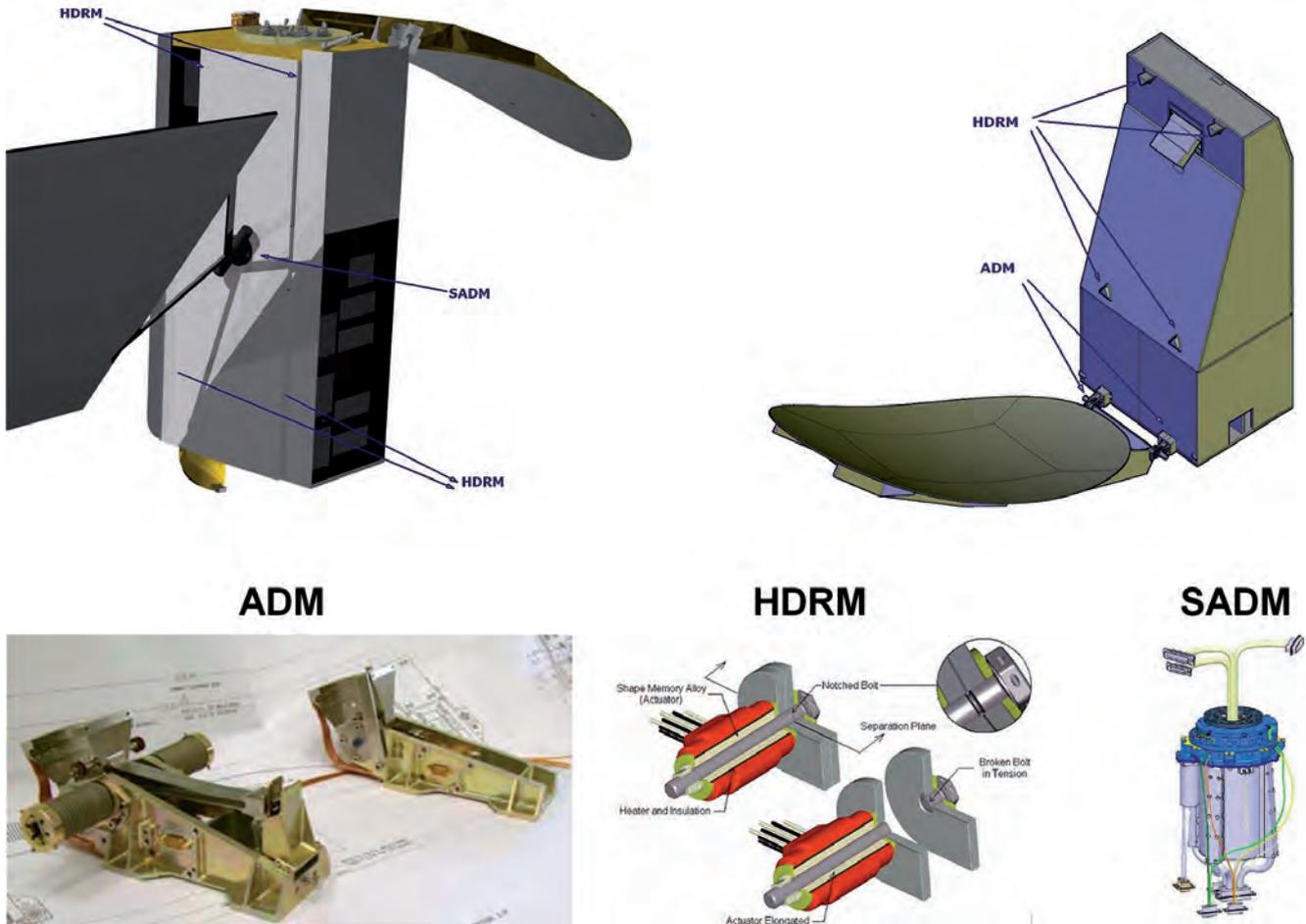


Figure 5.32. CoReH$_2$O mechanism locations (top) and implementation (spring for ADM bottom left, Frangibolt for HDRM bottom middle, and for rotary joint as a part of the SADM, bottom right). (Lower centre image: TINI Aerospace)

platform equipment interfaces not using the data bus. The command and data handling subsystem is developed to be compatible with ESA standards using packet-based communication, exploited with a series of customisable Packet Utilisation Services (PUS). The OBC, as the core part of this subsystem, provides the following functionality:

— Processing functions by means of the onboard software
— Data memory and safeguard memory management
— Onboard time generation, synchronisation, distribution and servicing
— Bus controllers for the MIL-1553B buses
— TT&C interface functions
— Reconfiguration functions

Realtime housekeeping telemetry is acquired by the OBC and transmitted to the ground using the S-band downlink. A dedicated interface between the OBC and the Solid State Mass Memory (SSMM) enables stored housekeeping telemetry to be downlinked by the Payload Data Handling and Transmission (PDHT) system. However, during emergency operations this function can also be carried out via the S-band TTC subsystem. The onboard time is maintained by the OBC and is synchronised to the UTC GPS time reference provided by the GNSS receiver.

For both concepts the payload interface is via an ICU (see also Fig. 5.11), which can transmit telemetry and execute low-level commands for payload
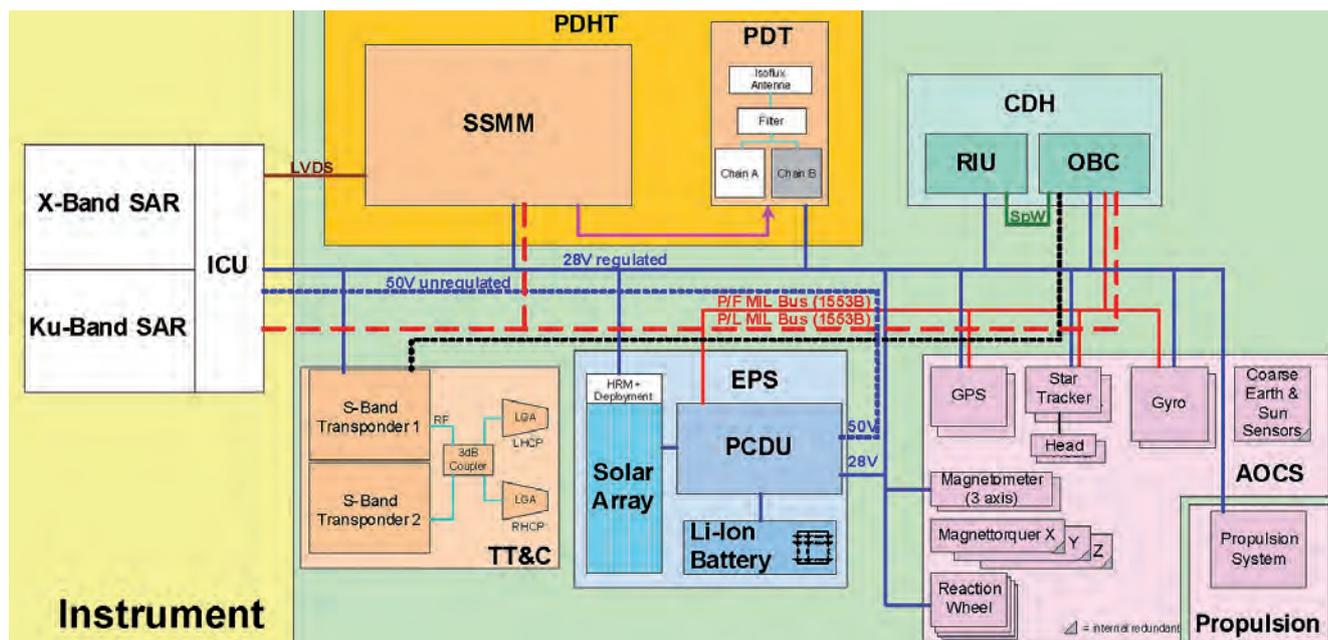
Figure 5.33. Electrical architecture (example for Concept A) showing the interfaces.

equipment. The data interface to the PDHT uses a high-speed data link, with a difference between the two concepts: Concept A is based on a serial configuration (LVDS lines), while Concept B is based on a multiplex configuration (Wizardlink bus).

The power is distributed on a 28 V DC bus to most equipment, with a dedicated 50 V DC bus for the payload and some specific units.

### 5.4.4.5 Payload data handling and transmission

The PDHT subsystem must transfer, format, store and downlink the payload data. The high volume of data of CoReH$_2$O is due to the combination of the dual-frequency, dual-polarisation SAR and of the long word length after analogue-to-digital conversion, which leads to an instrument data rate of ~170 Mbit/s. Combined with the high orbit duty-cycle (~15%), this implies that about 900 Gb of data are produced every orbit.

The PDHT needs can be satisfied by using state-of-the-art high-rate equipment. The selected solutions are based on recent GMES Sentinel developments with minor modifications. Concept B is based on the Sentinel-1 PDHT modified only to accommodate the different interface, whereas Concept A is an upgraded development from the Sentinel-2 solution.
An overview of the PDHT architecture for Concept B is shown in Fig. 5.34. This includes a modular mass memory unit using NAND flash technology (shown as DHSA), X-band RF transmitters (shown as TXA) and antennas (shown as XBAA). The transmitter for this concept consists of two parallel frequency-shifted channels to achieve the required downlink rate (520 Mbit/s). The other concept uses one channel only with a higher bandwidth, reaching a downlink rate of 460 Mbit/s. A 4D-TCM 8PSK modulation scheme has been selected for its high spectral efficiency (2–2.5 bit/s/Hz).

The required mass memory is about 900 Gb, which is driven by the second observation phase. The design of Concept A foresees the use of three memory modules based on NAND flash technology with a capacity of 2 Tb each at beginning of life. Concept B uses seven memory modules (six plus one in cold redundancy) of 192 Gbit. Concept A favours reusing an existing solution with
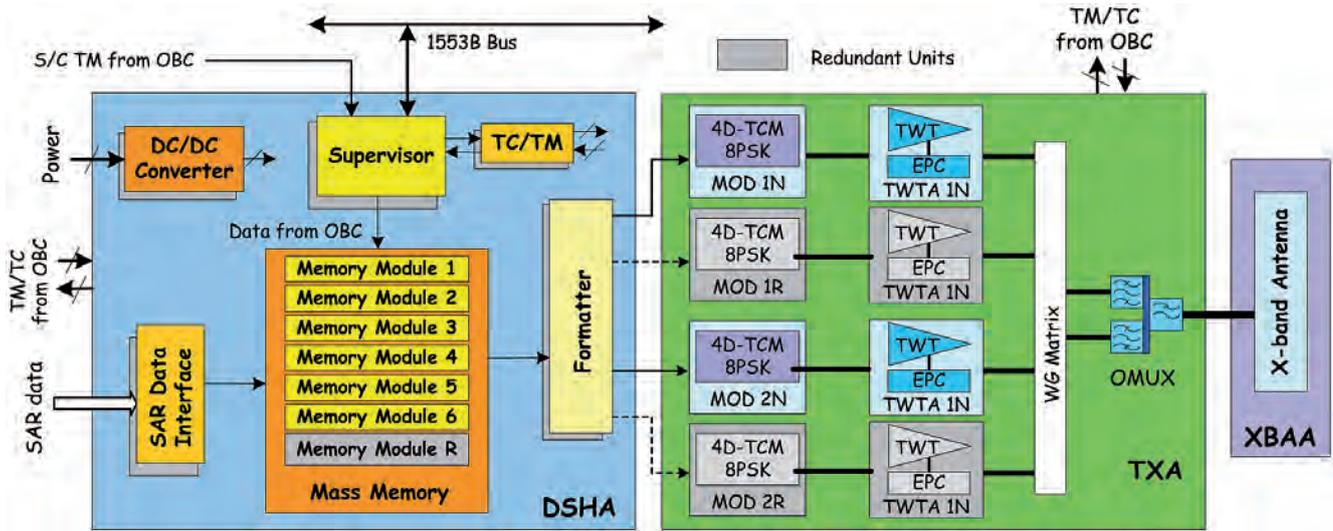
Figure 5.34. PDHT subsystem design (Concept B).

minor modifications, which is the reason for the oversized SSMM capacity with respect to the actual need of the mission.

### 5.4.4.6 Telemetry, tracking & command

This subsystem allows commanding and transmitting satellite telemetry in real time during communication passes with the TT&C ground station. A recurrent solution is proposed, using heritage design and equipment. Two antennas provide full coverage low-rate two-way communications (64 kbit/s uplink and 128 kbit/s downlink). These are used by the receive and transmit RF chains to downlink housekeeping telemetry (HKTM) and receive low-level or high-level commands which are then respectively executed directly in hardware or relayed to the onboard software. During nominal operations, the subsystem only transmits realtime HKTM, but in emergency operations it can also downlink playback (i.e. stored) data. Additionally, during emergency operations the TT&C hardware also allows the ground to perform ranging and Doppler tracking as a backup to onboard GNSS receiver.

For Concept B, the solution implies a change from traditional RF architecture due to configuration issues of S-band antenna placement (Subsection 5.4.2). The two antennas use two orthogonal polarisations since their fields of view overlap on the ground, which has to be taken into account in the operational planning.

### 5.4.4.7 Electrical power subsystem

The major driver for power generation, distribution and storage is clearly payload-related, considering the power needed with the selected observation technique and orbit duty-cycle: ~2.5 kW for around 15% of the orbit considering the worst case of parallel SAR and PDHT operations. The power generation benefits from a benign environment (constant solar angle) and the power distribution and storage can be based on heritage equipment, with only minor modifications. An example of functional block diagram for the Electrical Power Subsystem (EPS) is shown in Fig. 5.35.

The solar-array generator uses triple-junction GaAs solar cells covering 13–14 m$^2$ on a single wing with four deployed panels in a fixed Sun-facing attitude. The PCDU includes one or more units, depending on the implementation based on recurring equipment. This equipment provides the
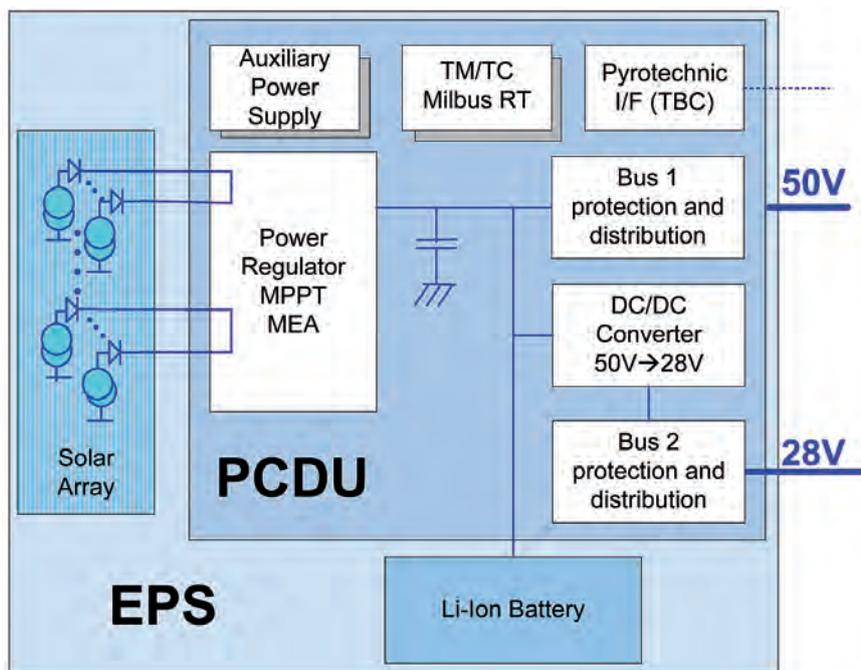
Figure 5.35. EPS block diagram (Concept A).

28 V and 50 V bus distribution as well as switching and current protection where appropriate. It also regulates the power from the array according to the Maximum Power Point Tracking (MPPT) method and the charging of the battery according to a Constant Current /Constant Voltage method.

The battery will be used in eclipse, for emergency operations and in nominal operations when the power demand of the SAR and PDHT exceeds the power generation capability of the solar array. For CoReH$_2$O the combination of high SAR power and long duty-cycle impacts the battery sizing. The power subsystem must be sized such that the array, battery and power demand are balanced at all times without oversizing. This is shown in Fig. 5.36 which illustrates the power demand and supply profile from the satellite, array, and battery. The battery is a specific implementation of off-the-shelf Li-ion space batteries with about 300 Ah capacity at most, with significant design margins. Overall, the EPS subsystem is based on mature solutions.

### 5.4.4.8 Attitude and orbit control subsystem

The AOCS subsystem is responsible for controlling the attitude of the satellite, from launcher separation to end-of-life disposal, and – supported by the propulsion subsystem – to execute the manoeuvres required to control the orbit. Both satellite concepts are based on an Earth-pointing, three-axis attitude control system. Figure 5.37 provides an overview of the different AOCS operation modes and the relevant state transition, identifying also those that can only be authorised via ground command. Beside the test and initialisation modes of the AOCS subsystem, the operational modes are:

— Acquisition mode: this is active after the separation from the launcher. It stabilises the satellite attitude by dumping its angular momentum, controlling the attitude after the solar-array deployment and acquiring the target attitude before transition to normal mode.

— Nominal mode: this includes attitude acquisition after mode transition and fine pointing mode to support nominal payload operation. A sub-mode to support reflector deployment is also included.

— Orbit control mode: this executes the slew manoeuvres required before and after in-plane and out-of-plane orbit correction manoeuvres and controls the attitude of the satellite during operation of the propulsion system.

— Safe mode: this can also be combined with the acquisition mode, it controls the satellite such that it is placed in a stable and thermally safe attitude with sufficient power generation capabilities to support the minimum loads required to maintain the satellite in a safe condition (payload is switched off).

For the different modes the AOCS makes use of different sensors and actuators as required by the specific performance needs, shown in Table 5.5. The designs evolved for the two concepts are quite similar and differ mainly for the specific control approach used in safe and orbit control modes.

For nominal operations, a startracker is used to provide accurate inertial attitude reference, whereas for other modes coarse sensors are used to provide a reference to the Sun or Earth. The proposed concepts for the actuators include a set of magnetic torquers for control and momentum dumping, and reaction wheels for nominal control. The actuators are sized for compensating all in-orbit disturbances, with the key disturbance being the gravity gradient caused by the elongated shape of the satellite. The application to implement the control laws and modes runs within the software on the OBC. As seen in Subsection 5.4.3, the nominal attitude is an off-nadir pointing (about 37°). The attitude guidance includes a small amplitude yaw steering to compensate for the rotation of Earth and, for Concept A, an additional roll steering as required by the error budget associated to the observation geometry.
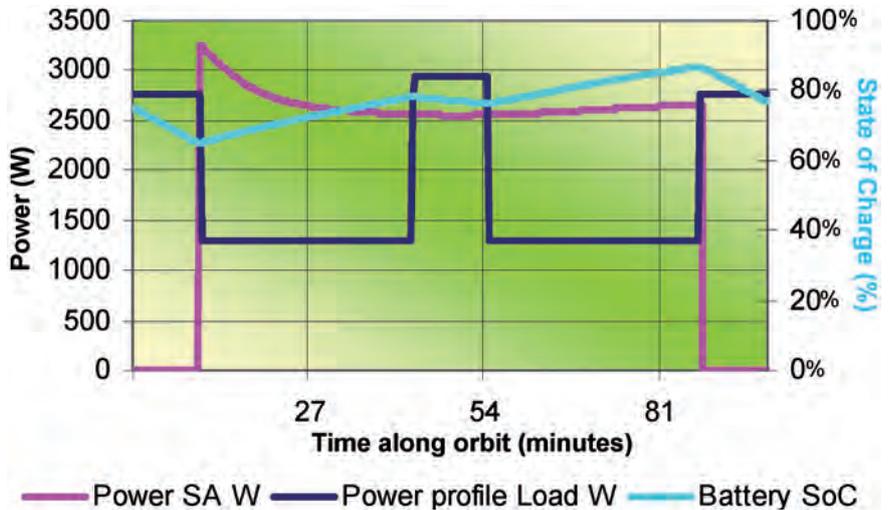


Figure 5.36. Typical power supply & demand profile for one orbit (Concept A).

Table 5.5. AOCS sensors and actuators used in the various modes. Usage of the propulsion subsystem in safe and acquisition modes applies to one concept only (indicated in brackets). The rate sensor is not used as a primary attitude sensor in nominal mode (indicated by asterisk).

| Mode | Actuators | | | Sensors | | | |
|------|-----------------|-------------------|-----------------------|-------------|---------------|-------------|-------------|
|      | Reaction wheels | Magnetic Torquers | Propulsion subsystem | Rate Sensor | Magnetometers | Sun sensors | Startracker |
| Acquisition mode | X | X | (X) | X | X | X | X |
| Orbit control | X | | X | X | | | X |
| Nominal pointing | X | X | | X* | X | | X |
| Safe mode | | X | (X) | X | X | X | |
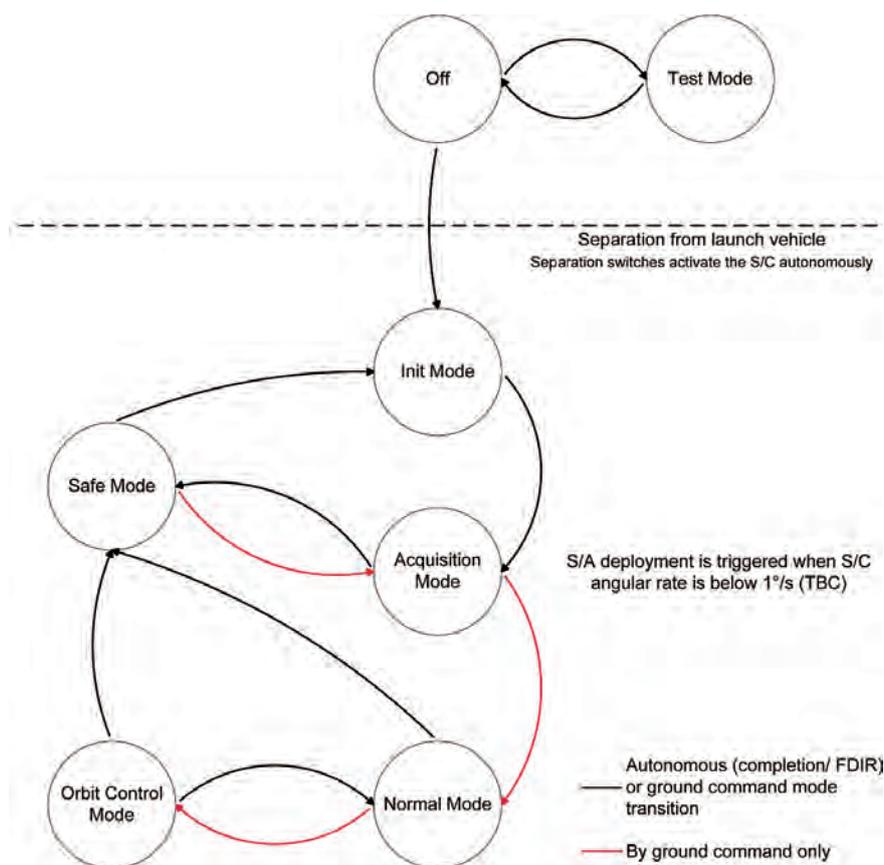
The AOCS also includes the sensors and actuators used for orbit control, although this function is controlled from the ground (Subsection 5.6.2 and 5.7.4). The main sensor used for orbit determination in nominal mode is the onboard GNSS receiver, which also provides Position-Velocity-Time (PVT) vectors that are downlinked to the ground within the HKTM data stream.

The key performance requirements for AOCS are related to the antenna Line-Of-Sight (LOS) pointing in nominal mode and derived from the SAR radiometric performance. They are listed in Table 5.6, with a more complete derivation addressed in Subsection 5.4.5 and Chapter 7. The requirements presented correspond to a preliminary error allocation to the relevant contributors (see Table 5.10 in Subsection 5.4.5). In fact, the predicted AOCS performance, being much better than the requirement, would allow a relaxed allocation to other contributors, if needed.

The results of pointing simulations and analysis confirming the proposed design are presented in the Chapter 7 (Performance). In summary, the proposed AOCS concepts make use of flight-proven, medium performance sensors and actuators and are based on flight-proven controller designs.

| AOCS Parameter | Performance | Requirement |
|---|---|---|
| Absolute Knowledge Error (mdeg) | 0.5 (Concept A) 0.7 (Concept B) | 3 (Concept A) 2 (Concept B) |
| Absolute Pointing Error (mdeg) | 1 (Concept A) 4.3 (Concept B) | 6 (Concept A) 6.5 (Concept B) |
| Relative Pointing Error (mdeg/s) | 0.12 (Concept B) | <0.7 |

Table 5.6. Summary of pointing requirements and performance, worst-case angle (roll).

Figure 5.38. CoReH$_2$O Concept A propulsion subsystem showing Sentinel-2 modular design.
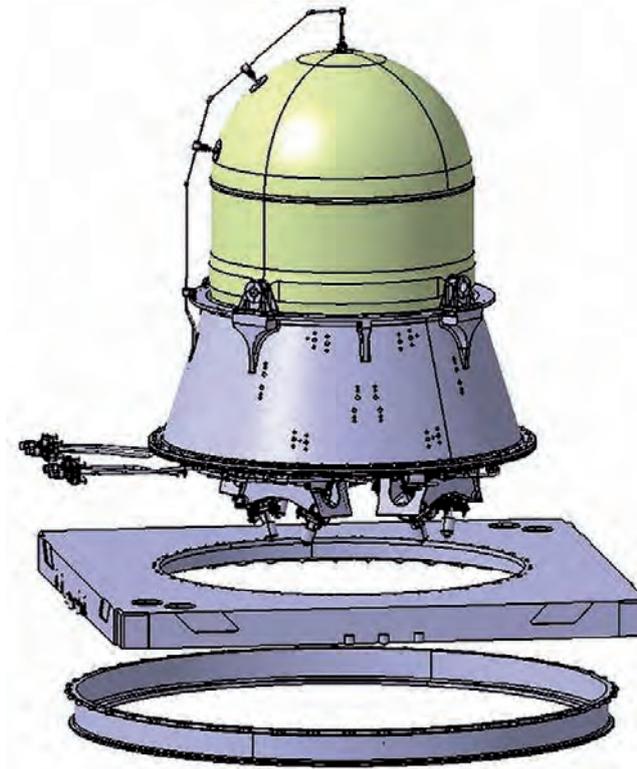


Figure 5.39. CoReH$_2$O Concept B thruster assembly.
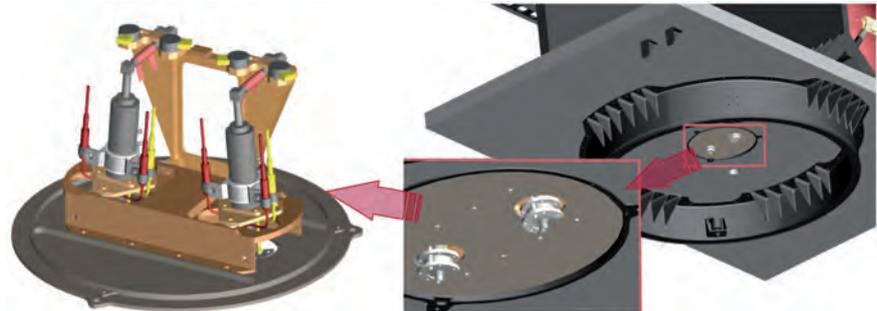


### 5.4.4.8.1 Propulsion Subsystem

The propulsion subsystem responds to the requirement of providing the necessary thrust for the correction of launcher injection errors, for orbit control manoeuvres and for the EOL deorbiting manoeuvre. Heritage equipment and standard solutions are used. The subsystem is based on a mono-propellant hydrazine system, pressurised with helium and operated in blow-down mode. The propellant tank is mounted inside the structural central cone of the platform and the thrusters assembly is located on the base-plate interface with the launcher. This is illustrated in Fig. 5.38.

The two concepts differ in the fact that Concept A, in addition to the orbit control requirements, is also designed to provide torques for initial rate damping and safe mode. This brings significant differences in the number of thrusters needed, propellant budget and tank capacity.

The design of Concept A foresees the use of two branches of four 1-N thrusters operated in cold redundancy. The propellant tank has a loading capacity of 130 kg and offers considerable growth capability with respect to the 92 kg allocated in the propellant budget.

Concept B, uses two redundant 1-N thrusters mounted on the SVM base plate as illustrated in Fig. 5.39. The propellant tank has a maximum loading

capacity of 68 kg, which is sufficient for the 45 kg of fuel allocated in the Concept B propellant budget.

## 5.4.5 Budgets

The main satellite budgets for the two concepts are shown in Tables 5.7–5.13. The overall mass for the two concepts is very similar (Table 5.7), but includes some significant differences at subsystem-level for the SAR central electronics, the satellite structure and the quantity of propellant. The difference in the central electronics comes from different assumptions on the maturity and the level of integration considered for each concept. The different structural mass is related to the specific concepts, i.e. integrated vs. modular. The propellant mass difference comes from the fact that only Concept A uses the propulsion for attitude control in safe mode and also from additional propellant margins. Mass margins with respect to the performance of the selected launchers are described in Section 5.5.

The power budgets are slightly different for the two concepts (Table 5.8). The main difference arises in the payload power, specifically in the transmit power needed by the HPA to provide a receive signal compatible with the sensitivity requirement. This stems from the use of different technologies in the payload (for the HPA, distribution network and multibeam feed) and from different assumptions about the losses and performance budget in the payload.

The data-flow budgets are fairly similar for both concepts (Table 5.9). The small differences in instrument rate come from different digitisation and multi-looking approaches. The differences in observation duty-cycles come from different optimisation techniques for the observation profile.

The pointing budgets presented in the following tables refer to the LOS of the SAR antenna in an inertial frame and address the main pointing parameters, i.e. pointing knowledge, pointing accuracy and pointing stability. The LOS pointing requirements are derived from the SAR radiometric requirements and based on the concept-specific allocations of the pointing error contribution to the overall SAR performance budgets (Chapter 7). The detailed derivation of the LOS pointing requirements is addressed in Chapter 7 and is based on the following key considerations:

— The LOS Absolute Knowledge Error (AKE) requirements impact the radiometric stability and bias performance.

— The LOS Absolute Pointing Error (APE) requirements are due to the need to limit the swath location errors and the consequent impact on radiometric sensitivity.

— The LOS Relative Pointing Error (RPE) requirements have been considered only in Concept B and are due to the need to limit the errors on the instrument Impulse Response Function and ultimately on the radiometric sensitivity.

The main contributors to the LOS pointing errors are: the platform pointing errors, indicated as AOCS contribution; the in-orbit thermo-mechanical distortion between the attitude reference and the relevant elements accommodated on the platform (MFA, antenna hinges), indicated as platform distortion; and finally the thermo-mechanical deformation of the reflector antenna, indicated as antenna distortion.

Given the use of external calibration to address slow-varying and permanent errors, it is assumed that all the bias contributors can be compensated. Therefore, only the random error contributions have been considered in the budget and added together as Root Sum Square (RSS).

The LOS pointing knowledge, accuracy, and stability budgets are presented in Tables 5.10–5.12. The different LOS pointing requirements between the

Table 5.7. Mass budgets, including maturity and system margins as per ESA requirements.

| Subsystem | Concept A (kg) | Concept B (kg) |
|---|---|---|
| Antenna | 74 | 62 |
| Distribution network | 17 | 14 |
| Active front-end and instrument harness | 128 | 132 |
| Central electronics | 72 | 25 |
| Payload | 291 | 233 |
| PDHT and TTC | 39 | 67 |
| EPS, avionics and harness | 294 | 268 |
| AOCS and propulsion | 84 | 85 |
| Structure and thermal | 252 | 371 |
| Platform | 669 | 791 |
| System margin | 143 | 153 |
| Propellant | 93 | 45 |
| Total at launch | 1196 | 1222 |

Table 5.8. Worst-case power budget (simultaneous observing and down-linking) including system and maturity margins.

| Subsystem | Concept A (W) | Concept B (W) |
|---|---|---|
| Active front-end | 1775 | 2415 |
| Central electronics and distribution network | 310 | 130 |
| Payload | 2085 | 2545 |
| PDHT and TTC | 265 | 315 |
| EPS, avionics and thermal | 300 | 275 |
| AOCS and propulsion | 95 | 85 |
| Platform | 660 | 675 |
| System margin | 410 | 480 |
| Total | 3155 | 3700 |

Table 5.9. Data flow budget.

| Contributor | Concept A | Concept B |
|---|---|---|
| X-Band VV (Mbit/s) | 37 | 45 |
| X-Band VH (Mbit/s) | 47 | 45 |
| Ku-Band VV (Mbit/s) | 37 | 45 |
| Ku-Band VH (Mbit/s) | 47 | 45 |
| Housekeeping and ancillary data (Mbit/s) | 0.4 | 0.4 |
| Total SAR data rate (Mbit/s) | 168 | 180 |
| Observation duty- cycle mins/orbit | 15 average 20 max | 18 average 26 max |
| Max data storage required (Gb) | 820 | 900 |
| Capacity (Gb) | >6000 | 1200 |
| Data storage margin | >>25% | 25% |
| PDHT downlink speed (Mbit/s) | 468 | 520 |
| Downlink capacity margin | 13% | 25% |

| Contributor | Concept A (mdeg) | Concept B (mdeg) |
|---|---|---|
| AOCS AKE | 0.5 | 0.7 |
| Platform distortion | 1 max | 4 |
| Antenna distortion | 4 max | 3 |
| Total (RSS) | 4.1 | 5.0 |
| Requirement | 18 | 6.5 |
| Margin | >100% | >30% |

Table 5.10. LOS pointing knowledge error budget – worst-case angle (roll).

| Contributor | Concept A (mdeg) | Concept B (mdeg) |
|---|---|---|
| AOCS APE | 1 | 4.3 |
| Platform distortion | 1 max | 5.5 |
| Antenna distortion | 4 max | 4 |
| Total (RSS) | 4.2 | 8.0 |
| Requirement | 18.2 | 9.5 |
| Margin | 100% | 19% |

Table 5.11. LOS pointing accuracy error budget – worst-case angles (roll).

| Contributor | Concept B (mdeg/s) |
|---|---|
| AOCS RPE | 0.12 |
| Platform distortion | 0 |
| Antenna distortion | 0 |
| Total (RSS) | 0.12 |
| Requirement | 0.7 |
| Margin | >100% |

Table 5.12. LOS pointing stability error budget – worst-case (overall magnitude).

| Contributor | Concept A (m/s) | Concept B (m/s) |
|---|---|---|
| Launch corrections | 18 | 28 |
| Phase-1 control | 2 | 1 |
| Phase-1–Phase-2 Transfer | 22 | 22 |
| Phase-2 control | 11 | 9 |
| EOL Disposal | 19 | 22 |
| Total | 72 | 82 |

Table 5.13. Delta-V budget.

two concepts are a consequence of the allocation given to the LOS pointing errors within the radiometric budgets. Similarly, the different weights of the contributors within the LOS pointing budgets are related to the specific error allocation strategies and to the actual estimated performance, which are concept-dependent. However, it is clear that for both concepts the required LOS pointing performance can be met with comfortable margins.

The delta-V budgets are very similar for both concepts (Table 5.13), as expected given that they use the same mission profile. Marginal differences come from assumptions about the space environment and the satellite drag area.

Figure 5.40. Vega launch configuration, Concepts A (left) and B (right) showing launch compatibility.
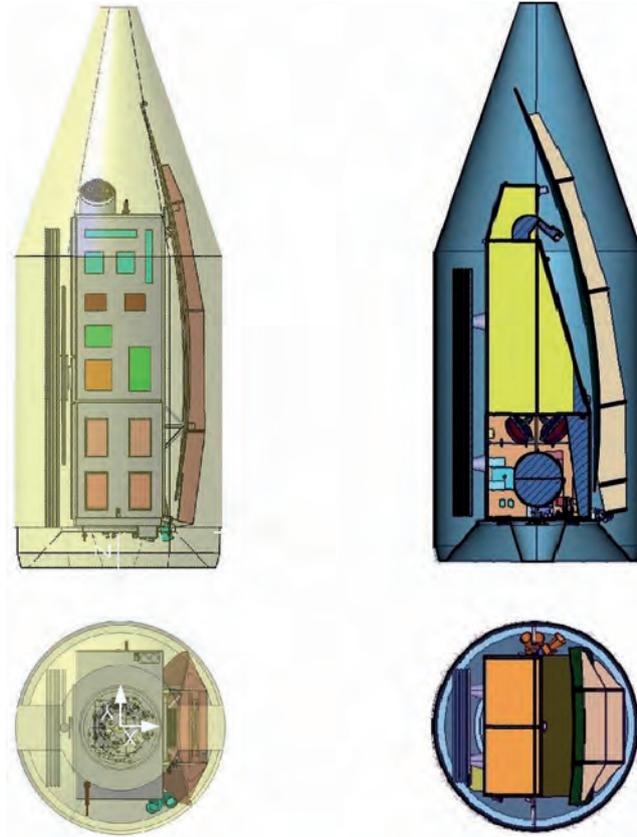
Table 5.14. Launch mass budget for Vega.

| | Concept A (kg) | Concept B (kg) |
|---|---|---|
| Satellite launch mass | 1196 | 1222 |
| Launch adapter | 60 | 60 |
| Total launch mass | ~1260 | ~1285 |
| Vega capacity at 666 km Sun-synchronous orbit | 1350 | 1350 |
| Growth capacity (i.e. launch margin) | 70 (6%) | 65 (5%) |

## 5.5  Launcher

Vega is the baseline launcher for CoReH$_2$O. A backup launcher was also selected, with PSLV from the Indian Space Research Organisation (ISRO) being the most suitable choice.

The compatibility of the space segment concepts with both main and backup launchers has been demonstrated. As shown in Fig. 5.40 and Table 5.14, the satellite fits in Vega with limited margins in terms of volume and mass. However, the Vega performance has been reduced by 100 kg from the figure quoted in the Vega User Manual (Arianespace, 2006) as an additional margin to take into account the current uncertainty in the injection performance. PSLV has equivalent or better mass and volume specifications than Vega, so compatibility is not an issue.
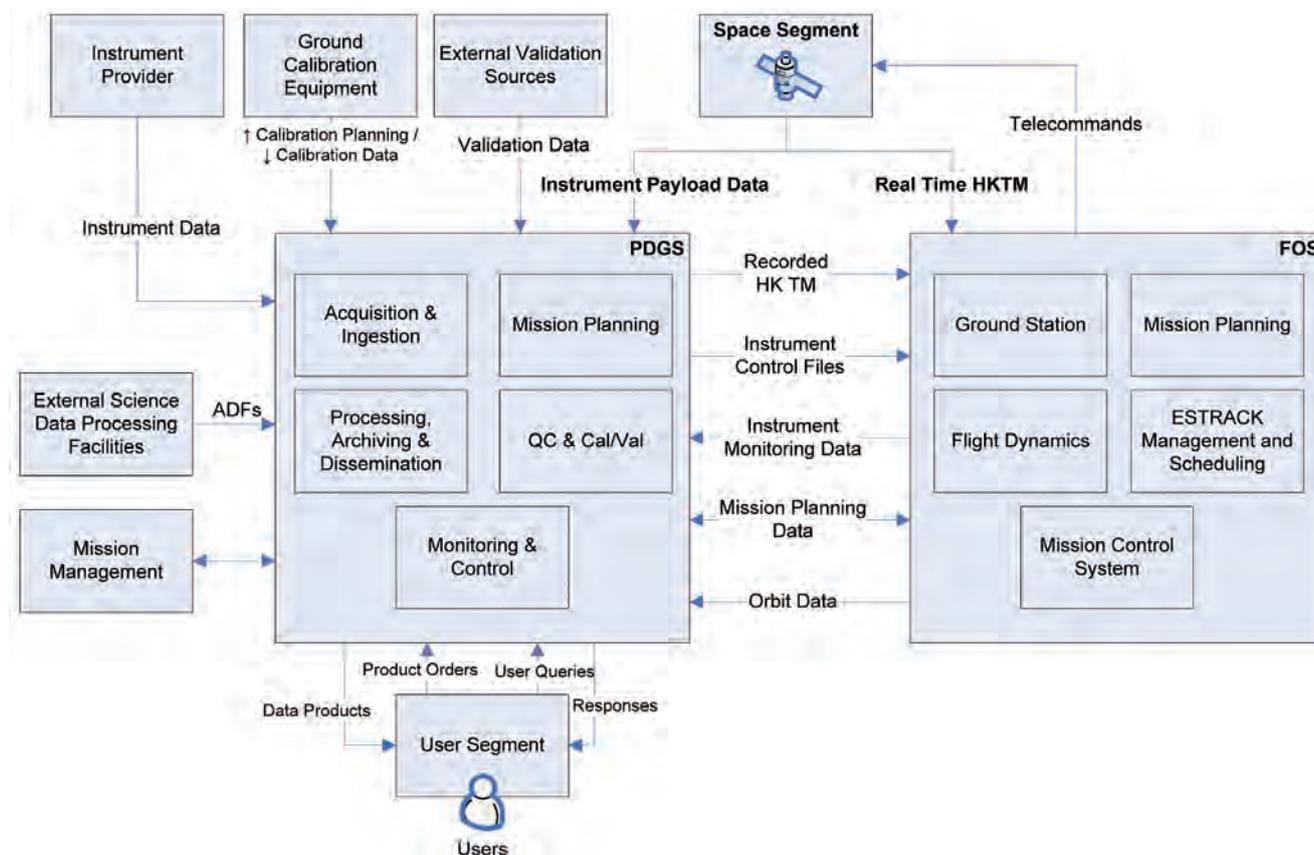
Figure 5.41. Ground segment architecture.

## 5.6 Ground Segment and Data Processing

### 5.6.1 Overview and External Interfaces

Following the approach of developing a multimission ground segment, the current generation of Earth Explorer ground segments has been designed, built and integrated using generic components configured or adapted to each satellite. This approach has been used for the six current Earth Explorers and will apply also for Earth Explorer 7. In line with this, the CoReH$_2$O ground segment consists of two main components, the FOS and the PDGS, as presented in Fig. 5.41.

The FOS includes the TT&C ground station and the FOCC. The TT&C ground station is used for up-linking telecommands from the FOCC, for acquiring the realtime HKTM and for tracking the satellite. During Launch and Early Orbit Phase (LEOP), this ground station is complemented by a dedicated LEOP ground station network. The LEOP network uses Estrack core and enhanced stations where possible. The FOCC will be based at ESA-ESOC and is primarily responsible for satellite monitoring and control, flight dynamics and manoeuvre planning, maintenance of onboard software and equipment, and generally all operations related to spacecraft command and control, including the management of all related facilities (ground station control, ground simulators etc.).

The PDGS is primarily responsible for receiving the science data from the satellite, applying the appropriate processing algorithms and delivering the data products to the users. It includes the PDAS ground station and a number of elements usually located in a single mission data centre.

The FOS and PDGS are kept as independent as possible. In particular, no payload data is processed by or transmitted through the FOS. Data exchanged between FOS and PDGS includes mission planning requests and results, orbit data, recorded HKTM from PDGS to FOS, and processed HKTM from FOS to PDGS. Existing interface formats and specifications supported by the ESA infrastructure software are used wherever applicable. The two elements are described in more detail in the next subsections.

## 5.6.2 Flight Operation Segment

The FOS is strongly based on existing ESA hardware and software infrastructure, adapted where necessary for CoReH$_2$O. The actual FOS elements include the TT&C ground station and, within the FOCC, the facilities for mission control system, flight dynamics, mission planning, and satellite ground simulator.

### 5.6.2.1 Telemetry tracking & command ground station

The baseline TT&C ground station is in Kiruna (SE). Both telemetry and telecommand functions are transmitted in S-band. No modification to the Kiruna ground station equipment is required. The primary data source for orbit determination is the onboard GNSS receiver. There is therefore no need for frequent ground station tracking data. The principal task for TT&C passes in routine operations is telecommand uplink. Realtime HKTM will be acquired during these passes but is not driving the required number of passes. The TT&C ground station is not dedicated to CoReH$_2$O alone, but shared between missions. Station allocation planning is performed by the Estrack Management and Scheduling system (EMS) in cooperation with the Mission Planning System (MPS). The EMS also generates the detailed operation schedules executed by the Estrack ground station monitoring and control systems.

### 5.6.2.2 Mission control system

The Mission Control System (MCS) is based on the Earth Explorer MCS (EEMCS), which is an extension of SCOS-2000. The EEMCS is continually upgraded to meet the needs of specific missions and is expected to be more widely useful. A certain degree of customisation of the system (including some functional modifications) is still likely to be necessary for CoReH$_2$O, according to satellite design, ground interface specifications, the final operations concept, and the existing capabilities of the EEMCS at the start of the implementation phase. No specific functional adaptation has been identified as necessary.

### 5.6.2.3 Flight dynamics

No mission-specific modifications to ESA flight dynamics infrastructure will be needed. Flight dynamics is a service provided to missions that delivers orbit information and event files to the various planning entities, as well as the orbital predictions used by the Estrack ground stations. It also generates command sequences that are transferred to the MCS directly or via the MPS. Flight dynamics receives radiometric measurements from ground stations as well as spacecraft monitoring data, including GNSS tracking data, from the MCS.

### 5.6.2.4 Mission planning system

The FOS MPS is based on the Earth Explorer MCS mission planning kernel. It generates schedules for execution by the MAS as well as command sequences for uplink to the satellite. The MPS will require configuration of mission-

specific rules and constraints. As for the MCS, some functional modification is likely to be needed, but specific modifications need not be identified at this stage. Estrack Management and Scheduling is responsible for planning ground station allocation to missions supported by Estrack, and generation of detailed ground station schedules.

### 5.6.2.5 Simulator

The satellite simulator is built using the SIMSAT infrastructure and the existing ground models and the generic dynamics and space environment models. Spacecraft subsystem models will, in general, need to be developed specifically, though reuse will be possible for heritage subsystems already modelled in predecessor simulators. The onboard flight software is executed on an emulator.

### 5.6.2.6 Flight operations segment: operations and implementation

The mission operations will be automated, as far as is reasonable, to minimise risk and to contain the size of the operations team. Operations support is restricted to normal working hours, i.e. five days per week. Should a serious anomaly occur out of hours, on-call engineers can be alerted automatically. A serious anomaly is one that threatens system availability, such as significant data loss or a danger to spacecraft health. The latter should, in principle, be excluded thanks to the spacecraft autonomy. Other anomalies will be investigated only during working hours. Contacts with the FOS ground station via the TT&C will be limited to those necessary for mission plan uplink. In nominal operations, this is foreseen twice per week (Monday and Friday), taking full advantage of the spacecraft autonomy. During commissioning, one pass per day is expected. In view of the low frequency of TT&C passes, regular spacecraft health monitoring is assured via recorded HKTM, downlinked in X-band and forwarded to the FOS from the PDGS. Frequency and latency are not critical, but nominally the TM would be acquired at each pass and forwarded as a single file after reception. No near-realtime planning is required. Regardless of the operations model selected for the nominal phase, the FOS development will still have to prepare for all reasonable eventualities. However, moving towards office-hours-only support and automated monitoring and alarms out of office hours is a natural evolution of the operations concept. Other than this, the design of the FOS is familiar in terms of the functional blocks to be used: the MCS will be based on the MCS Earth Explorer Kernel, the Mission Automation System will execute control procedures and schedules, the NAPEOS extension to the ORATOS platform will be used, a simple MPS will be developed from infrastructure elements or an existing Earth observation mission and, in general, the ESA Ground Operations System (EGOS) infrastructure will be employed.

### 5.6.3 Payload Data Ground Segment

Over the last decade, ESA's Earth observation missions have increasingly moved towards standardised, multimission payload data ground segments. The current generation of Earth Explorer ground segments have been designed using generic components that are configured or adapted to each satellite. This approach has been used for the six current Earth Explorers. Thus, for all Earth Explorer 7 candidates a standardised PDGS concept is planned, providing the following major functions:

— Payload data acquisition and ingestion for downlink of science data telemetry
— Processing
— Archiving

— Dissemination
— Mission planning
— User services

Other infrastructure is also needed at the interfaces, such as computers and communications infrastructure, external calibration and validation services, and auxiliary data providers, in this case only for the Digital Elevation Model (DEM).

The CoReH₂O recorded HKTM and science data will be downlinked via X-band at a high rate. The mission has a 24-hour delivery requirement to the end users from the time of sensing. Although this data latency requirement has an impact on the maximum processing times of each Level-1b product, it can be fulfilled with no special provisions. The resulting concepts for each element are described below.

### 5.6.3.1 Payload data acquisition station

The downlink of the science data and the recorded satellite telemetry will be performed via a radio link in the X-band. The choice of the acquisition stations is triggered mainly by the overall contact time of downlink passes and the maximum delay between them. As described in Subsection 5.7.3, a single station is able to fulfil the mission requirements. Several options exist, including the Kiruna and the Svalbard stations. A special PDAS option under consideration is the ground station being developed by the Finnish Meteorological Institute at the Sodankylä research centre (Chapter 9). The detailed compatibility of this new station with the CoReH₂O satellite needs to be consolidated, but there is, in principle, no critical point and, given the similar latitude of both stations (Fig. 5.42), schedule and duration of contact passes are also similar.
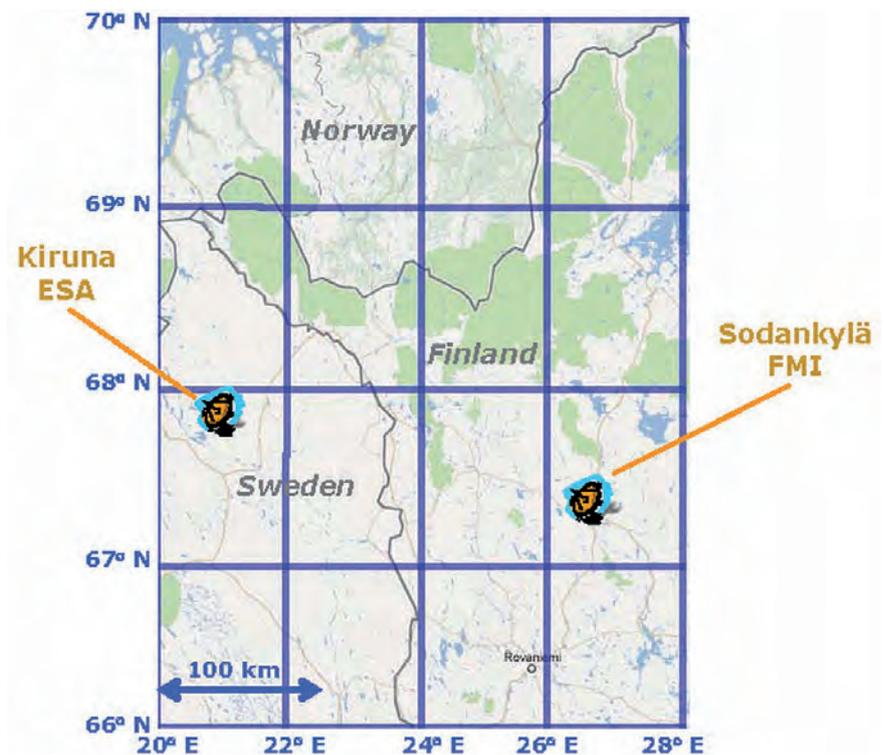


Figure 5.42. Close locations of Kiruna and Sodankylä potential PDAS for CoReH₂O.

### 5.6.3.2 Data processing and product generator

The PDGS will process the raw science data up to Level-1b and distribute them to the user segment using a data-driven architecture: processing starts as soon as the science data is available and generates data products to be archived and distributed simultaneously to the CoReH$_2$O users. Timeliness requirements are not stringent, Level-1 auxiliary data (i.e. DEM) is static, and the requirements on processing algorithms are not very demanding. This means that no complex, computationally-demanding algorithms are needed to meet the CoReH$_2$O requirements. It is even possible that some elements of previous SAR processors may be reusable, similarly to what was done, for instance, between Envisat ASAR and GMES Sentinel-1 (see Subsection 5.6.4 for more details). In any case, no criticality is expected here.

Note that for Concept A, after a trade-off between possible processing approaches, it was proposed to implement pipeline processing in the data processing chain (i.e. chopping the data stream into data granules). This implies parallelising data transfer, processing, and archival. Whilst this approach is not necessary, it could further increase performance margins.

### 5.6.3.3 Data quality control

Data Processing will encompass online data quality control. For Level-0, this is basically limited to checking format compliance and product confidence data in the instrument source packets, whereas Level-1 processing will involve more complex checks on internal calibration parameters. Only data products that meet minimum quality criteria will be distributed to the users.

### 5.6.3.4 Archiving and reprocessing

Raw data and Level-1a data will not be permanently archived. Consequently, the estimated data volumes are 150 GB per day, for a total of 1287 TB storage volume over the mission lifetime. A long-term archive will implement backup policies to ensure that no Level-0 or Level-1b data are lost. Advances in storage technology mean that this requirement is not critical. The current baseline is designed with the capability to perform reprocessing, but the frequency of reprocessing will be defined in later phases and is expected to be low.

### 5.6.3.5 Dissemination

The PDGS will routinely deliver the Level-1b data products to the CoReH$_2$O registered users. Systematic Level-0, Level-1a and calibration products will also be available for special users (e.g. calibration and validation teams, instrument specialists etc.). All the data will be made available on an FTP server to be accessible directly by the final users.

### 5.6.3.6 Instrument performance and monitoring

The PDGS directly checks the science data received from the satellite for corrupted, missing or otherwise non-nominal instrument source packets. System-level instrument performance is monitored using measurements obtained from the nominal data acquisition mode of the instrument over specific regions. For example, data on rainforest areas will be used to calibrate the antenna elevation patterns in flight and point target test fields for calibration of azimuth patterns and pointing. Instrument performance will be monitored. The calibration results may be used to update the satellite databases.

### 5.6.3.7 Mission planning

A key function of the PDGS is to define the plan of payload and PDHT activities for the observations and the downlink activities over the PDAS. Given that the mission normally performs systematic data acquisitions on predefined regions of interest (e.g. polar regions, Alps, etc.), the PDGS will be able to provide this function in a simplified and optimised manner. It is proposed to implement an operational concept based on a static approach, where the overall acquisition activities are planned on a seasonal or monthly basis, leaving to the satellite the task to perform the corresponding operations every repeat cycle according to the multirepeat-cycle strategy.

### 5.6.3.8 User services

The existing multimission user services will be adapted to handle CoReH₂O data products and end user needs. The services will have a web-based user interface that will support data product access (including subsets of the data product) and visualisation as well as provide general information on the mission status and helpdesk services.

### 5.6.4 Level-1 Mission Data Processing

A mission-specific SAR ground processor is required to provide the end users with Level-1b data for higher level processing up to Level-2 and above. Since all mission data are acquired in ScanSAR, only a single processor tailored to this mode is required. The classical data acquisition geometry and requested image accuracies allow for using well-established ScanSAR algorithms, which were already used for instruments such as ASAR. The main processing steps, which are applied systematically to each of the four Level-0 products, are summarised in Fig. 5.43.
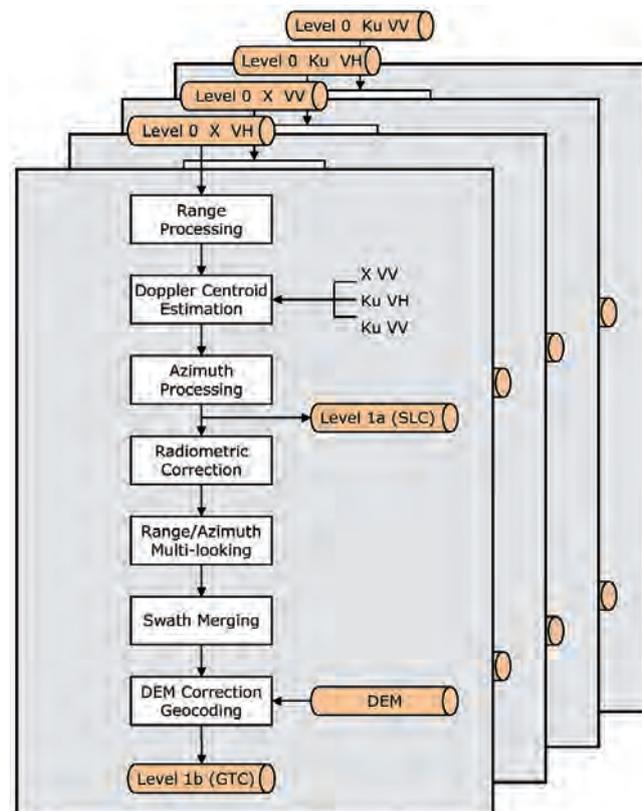


Figure 5.43. Processing chain for CoReH₂O Level-1b products.

The raw payload data together with related ancillary data (e.g. attitude and orbit data) are collated into four Level-0 products (time-ordered series for both polarisations of each of the two frequencies).

### 5.6.4.1 Range processing and Doppler centroid estimation

This step includes processing of the pulse replica, radiometric correction steps, and focusing of the data by matched filtering. Then inputs from all four channels are used to estimate the Doppler centroid. Depending on the approach, this step could also be performed before matched filtering in range.

### 5.6.4.2 Azimuth processing

This block includes further correction steps (e.g. range cell migration correction, de-ramping operations, etc.) and performs the focusing of the data in azimuth, which is based on the following possible algorithms:

— Conventional or modified SPECAN (SPECtral ANalysis), which is considered as a fast and robust solution that provides the required processing accuracy (Lanari et al., 1998; Cumming & Wong, 2005).

— ScanSAR Chirp Z-Transform (CZT) (Lanari, 1994), which achieves a higher accuracy at the cost of an increased number of processing steps compared to the conventional SPECAN.

After this, the Single Look Complex (SLC) image (Level-1a) is available. A separate SLC is obtained for each burst and each channel. The SLC will not be archived, but the Level-1a data can be made available to the scientific community upon request.

### 5.6.4.3 Radiometric correction and multi-looking

The radiometric correction aims at removing all effects that have affected the amplitude of the focused data, as e.g. antenna patterns, etc. This includes operations for descalloping the ScanSAR data. The pictures are only then multi-looked. The multi-looking is performed by forming a weighted sum of multiple detected SLC images. For azimuth, this means that each of the single bursts is processed separately, amplitude detected, and then buffered. The same burst can be processed more than once with different weighting functions, thereby leading to multiple detected images or 'looks'. Combination of these looks then leads to the multi-looked image, where the number of combined looks and the respective weighting of each look can vary depending on the frequency band. Multiple azimuth looks can be complemented by multiple looks in range. Regarding the order of processing steps, it is possible to perform the multi-look weighting included in the focusing or separately after the data are focused.

### 5.6.4.4 Geocoding and DEM correction

This represents the final step, leading to the Geocoded Terrain Corrected (GTC) image product (Level-1b). Regarding the DEM, ASTER GDEM (Land Processes Daac, 2012) meets the requirements and provides nearly global coverage (83°N–83°S) and an even more refined DEM is expected from the Tandem-X mission (Moreira et al., 2008). Level-1b products are systematically archived and made available to higher level processing.
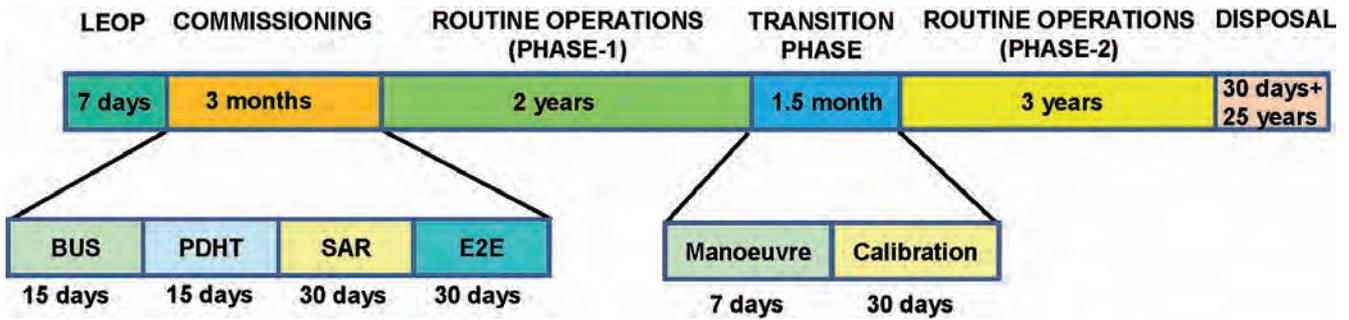
Figure 5.44. Operations phases.

### 5.6.4.5 Summary

In summary, no significant challenges are identified for the Level-1b SAR ground processor, which is based on conventional infrastructure and well-established algorithms, fully providing the requested accuracy. Assuming parallel processing of scenes, each of 100 km long, the time to generate Level-1b products is less than 10 minutes and thus has a minor impact on data latency.

## 5.7 Operations and Utilisation Concept

### 5.7.1 Overview

The mission operations include two nominal observation phases (Phase-1/Phase-2) with different orbits and different acquisition schemes, with a short transition phase between them (TRAN). These are complemented by the early phases of LEOP and COM and an EOL phase to comply with debris mitigation requirements. This is illustrated in Fig. 5.44. Additionally, the concept of operations also addresses contingency and emergency operations.

For the nominal phase, fixed or slowly-changing observation schemes are routinely loaded and executed by the space segment, which then prepares and downloads the raw data products using regular, planned passes. The calibration and orbit control events need to be planned. Because of the mission profile, the operations concept is repeatable and regular, allowing automation. The emergency operations and LEOP as well as the EOL deorbiting will still necessitate high operator involvement. The following sections discuss the modes and phases of the mission in more detail.

### 5.7.2 LEOP and Commissioning

The launch sequence is fixed by the launch provider (see Section 5.5). During launch the satellite is powered internally with minimal systems on. The launch sequence ends with the satellite release. The early orbit operations of the ground and space segment then include the following steps:

— Initialisation of major satellite platform subsystems
— Spin rate reduction and attitude acquisition
— Deployment of antenna reflector and solar array

Further LEOP operations controlled from the ground will correct launch injection errors, acquire nominal (accurate) attitude pointing and perform initial check-up of platform equipment.

Once the satellite is stabilised, COM operations will prepare the nominal phase. The platform equipment is first commissioned. The payload will then be commissioned and initial calibration will be performed. The whole end-to-end data chain is then verified (including ground processors) before nominal operations are cleared to start (see Subsection 5.7.4).

### 5.7.3 End-of-life and Emergency Operations

#### 5.7.3.1 End-of-life

After nominal operations are completed, the satellite will perform a last orbital manoeuvre, namely a lowering of the perigee by about 75 km, to an elliptical orbit that guarantees the reentry in less than 25 years thanks to atmospheric drag. The satellite will be 'passivated', i.e. all potential long-term sources of damage to the satellite integrity will be neutralised (battery cells, propellant tanks etc.) and the platform left inactive.

#### 5.7.3.2 Emergency operations

The operations concept must manage anomalies. These can occur both on board (space segment) and on the ground (ground segment). For the ground, they are dealt with by operators and maintenance crews, whilst on board they must be dealt with a combination of satellite autonomy and operator control through emergency operations. To cope with onboard anomalies, a Failure Detection, Isolation and Recovery (FDIR) approach is implemented. The FDIR approach includes several layers with different degrees of criticality and associated recovery actions. An example of a layered approach is shown in Fig. 5.45. At the lowest level, there are protections and monitoring of equipment (including electrical protection, voltage monitoring etc.). At higher levels there are tests within the control software applications to monitor anomalous

Figure 5.45. FDIR layered approach (Concept A example).
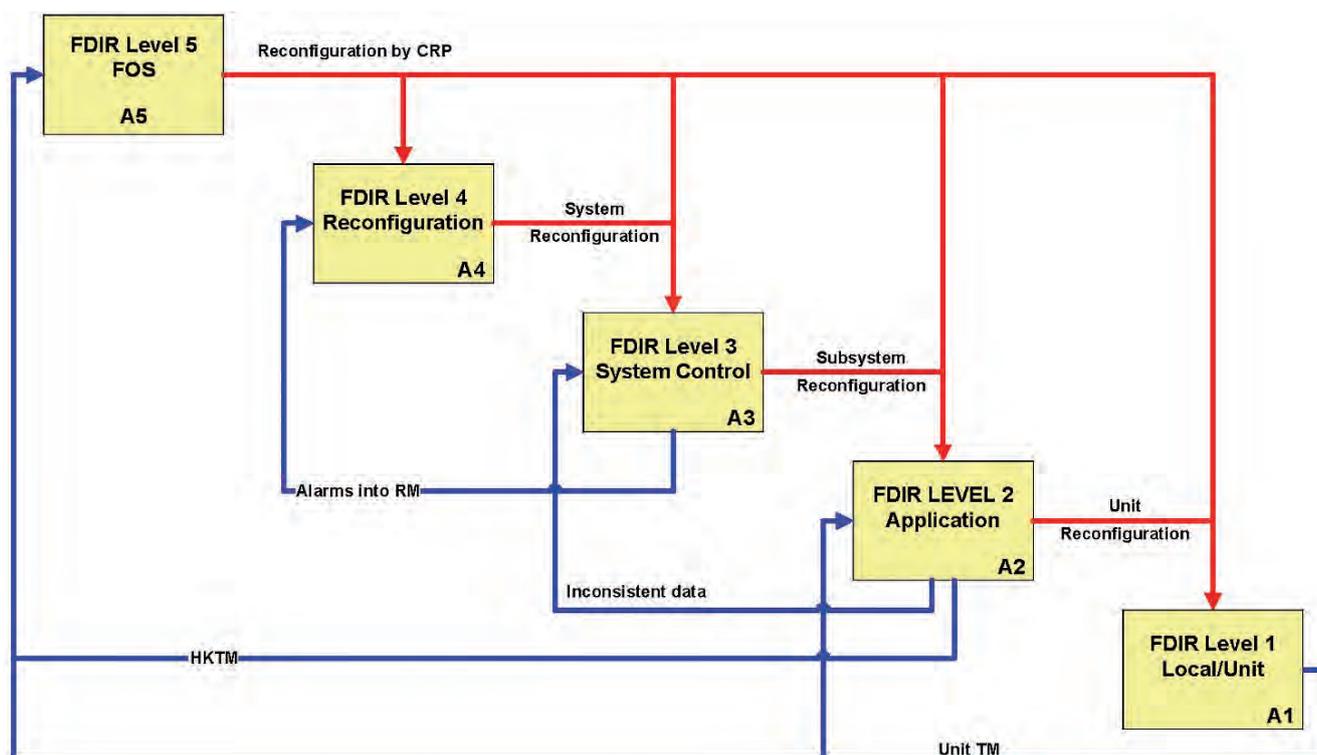
system operations parameters (such as drifting attitude or faulty computers). The recovery logic will perform the adequate action, from automatic correction to ultimately the switch to a robust safe mode to maintain the satellite in a stable state, waiting for ground intervention to perform corrective and recovery actions.

### 5.7.4 Routine Operations

During Phase-1 and Phase-2 operations are considered routine and focused towards the regular production of Level-1 data products as the main output of the system. The main tasks performed during routine operations are the mission planning of observation and data transfer to the ground, the maintenance of the orbit through regular orbit control manoeuvres, and the calibration operations.

Because of the repeat orbit and the nature of the observables, the mission operations are deterministic and repeatable every 3 days (Phase-1) or 15 days (Phase-2). A predefined multirepeat-cycle plan will be used over its applicability period. This is, at present, six months, based on the coverage maps (winter/summer), although in the future it may evolve towards more frequent updates of the coverage map. The observation plan is optimised to reduce the orbit duty-cycle, leading to a given orbit-per-orbit observation timeline. An example of the resulting duty cycle is shown in Fig. 5.46. The data downlink passes are driven by the blind orbits of the PDAS ground station (up to four blind orbits).

To maintain the orbit, regular manoeuvres are required. These are performed over one orbit and include a first series of firings to raise the orbit, and a second series to circularise it, with the relevant slew manoeuvres to align and realign the satellite. During the manoeuvres, SAR observations cannot be performed, but this is still compatible with the overall mission availability.

Finally, the other regular operation done in a routine manner is the calibration of the payload. As shown in the payload and performance sections (Subsection 5.4.3. and Chapter 7), internal and external calibrations are necessary. Only external calibration has an operational impact since internal calibration is included in the data acquisition. In terms of mission operations,
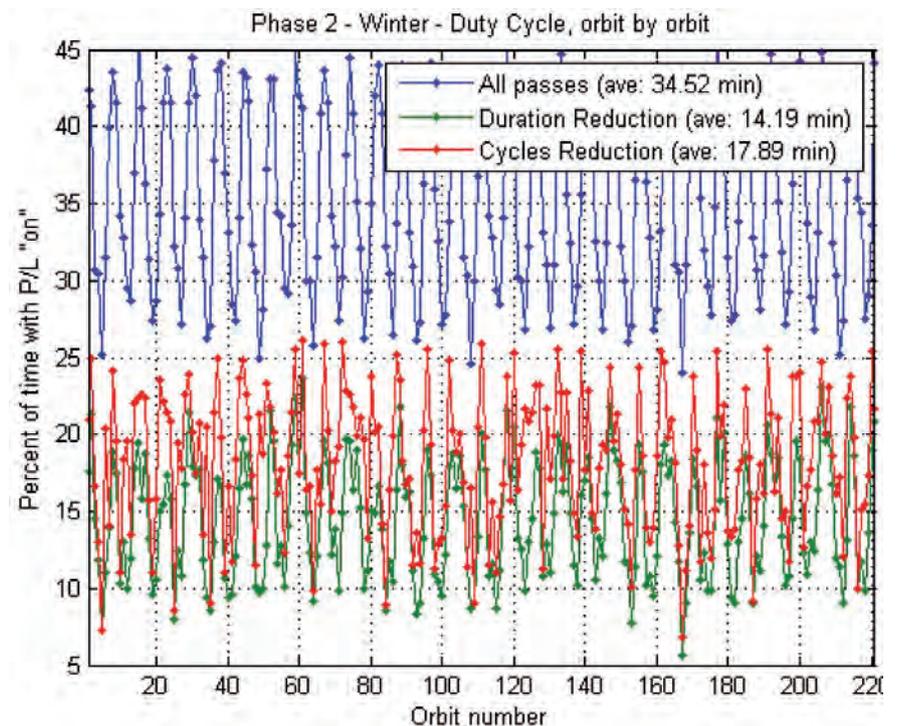


Figure 5.46. Concept B orbit duty-cycle over repeat cycle in Phase-2 (in red).
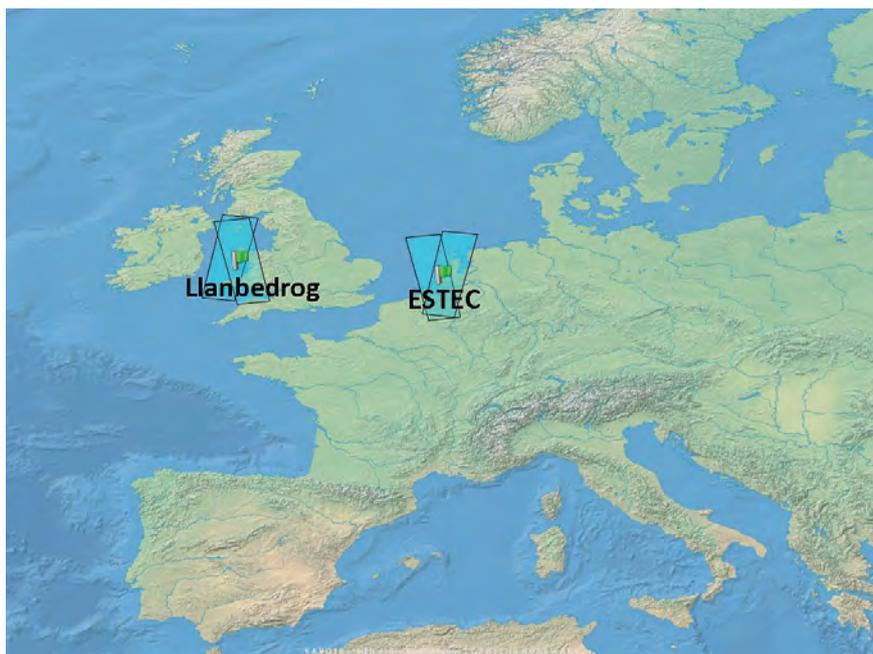
Figure 5.47. Calibration location example and Phase-2 coverage pattern overlay (Concept B).

the main impact is therefore the definition and execution of external calibration observations.

Two different sources of external calibration images are foreseen (Subsection 5.4.3): the Amazon rainforest, offering homogeneous backscatter level at these frequencies, will be used to calibrate the antenna pattern. Acquisitions over dedicated calibration sites including active and passive transponders will complete the overall radiometric calibration. Calibration will occur once or twice per week.

Owing to its large geographical extension the calibration over the rainforest area does not introduce any constraint on the mission, whereas the location of the active/passive transponders has to consider the actual coverage pattern. Fig. 5.47 shows as an example the location of two calibration sites for Concept B.

In conclusion, the nominal operations and the overall system concept for CoReH$_2$O is clearly defined, robust and optimised.

# → SCIENTIFIC DATA PROCESSING AND VALIDATION CONCEPT

# 6. Scientific Data Processing and Validation Concept

This chapter gives an overview on methods and tools for data processing with focus on primary geophysical products (Level-2). In addition, concepts for validation and assimilation of snow-cover products in snow-process models are presented.

## 6.1 Level-0 and Level-1 data

As a first step, raw data are transformed to Level-0 data products that are suitable for input to SAR image processors. The Level-0 product contains the SAR time-ordered signals, telemetry data, and auxiliary data required for data processing. At present, the delivery of Level-0 data products to the science community is not foreseen. However, it might be more economical to keep Level-0 products in the long-term archive rather than Level-1 products.

The following Level-1 (swath-based SAR image) products are presently foreseen:

— Single Look Complex (SLC) images
— Browse images
— Geocoded Terrain Corrected (GTC) images (multi-look)

Browse images correspond to reduced-resolution amplitude detected images of a single co-polarised channel (either X-VV or Ku-VV) in a common raster image format. The SLC product corresponds to calibrated single-look complex data in slant-range geometry in the four channels, generated from Level-0 data by means of phase-preserving SAR processing. GTC data are radiometrically corrected, multi-looked backscatter data of the four channels, re-sampled to a DEM and expressed on a geodetic grid (e.g. UTM) in geometric resolution of 50 m.

## 6.2 Level-2 Processing

Level-2 products will be swath-based maps of snow and ice parameters in a standard cartographic projection (UTM). Here the processing steps for the primary Level-2 products, specified in Table 4.1, are described. It is expected that Level-2 products on additional snow and ice parameters will be generated by the scientific community or at national data centres. Inputs to the retrieval of geophysical products are Level-1b calibrated Ku- and X-band co- and cross-polarised backscatter data (GTC images).

The general layout of the processing line for retrieval of the primary Level-2 products is shown in Fig. 6.1. It comprises a pre-processing module, a segmentation module, the module for iterative SWE retrieval, and the output module for the primary Level-2 products and data processing report. The Level-2 products are snow extent (classified as dry or wet snow), SWE on land and snow accumulation on glaciers.

The first processing step is the correction for atmospheric propagation losses, using as input Level-1b GTC data, vertical profiles of atmospheric parameters, and DEM data. The atmospheric correction procedure calculates the atmospheric transmissivity for the specified geographical location using gridded ECMWF analysis or forecast data of atmospheric parameters. The correction applied to the observed backscattering coefficients at pixel scale is calculated from the transmissivity for each grid cell, taking into account the
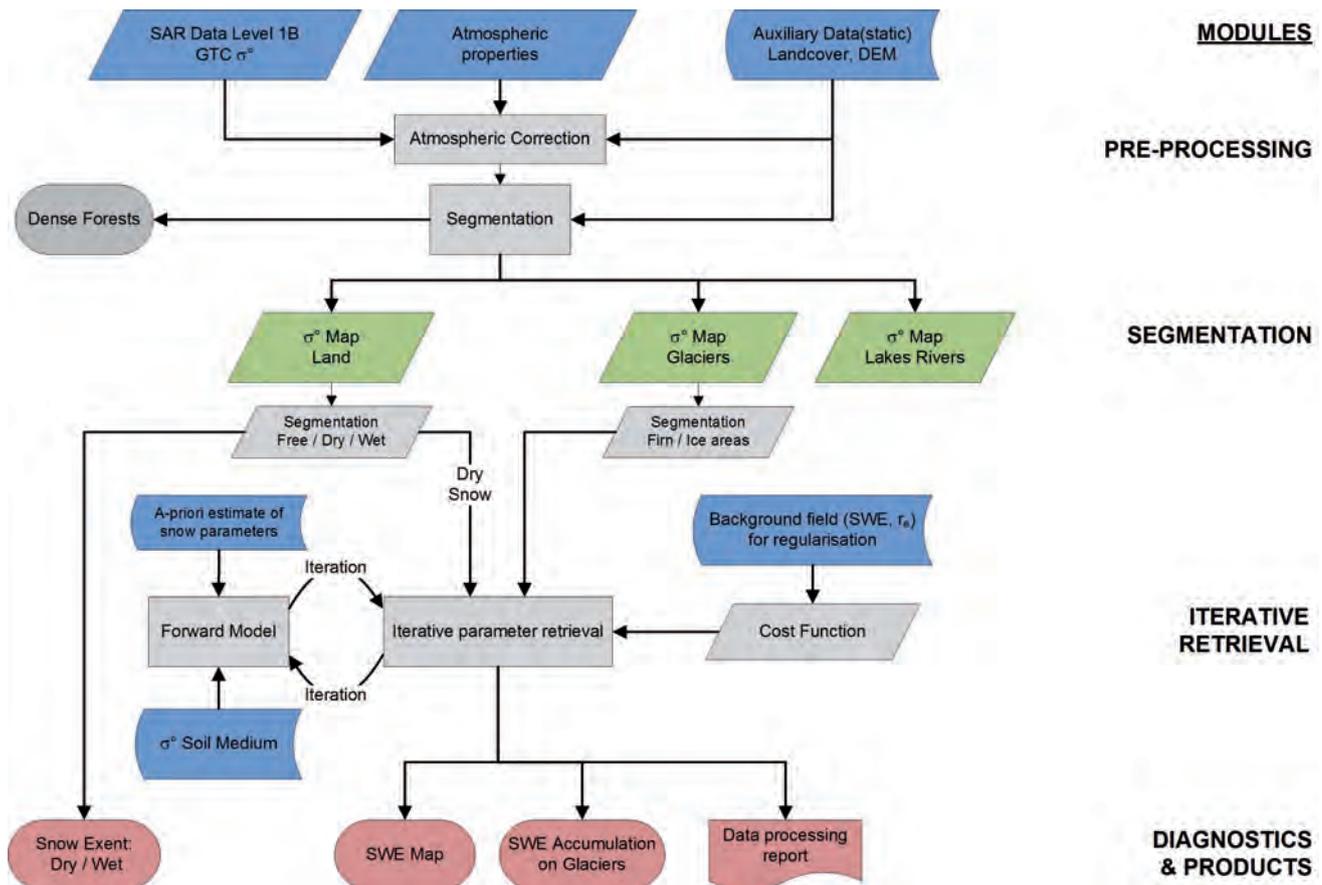
Figure 6.1. CoReH$_2$O processing line for retrieval of basic Level-2 products. (ENVEO)

topographic height from the DEM. For the period when dry snow is expected, the corrections are typically in the order of 0.05–0.1 dB at X-band and 0.15–0.25 dB at Ku-band (Fig. 4.12).

The next processing step is the segmentation. This is based on geocoded, atmospherically-corrected backscatter data, a DEM, maps of relevant surface types (e.g. from GlobCover) and glacier outlines (e.g. shape files from GlobGlacier and Global Land Ice Measurements from Space (GLIMS) projects). Based on land-cover data, dense forests are flagged and excluded from further processing. Water surfaces with and without ice cover (ocean, lake, rivers) are also identified and digital-backscatter maps are stored to provide input for optional retrievals of secondary Level-2 products. Glacier areas are masked out using the shape file, and the digital data are routed to segmentation of firn and ice area and to iterative retrieval of snow accumulation. The segmentation into firn areas (percolation zone) and ice areas on glaciers is performed on backscatter intensity in autumn to identify areas were retrievals of snow accumulation will be carried out. The remaining land-surface is separated into open land (including low vegetation) and open (sparse) forest based on land-cover data. For these areas, segmentation into dry snow, wet snow and snow-free surfaces is performed by means of multitemporal backscatter intensity ratios of co- and cross-polarisation channels applying pre-defined threshold values (Nagler et al., 2011). Maps of dry snow and melting snow areas are a basic product.

The same retrieval procedure for SWE applies to dry snowpack on open land (bare soil and sparse vegetation) and open forests. For open forest the attenuation of the signal is taken into account as described below. As for many inversion problems in the remote sensing of Earth-surface bio-geophysical

parameters, the retrieval of SWE on land surfaces and snow accumulation on glaciers is an ill-posed problem, which cannot be solved without *a priori* information (e.g. Twomey, 1977). For this type of problem, regularisation techniques are commonly applied to obtain unique, stable and reliable solutions (Acar & Vogel, 1994). Based on this concept, a statistical procedure is applied for SWE retrieval using (statistical) *a priori* information on snow properties for the regularisation parameters. A constrained minimisation approach is employed using the following cost function to iterate for two free variables:

$$J(x) = \sum_{i=1}^{4} \frac{1}{var_i}[\Phi(x_1, x_2; c_1, ..., c_r) - \sigma_i^0]^2$$
$$+ \sum_{j=1}^{2} \frac{1}{\lambda_j^2}(x_j - \hat{x}_j)$$

(6.1)

where:

| | |
|---|---|
| $\Phi(.)$ | sRT model for backscatter computation of snow covered ground |
| $i$ | index for CoReH$_2$O band (i=1,..,4 → X-VV, X-VH, Ku-VV, Ku-VH) |
| $x_1, x_2$ | free model parameters (SWE, effective grain radius Re) |
| $c_1,...,c_r$ | configuration parameters of sRT model |
| $\sigma^0{}_i$ | measured backscatter coefficient in CoReH$_2$O band $i$ |
| var$_i$ | variance of measured backscatter coefficient |
| j | index for free model parameters |
| $\hat{x}_j$ | mean value of regularisation parameter |
| $\lambda_j$ | standard deviation of regularisation parameter |

Using this approach, it is important to keep the number of free model parameters for iteration as small as possible while accurately describing the main physical interactions. For this reason, a radiative transfer model for a single snow layer is employed to relate backscatter signatures to physical properties of the snowpack and background medium. The iteration is performed for the two snow parameters that show high sensitivity in respect to backscatter, SWE and Re (Chapter 4). The iteration minimises the difference between measured and forward-modelled backscatter data. The applied sRT model provides a realistic representation of the radar-signal interactions with snow, as confirmed by comparisons with experimental backscatter data acquired by tower-based and airborne sensors in field campaigns in Scandinavia, the Alps, and North America (Rott et al., 2010; 2011).

The retrieval of SWE is essentially based on the volume backscatter contribution. The measured backscatter signal includes the signal of the snowpack and the signal of the soil below (attenuated by propagation through the snowpack) as described in Chapter 4. The background signal of snow-free ground, $\sigma^g$, is obtained from backscatter measurements before snowfall starts. In order to obtain backscatter signatures that are representative for the soil conditions below the snowpack, it is planned to acquire backscatter time series before first snowfall and during the early snow-cover period. Because of frequent repeat coverage, Phase-1 of the mission will observe possible temporal variations of the signal and help to develop relevant decision rules for Phase-2. For assessing freezing conditions of the top soil layer, the dual-frequency approach is useful. The X-band signal, which is little affected by shallow new snow, will allow possible changes in soil conditions to be detected during the initial snow-cover phase. Tools for exploiting the information content of backscatter time series should be further developed during the preparation of

the mission, both for checking the background signal of soil, and for detecting possible changes in snow morphology owing to melt/freeze cycles.

The radiative transfer model requires snow parameters (configuration parameters) that are estimated from external sources: snow temperature, snow density, and the roughness (RMS height) of the air/snow interface. Snow temperature and density can be estimated from snow process models using numerical meteorological data as input or from snow-cover statistics. Statistical models, taking into account snow-climate classes, enable the estimation of snow-bulk density with good accuracy (Sturm et al., 2010). The backscatter contribution of dry snow surfaces is very small, and consequently RMS height is of little relevance so that a fixed value can be applied. The mean temperature of the snowpack, to be derived from numerical meteorological data, is needed to estimate the volume absorption coefficient of the radiative transfer approach. The impact of these parameters on retrieval performance has been tested (Chapter 7).

The retrieval of snow accumulation on glaciers, which is applied after segmentation, uses the same algorithm as the retrieval of SWE on land. The backscatter response to snow accumulation (SWE of winter snow) on glaciers is related to signal attenuation, but the basic algorithm is also valid for this target. On glaciers, the background medium (refrozen firn in the percolation zone and glacier ice) has a higher scattering albedo than the snowpack accumulating in winter, which features smaller grains than snow on land surfaces because of different metamorphic processes (Rott et al., 2011). The extinction losses in winter snowpack cause a decrease in total backscatter with increasing accumulation (Fig. 4.9). The contrast between background and winter snow determines the sensitivity for retrieving accumulation. Therefore, at first segmentation, applying a backscatter threshold in autumn backscatter data, is applied to separate glacier areas for SWE retrieval (percolation facies and ice facies) from other glacier areas (dry-snow facies). These thresholds have been derived from simulated backscatter data and satellite observations at X-band (TerraSAR-X) and Ku-band (QuikSCAT) frequencies.

Procedures for compensating vegetation effects in the SWE retrieval algorithm have also been studied (Rott et al., 2011). The analysis deals with forested areas, with emphasis on coniferous trees which are the most representative species in boreal forests and consequently of great relevance to remotely sensing snow. Effects of cover fraction, biomass and tree height on the backscatter signal measured above forested areas with snow cover are considered in the developed electromagnetic model. The model requires information from auxiliary data on forest type, cover fraction CF, and forest structure, and accounts also for a radar shadow area (the snow area not covered by trees, but shadowed by trees). Information on the extent of this area can be derived from forest characteristics by using semi-empirical relationships. The retrieval of SWE is only performed for open forests, as the backscatter signal coming from soil or snow below the trees is very small in a closed canopy. The retrieval applies the same procedure as for open land by minimising the cost function where the backscatter forward-model for snow-covered terrain in open forest is implemented. Auxiliary data on vegetation type are obtained from different datasets (e.g. GlobCover) and by using semi-empirical relationships. The SWE retrieval for partially forested areas will be affected by the accuracy of the vegetation scatter model and the auxiliary data source. The present baseline version uses a resolution of 500 m for the SWE product in open forest. It is expected that improved global vegetation maps, useful for improving the retrieval accuracy, will be available before launch, or will be derived by the SAR data itself. For example, methods to obtain improved products on tree height or vegetation volume were recently proposed by Lefsky (2010) and Santoro et al. (2010). Preparatory work for the mission should also include the development of an improved vegetation scattering model at the CoReH$_2$O frequencies.

Combining GlobCover data and the global snow-cover mask presented in Chapter 4 (maximum extent), the percentage of land surface where vegetation correction should be applied was computed. It is estimated that 48% of the snow regions are located in open areas where correction is not necessary and 30% in open forests for which corrections can be applied to retrieve SWE. Dense forest account for 8%, which are masked out and not considered for the retrieval. For 19% of the areas, the applicability of forest correction still needs to be checked because of the uncertainties of land-cover maps.

## 6.2.1 Auxiliary Data

The CoReH$_2$O retrieval algorithm requires auxiliary data for geocoding, atmospheric correction and the iterative retrieval procedure. Table 6.1 lists the currently available input dataset and indicates whether these datasets are in line to meet the primary Level-2 product performances. Information on the impact of this input is provided in Chapter 7. A DEM, preferably with spatial resolution similar to or higher than the basic Level-1b product (50 m), is required for precision geocoding of the SAR images. Such data are available with the Advanced Spaceborne Thermal Emission and Reflection Radiometer (ASTER) Global DEM which features 30 m grid size. A land-cover dataset is needed for segmentation of various land-surface classes. The presently available data (GlobCover) have a grid size of 300 m, which is compliant for the product in forested areas (segmentation and snow retrieval), but slightly larger than the size of the snow product for open land.

Time-varying auxiliary data include gridded ECMWF data on atmospheric parameters, acquired close in time to the satellite overflight. These are used for computing the atmospheric attenuation by means of a radiative transfer model and also support the estimation of snow parameters as input to the cost function. Estimates of snow parameters are, on one hand, needed as configuration parameters (temperature and density) and, on the other hand,

Table 6.1. Auxiliary datasets and sources (present status).

| Parameter | Input data source | Spatial resolution | Temporal resolution | Comment |
|---|---|---|---|---|
| DEM | ASTER and national DEMs | Horizontal: 30 m Vertical: 1 m | Static | Compliant |
| Land-cover map | GlobCover | 300 m | Static | Product size partly compliant |
| Forest-cover fraction, CF, and characteristics | GlobCover | 500 m | Static | Partly compliant (see text on compensation of vegetation effects); to be derived from GlobCover |
| *A priori* SWE | ECMWF or GlobSnow | 0.125° | Daily | Derived from numerical meteorological data or from GlobSnow (downscaling procedure in development) |
| *A priori* effective grain radius | ECMWF or GlobSnow | 0.125° | Daily | Derived from meteorological data or GlobSnow (downscaling procedure in development) |
| Snow mean temperature | ECMWF and land-surface models | 0.125° | Daily | Derived from 2 m air and soil temperature (downscaling procedure in development) |
| Snow density | Snow climatology or ECMWF | 0.125° | Daily | Compliant |
| Atmospheric parameters | ECMWF | 0.125° | 6 hours | Compliant |
| Glacier outlines | GLIMS, GlobGlacier | 10–50 m | Static | Compliant |

for the regularisation (*a priori* estimates of SWE and Re). Values for these parameters can be taken from climatological snow-cover statistics. However, time-varying data are preferable, e.g. derived from land-surface components of numerical meteorological models. Another potential data source are low-resolution snow products (SWE, Re) derived from microwave radiometer data (e.g. delivered by the GlobSnow project at 25 km grid). These data need to be down-scaled, using digital-elevation data and land-cover data. For many regions (Europe, North America) snow auxiliary data can be taken from operationally-available daily snow-model products at high resolution (~1 km) (e.g. the NOAA National Snow Analyses, and the Integrated Nowcasting System of the Austrian Weather Service). Auxiliary data currently available for forested areas are based on the GlobCover database. Options for further improvement of the forest database before launch are addressed above.

## 6.3  Validation

Level-2 products of SWE on land surfaces and snow accumulation on glaciers will be validated at selected field sites by means of *in situ* measurements of snow accumulation at points and along profiles. Emphasis of validation activities will be during Phase-1 of the mission, using established sites dedicated to snow and glacier studies. These sites will also be available during Phase-2, and can then be complemented by additional sites due to wider coverage.

A subset of sites covered in Phase-1 is listed in Table 6.2. They include the main global snow regimes specified by Sturm et al. (1995), namely tundra, taiga, alpine, maritime, and prairie, as well as several glacier sites. The list is not exhaustive, and will be complemented by additional sites as the mission matures. These sites are equipped with automated measurement stations for atmospheric and snow parameters. In addition, intensive field campaigns will be performed at the sites at different times in winter to measure the spatial pattern of accumulation in the surroundings of the stations. Data for snow stations with advanced equipment for snow characterisation or networks (stations and snow surveys), operated by hydrological and meteorological services will also be used for validation (Fig. 6.2). For validation of the snow-

| Validation site | Coordinate | Snow regime |
|---|---|---|
| Sodankylä (FI) | 68°N,27°E | Taiga |
| Fairbanks (US) | 64°N,140°W | Taiga |
| Fraser(US) | 39°N,123°W | Alpine/Tundra/Taiga/ Praire |
| Reynolds and Dry Creek experimental watersheds(US) | 39°N,123°W | Alpine/Maritime/Prairie |
| Col de Porte (FR) | 45°N,5°E | Maritime/Alpine |
| Obergurgl (AT) | 47°N,11°E | Alpine |
| Babo River Basin (CN) | 38°N,99°E | Alpine |
| Samoylov (RU) | 72°N,126°E | Tundra |
| Ny Ålesund (NO) | 79°N,12°E | Tundra |
| Abisko (SE) | 68°N,19°E | Tundra |
| North Slope (US) | 67°N,155°W | Tundra |
| Waterloo (CA) | 43°N,80°W | Prairie |
| Tromsø (NO) | 70°N,19°E | Maritime |
| Hintereisferner (AT) | 47°N,11°E | Alpine glacier |
| Saint Sorlin Glacier (FR) | 46°N,10°E | Alpine/Maritime glacier |
| Kongsvegen (NO) | 79°N,12°E | Arctic glacier |

Table 6.2. Validation sites (subset) for different snow regimes covered in CoReH$_2$O Phase-1.
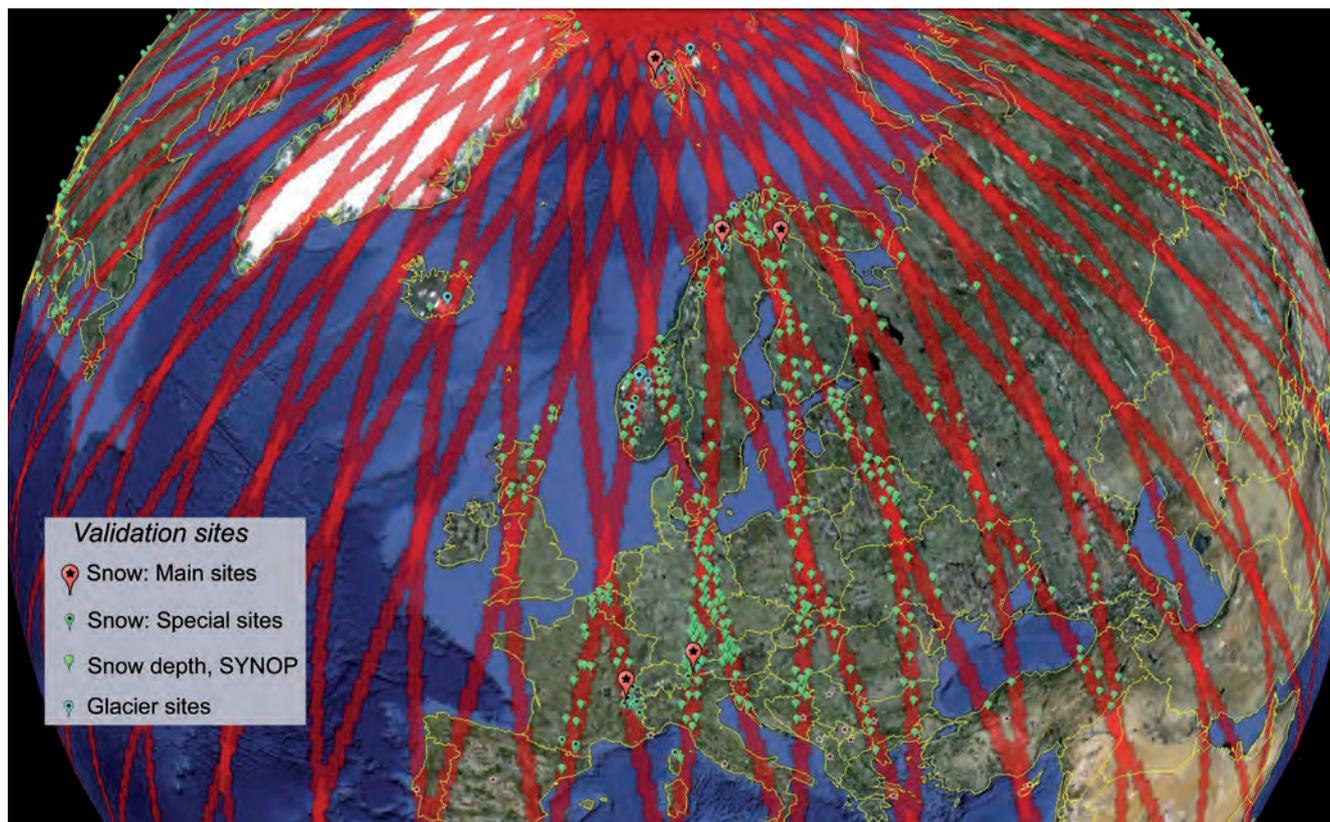
Figure 6.2. CoReH$_2$O Phase-1 coverage of a three-day orbit with marks for various potential validation sites for snow and glaciers. Main sites for intensive snow studies are also marked. (Norut, Google Earth).

extent product remote-sensing data from other sensors can be used such as medium- and high-resolution optical sensors (e.g. Sentinel-2).

## 6.3.1 Additional Validation Sources

In addition to the above mentioned validation sites, there are many other sources to validate the SWE and snow extent product. The availability of snow observations and requirements for different applications have been reviewed recently (IGOS, 2007; Brown and Armstrong, 2008). This section focuses on systematic observations suitable for model evaluations and data assimilation.

Routine measurements of snow depth and snow coverage are generally made daily at synoptic and climate stations. These networks have wide geographical distributions in the northern hemisphere, but are sparse in mountainous and high-latitude regions. Measurements are usually made at one or at a few points in open sites, so may not always be representative of wider surrounding areas. Daily snow-depth observations are transmitted by the WMO Global Telecommunication System, allowing assimilation in near-real time. In the 20th century, the number of stations delivering *in situ* measurements increased until the 1970s, but then decreased towards the end of the century. Station data on snowfall and maximum temperatures have been used with simple snow models to reconstruct long-term records of snow extent for North America from 1900–93 (Frei et al., 1999) and for Eurasia from 1915–97 (Brown, 2000). Brown et al. (2003) produced a gridded reanalysis of monthly snow-depths over North America for 1979–97.

Systematic and timely observations of SWE are less abundant. In many countries, measurements are made by hydrometeorological networks at dedicated sites, applying gravimetric sampling in snow pits at single points

or along snow courses. Automated measurements are made by snow pillows or attenuation of natural gamma or cosmic radiation. Data from more than 1200 manual snow courses and more than 750 automatic Snowpack Telemetry (SNOTEL) stations in western US can be downloaded from the Department of Agriculture Natural Resources Conservation Service. Serreze et al. (1999) used SNOTEL data to investigate regional snowpack characteristics, although Pan et al. (2003) found scale problems when using point SNOTEL data to evaluate grid-average model SWE predictions.

Figure 6.2 also includes sites within the swath of the satellite where meteorological stations report daily snow-depth measurements. Sites with enhanced equipment (snow pillows or climate stations) or sites where campaign activity will take place are flagged as special sites. The meteorological stations cover all snow regimes, but do not provide snow-density measurements routinely. Statistical models on snow-bulk density (Sturm et al., 2010) offer the possibility to extend the spatial validation of the SWE product by converting snow depths to estimates of SWE.

## 6.4 Assimilation of Snow Cover Products

Snow on the ground stores water and has a strong influence on energy exchanges between the surface and the atmosphere, so information on snow is valuable for periodic reinitialisation of hydrological and meteorological forecasting models. Operational analyses often use satellite observations of snow extent or ground-based observations of snow depth (Drusch et al., 2004), but current satellite retrievals of SWE are too unreliable and ground-based measurements are too sparse to be of practical use. SWE, however, is the model state variable that has to be estimated, so observation operators are required to link available observations to SWE. Snow density can be estimated from the model itself, empirical functions of depth or climatology to retrieve SWE from depth measurements. From fractional snow-cover for an area, SWE is found by inverting empirical snow-cover depletion functions, for which several forms are in common use (Clark et al., 2011). Both of these methods give uncertain measures of SWE. The CoReH$_2$O Level-2 product offers direct retrievals of SWE at high-spatial resolution and of sufficient temporal resolution and accuracy for operational analyses.

The aim of data assimilation is to combine uncertain observations with uncertain model forecasts to obtain statistically optimal estimates of the true state of a system. Typically, an analysed state is found by minimising squared differences with the model background state and the observations, normalised by their error variances. This formulation can be extended to include observations before the analysis time and to propagate information to other model state variables that are influenced by SWE, such as soil temperature. Several assimilation schemes differ only in how they handle the background error: it is given a fixed value in Optimal Interpolation (Brasnett, 1999), it is estimated from the spread in an ensemble of model forecasts in the Ensemble Kalman Filter (Slater & Clark, 2006) and it is predicted using a linearised forecast in the Extended Kalman Filter (Reichle et al., 2002). The assimilation techniques used in operational snow analyses currently lag behind the state-of-the-art in atmospheric and soil moisture analyses. A simplified form of the Extended Kalman Filter is already used at ECMWF to assimilate satellite soil moisture retrievals (Seuffert et al., 2004), and this will provide a convenient framework for the assimilation of CoReH$_2$O SWE retrievals.

Figure 6.3 shows simulations of SWE at Sodankylä in 2010–2011 with and without assimilation of SWE retrievals from SnowScat measurements in a snow model. The model is driven with high-quality *in situ* meteorological data and was calibrated using data from a previous winter, so the simulation is fairly good, even when run as an open-loop forecast without assimilation
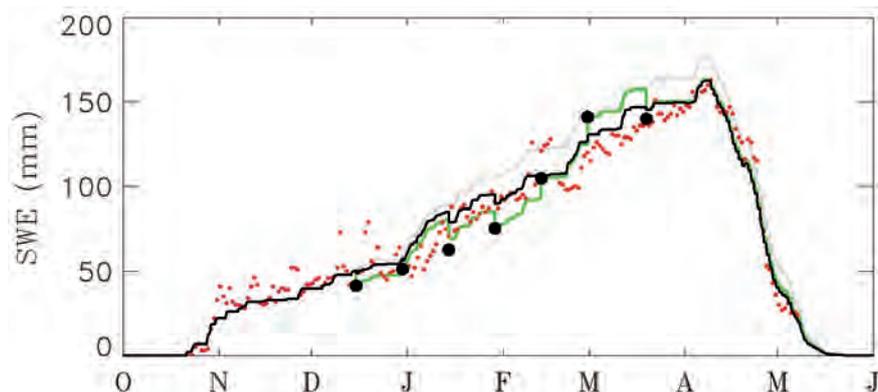
Figure 6.3. Observations and simulations of SWE at Sodankylä in 2010–2011. Red dots show *in situ* measurements and black dots show SWE retrievals based on SnowScat backscatter measurements, thinned to a 15-day repeat cycle. Simulations were run as an open-loop forecast (grey line), with direct insertion of the retrievals (green line) and with assimilation of the retrievals (black line). (University of Edinburgh)

of retrievals. Reinitialisation of the model every 15 days by direct insertion of retrievals reduces errors, but introduces some unrealistic jumps in the simulation. Assimilating the observations using a Kalman Filter gives errors that are lower than for either the model or the retrievals alone; root mean square errors over the whole winter are 16 mm for the open-loop simulation, 11 mm for direct insertion and 9 mm for the Kalman Filter assimilation.

Data from sparse observations, such as provided by ground-based networks, can be assimilated in 2D hydrological forecasts and snow-process models by interpolation, giving more weight to the observations in regions close to the observation locations or elevations and more weight to model background fields elsewhere (e.g. Drusch et al., 2004). Both modelling and observation of snow is challenging in mountainous regions owing to high-spatial variability, yet it is precisely in these regions that much of the snow accumulation, most important for water resources, occurs (Barnett et al., 2005). Andreadis and Lettenmaier (2006) investigated the impacts of assimilating different types of snow observations into the Variable Infiltration Capacity (VIC) macroscale hydrological model with Ensemble Kalman Filter. Using satellite observations of snow-cover extent and a snow-cover depletion curve or surface observations of SWE gave modest improvements over open-loop simulations. However, results from assimilation of AMSR-E passive microwave SWE retrievals, which have low-spatial resolution and underestimate SWE for deep snow, were not encouraging. Better spatial resolution as provided by CoReH$_2$O and more accurate SWE estimates will enable improvements.

# → PERFORMANCE ESTIMATION

# 7.    Performance Estimation

The performance of the proposed mission implementation concepts is assessed against the mission requirements presented in Chapter 4. The performance is expressed first for the system-level parameters described in Chapter 5 including coverage, data latency and availability. The observation performance at Level-1 and Level-2 product levels, as defined in Section 5.4 and Chapter 6, is also presented and compared to the relevant requirements in Sections 7.2 and 7.4. Additionally, some results from the end-to-end mission performance simulator, addressing the capability of the proposed observing system concepts to meet the mission requirements, are presented in Section 7.3.

## 7.1  Coverage, Data Latency, and Availability

As explained in Section 5.3.1, the orbit selection is driven by the required temporal revisit of snow-covered areas and by SAR performance considerations. For the selected orbit, the coverage of snow and ice areas for the Phase-2 of the mission depends on the instrument swath, which is required to be at least 100 km wide, and on the acquisition strategy. The latter is optimised such that each area within the coverage mask is only imaged once during the repeat period to avoid duplication and limit the SAR duty-cycle and the overall data volume. The resulting coverage pattern is shown in Fig. 5.6 in Subsection 5.3.2. The achieved coverage is presented in Table 7.1 for winter and summer.

The data latency is driven by the data volume, the number and location of the downlink ground stations, the capacity of the data links (space-to-ground and on the ground) and by the ground segment processing capability. The major contributors are the capacity of the space-to-ground link and the number of blind orbits with no data link passes to the PDAS. The ground infrastructure for internal data transfer and processing is not a driver. The performance achieved by the two concepts is shown in Table 7.2. The difference in individual contributors is due to the concept-specific sizing of the PDHT downlink, the selection of the PDAS, and the optimisation of the acquisition strategy.

Finally, the system availability is driven by the expected statistical outages in the space segment, by the deterministic outages primarily because of orbit control manoeuvres and by the overall availability of the ground segment. The achieved system availability is presented in Table 7.3 below for each implementation concept.

In summary, Concepts A and B meet all the mission-level performance requirements with margins.

| Case | Concept A | Concept B |
|---|---|---|
| Winter maps (required >85%) | 91% | 88.7% |
| Summer maps (required >85%) | 96% | 88.4% |

Table 7.1. Coverage performance in Phase-2 (northern hemisphere seasons).

| Step | Concept A | Concept  B |
|---|---|---|
| Space segment delay | 9.8 h | 9.5 h |
| Downlink and ground segment | 17 min | 17 min |
| Total (required <24 hr) | 10.1 h | 9.8 h |

Table 7.2. Worst-case data latency performance.

Table 7.3. Worst-case availability performance.

| Source | Concept A | Concept B |
|--------|-----------|-----------|
| Satellite failures and safe modes | 99% | 97.7% |
| Orbit control outages | 99.4% | 99.3% |
| Ground segment outages | 95% | 95% |
| Total (required >90%) | 93% | 92% |

## 7.2   Observing Mission Performance at Level-1b

The implementation choices presented in Chapter 5 determine the observation principle and geometry for each concept. This defines the timeline of the ScanSAR imaging sequence and the antenna patterns, which are designed for optimum coverage and performance. This Chapter analyses the resulting performance at Level-1b for each concept, covering the two nominal mission phases (Phase-1 and Phase-2). Performance analyses include swath width, geometric resolution, derived from the Impulse Response Function (IRF), radiometric resolution (ENL), sensitivity (NESZ), and ambiguity suppression (TAR). Finally, based on the assumptions made at system and instrument level, radiometric budgets and geometric budgets are presented, to verify full compliance with the system performance requirements.

### 7.2.1 Imaging Geometry

The main parameters of the imaging geometry are presented in Table 7.4, which considers the full range of altitudes encountered during the mission, i.e. from the lowest altitude of Phase-2 (~650 km) to the highest altitude of Phase-1 (~700 km).

As outlined in Subsection 5.4.3, Concept B keeps near constant incidence angles over both phases, while Concept A mitigates the variation of slant range with satellite altitude by continuously changing the incidence angle via a roll steering manoeuvre.

A swath width of at least 100 km is achieved by operating the instrument in ScanSAR mode, where the total swath is divided into several sub-swaths imaged with their specific PRF. Concept A is based on seven sub-swaths, while Concept B combines six slightly larger sub-swaths. Notably, elevation pointing errors do not impact on the coverage as a mispointing only leads to a slightly misaligned swath. The impact of such a misalignment on the imaging performance will be detailed in what follows, where applicable.

Table 7.4. Main observation geometry parameters.

| Parameter | Required | Concept A | | Concept B | |
|-----------|----------|-----------|-----------|-----------|-----------|
| | | Min | Max | Min | Max |
| Phase-1 (700 km) | | | | | |
| Incidence angle (°) | 30–45 | 36.08 | 42.13 | 38.90 | 44.65 |
| Sub-swath width (km) | | 13.5 | 15.5 | 14.2 | 18.6 |
| PRF (Hz) | | 6380 | 6790 | 5570 | 6440 |
| Swath width (km) | 100 | 101.4 | | 102.1 | |
| Phase-2 (650 km) | | | | | |
| Incidence angle (°) | 30–45 | 38.94 | 45.00 | 38.80 | 44.77 |
| Sub-swath (km) | | 13.4 | 15.6 | 15.9 | 18.0 |
| PRF (Hz) | | 6300 | 6750 | 5930 | 6710 |
| Swath width (km) | 100 | 101.4 | | 100.1 | |
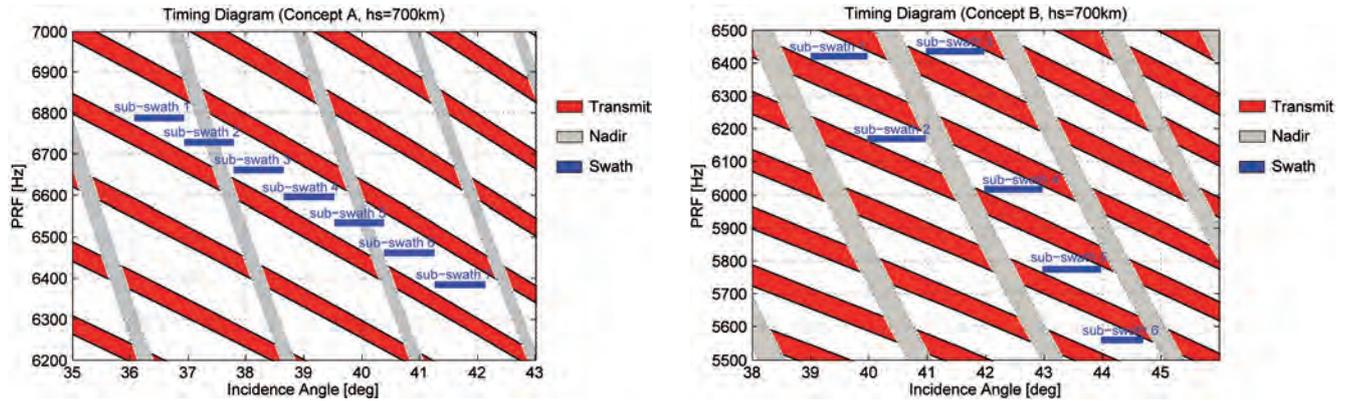
Figure 7.1. Timing examples for 700 km altitude, Concept A is shown on the left and Concept B on the right. Red represents transmission periods, blue reception periods, and grey nadir returns.
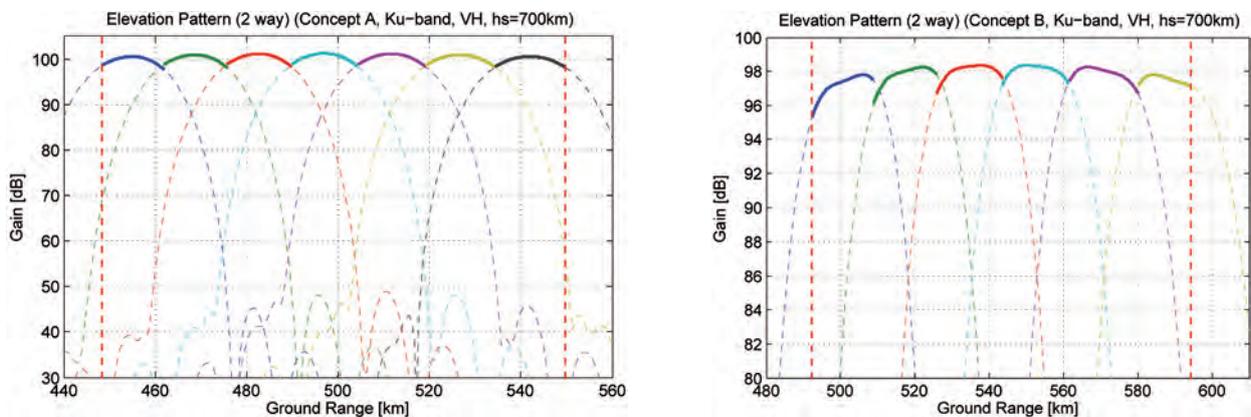


Figure 7.2. Overlapping elevation antenna patterns of different sub-swaths projected on the ground. An example of Ku-band for Concept A is on the left and Concept B on the right. Beam number increases with increasing range.

Figure 7.1 gives two examples for the allocation of sub-swaths vs. PRF and incidence angle. Blue indicates the swath locations, red the transmit events, which prevent reception, and grey the nadir return. For Concept A, the nadir return is attenuated by over 100 dB (two-way) due to the reflector antenna. This means that the potential interference with reception (blue overlap with grey areas) can be neglected. Concept B avoids interference of nadir returns and reception, which is achieved by increasing the PRF range. Note that the extension of nadir and transmit events is linked to the pulse length, which explains the differences between the concepts.

As already outlined in Subsection 5.4.3, full illumination of the swath is achieved by partially overlapping the antenna beams on ground, as shown in Fig. 7.2 (dashed lines). These elevation patterns are based on feed patterns measured during the pre-development activities (Fig. 5.19 in Subsection 5.4.3). The sub-swaths are represented by solid lines and the dashed red vertical lines indicate the swath borders. Figure 7.2 shows the Ku-band patterns, which represent a more challenging case than X-band.

Figure 7.3 shows an example for the azimuth antenna pattern vs. azimuth angle for beam-1 of both concepts. The pattern shape has an impact on azimuth ambiguities, the equivalent number of looks, and – via the azimuth beam shape losses – on the Noise Equivalent Sigma Zero (NESZ), as will be detailed in the following sections.
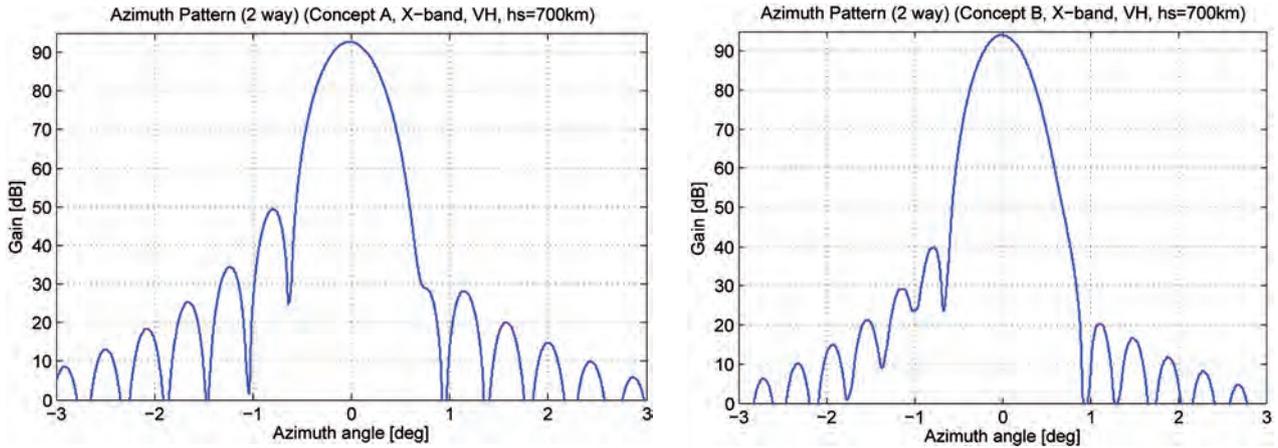
Figure 7.3. Example azimuth antenna pattern for beam-1. Concept A is shown on the left and Concept B on the right.

### 7.2.2 Impulse Response Function – Geometric Resolution

In the selected ScanSAR mode, a burst of data is acquired for each sub-swath before switching to the next. The burst duration – the time of continuous data acquisition – defines the resolution in the azimuth dimension and is therefore driven by the requirement of 50 m. The switching between beams is performed to revisit each sub-swath several times, allowing the generation of multiple azimuth looks. X- and Ku-bands are synchronised, which imposes identical illumination times for the bursts of both bands. As this leads to a better azimuth resolution in Ku-band, according to the ratio of wavelengths, the burst time is driven by X-band. In Ku-band, multiple looks of 50 m resolution are generated from each burst at the processing level.

Depending on the exact geometry, as well as the applied windowing function during processing, dwell times in the order of 35 ms are chosen, such that both concepts ensure the required resolution in azimuth. Table 7.5 summarises the worst-case azimuth resolutions, which occur at the maximum slant range, i.e. at an orbital altitude of 700 km in Phase-1 and 676 km in Phase-2. The reported values refer to a case without windowing, i.e. they show the optimum possible resolution with some margin to the required 50 m. This margin, which increases for decreasing slant ranges, can be used to optimise the sidelobes (i.e. Peak Side-Lobe Ratio and Integrated Side-Lobe Ratio) by applying appropriate windowing functions.

The range resolution is determined by the geometry and by the bandwidth of the transmitted chirp pulse. Both concepts define these bandwidths such that a ground-range resolution of better than 50 m is achieved at the driving near-range position on ground (Table 7.5).

Table 7.5. Worst-case ground resolutions without windowing function (required <50 m × 50 m).

| Geometric Resolution (m) | Concept A | | Concept B | |
|---|---|---|---|---|
| | X | Ku | X | Ku |
| Phase-1 | | | | |
| Azimuth | 47.3 | 47.3 | 48.3 | 48.4 |
| Ground Range | 47.3 | 47.3 | 48.9 | 49.3 |
| Phase-2 | | | | |
| Azimuth | 48.6 | 48.6 | 47.5 | 47.6 |
| Ground Range | 48.7 | 48.7 | 49.2 | 48.9 |
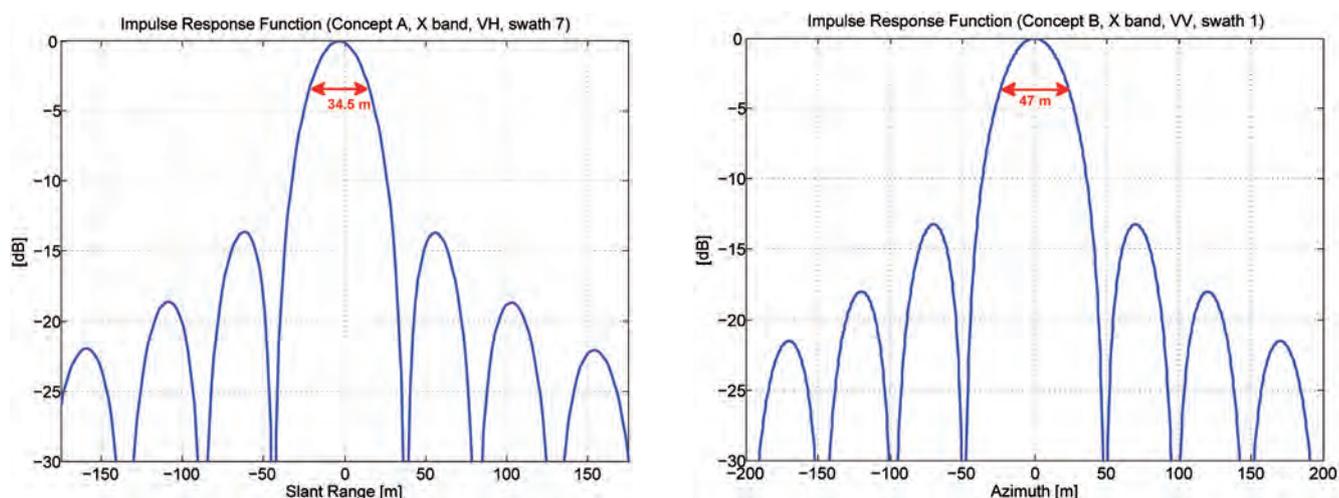
Figure 7.4. X-band IRF examples with windowing in slant range (left: Concept A, swath 7) and azimuth (right: Concept B, swath 1).

— Concept A transmits (single look) chirp pulses with a bandwidth of 4.3–4.8 MHz in Phase-1 and 4.1–4.5 MHz in Phase-2. The differences in bandwidth are due to the variation of incidence angle between the two mission phases.

— Concept B foresees bandwidths of 3.9–4.3 MHz in X-band (single look) and 4.7–5.2 MHz in Ku-band, to account for the 1.2 looks in range. In contrast to Concept A, the constant geometry ensures constant bandwidths for both mission phases.

Figure 7.4. shows examples for the IRF in the azimuth and slant-range directions, for different concepts and different swaths. The slant-range resolution of 34.5 m translates into a ground-range resolution as reported in Table 7.5. A geometric resolution better than 50 m is demonstrated for both directions.

## 7.2.3 Effective Number of Looks

As outlined in Subsection 5.4.3, multi-looking is an incoherent averaging of multiple weighted single-look images, which aims at decreasing the speckle. The multi-looking underlies a complex trade-off with respect to the weighting and combination of individual looks, which is briefly reported in the following. In addition, the azimuth antenna patterns have an impact and thus the optimum approach depends on the concept.

— Concept B has chosen simple pattern whitening as a weighting function. This minimises the required total Doppler bandwidth and consequently the associated azimuth beam shape losses, but the weighting itself can degrade the NESZ significantly. Furthermore, in the synchronised operation scheme

| ENL Concept A | | ENL Concept B | |
|---|---|---|---|
| X | Ku | X | Ku |
| VV | | | |
| ≥4.1 | ≥4.1 | ≥4.0 | ≥4.6 |
| VH | | | |
| ≥4.1 | ≥4.1 | ≥4.0 | ≥4.6 |

Table 7.6. Minimum ENL values.

127
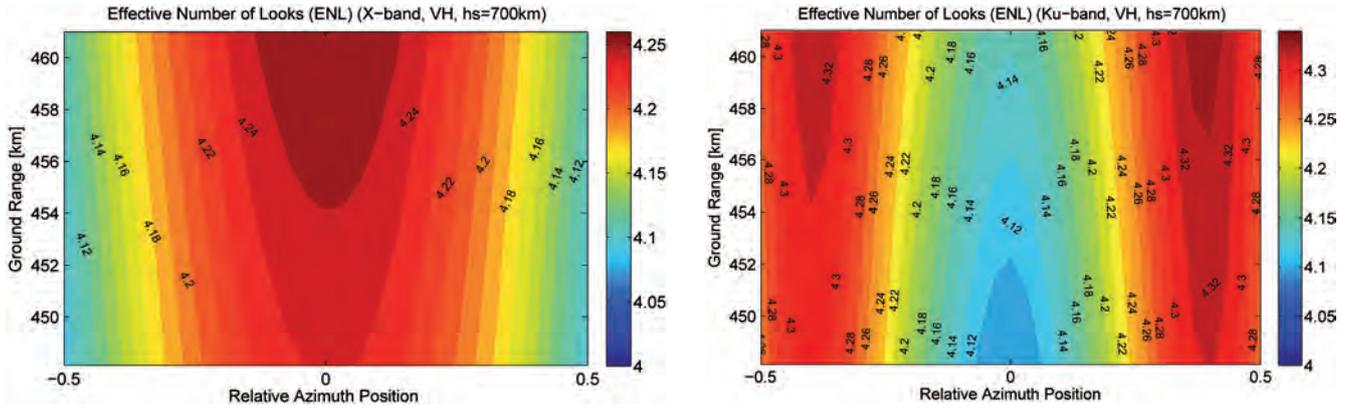
Figure 7.5. ENL examples for Concept A (700 km, sub-swath 1); Ku-band (left) and X-band (right).

of CoReH$_2$O, additional looks in the range dimension are needed for Ku-band, requiring an increased transmission bandwidth.

— Concept A employs a more complex weighting, which is optimised individually for each band and polarisation such that ENL >4 is achieved. This flexible weighting minimises the negative impact of the multi-look processing on the NESZ and avoids the need for additional looks in range. As a drawback, this approach requires more natural looks to be combined, which increases beam shape losses.

Both approaches ensure ENL ≥4, as summarised in Table 7.6. Notably, margins for azimuth resolution (see Table 7.5) represent a margin for ENL of the same order.

Figure 7.5 shows an example for the ENL achieved by Concept A at both frequencies and within sub-swath 1. Note that the ENL range colourbar starts at the required value to better visualise the margin with respect to the requirement.

The approach chosen by Concept B leads to a constant ENL characteristic across the swath.

## 7.2.4 Sensitivity – Noise Equivalent Sigma Zero

The sensitivity of the imaging system is quantified by the NESZ, which represents the target reflectivity that leads to a received signal level equal to the noise level. The main contributors to the sensitivity budget are:

— System losses in the RF hardware.

— Antenna pattern directivity (elevation and azimuth) and spread losses according to the distance between sensor and target.

— Losses from attenuation by the atmosphere, quantisation and processing.

Elevation pointing errors impact on the pattern directivity and, thus, affect the NESZ. For Concept A, a pointing error of about 18 mdeg (Root Mean Square (RMS)) leads to a worst-case degradation of NESZ around 0.31 dB. For Concept B, the worst case amounts to about 15 mdeg (RMS), translating into a NESZ degradation of 0.27 dB.

The average powers of the transmitted RF signals are 230 W (X-band) and 196 W (Ku-band) for Concept A and 310 W (X-band) and 380 W (Ku-band) for Concept B, respectively. The different power levels depend on various design and technology aspects, as explained in Subsection 5.4.3.
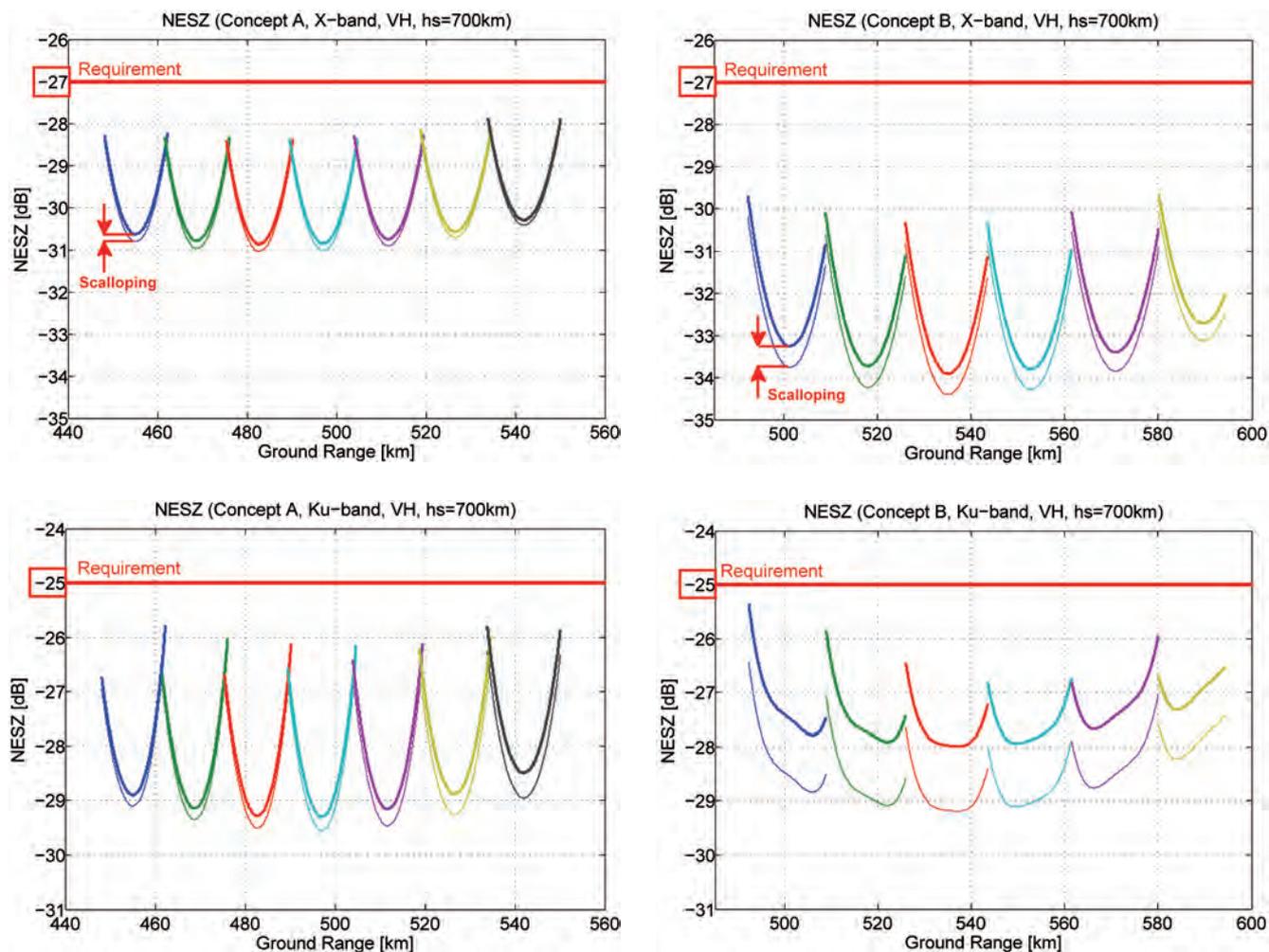
Figure 7.6. NESZ curves (VH, 700 km) for X-band (top) and Ku-band (bottom) for Concepts A (left) and B (right), showing all six or seven sub-swaths.

Figure 7.6 shows the NESZ achieved at the worst-case orbit altitude of 700 km, where thick and thin lines represent the variation owing to scalloping. Results are shown for VH polarization, where the required maximum values of −27 dB (X-band) and −25 dB (Ku-band) are far more stringent than those in VV, which are −23 dB (X-band) and −20 dB (Ku-band), respectively.

As shown in Table 7.7, for VH a margin of at least 0.8 dB is ensured in both bands for Concept A, while Concept B has a minimum margin of 0.3 dB in Ku-band and 2.0 dB in X-band. The NESZ for an altitude of 650 km is not critical for either concept; the requirement is met with 1 dB margin or more. The requirement for VV is met with a large margin of at least 4.9 dB in both concepts. Note that these results consider the worst-case elevation pointing errors.

Table 7.7. Worst-case NESZ for Phase-1 at 700 km altitude and Phase-2 at 650 km altitude.

| Worst-case NESZ | Concept A (dB) | | | | Concept B (dB) | | | |
|---|---|---|---|---|---|---|---|---|
| | X VV | X VH | Ku VV | Ku VH | X VV | X VH | Ku VV | Ku VH |
| Requirement | −23.0 | −27.0 | −20.0 | −25.0 | −23.0 | −27.0 | −20.0 | −25.0 |
| Phase-1 (700 km altitude) | −28.1 | −27.8 | −25.5 | −25.8 | −28.9 | −29.3 | −24.9 | −25.3 |
| Phase-2 (650 km altitude) | −28.6 | −28.3 | −26.0 | −26.2 | −29.7 | −30.3 | −25.8 | −26.1 |

129
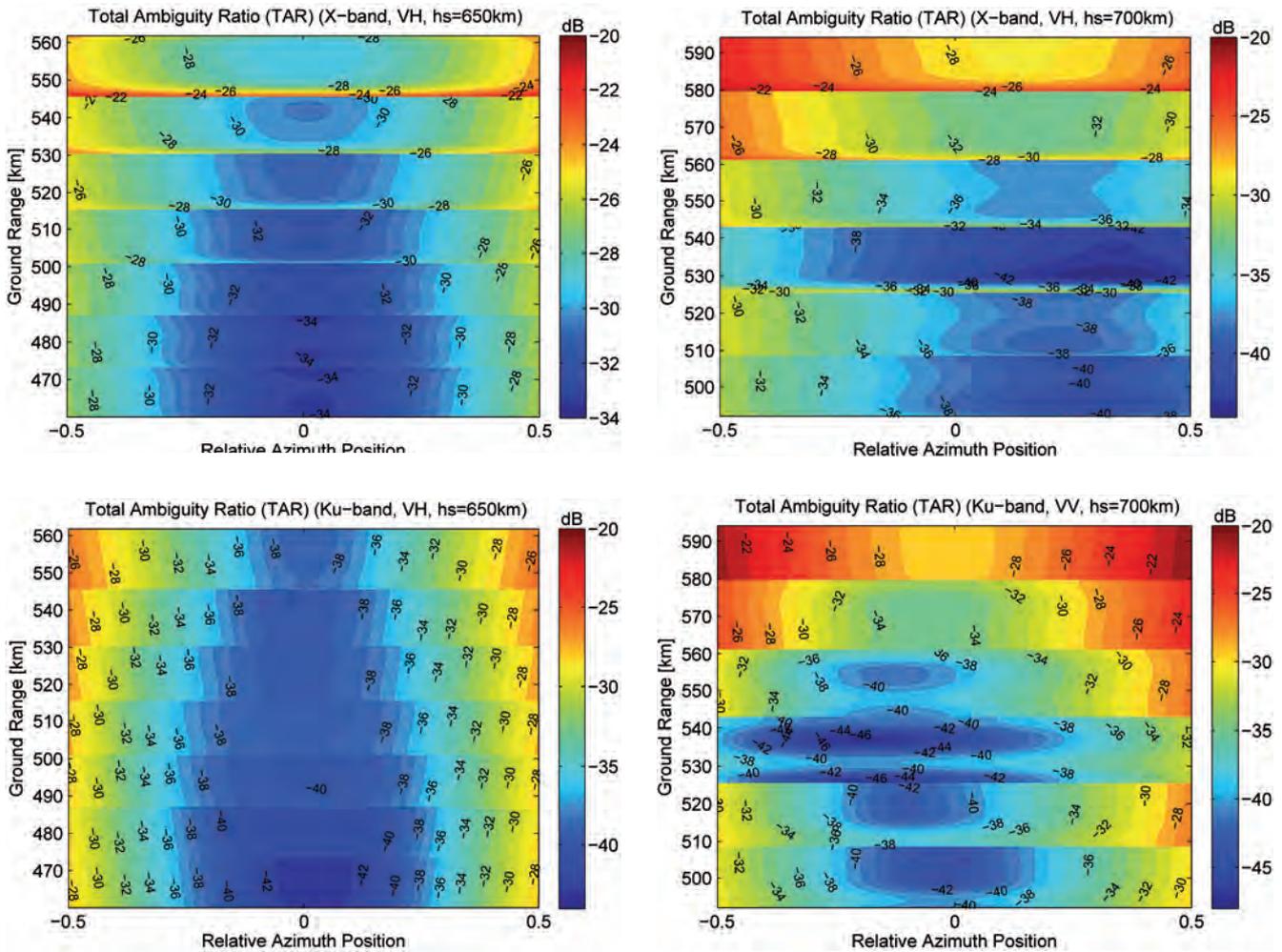
Figure 7.7. TAR curves for X-band (top) and Ku-band (bottom) for Concepts A (left) and B (right).

## 7.2.5 Ambiguity Suppression

The Total Ambiguity Ratio (TAR) is the ratio of summed azimuth and range ambiguous powers to signal power. The achievement of TAR performance underlies a complex trade-off, mainly with respect to the PRF and the antenna patterns in azimuth and elevation. Figure 7.7 illustrates the TAR for both concepts and both bands. The contour plots represent TAR vs. relative azimuth position and ground-range covering all sub-swaths. For Concept A, examples are shown for the lowest orbit altitude, which represents the worst case regarding TAR. For Concept B, examples are shown for the highest orbit altitude, which represents the worst case for TAR. Note that the TAR range colourbar starts at the required value of –20 dB, to better visualise the margin with respect to the requirement.

Table 7.8 summarises the worst-case TAR values, considering the impact of the maximum elevation pointing errors on range ambiguities.

Table 7.8. Worst-case TAR values (required: <–20 dB).

| Worst-case TAR | Concept A (dB) | | | | Concept B (dB) | | | |
|---|---|---|---|---|---|---|---|---|
| Frequency, Polarisation | X VV | X VH | Ku VV | Ku VH | X VV | X VH | Ku VV | Ku VH |
| Phase-1 (700 km altitude) | –24.3 | –24.3 | –27.7 | –28.2 | –20.3 | –20.1 | –20.3 | –20.9 |
| Phase-2 (650 km altitude) | –21.5 | –21.5 | –25.5 | –26.0 | –22.6 | –22.4 | –24.3 | –24.9 |

## 7.2.6 Radiometric Budgets

The two key performance parameters are radiometric stability and absolute radiometric bias. The radiometric stability represents the measurement uncertainty of the instrument. The main contributors and allocations to the budget are:

— Elevation pointing (knowledge) errors, which translate via the antenna pattern slope directly into a radiometric measurement uncertainty. This is a major contributor to the radiometric stability budget and the allocation to this error has a consequence for the pointing requirements. In the given example, an RMS pointing knowledge error of 18 mdeg or better is required and fulfilled.

— Uncertainties in the knowledge of the antenna pattern and the instrument characterisation; allocation to the latter impacts the required internal calibration accuracy. The chosen design of the internal calibration network meets the requirement.

— Other errors, such as contributions from processing or angular target location uncertainties, the latter originating mainly from the DEM quality.

The radiometric stability budget is presented in Table 7.9. The total is computed as the Root Square Sum (RSS) of the individual contributions. Concept B, which is based on a slightly different approach entailing a different allocation of errors, achieves a radiometric stability of 0.41 dB. The absolute radiometric bias ('accuracy') represents the total (absolute) uncertainty of any reflectivity measurement. The main contributors and allocations to the budget are:

— Radiometric stability, as reported above.

— External calibration accuracy, combining uncertainties of reference targets and their measurement. The allocation to the reference target impacts, for example, on the size of a corner reflector or the required accuracy of transponders.

— Dynamic range errors and atmospheric disturbances, assuming a worst case of 0.25 dB for Ku-band.

| Contributor/Allocation | Concept A (dB) |
| --- | --- |
| Elevation pointing errors (knowledge) | 0.31 |
| Target location error | 0.04 |
| Instrument and antenna pattern | 0.32 |
| Processing errors | 0.10 |
| Total (required <0.5 dB) | 0.47 |

Table 7.9. Radiometric stability budget (example Concept A).

| Contributor/Allocation | Concept A (dB) |
| --- | --- |
| Radiometric stability | 0.47 |
| External calibration accuracy | 0.57 |
| Dynamic range error | 0.20 |
| Atmosphere | 0.25 |
| Total (required <1 dB) | 0.83 |

Table 7.10. Absolute radiometric bias budget (example Concept A).

The absolute radiometric bias budget is presented in Table 7.10. The total is computed as the RSS of the individual contributions. Concept B shows an absolute radiometric bias of 0.87 dB. Hence, both concepts are compliant to the requirement.

## 7.2.7 Geometric Budgets

### 7.2.7.1 Geo-location

The required geo-location accuracy, expressed as the accuracy of any image pixel position relative to a pre-defined geo-referenced grid, is less than 50 m. This is met with comfortable margins, as the achieved geo-location accuracies are 33 m (Concept A) and 24 m (Concept B), respectively.

### 7.2.7.2 Co-registration

Spatial co-registration defines the relative position error between two corresponding pixels of any pair of Level-1b image products (i.e. any combination of VV, VH, Ku-band or X-band). The required accuracy of better than 20 m is met for both concepts with considerable margins.

### 7.2.7.3 Collocation

This requirement refers to the collocation of repeating observations of the same area and is required to be equal or better than 1 km (RMS). This turns into a requirement on the accuracy of the repeating orbits (ground track error), which defines the orbit control manoeuvres frequency, as described in Subsection 5.3.1. The impact of these manoeuvres on availability is also taken into account in the budget shown in Section 7.1.

## 7.2.8 Performance Summary

Table 7.11 presents a summary of the observation performance requirements at Level-1b together with the estimated performance of the two implementation concepts. The performance figures demonstrate that both system concepts ensure full compliance vs. all Level-1b requirements with margins.

Table 7.11. Main observing mission parameters at Level-1b: required and achieved worst-case performance.

| Parameter | | Requirement | | Concept A | | Concept B | |
|---|---|---|---|---|---|---|---|
| | | VV | VH | VV | VH | VV | VH |
| Sensitivity (NESZ) | X band | ≤−23 dB | ≤−27 dB | −28 dB | −27.8 dB | −28.9 dB | −29.3 dB |
| | Ku band | ≤−20 dB | ≤−25 dB | −25.5 dB | −25.8 dB | −24.9 dB | −25.3 dB |
| Ambiguity suppression (TAR) | | ≤−20 dB | | −21.5 dB | | −20.1 dB | |
| Geometric resolution (rg × az) | | ≤50 m × 50 m | | 48.6 m × 48.7 m | | 48.4 m × 49.2 m | |
| Effective Number of Looks | | ≥4 | | 4.1 | | 4.0 | |
| Swath width | | ≥100 km | | 101.4 km | | 100.1 km | |
| Incidence angle range | | 30–45° | | 36.1–45.0° | | 38.8–44.8° | |
| Radiometric stability | | ≤0.5 dB | | 0.47 dB | | 0.41 dB | |
| Absolute radiometric bias | | ≤1.0 dB | | 0.83 dB | | 0.87 dB | |
| Geo-location | | <50 m | | 33 m | | 24 m | |
| Co-registration | | ≤20 m | | <<20 m | | 2.33 m | |
| Collocation | | ≤1 km | | <1 km | | <1 km | |

Consequently, both concepts represent viable solutions to achieve the mission goals of CoReH$_2$O.

## 7.3   End-to-end Mission Performance Simulator

As part of CoReH$_2$O Phase-A activities, an End-to-End Simulator (E2ES) was designed and developed to predict end-to-end mission performance. This simulator models the complete chain starting from the observed scene, then simulates the response of the observing system at Level-1b and finally generates the retrieved Level-2 output product. The simulator provides an end-to-end simulation capability so that an assessment can be made as to whether the science goals and mission requirements can be met. Furthermore, the simulator is able to support the following functions:

— Evaluation of the performance of Level-1 and Level-2 simulated data products.

— Assessment of the impact of the most relevant error sources on the mission products.

— Assessment of data correction and retrieval algorithms.

— Assessment of the impacts of geophysical conditions.

— Statistical analyses using the above functions.

The CoReH$_2$O E2ES is able to generate all the simulated mission products both error-free and with all or some errors applied. It was first used to demonstrate the consistency of the observation concept and processing chain and to check the correct integration of the different modules. Secondly, it was used to provide illustrations of the mission output, notably with respect to spatial aspects of a realistic scene, complementing the results in Section 7.4. Further experiments with the E2ES are underway that analyse the influence of individual (instrument) error sources on the Level-1b and Level-2 products.

### 7.3.1 End-to-end Architecture

Figure 7.8 shows the simulator architecture. It is composed of five main modules embedded into the OPENSF (Deimos Space, 2009) software simulator framework. The modules are described below.

The scene generation module includes the scene model and the interaction model. The scene model describes the geophysical parameters of the ground scene that is being imaged and the interaction model simulates the physical parameter (reflectivity) that is detected by the instrument. The scene generation module generates a 2D scene/image, which can include topography by using a DEM.

Two models account for the space segment, the geometry module and the observing system simulator. The geometry module includes the orbit and attitude model, describing sensor geometry and attitude parameters. It models the antenna pointing and the mission observation geometry, and provides the transformations between the coordinate systems used by different modules. The observing system simulator module consists of the IRF module, which computes the Instrument Response Function, and the error/sensitivity module, which simulates errors in line with the instrument performance model and requirements. The IRF module includes contributions from multiplicative noise, additive noise, ambiguities in range and azimuth, modulation owing to the antenna pattern, and the scalloping effect. The error/sensitivity module simulates the instrument absolute radiometric bias, radiometric stability,

Figure 7.8. Simulator architecture showing modules and interfaces. (Aresys)
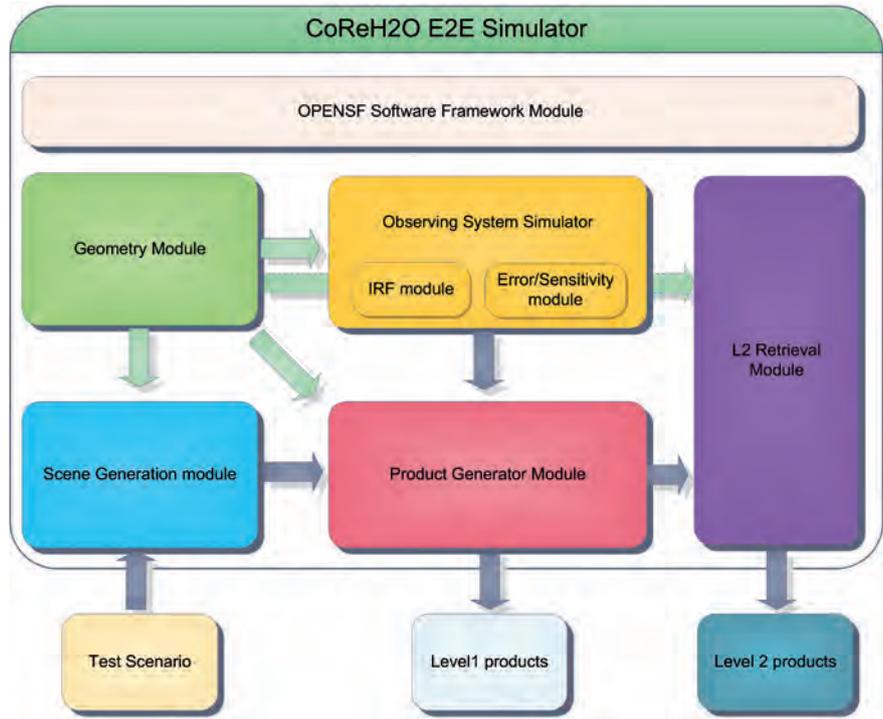
phase stability, channel imbalance, and polarisation cross-talk estimation. Two observing system simulator modules representing Concept A and Concept B have been implemented in the E2ES.

The simulated Level-1b products are generated with the product generator module, which combines the IRF with the $\sigma^0$ backscatter intensity data and applies the errors. SWE and the other main Level-2 products are then obtained by applying the retrieval algorithm to Level-1b products – as implemented in the Level-2 retrieval module, which is the same as used in Section 7.4.

## 7.3.2 End-to-end Performance Results

The E2ES tests compare the Level-2 retrieval module output with the original input test scene. For this purpose, example input files to the E2ES have been defined over an alpine area, see Fig. 7.9.

In a first step, the scene generation module generates backscatter intensity images with dynamics linked to the input scene for Ku-band and X-band at co-(VV) and cross-polarisation (VH). The four resulting maps on flat topography are shown in Fig. 7.10.

In the next step, the E2ES translates these geophysical maps into four radar images, representing the four channels of a CoReH$_2$O acquisition. The generated Level-1b radar images take into account the characteristics of the radar instrument such as observation geometry (e.g. incidence angles) and



Figure 7.9. Optical map of the imaged alpine area (Google Maps) and SWE input map in m.
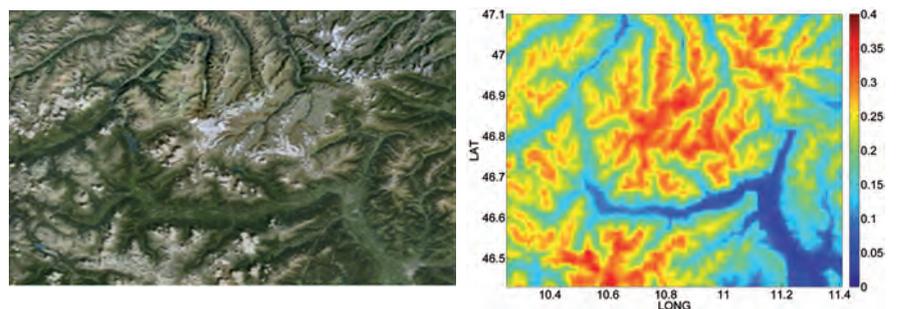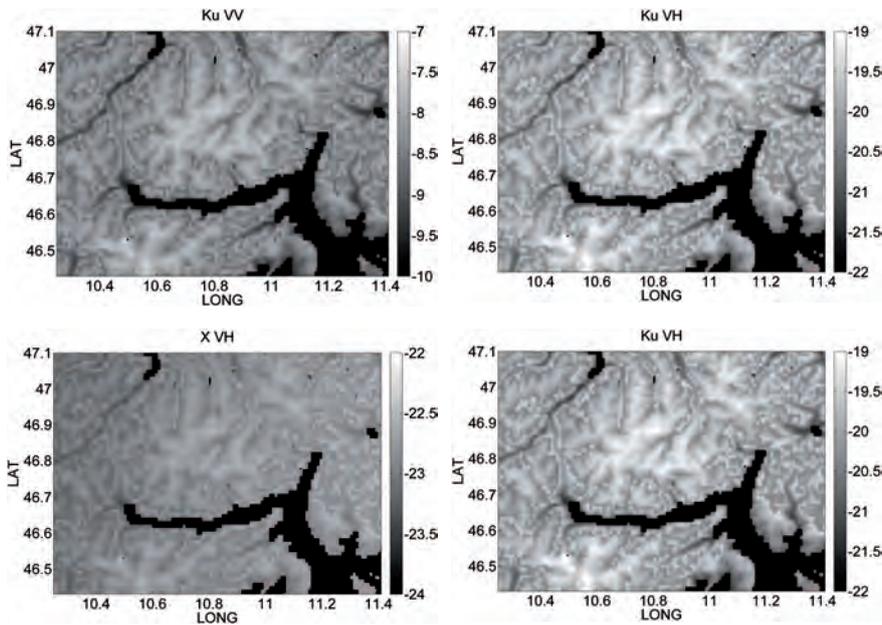
Figure 7.10. Backscatter intensity images in dB for the four channels as generated by the scene generation module.

represent the instrument performance in terms of geometric resolution, radiometric performance, noise levels, and ambiguities.

The Level-1b images are input to the Level-2 retrieval module that generates the Level-2 output with the baseline retrieval algorithm described in Chapter 6. By means of the land-cover data, the land surface is separated into different areas. For the areas with open land and low vegetation, a segmentation into dry snow, wet snow and snow-free surfaces is performed. Maps of dry snow and melting snow areas are a basic Level-2 product and an example output for dry snow is shown in Fig. 7.11 (middle plot). When comparing the retrieved product with the reference input map (left plot in Fig. 7.11), the performance is in line with the snow extent requirement and the results obtained in Section 7.4. The incorrectly classified pixels are mainly located at the edges between dry snow and wet snow areas and corresponding to shallow snow areas. The snow extent product quality did not change significantly when using the observation system modules of Concept A or Concept B.

Under nominal imaging conditions, i.e. all design parameters and all instrument errors applied, Level-2 SWE maps as shown in Fig. 7.12 are obtained. The SWE maps are generated with Level-1b characteristics of one of the observing system modules. The results assume that all configuration input is readily available and the regularisation values are unbiased. The SWE maps compare well with the reference SWE map (Fig. 7.9 right) though small

Figure 7.11. Level-2 snow extent/segmentation product for dry snow. (Aresys)



135
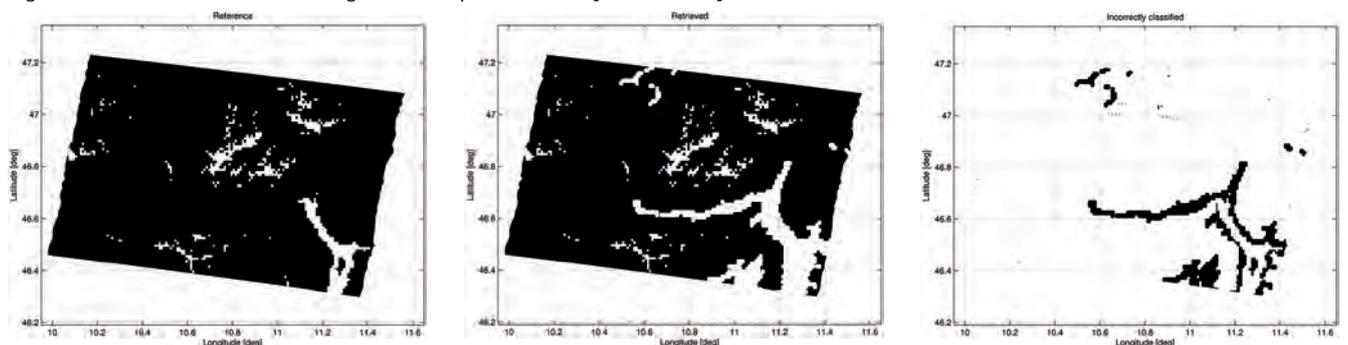
Figure 7.12. Level-2 SWE output product in m based on Level-1b products from one of the two observing system simulators.
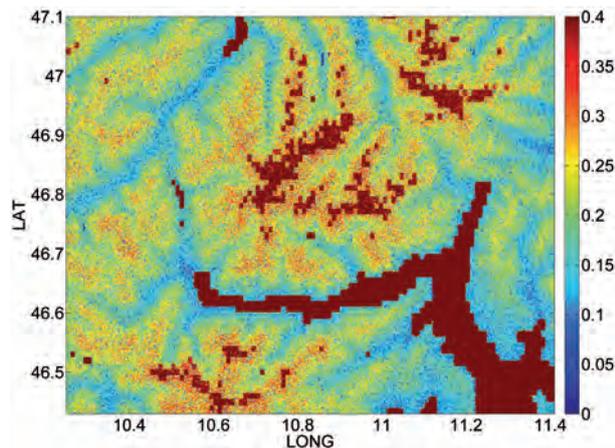


Figure 7.13. Accuracy of Level-2 SWE output based on the observing system simulator of Concept B.
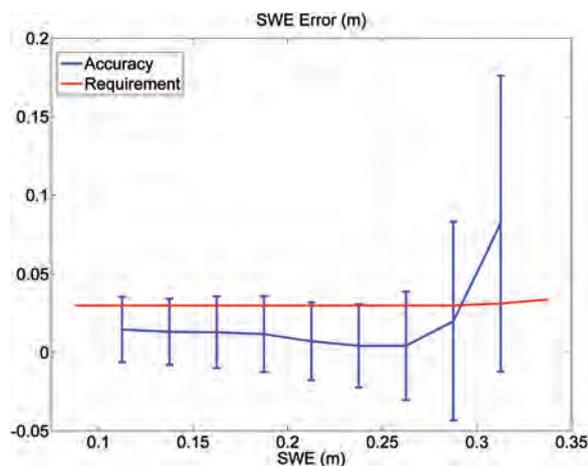
differences between the two solutions can be observed owing to different performance at Level-1b.

The accuracy of the SWE maps over the considered scene is summarised in Fig. 7.13, showing the mean error and standard deviations around the mean binned into nine classes. The requirement can be met for most of the alpine snow regime except for deep snow (≥300 mm). In this example, smaller grain sizes at deep snow lead to larger SWE errors when compared to the requirement.

In summary, the end-to-end simulations enable the validation of the overall processing concept, the assessment of mission performance and allow to study the impact of instrument performance on retrieval performance. In the example, all three Level-2 products can be obtained with an accuracy and resolution that meet the requirements except for some snow conditions further elaborated in Section 7.4. Further work with the E2ES is ongoing to investigate the influence of individual (instrument) error sources on the Level-1b and Level-2 products.

## 7.4  Mission Performance at Level-2

The performance estimation for Level-2 product retrievals has been carried out using simulated and experimental backscatter data. The retrieval performance tests focussed on primary geophysical parameters, to be retrieved from the Level-1b products (calibrated, geocoded, terrain-corrected backscatter data); namely, snow area extent (dry and melting snow areas), SWE on land surfaces and snow accumulation on glaciers. In addition, CoReH₂O data show great potential for retrieving several other parameters of the land cryosphere and sea ice (Table 4.1). Work on retrieval of several of these parameters is ongoing.

## 7.4.1 Performance Estimation Based on Simulated Data

The objective of performance analysis with simulated data is to analyse and validate the accuracy of retrieved Level-2 products when the input data to the retrievals match the main technical specifications of the system as developed during the Phase-A studies (Chapter 5). Simulated data for retrieval input have been produced with a Synthetic Scene Generator (SSG) (Rott et al., 2011). The SSG uses the semi-empirical RT (sRT) forward model (Chapter 6) to compute backscatter values at X- and Ku-band for snow-free surfaces and snow covered terrain. Physical properties of the background medium (soil) and of the snowpack can be specified. The SSG computes local incidence angles for specified observation geometries, simulates $\sigma^0$ values in X- and Ku-band according to the sRT backscatter model, allows for compensation of atmospheric attenuation and generates single-look complex synthetic SAR images matching slant-range geometry and system parameters of the CoReH$_2$O mission, including speckle and noise. In a second step, multi-looking is performed and the backscatter data are transformed to ground-range map projection as input for retrievals. The SSG is a precursor to the E2ES with similar functionality and the same options for input and output. The main difference is a simplified representation of sensor performance characteristics in the Observing System Simulator (OSS), in which some minor technical aspects (e.g. ambiguities) are not taken into account in the SSG. The procedure for evaluating the retrieval performance includes the following steps:

— Generation of CoReH$_2$O backscatter data by means of the SSG as input for the retrieval algorithm. As input to the tests shown here, homogenous scenes of 260 × 260 Level-1b pixels were generated.

— Retrieval of Level-2 products with the inversion algorithm (Chapter 6).

— Assessment of the retrieval results.

In the first part of the retrieval processing, the segmentation is performed based on backscatter values to separate the classes of wet snow, dry snow and snow-free land (Fig. 6.1). The output of this step is the Level-2 product of snow extent separated into dry and wet snow classes. The performance of the segmentation algorithm was tested using simulated data as input. Very good performance (classification error <1 % of area) is achieved for separating wet snow from dry snow and snow-free surfaces, due to high contrast in backscatter. The tests were performed for snow with liquid water content of 1%, 3% and 5% by volume.

Test results for separation of dry snow vs. snow-free ground show a spread in performance, depending on the state of the snowpack. Thin snow cover
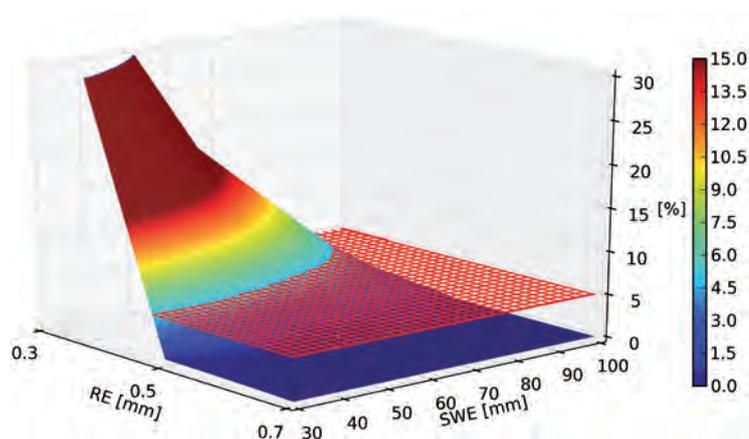


Figure 7.14. Performance of segmentation for dry snow area. Percentage of correctly classified pixels. The red grid indicates the required statistical threshold (5% of area) for snow classification. (ENVEO)

does not meet the requirement in terms of classification of dry snow area for small grains (Fig. 7.14). This agrees with observations of passive microwave signals that also show low contrast for thin snow. The use of optical satellite images, complementing microwave data, can compensate for this deficiency (Tait et al., 2000). Options for improving the classification results include the application of noise reduction filters optimised for 2D SAR image segmentation (e.g. Jarabo-Amores, 2011) and synergy with optical snow-mapping products as, for example, those available from the ESA GlobSnow project.

Tests on the retrieval of snow extent have also been performed with the E2ES. An example is shown in Chapter 7.4, where the classification accuracy is high for the main parts of the snow covered area, and declines in the boundary zone featuring shallow snowpack.

Here results of the performance analysis for SWE retrieval with simulated data are addressed. As input, the tests backscatter data were simulated with the SSG matching the sensor specifications described in Chapter 5. The effects of the following parameters on the performance of retrieved SWE were investigated (Rott et al., 2011):

— Atmospheric transmittance (for correction of signal propagation losses).

— Configuration parameters of the snowpack (snow density, snow temperature, roughness of snow/air interface).

— Regularisation parameters: mean and standard deviation of *a priori* values of effective grain radius, Re, and of SWE.

— State of background medium (tests were performed for several soil classes characterised by wetness, temperature, surface roughness; in case of glaciers for frozen firn and ice with different scattering properties).

— For forested areas: cover fraction and tree height.

— Local incidence angle of the radar beam.

The test results point out that, for the given sensor configuration, the regularisation parameters are of main concern for retrieval performance. Examples of these tests are shown below. Atmospheric propagation has a small effect and attenuation losses can be well corrected (Chapter 4). Tests on impact of local incidence angle (e.g. on mountain slopes) show similar performance for the angular range of 20–70°. Configuration parameters on snow properties can be obtained with the required accuracy from climatological databases or numerical meteorological models.

In addition to the tests with Level-1b input data matching the specifications of CoReH$_2$O SAR listed above, tests for different sensor specifications (regarding ENL and NESZ) were performed. These tests show deterioration of retrieval performance for cases when ENL or NESZ are relaxed vs. the selected sensor configuration, confirming the choice of the sensor configuration.

The majority of retrieval tests were performed for Level-2 products of 200 m × 200 m grid size. This corresponds to ENL ≥64 for input backscatter data of the sensor as defined in Phase-A. The ENL numbers show some variation with the incidence angle and NESZ. For forested areas and glaciers, tests were also performed for 500 m × 500 m grid size. The test examples shown here refer to an incidence angle of 40°.

In the tests the selected settings for the free parameters (SWE, Re) are spanning a large percentage of the expected range of the global seasonal snow cover: 100 mm ≤SWE ≤500 mm; 0.3 mm ≤Re ≤0.7 mm.

To indicate the expected range of SWE for seasonal snow cover, Fig. 7.15 shows the distribution of SWE values measured at snow courses spreading
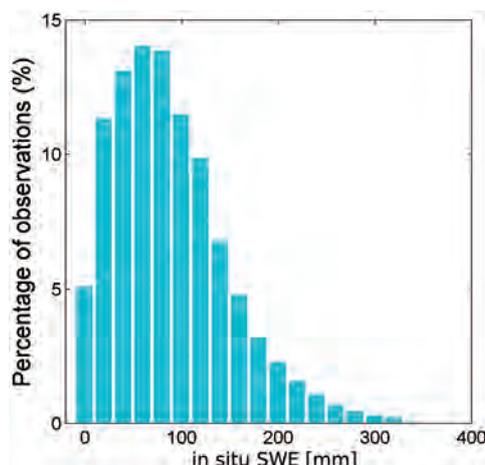
Figure 7.15. Distribution of SWE values measured in 1979–2000 over the former Soviet Union and Russia (after Takala et al., 2011).

over the former Soviet Union and Russia. The snow surveys were made from 1979 to 2000 bi-monthly at 1264 sites (Takala et al., 2011). The SWE maximum in winter reaches values >300 mm only at very few sites. Nevertheless, in the tests the selected range for SWE is extended up to 500 mm to cover also deep snowpacks. For various cases tests were also performed for SWE <100 mm (e.g. Fig. 7.16). These are less challenging than for deeper snow, as the observational requirement (±30 mm) translates to relaxed requirement in percentage relative to the mean value.

Numerical values for effective grain size are available from experimental data at several test sites, obtained by inverting backscatter measurements in terms of Re. Inversions of SnowScat measurements with respect to effective grain size, performed at Sodankylä (northern Finland) using the sRT model, show mean values Re = 0.5 mm, with standard deviation ±0.05 mm (Lemmetyinen et al., 2012b). Inversions of PolScat Ku-band backscatter measurements at CLPX test sites in Colorado and on the Alaska North Slope yield Re values between 0.45 mm for mountain snowpack and 0.6 mm for tundra snow (ESA, SP-1313/3). Inversions of QuikScat Ku-band backscatter data over the extended Alaska North Slope region in different years show Re values of 0.4–0.7 mm; the higher values are observed in the foothills region with shallow snow (Lemmetyinen et al., 2012a).

Figure 7.16 shows an example for output statistics with the basic test configuration. The input data to the retrieval with the SSG match the sensor specifications of CoReH$_2$O. The mean value of the regularisation parameters (SWE, Re) (second term on right side of retrieval cost function, Chapter 6) is assumed to be equal to the value of these parameters for the generation of
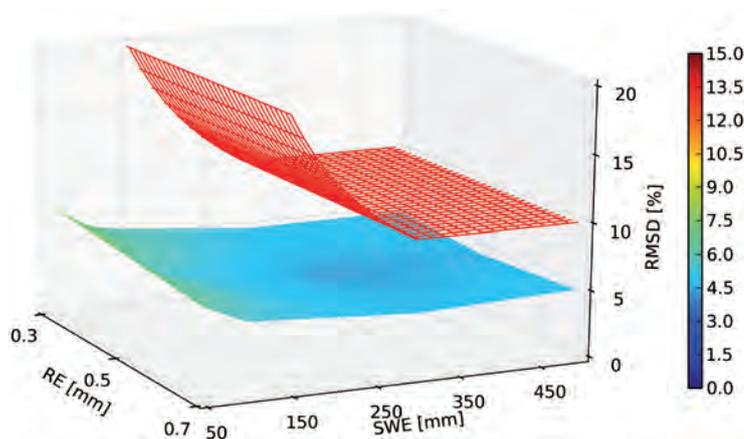


Figure 7.16. Relative root mean square difference (RMSD relative to the mean) between retrieved and true value of SWE for open land, basic test. RE: effective grain radius of snow; SWE: snow water equivalent. The red grid indicates the benchmark for the SWE product (±30 mm for SWE ≤300 mm, ±10% for SWE >300 mm). (ENVEO)

retrieval input data, with assumed standard deviations of 50 % for SWE and 0.1 mm for Re. Interannual statistics of snow depth (>50-year time series) at stations in the former Soviet Union show standard deviations for individual winter months within 50% of the mean (Kripalani & Kulkarini, 1999). Similar interannual variability can be assumed for SWE. In Fig. 7.16 the Root Mean Square Difference (RMSD) between the expected SWE value (corresponding to the value used for simulation of input data) and the inversion result is shown. The retrieval output is compliant with observation requirements for the SWE product (±30 mm for SWE ≤300 mm, ±10% for SWE >300 mm) with significant margin to the benchmark. For small grains the mean value of RMSD values is slightly higher than for medium-sized and large grains because of the smaller dynamic range of the backscatter signal in respect to SWE. Differences between small and large grains are more pronounced in the individual pixel statistics where variability is higher for small grain size retrievals.

Examples of test runs to check effects of a bias in regularisation parameters on retrieval performance are shown in Figs. 7.17 and 7.18. The test for Re, assuming a bias of 15% for the *a priori* mean value used in the regularisation, shows that for small and medium-sized grains the benchmark requirements are still met, but are slightly exceeded for the largest grains (Fig. 7.17). This test suggests that an accuracy better than 15% for Re should be achieved for input to the regularisation.

An example for demonstrating the improvement of retrieved SWE compared to the *a priori* value (used for regularisation) is shown in Fig. 7.18. In this test, a bias of 50% is assumed for the mean value of SWE used in the regularisation,



Figure 7.17. Relative root mean square difference (RMSD relative to the mean) between retrieved and true values of SWE for open land. 15% bias for the regularisation parameter Re (mean value) is assumed. (ENVEO)
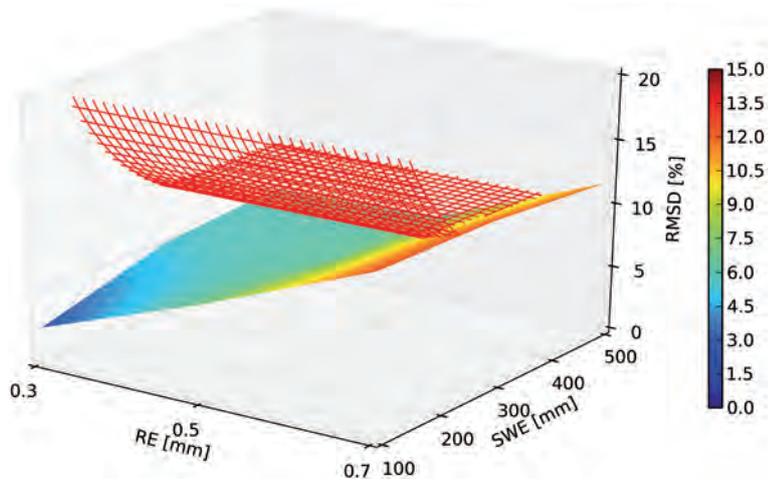


Figure 7.18. Impact of measurements for SWE retrieval on open land. Black grid: *a priori* estimate of SWE (assuming a bias of 50% for the mean value). Coloured ramp: Retrieved SWE. (ENVEO)
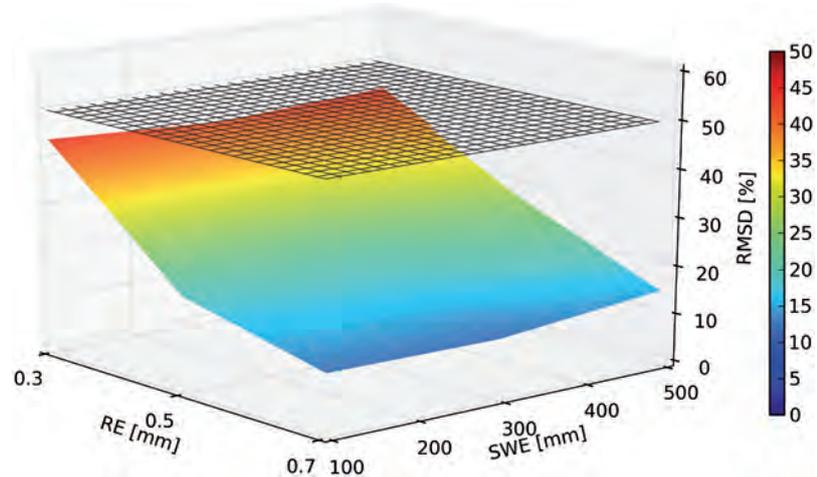
and an unbiased value for grain size. For small grain sizes the impact of the measurements only amounts to a few percent, whereas for medium and large grains major improvement is achieved.

For forested areas the SWE retrieval performance in general deteriorates compared to open land, because trees almost completely hide the signal of snow-covered ground. Therefore, SWE retrieval is feasible only in open forests where part of the radar signal illuminates snow-covered ground directly. Sensitivity studies based on forward simulations show that SWE retrievals are feasible in case of boreal forest for cover density smaller than about 30% (Rott et al., 2011). Because of the reduced dynamic sensitivity of the snow backscatter signal in forested areas, the statistical uncertainty of retrieved SWE is higher than on open land.

Performance analyses for SWE retrievals in open forest showed that, for the 200 m × 200 m SWE product, the threshold requirements are, in many cases, exceeded for small grains. The performance can be significantly improved by selecting larger product size, as shown by retrievals for the 500 m SWE product. This corresponds to a significant reduction of speckle for the corresponding input data (ENL≈400). For the example in Fig. 7.19, the standard settings for snow parameters, a forest cover density of 20% for forward backscatter modelling and of 30% for the retrieval are assumed, in order to check the impact of uncertainty in forest cover density. The Level-2 product grid size of 500 m corresponds to global products (Table 4.1), and also matches better the grid size of global forest cover data (500 m) that are used as auxiliary information.

The retrieval of the mass of winter snow (SWE) accumulation on glaciers relies on the contrast of the scattering albedo of fine grained winter snow vs. the high background signal of frozen firn or glacier ice (see backscatter signal in Fig. 4.9). An increase of SWE results in a decrease of the observed backscatter coefficient. The relative dynamic range of the signal is smaller than for snow accumulating on open land. Segmentation, based on backscatter data of the autumn period, is performed to identify the percolation zones and glacier ice zones for which the snow-mass retrievals are carried out (Rott et al., 2011). Due to reduced temperature gradients in the snowpack on glaciers compared to ice-free land surfaces, the effective radius of snow grains is rather small. Inversions of satellite-borne Ku-band scatterometer data and 18 GHz microwave of the percolation zone of Greenland, using the sRT model, show values for effective grain radius in the range 0.2–0.3 mm (Lemmetyinen et al., 2011). On the other hand, glaciers tend to form in regions of substantial snow accumulation, in general, implying larger SWE values than for the seasonal winter snow on land (Oerlemans, 2001). Therefore the following range for
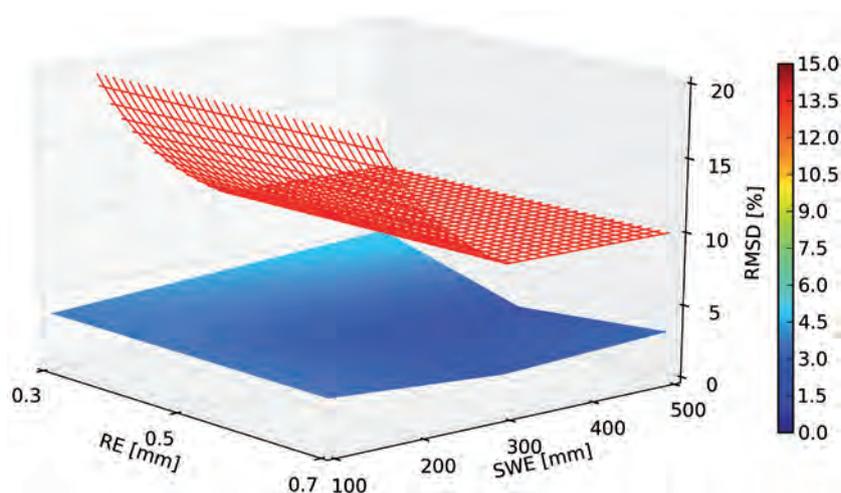


Figure 7.19. Relative root mean square difference (RMSD relative to the mean) between retrieved and true values of SWE for open forest, assuming 20% fractional cover for backscatter simulation (retrieval input data), 30% fractional cover fractional for SWE retrieval. Re: effective grain radius of snow; SWE: snow water equivalent. The red grid indicates the benchmark for the SWE product. Product grid size 500 m × 500 m. (ENVEO)

Figure 7.20. Relative root mean square difference (RMSD relative to the mean) between retrieved and true value of SWE for winter snow accumulation on glaciers (percolation zone). The red grid indicates the benchmark for the snow accumulation product (10% of winter maximum). Product grid size 500 m × 500 m. (ENVEO)
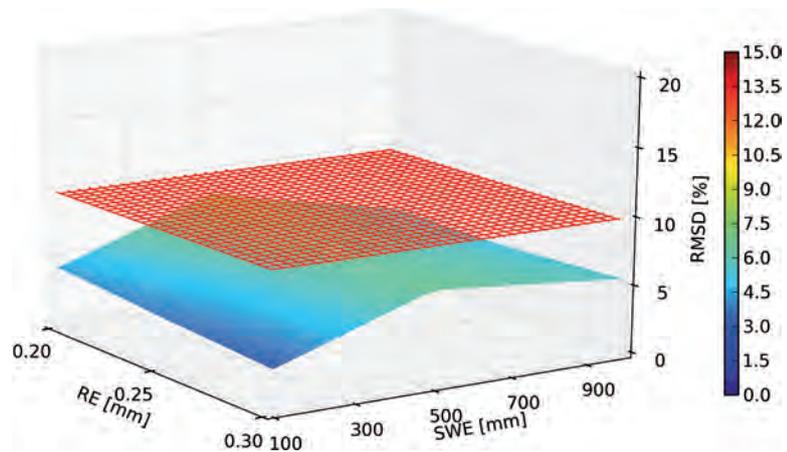
the free variables was selected for performance tests with SWE between 100–1000 mm, and Re (grain radius) between 0.2–0.3 mm (Fig. 7.20).

Retrieval accuracy for the 200 m × 200 m SWE product of winter snow accumulation on glaciers does not fully comply with the threshold requirement. The performance is significantly improved by increasing the grid size of the product, as the retrieval values for the 500 m SWE product show (Fig. 7.7), suggesting the use 500 m grid size as default.

The performance analysis with simulated data, complemented by tests with experimental data (Subsection 7.4.2), provides information on accuracy requirements for configuration parameters and *a priori* estimates of free variables to be obtained from auxiliary data sources. These requirements vary significantly with the snowpack state, in particular with the grain size. Table 7.12 indicates typical requirements in auxiliary information for snowpacks with medium-sized grains (Re≈0.5 mm). Information on snow density can be obtained from statistical data and numerical models. Daily values of bulk snow density and snowpack temperature are operationally delivered by land surface models of GCMs (e.g. Dutra et al., 2011) and regional meteorological forecast models. Sturm et al. (2010) report bulk snow-density data for main snow classes based on a set of 25 688 depth-density-SWE data collected in the US, Canada, and Switzerland. The values range from 217 kg m⁻³ (mean) ±56 kg m⁻³ (standard deviation) for taiga snow to 335 kg m⁻³ ±86 kg m⁻³ for alpine snow.

Table 7.12. Requirements for configuration parameters, *a priori* estimates of free variables, and auxiliary data needed as input to the Level-2 processing line.

| Task in processing | Parameter | Accuracy /Comment |
|---|---|---|
| Configuration parameter | Snow density (mean) | ±50 kg m⁻³ |
| | Snow temperature (mean) | ±5° |
| | RMS roughness of snow/air interface | Very small impact; use of mean value for dry snow (3 mm) proposed |
| Regularisation | Mean value of Re | 15% of mean value |
| | Mean value of SWE | 50% of mean value |
| Forest cover mask | Fractional cover | 10% |
| Background signal | σ⁰ snow-free surface | 0.5 dB, from pre-snowfall time series measured by CoReH₂O SAR |
| DEM (geocoding) | Surface topography | Raster ≤3 arcsec (90 m), vertical accuracy ±10 m. For geocoding (Level-1b processing) and retrieval |
| Atmospheric correction | Total atmospheric transmission coefficient τ | τ ≤0.01 (linear scale) |

In addition to the snowpack parameters required as input to the cost function, there are several other auxiliary data required in support of processing Level 1b data and for segmentation. Digital elevation data are needed for geocoding. A suitable global DEM database is available (Chapter 6). A by-product of geocoding is a map of local incidence angle, which is used in the retrieval. In mountain areas SAR data from both the ascending and descending orbits are acquired so that locally the optimum incidence angle can be selected. Computation of atmospheric transmission, based on numerical meteorological data matches the requirement for correcting atmospheric propagation losses (error for transmission losses ≤0.1 dB) (Chapters 4 and 6).

### 7.4.2 Performance Analysis based on Experimental Data

Backscatter time series were measured in Sodankylä during the NoSREx field experiment at Ku-band and X-band frequencies with the ground-based SnowScat system. SnowScat was mounted on a tower and measured snow in a clearing within boreal forest. Measurement scans covered a range of incidence and azimuth angles. A continuous backscatter time series is available through winter 2010–11 (Fig. 7.21). In addition to point measurements, there are two datasets of Ku- and X-band backscatter images, acquired by SnowSAR in the region of Sodankylä, respectively by PolScat and TerraSAR-X on the North Slope of Alaska (ESA, SP-1313/3).

Figure 7.21 shows the time series of X-band (10.2 GHz) and Ku-band (16.6 GHz), VV and VH polarised backscatter coefficients, measured at 40° incidence angle in winter 2010–11 (mean values of $\sigma^0$ measured at 13 azimuth angles). After soil melt/freeze events during October, reflected in temporal variations of $\sigma^0$, a shallow snow layer fell in November. Between 10 November and end of February, the air temperature stayed below 0°C. In March, three short melt events occurred, evident as small dips in the backscatter time series. Snow accumulation during the winter months is reflected in a gradual increase of backscatter in the Ku-band channels. In X-band the signal shows some decrease in the early snow season related to the freezing of soil. Later on, the X-band VH signal backscatter increases by 1.5 dB, and the co-polarised signal by 0.5 dB.

For the interpretation of data and validation of retrieved SWE *in situ* observations of snow, soil and meteorological parameters were made. Daily SWE values were obtained from a recording Gamma-Wave Instrument (GWI), and SWE was measured in snow pits at roughly weekly intervals. The SWE retrievals in Fig. 7.22 are based on the SnowScat measurements shown in Fig. 7.21. A single *a priori* value (Re=0.5 mm) is used for effective grain radius in the regularisation functional for the full time series. *A priori* estimate SWE is not employed in the regularisation. This allows the impact of backscatter measurements to be checked without any pre-setting for SWE. Using SWE for
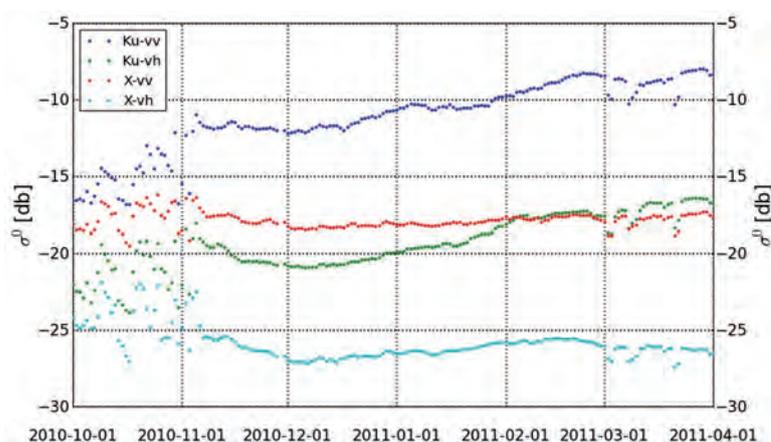


Figure 7.21. Daily averages of X- and Ku-band, VV- and VH-polarised backscatter coefficients $\sigma^0$ measured by SnowScat at 40° incidence angle during the NoSREx campaign 2010–11. The variation of $\sigma^0$ during October is related to melt-freeze cycles of soil. Dips in $\sigma^0$ on several days in March are caused by temporary melt of the snow surface. (ENVEO)

Figure 7.22. Daily SWE values retrieved by inversion of SnowScat measurements made in Sodankylä, Finland, using two different values for $\sigma^0$ of the background medium. Black: background $\sigma^0$ from mid-October 2010 (frozen soil). Red: background $\sigma^0$ from 1 December 2010 (frozen soil with shallow snow). Blue: *in situ* measurements of SWE (Gamma Wave Instrument). Green: snow pit measurements. The bars indicate the observational requirement for SWE (±30 mm) assuming snow pit data as reference. (ENVEO)
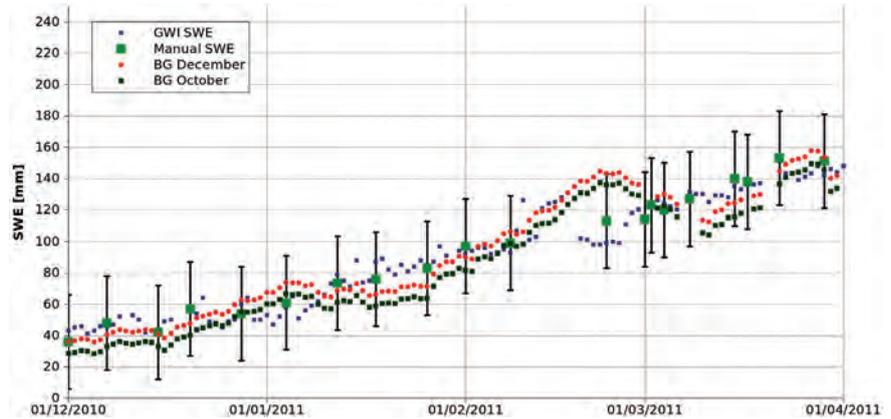
regularisation for the winter time series would require the re-adjustment of the *a priori* values of SWE sequentially during the season; tests applying this procedure produce similar results (Rott et al., 2011).

To check the sensitivity of retrievals to backscatter values of the background medium, two different cases have been analysed (Fig. 7.22). The retrieved SWE values show a parallel shift for the two background values, either taken from $\sigma^0$ measurements in mid-October (bare frozen soil) or from 1 December (frozen soil covered by shallow snow). Both retrievals fit the observational requirement for SWE (specified as standard deviation of ±30 mm) for the whole period. For the October background, the mean SWE value shows a bias of −6.6 mm and standard error of estimate (referring to the snow pit data) of 13.0 mm, for the 1 December background the corresponding values are +2.5 mm and 11.4 mm. For this dataset the differences are not significant, but it has to be pointed out that the date for selection of the background signal may affect the retrieval results.

In order to validate the retrieval algorithms for CoReH$_2$O, a polarimetric airborne SAR (SnowSAR) operating at central frequencies of 9.6 GHz (X-band) and 17.2 GHz (Ku-band) was developed for ESA (Meta et al., 2011). SnowSAR has been designed for operation on a small aircraft, with a typical operating altitude of 1600 m above ground, resulting in a swath width of 400–500 m. Over snow-covered areas SnowSAR was first deployed on 15 March 2011 in the Sodankylä region, when four swathes were acquired. Intensive campaign activities with SnowSAR were performed in winter 2011–12; complete processing of SAR data from this campaign is still in progress. Here we show the initial analysis of the March 2011 data.

Figure 7.23 shows a SWE map, retrieved from two SnowSAR swathes that were acquired in parallel with some overlap. Because SnowSAR was not yet available in the 2010 pre-snowfall period or early snow season, the background backscatter map for the retrieval had to be simulated. For X-band this was achieved by adjusting the background backscatter map of 15 March 2011 assuming a small temporal change of backscatter as observed by SnowScat. The Ku-band early snow season backscatter map was deduced from the X-band backscatter map, taking into account the frequency dependence for rough surfaces using the Oh surface scatter model. For regularisation in the retrieval for SnowSAR the same Re value (0.5 mm) has been used as for the SnowScat retrieval, and for SWE the snow pit value measured in the test site.

The SWE map in Fig. 7.23 is based on 10 m × 10 m $\sigma^0$ input data, with about 100 equivalent looks. This corresponds to speckle-related uncertainty of 0.4 dB, a very small difference to 0.5 dB for the 64 looks of the CoReH$_2$O sensor. The output product (SWE map) has the same raster size. The computations were performed for open areas and for open forest up to 25% cover density. Forest with cover density >25% is masked out. The comparison with *in situ*
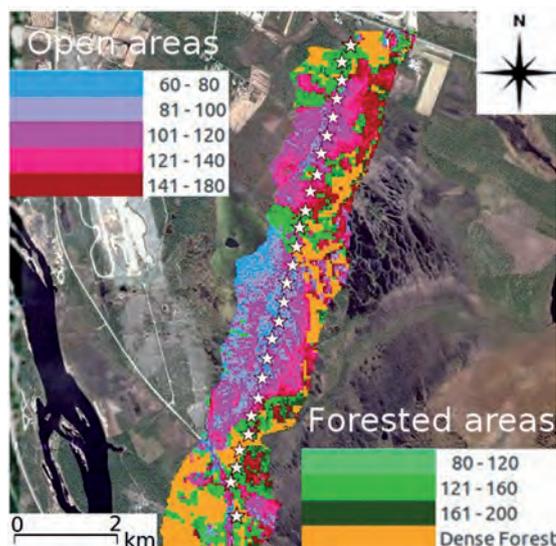
Figure 7.23. SWE map (mm) derived from SnowSAR measurements, Sodankylä, 15 March 2011, superimposed on a Google Earth image. The colours correspond to SWE values on open land and forest, respectively. Dense forest (cover fraction >25%) is masked. The stars show points of *in situ* snow depth and SWE measurements. (ENVEO)
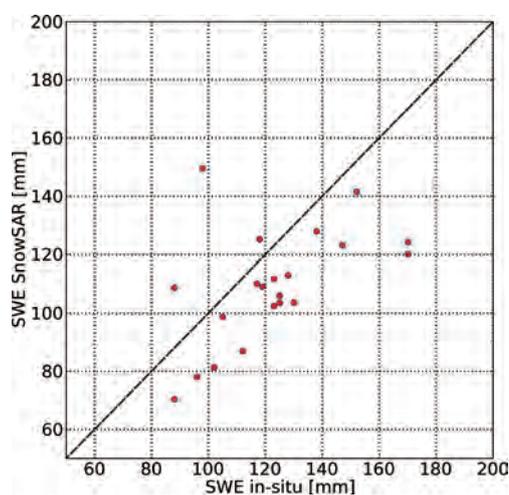


Figure 7.24. Comparison of SWE retrieved from SnowSAR data (open land) versus measured *in situ*. The dotted diagonal indicates full agreement. (ENVEO)

measurements of SWE shows on average some underestimation by SnowSAR (13 mm for the mean value); according to the standard error of estimate (16.5 mm SWE) the results are well within the benchmark (requirement ±30 mm for SWE ≤300 mm). The *in situ* SWE values for validation in Fig. 7.24 have partly been measured directly with the snow density sampler, partly computed by multiplying measured snow-depth measurements with mean snow density for a given surface class.

Another Ku- and X-band spatially distributed dataset for testing the SWE retrieval algorithm is available for Kuparuk River study site on the Alaska North Slope. Ku-band backscatter data were acquired in November 2007 and February 2008 with the airborne PolScat of NASA-JPL, for the Cold Land Processes Experiment (CLPX-II) of NASA-JPL and NOAA. X-band backscatter data at VV and VH polarisations were available from the TerraSAR-X satellite. The derived SWE map shows good compliance with the observational requirements for the CoReH$_2$O mission (reported in ESA, SP-1313/3).

## 7.4.3 Summary on Retrieval Performance

Analysis of retrieval performance for primary Level-2 products of the CoReH$_2$O mission has been performed for a wide range of snow cover states based on simulated data, generated with the Synthetic Scene Generator. In addition,

experimental data of test sites in northern Finland and on the Alaska North Slope, acquired by ground-based scatterometer and airborne sensors, were used for retrieval tests. The performance analysis has been conducted for the main Level-2 products (SWE and area extent on land surfaces, snow accumulation on glaciers) applying the baseline version of the retrieval algorithm.

Regarding the snow extent product, the requirement for classification of wet snow areas is fully met, whereas the identification of dry snow causes problems for shallow snow with small grain size. This problem is also known from microwave radiometry. For compensation of this deficiency, application of noise reduction filters optimised for 2D SAR image segmentation and synergy with optical snow-mapping products are proposed.

Table 7.13 provides a summary on compliance of retrieved SWE products in regard to the specified measurement requirements for geophysical products. Tests with simulated data indicate significant differences in performance for different snow types. For snowpacks with small grains the simulations indicate that the threshold performance cannot be met in all cases. The reduced backscatter sensitivity to SWE results in less impact of measurements compared to larger grains (Fig. 7.18). This affects in particular deep snow, which usually has small average grain size. Such snowpacks represent a very small percentage of the global seasonal snow, but nevertheless are of interest for water supply in some regions. Also fresh snow has small grains. Temperature gradient metamorphism results in substantial grain growth within a few days (Flanner & Zender, 2006). This is reflected in backscatter time series, as for example observed during the NoSREx campaign, which enables to track the snow accumulation during winter.

On the other hand, the SWE retrievals with available experimental data sets show full compliance within the specified observational requirements. For open forest and winter snow on glaciers the dynamic range of the backscatter signal is reduced compared to open land. This problem can be overcome by relaxing the product grid resolution to 500 m, as explained in Subsection 7.4.1.

A critical parameter for retrieval performance is the *a priori* value of effective grain radius. Reference tests indicate accuracy for the *a priori* value of effective grain radius within 15% of the mean value. The *a priori* value for SWE is less critical as various tests are showing. The retrieval of SWE from SnowScat time series of winter 2010–11, for example, shows good performance even if SWE is not used at all for regularisation (Fig. 7.22). Tests with experimental data show the importance of the backscatter value of the background medium (soil) at the beginning of the snow cover season. X-band time series enable to identify the date when soil freezing is attained, which can be identified by the minimum $\sigma^0$ value in the backscatter time series. The high temporal-repeat rate of Phase-1 will enable to consolidate and validate the approach for reference date selection in different climate zones.

The retrieval tests with simulated and experimental data clearly demonstrate the feasibility of the proposed sensor configuration and retrieval concept for a wide range of states of the global snow cover. Under certain snow

Table 7.13. Compliance of retrieved SWE products with requirements specified in Table 4.1. Estimates are based on performance analysis with simulated and experimental data.

| Background medium | Snow type | Compliance |
|---|---|---|
| Open land and low vegetation | Medium and large grains | Compliant |
| | Small grains | Partly compliant |
| Open forest (FC ≤30%) | Medium and large grains | Compliant for grid size 500 m |
| | Small grains | Partly compliant |
| Snow on glaciers | Winter snow on frozen firn | Compliant for grid size 500 m |
| *Medium and large grains refer to test cases with Re=0.5 mm and 0.7 mm, small grains refer to test cases with Re=0.3 mm. FC: fractional forest cover.* | | |

conditions (related to small grain size) the threshold requirements are hard to achieve. However, the expected CoReH$_2$O performance matches the bulk of snow-cover states for seasonal snow globally and meets the main scientific objectives addressed in Chapters 2 and 3.

# → MISSION CONTEXT

# 8 Mission Context

## 8.1 User Community Readiness

The CoReH$_2$O mission will make significant contributions to the progress of Earth system science, addressing cryosphere, hydrosphere and atmosphere processes and interactions. The science communities in these fields are ready to use CoReH$_2$O products to improve the treatment of snow and ice processes in climate, weather forecasting and hydrological models, including the initialisation, parameterisation and validation of these models.

The communities have a long history of participation in international model intercomparison projects (e.g., AMIP-2, Arctic Ocean Model Intercomparison Project (AOMIP), SnowMIP, SnowMIP-2, Project for Intercomparison of Land-surface Parameterization Schemes (PILPS) Phase-2d) involving the evaluation of many physically-based snow and ice process models, some of which are used as parameterisation schemes in atmospheric and hydrological models (Irannejad and Henderson-Sellers, 2007; Proshutinsky et al., 2011; Etchevers et al., 2004; Rutter et al., 2009; Slater et al., 2001). Research groups will draw from experience gained in intercomparison projects, recent ESA-sponsored projects (e.g. DUE-GlobSnow, DUE-Permafrost, Climate Change Initiative-Glaciers, Support to Science Element – North Hydrology) and active participation in the WCRP-CliC project to advance snow- and ice-process understanding and modelling capabilities made possible with the availability of products generated by the CoReH$_2$O mission.

In cooperation with national and international agencies the CliC project develops a conceptual framework for the Cryosphere Observing System in which satellite observations, such as those to be generated by the CoReH$_2$O mission, play an important role. CliC works closely with the Global Energy and Water Cycle Experiment (GEWEX) and Climate Variability and Predictability (CLIVAR) to advance research on the development and validation of physically-based land-atmosphere-cryosphere process models, including permafrost-hydrology and carbon cycle interactions, with appropriate complexity for their use in coupled climate models across a range of spatial and temporal scales. CoReH$_2$O would be a strong contributor to CliC's future plans since its mid- to long-term (next five years and beyond) objectives seek to improve regional climate models with interactive climate-cryosphere/hydrosphere schemes to allow assessments of: (1) impacts of climate variability and change on the terrestrial cryosphere and water resources, and (2) the effects of changes in the cryosphere on regional climates for the mountain and watershed systems. The role of river- and lake-ice processes in watershed hydrology over the cold regions, notably the Arctic, is a key topic also identified for future development by CliC in the WCRP 2010–2015 Implementation Plan (WCRP, 2009). Another of CliC's priorities is to improve models on spatial and temporal variability of the mass budget of glaciers, ice caps and ice sheets, including the assessment of vulnerability of the ice masses to climate change.

Contributions specific to the hydrological modelling and forecasting, and the atmospheric (climate and weather prediction) modelling communities are highlighted below. These two communities are fully aware of limitations in: (1) the representation of snow and ice processes in hydrological and atmospheric models, and (2) the satellite-derived snow and ice products currently being assimilated in these models. They are well-prepared to start using data from CoReH$_2$O as soon as they become available.

### 8.1.1 Hydrological Modelling and Forecasting

Accurate prediction or observations of snow properties is important to reduce uncertainties in streamflow and flood forecasting. The hydrology community has long recognised the value of remotely sensing derived snow parameters, such as snow extent (SE) and SWE, for validating and improving predictive hydrological models. Some models (e.g. Hydrological Predictions for the Environment (HYPE) of the Swedish Meteorological and Hydrological Institute) currently rely on the use of daily temperature and precipitation measurement to estimate snow accumulation and melt over sub-basins. Others use SE derived from remote-sensing data to infer the most critical snow parameter, SWE, during periods of snow accumulation and melt (e.g. Watershed Simulation and Forecasting System (WSFS), Finnish Environment Institute, and VIC model, University of Washington). This latter approach relies on the use of simple snow accumulation and depletion curves necessary for a SWE-SE inversion. SWE estimates derived from this approach using optical satellite (MODIS) SE data assimilated in the VIC model have shown to provide moderate improvements (2% better SWE) when compared to measurements from the SNOTEL network in a mountainous river basin in western US (e.g. Andreadis & Lettenmaier, 2006). CoReH₂O snow-cover products will permit the validation of snow accumulation and melting over many river basins and improve the general approach used by different hydrological modelling groups.

The hydrological modelling and forecasting community is unanimous in their need for high-resolution SWE, particularly over areas of moderate to complex topography where the snowpack can be very heterogeneous. According to the Finnish Environment Institute Hydrological (pers. comm., 2011), the quality of flood forecasting in spring depends greatly on accurate spatial SWE data. Better estimates of SWE are needed to improve the accuracy of streamflow and flood forecasts. This requirement, however, is not met with currently available SWE datasets that rely on coarse-resolution passive microwave observations (e.g., SSM/I derived 25 km GlobSnow product). High-resolution observations provided by the CoReH₂O mission are expected to increase retrieval accuracy through the reduction of non-linearity errors arising in estimates over heterogeneous areas, and to permit the development of techniques to downscale passive microwave data. Overall, the lack of high-resolution spatially-distributed SWE data has been a limiting factor to a greater adoption of satellite-derived snow products for operational streamflow and flood forecasting. The CoReH₂O mission will offer an opportunity for the hydrological modelling and forecasting community to reassess this.

### 8.1.2 Climate Modelling and Numerical Weather Prediction

Accurate representation of snow and ice processes occurring on Earth's surface (land and oceans) is key for advancing the predictive capabilities of climate and NWP models. While impressive advances have occurred in the development of snow and ice process models, the availability of consistent, spatially coherent data has generally been lacking for validating parameterisation schemes and for initialising and validating global to regional scale (GCM, RCM, NWP) models.

The climate modelling and numerical weather prediction user community is well-prepared to handle the observations and to exploit the unique dataset that CoReH₂O will provide. For example, NWP groups are already testing existing satellite-derived snow datasets in prediction algorithms, in particular the near-realtime estimate of snow extent. The applied prediction methods are seen to be most sensitive to snow parameters when the snow cover is thin owing to the ice/albedo effect and the impact on energy fluxes. In general, lack of reliable snow information over sea and lake ice, glaciers and mountainous

areas is an identified limitation, as well as the inaccuracy of estimates during snow-cover onset and melting periods. Other problems with existing datasets, in terms of NWP needs, include deficient accuracy of estimates, challenges in quantifying observational uncertainty and insufficient horizontal resolution (tens of kilometres in the case of passive microwave datasets). $CoReH_2O$ will especially address the need for high-resolution snow-cover products for validating and initialising surface/atmosphere exchange processes in atmospheric circulation models.

Globally, comparison of numerical model results with data provided by $CoReH_2O$ will be utilised to identify model biases in the representation of snow and ice processes (snow cover, glacier melt, lake ice and sea ice), and to understand the origin of these biases in a more thorough way than was possible with the spatially-limited data available in model intercomparison projects (AMIP-2, AOMIP, SnowMIP, SnowMIP2, PILPS Phase-2e). Subsequent snow and ice model improvements will enable climate models to simulate and predict current and future climate conditions more accurately, and NWP models to provide more accurate and reliable weather forecasts needed by society.

## 8.2 Global Context

### 8.2.1 Complementarity of $CoReH_2O$

In the field of hydrology, $CoReH_2O$ is complementary to ESA's Soil Moisture and Ocean Salinity mission and NASA's future Soil Moisture Active-Passive mission. Precipitation missions such as the Tropical Rainfall Measuring Mission and the Global Precipitation Measurement Mission address liquid precipitation. $CoReH_2O$ is, therefore, very important to obtain accurate information on the role of solid precipitation in the water cycle. $CoReH_2O$ products are complementary to snow and ice albedo from optical satellite sensors (e.g. Sentinel-2 and Sentinel-3 missions), jointly providing an excellent basis for quantifying surface energy and moisture fluxes.

In addition, $CoReH_2O$ is highly complementary to C- and L-band SAR systems because these wavelengths are not sensitive to dry snow. For sea ice, the different penetration depths and scattering properties of multifrequency radar data enable improved classification of ice types and their physical properties. Opportunities of overlapping swathes of Sentinel-1, the Radarsat constellation (C-band) and $CoReH_2O$ should be exploited for studies of backscatter physics and basic retrieval methods, not only for sea ice, but also for other targets such as soil, vegetation, and convective rainfall events. $CoReH_2O$ is also complementary to TerraSAR-X and COSMO-SkyMed-like missions, as it provides frequent repeat observation at two frequencies and single operation mode, whereas these other two missions offer around 100 different operation modes at a single frequency (X-band) and focus at very high-resolution mapping and monitoring tasks.

The snow and ice products from $CoReH_2O$ will be useful for downscaling and reducing uncertainty (e.g. SWE maps in regions of complex terrain and land cover, and effects of sub-grid scale lakes in SSM/I products) in coarse-resolution passive microwave time series used for climate studies (Lemmetyinen et al., 2011).

$CoReH_2O$ is highly complementary to CryoSat-like missions and other altimetry missions that provide precise elevation data over ice sheets and glaciers. $CoReH_2O$ addresses processes of surface/atmosphere interaction, hydrology, and snow and ice accumulation at high temporal and spatial scales, whereas CryoSat delivers very precise measurements of surface topography of large glaciers, ice sheets and sea ice. Process understanding, addressed by $CoReH_2O$, is very relevant for providing the link between precise altimetry measurements from CryoSat-like missions and climate models.

The high-resolution X-/Ku-band SAR radar measurements from CoReH$_2$O will offer opportunities to complement observations of Sentinel-1 and Radarsat C-band SAR for surface wind observations in coastal areas, whenever near-coincident data acquisitions would occur. The information will be of great value for coastal research as well as weather forecasting. This will be a major improvement over coarser-resolution scatterometer measurements (e.g. MetOp's Advanced Scatterometer, India's Oceanscat and past QuikSCAT) which have been providing coarse resolution (20–50 km) data on ocean-surface winds over open oceans (20 km or more offshore).

## 8.2.2 Contribution to International Programmes

The CoReH$_2$O mission aims to supply essential data for filling gaps in the representation of snow and ice processes and feedbacks in climate models, addressed in the IPCC 2007 Physical Sciences report.

The need for improved, satellite-based snow and ice observations is explicitly addressed in numerous documents and international programme reports, including:

— The United Nations Framework Convention on Climate Change (UNFCCC). "Encouraging Parties to enhance their work and collaboration on observation of the essential climate variables and on development of climate products to support the needs of the Convention, including through participation in the Global Climate Observing System cooperation mechanism". Specifically, snow cover, glacier and ice-sheet mass balance, permafrost thickness, and sea-ice concentration are addressed as Essential Climate Variables in report FCCC/SBSTA/2007/L.14/, December 2007.

— The WCRP-CliC project, referred to in some details in Section 8.1.

— The IGOS cryosphere component of WMO-WCRP, the UN Educational, Scientific and Cultural Organization, and the International Council for Science, addressed in the IGOS Cryosphere Theme Report (IGOS, 2007) specify in detail the needs for improved observations on snow cover, glacier and ice-sheet mass balance, sea-ice characteristics, and of the other elements of the cryosphere.

— The Global Cryosphere Watch (GCW) Programme, was approved at the 16th WMO Congress in May 2011. The importance of improved satellite-borne cryosphere observations is highlighted in this programme. It was decided to develop the GCW as an International Polar Year (IPY) legacy project with a view to providing global cryosphere information for weather, climate, water and environmental matters.

— Snow and ice observations are also important components of the Global Monitoring for Environment and Security (GMES) and Global Earth Observation System of Systems (GEOSS) programmes, which are concerned with the use of satellite observations for a wide range of environmental and commercial applications. In this context, the CoReH$_2$O mission specifications take into account the needs of meteorological and hydrological services and of environmental agencies.

## 8.3 Application Potential

Water is a prerequisite of all life on Earth, a basic resource for agriculture and a requirement for many domestic and industrial processes. The focus of CoReH$_2$O is water in its solid form, including the contribution of this resource

to streamflow and to the replenishment of reservoirs above and below the surface. Consequently, the scientific advancements in observation and modelling of snow and ice resources, to be triggered by CoReH$_2$O, will find applications and be of significant benefit to environmental and industrial water-related activities, in addition to improved weather forecasting and climate predictions identified in Section 8.1. Significant socio-economic benefit from the improvements of snow and ice observations and process modelling is expected in particular for:

— Streamflow forecasting, supporting water-supply management, hydropower production, irrigation, and river navigation.

— Natural hazard assessment and warning, by supporting flood forecasting, avalanche warnings, predictions of water outbreaks from glacial and periglacial lakes.

— Support of timely measures to prepare for decreasing water resources from snow and glaciers resulting from climate change.

Finally, as explained in Section 8.1, the operational community is also actively preparing for the use of CoReH$_2$O observations. This implies that, should the mission be selected, there could be an operational follow-on mission dedicated to the monitoring of global snow and ice resources with a similar or enhanced payload and orbital characteristics that would benefit society as a whole.

# → PROGRAMMATICS

# 9 Programmatics

## 9.1 Introduction

This chapter presents the technical maturity, the heritage and the risks associated with both the mission-level scientific concepts and the system-level technical concepts as developed in the frame of the scientific and industrial Phase-A studies in Sections 9.2 and 9.3. The corresponding development approach and schedule is presented and discussed in Section 9.4 with respect to the compatibility with a target launch in 2019 for the seventh Earth Explorer mission.

## 9.2 Scientific Maturity, Critical Areas and Risks

The CoReH$_2$O mission concept is considered in light of previous Earth Science Advisory Committee (ESAC) recommendations and in terms of scientific maturity, residual open scientific issues and associated remaining risks.

### 9.2.1 Previous ESAC Recommendations

During Phase-A, supporting scientific studies were initiated to specifically target and address each of the issues raised by ESAC at the mission down-selection after the CoReH$_2$O Assessment Phase (Phase-0). Several areas were identified, namely:

(a) To further quantify the impact and define mitigation strategies for vegetation cover and topography on retrieval algorithm.

(b) To perform dedicated field measurements under different dry and multilayered snow conditions to demonstrate the robustness of retrieval algorithms.

(c) To explore potential synergy with passive microwave remote-sensing and propose an approach to bridge the scale gap between active and passive observations of SWE.

(d) To define a post-launch protocol for validation with *in situ* data at a global scale.

(e) To identify contributions to representations of ice and snow processes in models on varying scales and specify how intended observations contribute to improving the parameterisation of snowmelt and river run-off models.

(f) To investigate the potential and need for near-realtime data supply.

To minimise the scientific risk associated with each of the above points made by ESAC, and to maximise the scientific output from the mission concept, each of the areas were addressed by study activities. To address point (a), vegetation-cover correction algorithms have been devised and implemented in the retrieval algorithms, see Chapters 4, 6, and 7. The validation of the algorithms is being addressed by means of dedicated campaign activities. With respect to the influence of topography, the impact of errors/uncertainty in DEMs has been analysed (Rott et al., 2011) and taken into account in the retrieval algorithms and error budget. Over mountainous areas, an accompanying observation

strategy has been defined with observations made on both ascending and descending orbital passes, as described in Chapter 5.

To address point (b), extensive field measurements have been initiated and conducted at different locations under varying snow conditions. Time-series measurements have been acquired to capture temporal changes in the snowpack. Instruments have been specifically developed for the purpose, namely the tower-based scatterometer operated at FMI's *in situ* measurement site at Sodankylä, during the last winters and the newly developed Ku-/X-band airborne SnowSAR sensor. Results using the campaign data are shown in Chapters 4 and 7.

To address point (c), a study was carried out to develop and evaluate concepts for synergy of the proposed dual-frequency active measurements with passive microwave observations. An impact analysis showed the benefit of using CoReH$_2$O data with passive microwave data for snow observations, as well as of using passive microwave data in support of CoReH$_2$O retrievals (Lemmetyinen et al 2011).

With regard to point (d), validation sites have been defined in Chapter 6 to cover a representative range of global snow conditions. With respect to the definition of a post-launch SWE validation protocol, this is typically defined closer to launch when the validation participants have been confirmed and common measurement standards and *in situ* instrumentation have been characterised and documented. This step is also accompanied by the preparation of a calibration and validation strategy and implementation plan, which are then used during the commissioning and operations phases of the approved mission.

With respect to point (e), Chapter 2 and 4 describes in detail how the CoReH$_2$O observation requirements have been defined to respond to the need for improved representation of snow in models at global and regional scales. Chapter 7 indicates the end-to-end performance to the specific snow data requirements.

With respect to (f), a supply of near-realtime data is of great relevance to CoReH$_2$O and significant interest has been expressed by hydrological and meteorological agencies in Europe and North America. Corresponding CoReH$_2$O snow-cover product timeliness requirements have been established to enable a pre-operational demonstration of the benefits of using the products. In response to these requirements, the concept is compliant with the delivery of Level-2 data products within 24 hours of acquisition for both mission phases.

### 9.2.2 Maturity

The CoReH$_2$O mission concept is scientifically unique and the observation requirements are stable and mature. CoReH$_2$O will deliver spatially-detailed (200–500 m) measurements of snow and ice masses compared to presently available low-resolution (>20 km) passive microwave data. The data are also highly complementary to snow extent products that can be derived from other future satellite missions such as Sentinel-3 (Ocean and Land Colour Instrument and Sea and Land Surface Temperature Radiometer). The scientific community is well prepared for using CoReH$_2$O products in process studies and models for hydrology and cryosphere/climate interactions. Distributed and semi-distributed snow-process models and hydrological models are available that would profit from spatially-detailed information on snow-cover extent and SWE.

A baseline retrieval algorithm has been developed and intensively tested using simulated data that reproduces the threshold performance of the baseline concepts (see Chapter 7). The algorithm has been used successfully on available campaign data covering a variety of snow conditions. For the considered areas showing different snow conditions, topography and vegetation, and provided that the necessary auxiliary information is available and sufficiently accurate,

the requirements at Level-2 are met. The main areas influencing the retrieval performance and selected retrieval algorithm have been recognised and accompanying targeted risk reduction measures identified for treatment during the extended Phase-A activities.

### 9.2.3 Critical Areas

To date, preparations for $CoReH_2O$ have been limited in part by the availability of a suitable dual-frequency system for which an airborne SAR instrument had to be developed. The lack of spatially-distributed, coincident and collocated Ku- and X-band backscatter image data has thus retarded the testing and potential enhancement of the SWE retrieval algorithms. With the recent completion of the SnowSAR airborne instrument this limitation has been overcome and recent airborne campaigns have collected valuable new data to perform further risk reduction from an algorithm and retrieval perspective.

Retrieval methods and tools for integrating $CoReH_2O$ products with data from other sources is being improved and tested over different snow regimes and glacier regions within the Phase-A extension activities. A major task in this context is the enhancement of the SWE retrieval algorithm, in particular towards minimising the need for auxiliary information. This is planned to be achieved by iterative and progressive improvements in the retrieval methods, for example, through the use of spatial data structure and context, which, so far, has been impeded because of the lack of temporally and spatially coincident co- and cross-polarised Ku- and X-band backscatter images.

Of particular interest in support of mission exploitation is the adaptation and validation of 2D (spatial) and 3D (spatial and temporal) data assimilation techniques for integrating $CoReH_2O$ observations in land-surface process models and hydrological models. Data assimilation concepts and downscaling methods are also to be pursued for advancing methods to derive statistical background fields on snow parameters (grain size and SWE) for the retrieval cost function, which is considered to be a key area for enhancing the robustness of the Level-2 products. This is being assessed in detail through an ongoing study activity.

### 9.2.4 Risks

It is recognised that due to logistics and natural conditions, no amount of campaign activity can guarantee to address all the potential snow regimes or conditions that $CoReH_2O$ may be encounter globally. Nevertheless, the recent completion of the SnowSAR airborne instrument, together with its successful first campaigns, provides the capability to acquire data under a broad variety of snow conditions in the future to enable the necessary algorithm refinements. In the cases for which simulated products indicate that the Level-2 product performance is marginal in respect to the requirements, further campaigns will be designed to acquire data to target and address these conditions and to refine or adapt the retrieval algorithms accordingly. Additional experiments with the E2ES are in progress to test the range of natural variability under synthetic conditions. Notably, the mission operations profile has also been adapted, with the specific intention to allow the mission to cover all relevant snow conditions in Phase-1 before undertaking an operational demonstration in Phase-2.

## 9.3  Technical maturity, Critical Areas and Risks

### 9.3.1 Satellite and Platform

As shown in Chapter 5, the overall similarity of the two satellite concepts increases confidence in the maturity of the technical solution in terms of

overall satellite design and platform concept. The proposed baseline designs present adequate margins at this stage of the mission definition with some growth capacity. Analyses of the platform equipment show that the majority are all at Technology Readiness Level (TRL) 8 or 9, having flown on a number of spacecraft missions in the past. For all other platform equipment the TRL is considered ≥6 because of the minor adaptations required to fulfil the specific mission needs.

### 9.3.2 Dual-frequency, Dual-polarisation SAR Payload

The payload has heritage from past X-band SAR missions like SAR-Lupe, TerraSAR-X, and Cosmo-SkyMed. It also benefits from past developments in telecommunications programmes using similar technologies like ARTES, Astra 1K, Express MD3. The criticality is assessed for all subsystems separately.

#### 9.3.2.1 Reflector antenna and feed

The reflector antenna and associated mechanisms have extensive heritage in Europe from telecommunication programmes. For the Ku-band feed, two parallel pre-developments allowed to build and successfully test breadboard models using space-qualified materials (Figs. 5.15 and 5.18). The current TRL is 4 with the realistic objective to reach a TRL of 5 before mission selection on the basis of ongoing activities. With regard to the X-band feed, a complete Engineering Model (EM) was already built and successfully tested, and a parallel pre-development is proceeding. Based on these pre-developments, the current TRL is 4 with the realistic objective to reach a TRL of 5 before mission selection.

#### 9.3.2.2 Switch matrix and distribution network

Two parallel pre-developments based on two different technologies (Subsection 5.4.3.5) are ongoing. These activities include the breadboarding and testing of partial distribution network both in Ku-band and in X-band using space-qualified materials and manufacturing process. The current TRL is 4 and with the planned multipaction tests the TRL will be 5 before the mission selection.

#### 9.3.2.3 Active front-end

Two parallel pre-developments based on alternative technologies, but applicable to both system concepts (Subsection 5.4.3.6), are ongoing. A pre-development of the TWT Ku-band sub-assemblies is ongoing bringing the current TRL to 3. A complete EM model is required to bring the TRL to 4 or 5. Regarding the X-band TWT, the TRL depends on the level of power required, which means a TRL of 5 for Concept A and a TRL of 3 if it has to be used for Concept B.

A first EM of the Klystron technology was built and tested in Ku-band achieving a TRL of 4. A life test is included in the current activity with the objective to reach a TRL of 5. A first EM in X-band is ongoing with the objective of reaching a of TRL 4 before the mission selection. For this, a life test is included in the current activities with the objective to reach a TRL of 5 by the second quarter of 2013.

#### 9.3.2.4 Central electronics

The central electronics build on heritage from previous SAR missions, particularly for X-band. Many of the required components, e.g. local oscillators, mixers, amplifiers, Application Specific Integrated Circuits (ASICs) and Field Programmatic Gate Arrays (FPGAs) have flight heritage and can be reused for

| Element | Current TRL | Current status | Phase-B1 expected TRL |
|---|---|---|---|
| Feed subsystem Ku-band | 4 | Two parallel pre-developments ongoing | 5 |
| Feed subsystem X-band | 4 | One pre-development finalised One pre-development ongoing | 5 |
| Switch matrix and distribution network | 4 | Two parallel pre-developments ongoing Multipaction test planned | 5 |
| TWT HPA X-band (Concept A) X-band (Concept B) | 5 3 | Pre-development ongoing (*) Pre-development ongoing (*) | 5 5 |
| TWT HPA Ku-band | 3 | Pre-development ongoing (*) | 5 |
| Klystron HPA Ku-band X-band | 4 4 | EM finalised, life test to be complete EM ongoing, life test to be complete | 5 5 |
| *For the TWT a single pre-development activity addresses both frequencies.* | | | |

Table 9.1. Development status and plans of payload critical elements.

developing the central electronics. The TRL of the equipment is 6 except for a few items that will need adaptations to work in Ku-band, implying a TRL of 4.

### 9.3.2.5 Overall maturity and critical items

For all critical items, the design and test results so far show that the proposed equipment can meet the requirements. This is also true of the HPA technologies (TWT and Klystron) for which analyses of designs based on heritage equipment, breadboarding and tests have demonstrated feasibility, with the limiting factor being the number of on/off cycles for the TWT where non-compliance to initial requirements constrains the system and operation concept (Subsection 5.4.3).

Thus, the criticality is mainly related to the schedule of development plans for the equipment not having reached TRL 5. Table 9.1 shows a summary of the current TRL, state of development and expected state at the end of all the activities leading up to Phase-B1, assuming they are successful. Apart from the TWT HPA, it is anticipated that all the critical elements will have the required TRL at the start of the implementation phase.

### 9.3.3 PDGS Ground Segment Development

In general, the ground segment is not critical, as discussed in Chapter 5. All elements either build on heritage or have non-critical requirements well in line with current capabilities. For CoReH$_2$O one of the scientific institutions proposing the mission, the FMI, has proposed an in-kind contribution in the form of part or all of the PDGS to be sited at its Artic Research Centre in Sodankylä. FMI has existing infrastructure for data reception and processing from other Earth observation missions, and has recently commissioned a new data reception station that is proposed for use as the PDAS. The exact impact of such a potential implementation option is being assessed in detail.

## 9.4 Development Approach and Schedule

### 9.4.1 Overall Design and Development Approach

CoReH$_2$O will follow the traditional phased development process (Phases B/C/D/E) with system reviews (System Requirements Review (SRR), Preliminary Design Review (PDR), Critical Design Review (CDR) etc.) to assess

the status of the system design, development, procurement and integration of the flight models. In order to establish a robust development schedule, instrument and satellite platform development are decoupled, i.e. parallel development activities on the instrument, platform and spacecraft level are foreseen, with integration performed during the Assembly, Integration and Testing (AIT) phase.

For both concepts, the model philosophy at system level aims to maximise the reuse of models considered essential for the safe development of the satellite. At satellite level, a 'hybrid approach' according to ECSS-E-10-03A has been chosen. It comprises the following models:

— Proto Flight Model (PFM) for full qualification and acceptance testing, in terms of environmental and functional requirements;

— Structural Model (SM) for qualification of the structure against launch loads, for verification of structural stability, strength and stiffness, for verification of the finite element model and for validation of the interface loads for platform equipment and for instruments;

— Electrical and Functional Model (EFM) or 'FlatSat' for electrical interface verification of the platform avionics, for onboard software verification, for AOCS performance verification by closed loop testing, and for initial validation of onboard flight procedures. This model initially uses EMs of the OBC, RIU and SSMM in conjunction with numerical models of the sensors and actuators. As flight hardware deliveries become available, these are integrated and tested on the EFM prior to their integration to the satellite PFM.

At equipment or subsystem level, development models are included in the plan based on the maturity and criticality as analysed in the previous section. The equipment model philosophy is shown in Table 9.2. It is very similar for both system concepts.

## 9.4.2 Assembly, Integration and Testing

After passing the CDR, procurement and integration of the flight models will take place. The foreseen AIT sequence is fairly traditional. It includes integration and testing to establish the first functional baseline test, then a number of environmental tests (mechanical sine and acoustic, thermal, electromagnetic compatibility) with functional checks in between, and final checking before the launch campaign. The integration of Concept B includes

| Element | Model Philosophy |
|---|---|
| Payload | Testbed (EM)/PFM |
| Antenna Reflector & Feed | SM/PFM |
| Distribution Network & Switch Matrix | EM/PFM |
| Active Front-end | (EM)/EQM/PFM/FM |
| Central Electronics | E(Q)M/PFM/FM |
| Platform | Structure SM/PFM<br>Avionics PFM |
| PDHT and TT&C | PFM/FM |
| EPS, Avionics and Harness | PFM/FM<br>OBC EM for OBSW testing |
| AOCS and Propulsion | PFM/FM |
| Structure & Thermal | PFM/FM |

Table 9.2. Model philosophy (in addition to current pre-development models).

an earlier module-level delivery, so satellite integration is focused on modular mating, integration and testing of deployable equipment (reflector, solar array) and verification of system-level interfaces, e.g. antenna and startracker alignments.

### 9.4.3 Schedule

The schedule of the development phase is constrained by the procurement of the payload. The single most critical path is with the HPA as the production of the flight models takes 15–18 months depending on the technology. In particular, the TWT option appears critical, as actual EM developments are not yet started. The actual availability of the TWT HPA must therefore be reviewed after mission selection. In any case, at least one HPA technology (Klystron) is on track and available.

The overall reference baseline schedule for Concept B is shown in Fig. 9.1, which underlines the criticality of the payload development. A launch date in 2019 is considered achievable.

## 9.5 Conclusion

Subject to the successful outcome of pre-developments, the maturity of critical technologies will reach the required level prior to the start of the implementation phases, with the risks being limited to the TWT technology for the HPA. The development schedule is compatible with a launch in 2019.

Figure 9.1. Outline schedule for Concept B.
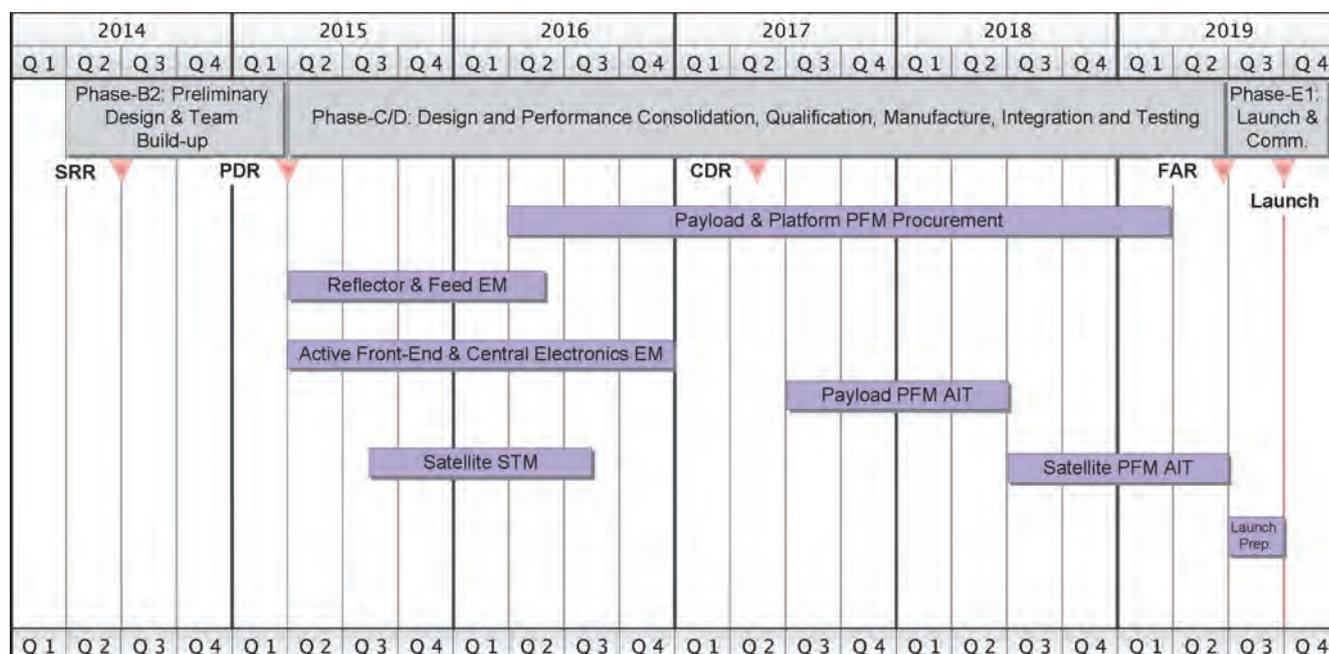
# → REFERENCES

# References

Abatzoglou, J.T. (2011). Influence of the PNA on declining mountain snowpack in the Western United States. *International Journal of Climatology* **31**(8), pp1135–1142.

Acar, R. & Vogel, C.R. (1994). Analysis of bounded variation penalty methods for ill-posed problems. *Inverse Problems* **10**, pp1217–1229.

ACIA (2005). Arctic Climate Impact Assessment. In *Arctic Council and the International Arctic Science Committee Scientific Report*, Cambridge University Press, Cambridge, GB. Online at *http://www.acia.uaf.edu/pages/scientific.html* (as of January 2012).

Anderton, S.P., White, S.M. & Alvera, B. (2004). Evaluation of spatial variability in snow water equivalent for a high mountain catchment. *Hydrological Processes* **18**, pp435–453.

Andreadis, K.M. & Lettenmaier, D.P. (2006). Assimilating remotely sensed snow observations into a macroscale hydrology model. *Advances in Water Research* **29**, pp872–886.

Anisimov, O., Fitzharris, B., Hagen, J.O., Jeffries, R., Nelson, F., Prowse, T.D. & Vaughan, D. (2001). Polar Regions (Arctic and Antarctic). In *Climate Change 2001, Impacts, Adaptation, and Vulnerability*, Contribution of Working Group II to the Third Assessment Report of the Intergovernmental Panel on Climate Change, Cambridge University Press, Cambridge, GB, pp801–841.

ASTER. Online at *https://lpdaac.usgs.gov/content/view/full/11350* (as of January 2012).

Barnett, T.P., Adam, J.C. & Lettenmaier, D.P. (2005). Potential impacts of a warming climate on water availability in snow-dominated regions. *Nature* **438**, doi: 10.1038/nature04141.

Barstow, R. (2007). Envisat-1 Products Specifications Volume 8. *ASAR Products Specifications*. In Issue 4, Revision B, internal report PO-RS-MDA-GS-2009, European Space Agency, Noordwijk, The Netherlands.

Bavay, M., Lehning, M., Jonas, T. & Löwe, H. (2009). Simulations of future snow cover and discharge in Alpine headwater catchments. *Hydrological Processes* **23**, pp95–108.

Beaven, S.G., Lockhart, G.L., Gogineni, S.P., Hosseinmostafa, A.R., Jezek, K., Gow, A.J., Perovich, D.K., Fung, A.K. & Tjuatja, S. (1995). Laboratory measurements of radar backscatter from bare and snow-covered saline ice sheets. *International Journal of Remote Sensing* **16**(5), pp851–876.

Benson, B.J., Magnuson, J.J., Jensen, O.P., Card, V.M., Hodgkins, G., Korhonen, J., Livingstone, D.M., Stewart, K.M., Weyhenmeyer, G.A. & Granin, N.G. (2011). Extreme events, trends, and variability in Northern Hemisphere lake-ice phenology (1855–2005). *Climatic Change*, doi: 10.1007/s10584-011-0212-8.

Berezovskaya, S.L., Hilton, K.M , Derry, J.E., Youcha, E., Kane, D.L., Gieck, R.E., Homan, J. & Lilly, M.R. (2010). Snow Survey Data for the Central North Slope Watersheds: Spring 2010. University of Alaska Fairbanks, Water and Environmental Research Center, Report INE/WERC 10.01, Fairbanks, Alaska, p50.

Blöschl, G. (1999). Scaling issues in snow hydrology. *Hydrological Processes* **13**, pp2149–2175.

Bonsal, B.R., Prowse, T.D., Duguay, C.R. & Lacroix, M.P. (2006). Impacts of large-scale teleconnections on freshwater-ice duration over Canada. *Journal of Hydrology* **330**, pp340–353.

Braithwaite, R.J. (2009). After six decades of monitoring glacier mass balance we still need data but it should be richer data. *Annals of Glaciology* **50**, pp191–197.

Brasnett, B. (1999). A global analysis of snow depth for numerical weather prediction. *Journal of Applied Meteorology* **38**, pp726–740.

Brown, L.C. & Duguay, C.R. (2010). The response and role of ice cover in lake-climate interactions. *Progress in Physical Geography* **34**(5), pp671–704, doi:10.1177/0309133310375653.

Brown, R.D. (2000). Northern Hemisphere snow cover variability and change, 1915–1997. *Journal of Climate* **13**, pp2339–2355.

Brown, R.D., Brasnett, B. & Robinson, D. (2003). Gridded North American monthly snow depth and snow water equivalent for GCM evaluation. *Atmosphere-Ocean* **41**, pp1–14.

Brown, R.D. & Armstrong, R. (2008). Snow-cover data: measurement, products, and sources. In *Snow and Climate 'Physical Processes, Surface Energy Exchange and Modelling'* (Eds. R.L. Armstrong & E. Brun), Cambridge University Press, Cambridge, GB, pp181–216.

Brown, R.D. & Mote, P.W. (2009). The response of northern hemisphere snow cover to a changing climate. *Journal of Climate* **22**, pp2124–2145.

Brown, R.D., Derksen, C. & Wang, L.B. (2010). A multi-data set analysis of variability and change in Arctic spring snow cover extent, 1967–2008. *Journal of Geophysical Research Atmospheres* **115**, D16111.

Brown, L.C. & Duguay, C.R. (2011a). The fate of lake ice in the North American Arctic. The Cryosphere 5, 869–892, doi: 10.5194/tc-5-869-2011.

Brown, L.C. & Duguay, C.R. (2011b). A comparison of simulated and measured lake ice thickness using a Shallow Water Ice Profiler. *Hydrological Processes* **25**, pp2932–2941, doi: 10.1002/hyp.8087.

Brown, R.D. & Robinson, D.A. (2011). Northern Hemisphere spring snow cover variability and change over 1922–2010 including an assessment of uncertainty. *Cryosphere* **5**(1), pp219–229.

Busche, T., Hajnsek, I., Papathanassiou, K., Krumpen, T., Hoelemann, L.J., Haas, C. & Willmes, S. (2009). Comparison of helicopter-borne thin sea ice thickness with polarimetric signatures of dual-pol TerraSAR-X data. In *Proc. 'IGARSS 2009'*, II-222–II-225.

Cecchini, P., Orlando, G., Mizzoni, R., Hélière, F. & van't Klooster, K. (2011). X/Ku Band Array-fed Reflector ScanSAR Antenna for CoReH$_2$O mission. In *Proc. 33rd ESA Antenna Workshop*, European Space Agency, Noordwijk, The Netherlands.

Cecchini, P., Orlando, G., Mizzoni, R., Hélière, F. & van't Klooster, K. (2012). A Dual Band Array-fed Reflector ScanSAR Antenna. In *Proc. European Conference on Antennas and Propagation (EUCAP)*, Prague, Czech Republic.

Chen, C.-T., Tsang, L., Guo, J., Chang, A.T.C. & Ding, K.-H. (2003). Frequency dependence of scattering and extinction of dense media based on three-dimensional simulations of Maxwell's equations with applications to snow. *IEEE Transactions on Geoscience and Remote Sensing* **41**(8), pp1844–1852.

Clark, M.P., Hendrikx, J., Slater, A.G., Kavetski, D., Andrson, B., Cullen, N.J., Err, T., Hreinsson, E.O. & Woods, R.A. (2011). Representing spatial variabilityof snow water equivalent in hydrologic and land-surface models: A review. *Water Resources Research* **47**, doi: 10.1029/2011WR010745.

CliC (2001). World Climate Research Programme. Climate and Cryosphere (CliC) Project. Science and Co-ordination Plan (Eds. I. Allison, R.G. Barry & B.E. Goodison), WCRP-114, (WMO/TD No. 1053).

Clifford, D. (2010). Global estimates of snow water equivalent from passive microwave instruments: history, challenges and future developments. *International Journal of Remote Sensing* **31**(14), pp3707–3726.

Cogley, J.G. (2005). Mass and energy balances of glaciers and ice sheets. In *Encyclopedia of Hydrological Sciences* (Eds. M. Anderson), John Wiley & Sons, Ltd, Chichester, GB pp2555–2573.

Cogley, J.G. (2009). Geodetic and direct mass-balance measurements: comparison and joint analysis. *Annals of Glaciology* **50**, pp96–100.

Cogley, J.G., Kargel, J.S., Kaser, G. & Van der Veen, C.J. (2010). Tracking the source of glacier misinformation. *Science* **327**(5965), p522.

Colbeck, S.C. et al. (1990). The International Classification for Seasonal Snow on the Ground. IAHS – Int. Association of Hydrological Sciences, CEH Wallingford, GB.

Cumming, I. & Wong, F. (2005). Digital Processing of Synthetic Aperture Data, Artech House, Norwood, MA, USA.

Davidson, E. & Janssens, I. (2006). Temperature sensitivity of soil carbon decomposition and feedbacks to climate change. *Nature* **440**, pp165–173.

Denman, K.L., et al. (2007). Couplings Between Changes in the Climate System and Biogeochemistry. In *Climate Change 2007: The Physical Science Basis. Contribution of Working Group I to the Fourth Assessment Report of the Intergovernmental Panel on Climate Chang*, Cambridge University Press, Cambridge, GB and New York, NY, USA.

Deimos Space (2009). Open SF System User's Manual. OPENSF-DMS -SUM-001, Issue 1, Rev 1.

Dierking, W., Pettersson, M.I. & Askne J. (1999). Multifrequency scatterometer measurements of Baltic Sea ice during EMAC-95. *International Journal of Remote Sensing* **20**(2), pp349–372.

Dolman, A.J., van der Werf, G.R., van der Molen, M.K., Ganssen, G., Erisman, J.-W., Strengers, B. (2010). A carbon cycle science update since IPCC AR-4. *Ambio* **39**, pp402–412.

Douville, H., Royer, J.-F. & Mahfouf, J.-F. (1995). A new snow parameterization for the Météo-France climate model. Part I: validation in stand-alone experiments. *Climate Dynamics* **12**, pp21–35.

Duguay, C.R., Flato, G.M., Jeffries, M.O., Ménard, P., Morris, K. & Rouse, W.R. (2003). Ice cover variability on shallow lakes at high latitudes: Model simulations and observations. *Hydrological Processes* **17**(17), pp3465–3483.

Duguay, C.R., Prowse, T.D., Bonsal, B., Brown, R.D., Lacroix, M. & Ménard, P. (2006). Recent trends in Canadian lake ice covers. *Hydrological Processes* **20**(4), pp781–801.

Dutra, E., Balsamo, G., Viterbo, P., Miranda, P.M.A., Beljaars, A., Schär, C. & Elder, K. (2010). An improved snow scheme for the ECMWF land surface model: Description and offline validation. J*ournal of Hydrometeorology* **11**(4), pp899–916.

Dutra, E., Schaer, C., Viterbo, P., & Miranda, P.M.A. (2011). Land-atmosphere coupling associated with snow cover. *Geophysical Research Letters* **38**, L15707, doi: 10.1029/2011GL048435.

Drusch, M., Vasiljevic, D. & Viterbo, P. (2004). ECMWF's global snow analysis: Assessment and revision based on satellite observations. *Journal of Applied Meteorology* **43**, pp1282–1294.

Dyurgerov, M., & Meier, M.F. (2005). Glaciers and the Changing Earth System: A 2004 Snapshot. Occasional Paper 58, Institute of Arctic and Alpine Research, University of Colorado, Boulder, CO, p118.

EADS Astrium GmbH (2012). CRH.ASG.RP.00018 Issue 2, CoReH$_2$O Final Report.

Eerola, K., Rontu, L., Kourzeneva, E., & Shcherbak, E. (2010). A study on effects of lake temperature and ice cover in HIRLAM. *Boreal Environment Research* **15** pp130–142.

ESA (2006). The Changing Earth. New Scientific Challenges for ESA's Living Planet Programme. In ESA SP-1304, ESA Communication Production Office, European Space Agency, Noordwijk, The Netherlands.

Escher-Vetter, H., Kuhn, M., & Weber, M. (2009). Four decades of winter mass balance of Vernagtferner and Hintereisferner: Methodology and results. *Annals of Glaciology* **50**, pp87–95.

Essery, R., Heidinger, M., Nagler, T., Rott, H., Pulliainen, J., Rontu, L., Ryyppö, T., Lejeune, Y., & Morin, S. (2011). The CoReH$_2$O Snow Data Assimilation Study. Summary Report, 2011.

Etchevers, P. & 22 other authors (2004). Validation of the energy budget of an alpine snowpack simulated by several snow models (SnowMIP project). Annals of Glaciology **38**(1) pp150–158.

Fiedler, E.K., Lachlan-Cope, T.A., Renfrew, I.A. & King, J.C. (2010). Convective heat transfer over thin ice covered coastal polynyas. *Journal of Geophysical Research* **115**, C10051, doi: 10.1029/2009JC005797.

Fischer, A. (2011). Comparison of direct and geodetic mass balances on a multi-annual time scale. *The Cryosphere* **5**, pp107–124, doi: 10.5194/tc-5-107-2011.

Flanner, M.G. & Zender, C.S. (2006). Linking snowpack microphysics and albedo evolution. *Journal of Geophysical Research* **111**, D12208, doi: 10.1029/2005JD006834.

Floricioiu, D. & Rott, H. (2001). Seasonal and short-term variability of multifrequency, polarimetric radar backscatter of alpine terrain from SIR-C/X-SAR and AIRSAR data. *IEEE Transactions on Geoscience and Remote Sensing* **39**(2), pp2634–2648.

Frei, A., Robinson, D.A. & Hughes, M.G. (1999). North American snow extent: 1900-1994. *International Journal of Climatology* **19**, pp1517–1534.

Frei, A., Miller, J.M. & Robinson, D.A. (2003). Improved simulations of snow extent in the second phase of the Atmospheric Model Intercomparison Project (AMIP-2). *Journal of Geophysical Research* **108**, doi: 10.1029/2002JD003030.

Fügen, T., Grafmüller, B., Viberg, M., Riegger, S., Hélière, F. & van't Klooster, K. (2011). Dual-Polarised Ku-band multi-feed antenna for the CoReH$_2$O SAR instrument. In *Proc. 33rd ESA Antenna Workshop*, European Space Agency, Noordwijk, The Netherlands.

Fügen, T., Grafmüller, B., Viberg, M., Riegger, S., Hélière, F. & van't Klooster, K. (2012). Dual-Polarised Ku-band multi-feed antenna for the CoReH$_2$O SAR instrument. In *Proc. European Conference on Antennas and Propagation (EUCAP)*, Prague, Czech Republic.

Ghatak, D., Frei A., Gong G., Stroeve, J. & Robinson, D. (2010). On the emergence of an Arctic amplification signal in terrestrial Arctic snow extent. *Journal of Geophysical Research* **115**, D24105, doi: 10.1029/2010JD014007.

GCOS (2006). Systematic Observation Requirements for Satellite-based Products for Climate. Supplemental details to the satellite-based component of the Implementation Plan for the Global Observing System for Climate in Support of the UNFCCC–September 2006. GCOS-107. Online at *http://www.wmo.ch/pages/prog/gcos/* (as of January 2012).

Ge, Y. & Gong, G. (2007). Observed inconsistencies between snow extent and snow depth variability at regional/continental scales. *J Climate* **21**, pp1066–1082.

Gerbaux, M., Genthon, C., Etchevers, P., Vincent, C., & Dedieu, J.P. (2005). Surface mass balance of glaciers in the French Alps: Distributed modelling and sensitivity to climate change. *J. Glaciol.* **51**(175), pp561–572.

Germani, C., Venturini, R., Cecchini, P., Orlando, G., Gebert, N., Hélière, F. & Lecuyot, A. (2011). The CoReH$_2$O SAR Instrument. In *Proc. Advanced RF Sensors and Remote Sensing Instruments*, European Space Agency, Noordwijk, The Netherlands.

Haarpaintner, J., O'Dwyer, J., Gascard, J.-C., Haugan, P.M., Schauer, U. & Osterhus, S. (2001). Seasonal transformation of water masses, circulation and brine formation observed in Storfjorden, International Symposium on Sea Ice and Its interaction with the Ocean, Atmosphere and biosphere, Fairbanks, Alaska, 19-23 June 2000. *Annals of Glaciology* **33**, pp437–443.

Haas, C., Thomas, D.N. & Bareiss, J. (2001). Surface properties and processes of perennial Antarctic sea ice in summer. *Journal of Glaciology* **47**(159), pp613–625.

Haas, C., Pfaffling, A., Hendricks, S., Rabenstein, L., Etienne, J.-L. & Rigor, I. (2008). Reduced ice thickness in Arctic Transpolar Drift favours rapid ice retreat. *Geophysical Research Letters* **35**, L17501, doi: 10.1029/2008GL034457.

Hall, D.K., Riggs, G.A. & Salomonson, V.V. (2006) (updated monthly): MODIS/Terra Snow Cover Monthly L3 Global 0.05Deg CMG V005, [2000 - 2010]. Boulder, Colorado USA: National Snow and Ice Data Center. Digital media.

Hall, A., & Qu, X. (2006). Using the current seasonal cycle to constrain snow albedo feedback in future climate change. *Geophysical Research Letters* **33**, L03502, doi: 10.1029/2005GL025127.

Heer, C., Grafmüller, B., Kanderhag, L., Viberg, M. & van 't Klooster, K. (2004). A Low Cost Multifeed Antenna. In *Proc. European Conference on Synthetic Aperture Radar (EUSAR)*, Ulm, Germany, pp497–500.

Heer, C., Grafmüller, B., Astrium GmbH (81663 München, Germany). Method of generating multiple SAR transmit beams and a SAR antenna system. European Patent EP1471600, Application number EP20040008173, Published 12/10/2008, filed 04/03/2004.

Hendricks, S., Gerland, S., Smedrud, L.H., Haas, C., Pfaffhufber, A.A. & Nilsen, F. (2011). Sea ice thickness in Storfjorden, Svalbard. *Annals of Glaciology* **52**(57), pp61–68.

Hollesen J., Elberling, B. & Jansson, P.E. (2011). Future active layer dynamics and carbon dioxide production from thawing permafrost layers in Northeast Greenland. *Global Change Biology* **17**(2), pp911–926.

Howell, S.E.L., Brown, L.C., Kang, K.-K. & Duguay, C.R. (2009). Variability in ice phenology on Great Bear Lake and Great Slave Lake, Northwest Territories, Canada, from SeaWinds/QuikSCAT: 2000-2006. *Remote Sensing of Environment* **113**, pp816–834.

Horoyski, P., Berry D. & Steer B. (2011). Compact High Power Klystrons for the CoReH$_2$O Earth Explorer Candidate Core Mission. In *Proc. International Vacuum Electronics Conference (IVEC)*, Bangalore, India, p85.

IPCC (2007). Summary for Policymakers. In *Climate Change 2007: Impacts, Adaptation and Vulnerability. Contribution of Working Group II to the Fourth Assessment Report of the Intergovernmental Panel on Climate Change* (Eds. M.L. Parry, O.F. Canziani, J.P. Palutikof, P.J. van der Linden and C.E. Hanson), Cambridge University Press, Cambridge, GB, pp7–22.

Irannejad, P. & Henderson-Sellers, A. (2007). Evaluation of AMIP II global climate model simulations of the land surface water budget and its components over the GEWEX-CEOP regions. *Journal of Hydrometeorology* **8**, pp304–326.

Jarabo-Amores, P., Rosa-Zuera, M., De la Mata-Moya, D., Vicen-Bueno, R. & Maldando-Bascon, S. 2011. Spatial-Range Mean-Shift Filtering and Segmentation Applied to SAR Images. *IEEE Transactions on Instrumentation and Measurement* **60**(2), pp584–596.

Jarvis, P., & Linder, S. (2000). Constraints to growth of boreal forests. *Nature* **405**, pp904–905.

Jeffries, M.O., Zhang, T., Frey, K. & Kozlenko, N. (1999). Estimating late-winter heat flow to the atmosphere from the lake-dominated Alaskan North Slope. *Journal of Glaciology* **45**, pp315–324.

Jin, J., & Miller, N.L. (2007). Analysis of the impact of snow and daily weather variability in mountainous region using MM5. *J. Hydromteorol.* **8**(2), pp245–258.

Kazama, S. (1998). Development of Simple Snow Density Model for Wide Area. Water Resources Engineering '98. In *Proceedings of the International Water Resources Engineering Conference,* Memphis, Tennessee, August 3-7, 1998, pp1230–1235.

Kern, S., Ozsoy-Cicel, B., Willmes, S., Nicolaus, M., Haas, C. & Ackley, S. (2011). An intercomparison between AMSR-E snow-depth and satellite C- and Ku-band radar backscatter data for Antarctic sea ice. *Annals of Glaciology* **52**(57), pp279–290.

Key, J. et al. (2007). IGOS Cryosphere Theme Report. WMO/TD-No. 1405.

Khairuddin, I., McLaren, C., Morgan, I., Abuelmaatti, A. & Muhammed, I. (2009). Ferrite Switches: Means of Average Power Handling Improvements in Space Instrument. In *Proc. Advanced RF Sensors and Remote Sensing Instruments*, European Space Agency, Noordwijk, The Netherlands.

Kim, Y.S., Onstott, R.G., & Moore, R.K. (1984). The effect of a snow cover on microwave backscatter from sea ice. *IEEE Journal of Oceanic Engineering* **OE-9**(5), pp383–388.

Kittel, T. G. F., Baker, B.B., Higgins, J.V. & Haney, J.C. (2011). Climate vulnerability of ecosystems and landscapes on Alaska's North Slope. *Regional Environmental Change* **11**(Suppl. 1), ppS249–S264.

Koch, P., Fischer, C. & Viberg, M. (2007). Multibeam Feed-Cluster for a Reflector-Based SAR Antenna. In *Proc. 29th ESA Antenna Workshop*, European Space Agency, Noordwijk, The Netherlands.

Kourzeneva, E., Samuelsson, P., Ganbat, G. & Mironov, D. (2008). Implementation of lake model FLake into HIRLAM. *HIRLAM Newsletter* **54**, December 2008.

Kreyling, J., Jurasinski, G., Grant, K., Retzer, V., Jentschand, A. & Beierkuhnlein, C. (2011). Winter warming pulses affect the development of planted temperate grassland and dwarf-shrub heath communities. *Plant Ecology and Diversity* **4**, pp13–21.

Kripalani, R.H. & Kulkarini, A. (1999). Climatology and variability of historical Soviet snow depth data: some new perspectives in snow – Indian monsoon teleconnections. *Climate Dynamics*, **15**, pp475–489.

Kuhn, M., Dreiseitl, E., Hofinger, S., Kaser, G., Markl, G. & Span, N. (1999). Measurements and models of the mass balance of Hintereisferner. *Geografiska Annaler* **81A**(4), pp659–670.

Kundzewicz, Z.W., et al. (2007). Freshwater resources and their management. In *Climate Change 2007: Impacts, Adaptation and Vulnerability. Contribution of Working Group II to the Fourth Assessment Report of the Intergovernmental Panel on Climate Change*, Cambridge University Press, Cambridge, GB and New York, NY, USA.

Kurtz, N.T., Markus, T., Farrell, S.L., Worthen, D.L. & Boisvert, L.N. (2011). Observations of recent Arctic sea ice volume loss and its impact on ocean-atmosphere energy exchange and ice production. *Journal of Geophysical Research* **116**, C04015, doi: 10.1029/2010JC006235.

Lacroix, M., Prowse, T.D., Bonsal, B.R., Duguay, C.R. & Ménard, P. (2005). River ice trends in Canada. In *Proc. of 13th Workshop on the Hydraulics of Ice Covered Rivers*, Hanover, New Hampshire, 15-16 September, p14, (CD-ROM).

Lanari, R. (1994). A new method for wide field synthetic aperture radar processing. In *Proc. International Geoscience and Remote Sensing Symposium (IGARSS)*, Pasadena, CA, USA, pp1961–1963.

Lanari, R., Hensley, S. & Rosen, P. (1998). Modified SPECAN algorithm for ScanSAR data processing. In *Proc. International Geoscience and Remote Sensing Symposium (IGARSS)*, Seattle, WA, USA, pp636–638.

Land Processes DAAC (Distributed Active Archive Center) (2012). ASTER GDEM Version 2 Validation. Online at *https://lpdaac.usgs.gov/content/view/full/11350* (as of 17 February 2012).

Langer M., Westermann, S., Muster, S., Piel, K. & Boike, J. (2011). The surface energy balance of a polygonal tundra site in northern Siberia – Part 1: Spring to fall. *The Cryosphere* **5**, pp151–171.

Lefsky, M.A. (2010). A global forest canopy height map from the Moderate Resolution Imaging Spectroradiometer and the Geoscience Laser Altimeter System. *Geophysical Research Letters* **37**, L15401, doi: 10.1029/2010GL043622.

Lemke, P., Ren, R.B., Alley, J., Allison, R., Carrasco, I., Flato, J., Fujii, G., Kaser, Y., Mote, G., Thomas, P., & Zhang, T. (2007). Observations: Changes in Snow, Ice and Frozen Ground. In: Climate Change 2007: The Physical Science Basis. Contribution of Working Group I to the Fourth Assessment Report of the Intergovernmental Panel on Climate Chang. Cambridge University Press, Cambridge, GB and New York, NY, USA.

Lemmetyinen, J. & 22 others (2011). Synergy of CoReH₂O SAR and Microwave Radiometry data to retrieve snow and ice parameters. ESA Study, Contract 22829/09/NL/JC (2009-2011).

Lemmetyinen J., Kontu, A., Pulliainen, J., Wiesmann, A., Werner, C., Nagler, T., Rott H. & Heidinger, M. (2011b). Technical assistance for the deployment of an X- to Ku-band scatterometer during the NoSREx II experiment. ESA ESTEC Contract No. 22671/09/NL/JA, CCN, Final Report.

Lin, H. & Wu, P. (2011). Contribution of the autumn Tibetan Plateau snow cover to seasonal prediction of North American winter temperature. *Journal of Climate* **24**(11), pp2801–2813.

Liston, G.E. (2004). Representing Subgrid Snow Cover Heterogeneities in Regional and Global Models. *Journal of Climate* **17**(6), pp1381–1397.

Liston, G.E., Hiemstra, C.A. (2011). Representing grass-and shrub-snow-atmosphere interactions in climate system models. *Journal of Climate* **24**, pp2061–2079.

Luce, C.H., Tarboton, D.G., & Cooley, K.R. (1999). Subgrid parameterizations of snow distribution for an energy and mass balance snow cover model. *Hydrological Processes* **13**(12–13), pp1921–1933.

Magnuson, J.J., Robertson, D.M., Wynne, R.H., Benson, B.J., Livingstone, D.M., Arai, T., Assel, R.A., Barry, R.D., Card, V., Kuusisto, E., Granin, N.G., Prowse, T.D., Stewart K.M., & Vuglinski, V.S. (2000). Ice cover phenologies of lakes and rivers in the Northern Hemisphere and climate warming. *Science* **289**(5485), pp1743–1746.

Malone, E.L. (2010). Changing Glaciers and Hydrology in Asia: Adressing Vulnerabilities to Glacier Melt Impacts. Final Report, US EHIQC, Contract GHA-I-00-04-00006.

Marzano, F.S., Mori, S. & Weinman, J.A. (2008). High-resolution rainfall retrieval over land from satellite synthetic aperture radar measurements at X, Ku and Ka band. In *Proc. ERAD, 2008: 5th European Conf. on Radar in Meteorology and Hydrology*.

Maslanik, J., & Stroeve, J. (1999) (updated daily): Near-Real-Time DMSP SSM/I-SSMIS Daily Polar Gridded Sea Ice Concentrations, [1979–2007]. Boulder, Colorado USA: National Snow and Ice Data Center. Digital media.

Massom, R.A., Eicken, H., Haas, C., Jeffries, M.O., Drinkwater, M.R., Sturm, M., Worby, A.P., Wu, X., Lytle, V.I., Ushio, S., Morris, K., Reid, P.A., Warren, S., & Allison, I. (2001). Snow on Antarctic sea ice. *Reviews of Geophysics* **39**(3), pp413–445.

Mätzler, C. (1987). Applications of the interaction of of microwaves with the natural snow cover. *Remote Sensing Review* **2**, pp259–387.

Maurer, E.P., Brekke, L.D. & Pruitt, T. (2010). Contrasting lumped and distributed hydrology models for estimating climate change impacts on California watersheds. *Journal of the American Water Resources Association (JAWRA)* **46**(5), pp1024–1035. doi: 10.1111/j.1752-1688.2010.00473.

McGuire A.D., Anderson, L.G., Christensen, T.R., et al. (2009). Sensitivity of the carbon cycle in the Arctic to climate change. *Ecological Monographs* **79**(4), pp523–555.

Meier, M.F. & Bahr, D.B. (1996). Counting Glaciers: Use of Scaling Methods to Estimate the Number and Size Distribution of the Glaciers of the World. *CRREL Special Reports*, pp96–27, pp89–94.

Meier, M.F., et al. (2007). Glaciers dominate eustatic sea-level rise in the 21st century. *Science* **317**, pp1064–1067, 1064. doi: 10.1126/science.1143906.

Meta A., Trampuz, C., Coccia, A., & Imbembo, E. (2011). Technical assistance for the development and deployment of an X-band and Ku-band MiniSAR airborne system. ESTEC Contract 4000101697/10/NL/FF/EF. Final Report.

MeteoSwiss (2011). Online at *http://www.meteoschweiz.admin.ch/web/en/weather/models/cosmo.html* (as of January 2012).

Moreira, A., Krieger, G., Fiedler, H., Hajnsek, I., Younis, M., Zink, M. & Werner, M. (2008). Advanced interferometric SAR techniques with TanDEM-X. In *Proc. Radar Conference (RADAR)*, Rome Italy.

Morgner, E., Elberling, B., Strebel, D. & Cooper, E.J. (2010). The importance of winter in annual ecosystem respiration in the High Arctic: effects of snow depth in two vegetation types. *Polar Research* **29**(1), pp58–74.

Nagler, T., & Rott, H. (2000). Retrieval of wet snow by means of multitemporal SAR data. *IEEE Transactions on Geoscience and Remote Sensing* **38**(2), pp754–765.

Nagler, T., Rott, H., Heidinger, M., Malcher, P., Macelloni, G., Pettinato, S., Santi, E., Essery, R., Pulliainen, J., Takal, M., Malnes, E., Storvold, R., Johnson, H., Haas, C. & Duguay, C. (2008). Retrieval of physical snow properties from SAR observations at Ku- and X-band frequencies. Final Report. European Space Agency, ESTEC contract 20756/56/07/NL/CB, p328.

Nagler, T., Rott, H., Heidinger, M., Pulliainen, J., Macelloni, G., Montomoli, F., & Flach, D. (2011). CoReH$_2$O Algorithm Theoretical Basis Document (ATBD). D7, ESA ESTEC Contract No. 22830/09/NL/JC.

Natali, S.M., Schuur, E.A.G., Trucco, C., Pries, C.E.H., Hicks, C.E., Crummer, K.G., & Lopez, A.F.B. (2011). Effects of experimental warming of air, soil and permafrost on carbon balance in Alaskan tundra. *Global Change Biology* **17**(3), pp1393–1407.

Navascués B., Rodriguez, E., Ayuso, J.J. & Järvenoja, S. (2003). Analysis of surface variables and parameterization of surface processes in HIRLAM. Part II: Seasonal assimilation experiment. Online at *http://hirlam.org/publications/TechReports/index.html* (as of January 2012).

Nghiem, S.V., Van Woert, M.L. & Neumann, G. (2005). Rapid formation of a sea ice barrier east of Svalbard. *Journal of Geophysical Research* **33**, L17501, doi: 10.1029/2006GL027198.

Nihashi, S., Ebuchi, N., Fukamachi, Y. & Takahashi, S. (2011). Characteristics of sea ice in the Okhotsk coastal polynyas revealed by satellites, ice-profiling sonar and digital camera observations. *Annals of Glaciology* **52**(57), pp133–139.

NSIDC (2011). Arctic Sea Ice News and Analysis. Online at *http://nsidc.org/arcticseaicenews/* (as of January 2012).

Oerlemans, J. (2001). *Glaciers and Climate Change*, AA. Balkema Publ., Lisse, NL.

Ohmura, A. (2004). Cryosphere during the twentieth century. In *The State of the Planet: Frontiers and Challenges in Geophysics* (Eds. R.S.J. Sparks & C.J. Hawkesworth). *Geophysical Monograph* **150**, IUGG and AGU, pp239–257.

Omann, I., Stocker, A. & Jaeger, J. (2009). Climate change as a threat to biodiversity: An application of the DPSIR approach. *Ecological Economics* **69**, pp24–31.

Onstott, R.G., Moore, R.K. & Weeks, W.F. (1979). Surface based scatterometer results of Arctic sea ice. *IEEE Transactions on Geoscience and Remote Sensing* **17**(3), pp78–85.

Onstott, R.G., Moore, R.K., Gogineni, S. & Delker, C. (1982). Four years of low-altitude sea ice broad-band backscatter measurements. *IEEE Journal of Oceanic Engineering* **OE-7**(1), pp44–50.

Osterkamp, T.E. (2008). Thermal state of permafrost in Alaska during the fourth quarter of the twentieth century. In *Proc. of Ninth Int. Conference on Permafrost* (Eds. D.L. Kane & K.M. Hinkel), 29 June–3 July 2008, Fairbanks, Alaska. Institute of Northern Engineering, University of Alaska Fairbanks, pp1333–1338.

Pan, M. & 13 others (2003). Snow process modelling in the North American Land Data Assimilation System (NLDAS): 2. Evaluation of model simulated snow water equivalent. *Journal of Geophysical Research* **22**, art. no. 8850.

Parry, M.L., Canziani, O.F., Palutikof, J.P., et. al. (2007). Technical Summary. Climate Change 2007: Impacts, Adaptation and Vulnerability. In *Contribution of Working Group II to the Fourth Assessment Report of the Intergovernmental Panel on Climate Change* (Eds. M.L. Parry, O.F. Canziani, J.P. Palutikof, P.J. van der Linden & C.E. Hanson), Cambridge University Press, Cambridge, GB, pp23–78.

Partington, K.C. (1998). Discrimination of glacier facies using multi-temporal SAR data. *Journal of Glaciology* **44**(146), pp42–53.

Pearce, F. (2005). Climate warning as Siberia melts. *New Scientist* **2512**, 11 Aug. 2005, 12.

Peings, Y. & Douville, H. (2010). Influence of the Eurasian snow cover on the Indian summer monsoon variability in observed climatologies and CMIP3 simulations. *Climate Dynamics* **34**(5), pp643–660.

Perovich, D.K., Nghiem, S.V., Markus, T. & Schweiger, A. (2007). Seasonal evolution and interannual variability of the local solar energy absorbed by the Arctic sea ice–ocean system. *Journal of Geophysical Research* **112**, C03005, doi: 10.1029/2006JC003558.

Picard G., Quegan, S., Delbart, N., Lomas, M.R., Woodward, F.I., & Le Toan, T. (2005). Bud-burst modelling in Siberia and its impact on quantification of the carbon budget. *Global Change Biology* **11**(12), pp2164–2176.

Proshutinsky, A., Aksenov, Y., Clement Kinney J., Gerdes, R., Golubeva, E., Holland, D., Holloway, G., Jahn, A., Johnson, M., Popova, E., Steele, M., & Watanabe, E. (2011). Recent advances in Arctic ocean studies employing models from the Arctic Ocean Model Intercomparison Project. *Oceanography* **24**(3), pp102–113.

Prowse, T.D., Bonsal, B.R., Duguay, C.R., & Lacroix, M.P. (2007). River-ice break-up/freeze-up: A review of climatic drivers, historical trends, and future predictions. *Annals of Glaciology* **46**, pp443–451.

Radic, V. & Hock, R. (2011). Regionally differentiated contribution of mountain glaciers and ice caps to future sea-level rise. *Nature Geoscience* **4**(2), pp91–94.

Randall, D.A., et al. (2007). Climate Models and Their Evaluation. In *Climate Change 2007: The Physical Science Basis*. Contribution of Working Group I to the Fourth Assessment Report of the Intergovernmental Panel on Climate Chang. Cambridge University Press, Cambridge, GB and New York, NY, USA.

Reichle, R.H., Walker, J.P., Koster, R.D. & Houser, P.R. (2002). Extended versus Ensemble Kalman Filtering for land data assimilation. *Journal of Hydrometeorology* **3**, pp728–740.

Rogers, M.C., Sullivan, P.F. & Welker, J.M. (2011). Evidence of nonlinearity in the response of net ecosystem CO(2) exchange to increasing levels of winter snow depth in the high Arctic of northwest Greenland. *Arctic and Alpine Research* **43**(1), pp95–106.

Rott H., Sturm, K., & Miller, H. (1993). Active and passive microwave signatures of Antarctic firn by means of field measurements and satellite data. *Annals of Glaciology* **17**, pp337–343.

Rott, H., Nagler, T., Malcher, P. & Müller, F. (2008). Satellite based information system for glacier monitoring and modelling. GeoInformation in Europe. In *Proc. 27th EARSeL Symposium* (Eds. M.A. Gomarasca), 2008 Millpress, Rotterdam, pp395–402.

Rott, H., Yueh, S.H., Cline, D.W., Duguay, C., Essery, R., Haas, C., Hélière, F., Kern, M., Macelloni, G., Malnes, E., Nagler, T., Pulliainen, J., Rebhan, H. & Thompson, A. (2010). Cold Regions Hydrology High-resolution Observatory for Snow and Cold Land Processes. *Proceedings of the IEEE* **98**(5), pp752–765. 10.1109/JPROC.2009.2038947.

Rott, H., Nagler, T., Heidinger, M., Müller, F., Macelloni, G., Montomoli, F., Fontanelli, G., Cortezi, U., Gai, M., Liguri, R., Scheiber, R., Hajnsek, I., Flach, D., Pulliainen, J., Arslan, A., Malnes, E., Tøllefsen, T., Grøttum, K.J., Etchevers, P. & Durand, Y. (2011). Development of Snow Retrieval Algorithms for CoReH$_2$O. Final Report. ESA ESTEC Contract No. 22830/09/NL/JC.

Rouse, W.R., Oswald, C., Binyamin, J., Spence, C., Schertzer, W., Blanken, P., Bussières, N., & Duguay, C.R. (2005). Role of northern lakes in a regional energy balance. *Journal of Hydrometeorology* **6**(3), pp291–305.

Rouse, W.R., Blanken, P.D., Duguay, C.R., Oswald, C.J., & Schertzer, W.M. (2008a). Climate-lake interactions. Chapter 8 in Cold Region Atmospheric and Hydrologic Studies: The Mackenzie GEWEX Experience, Volume 2: Hydrologic Processes. Springer-Verlag, pp139–160.

Rouse, W.R., Binyamin, J., Blanken, P.D., Bussières, N., Duguay, C.R., Oswald, C.J., Schertzer, W.M., & Spence, C. (2008b). The Influence of lakes on the regional heat and water balance of the central Mackenzie River Basin. Chapter 18 in Cold Region Atmospheric and Hydrologic Studies: The Mackenzie GEWEX Experience, Volume 1: Atmospheric Dynamics. Springer-Verlag, pp309–325.

Rutter, N., Essery, R., Pomeroy, J., & 41 other authors (2009). Evaluation of forest snow processes models (SnowMIP2). *Journal of Geophysical Research Atmosphere* **114**, D06111, doi: 10.1029/2008JD011063.

Samuelsson, P., Kourzeneva, E. & Mironov, D. (2010). The impact of lakes on the European climate as simulated by a regional climate model. *Boreal Environment Research* **15**, pp113–129.

Santoro M., Beer, C., Cartus, O., Schmullius, C., Shvidenko, A., McCallum, I., Wegmüller, U. & Wiesmann, A. (2011). Retrieval of growing stock volume in boreal forest using hyper-temporal series of Envisat ASAR ScanSAR backscatter measurements. *Remote Sensing of Environment* **115**(2), pp490–507.

Screen, J.A. (2011). Sudden increase in Antarctic sea ice: Fact or artifact? *Geophysical Research Letters* **38**, L13702, doi: 10.1029/2011GL047553.

Seuffert, G., Wilker, H., Viterbo, P., Drusch, M. & Mahfouf, J.-F. (2004). The usage of screen-level parameters and microwave brightness temperature for soil moisture analysis. *Journal of Hydrometeorology* **5**, pp516–531.

Serreze, M.C., Clark, M.P., Armstrong, R.L., McGinnis, D.A. & Pulwarty, R.S. (1999). Characteristics of the western United States snowpack from snowpack telemetry (SNOTEL) data. *Water Resources Research* **35**, pp2145–2160.

Shepherd, A. & Wingham, D. (2007). Recent Sea-Level Contributions of the Antarctic and Greenland Ice Sheets. *Science* **315**(5818), pp1529–1532.

Slater, A.G. & 33 other authors (2001). The representation of snow in land surface schemes: results from PILPS-2(d). *Journal of Hydrometeorology* **2**, pp7–25.

Slater, A.G., & Clark, M.P. (2006). Snow data assimilation via an Ensemble Kalman Filter. *Journal of Hydrometeorology* **7**, pp478–493.

Sobolowski, S., Gong, G. & Ging, M.F. (2011). Investigating the linear and nonlinear stationary wave response to anomalous North American snow cover. *Journal of Atmospheric Sciences* **68**(14), pp904–917.

Stewart, I.T., Cayan, D.R., & Dettinger, M.D. (2005). Changes toward earlier streamflow timing across western North America. *Journal of Climate* **18**, pp1136–1155.

Stieglitz, M., Déry, S.J., Romanovsky, V.E. & Osterkamp, T.E. (2003). The role of snow cover in the warming of arctic permafrost. *Geophysical Research Letters* **30**(13), 1721, doi: 10.1029/2003GL017337.

Sturm, M., Holmgren, J. & Liston, G.E. (1995). A seasonal snow cover classification system for local to global applications. *Journal of Climate* **8**, pp1261–1283.

Sturm, M., Taras, B., Liston, G.E., Derksen, C., Jonas, T. & Lea, J. (2010). Estimating snow water equivalent using snow depth data and climate classes. J*ournal of Hydrometeorology* **11**, pp1380–1394.

Stroeve, J., Holland, M.M., Meier, W., Scambos, T. & Serreze, M. (2007). Arctic sea ice decline: Faster than forecast. *Geophysical Research Letters* **34**, L09501, doi: 10.1029/ 2007GL029703.

Tait A.B, Hall, D.K., Foster, J.L. & Armstrong, R.L. (2000). Utilizing multiple datasets for snow-cover mapping. *Remote Sensing of Environment* **72**, pp111–126.

Takala, M., Luojus, K., Pulliainen, J., Derksen, C., Lemmetyinen, J., Kärnä, J.-P., Koskinen, J., & Bojkov, B. (2011). Estimating northern hemisphere snow water equivalent for climate research through assimilation of space-borne radiometer data and ground-based measurements. *Remote Sensing of Environment,* doi: 10.1016/j.rse.2011.08.014.

Tedesco, M. & Narvekar, P.S. (2010). Assessment of the NASA AMSR-E snow product. *IEEE J. Applied Earth Observation and Remote Sensing* **3**(1), pp141–159.

Thales Alenia Space Italy (2012). RPT-CORE-0010-TASR Issue 4, Earth Explorer – CoReH$_2$O Final Report.

Thomas, R., Davis, C., Frederick, E., Krabill, W., Li, Y., Manizade, S. & Martin, C. (2008). Comparison of Greenland ice-sheet volume changes derived from altimetry measurements. *Journal of Glaciology* **54**(185), pp203–212.

Trenberth, K.E., et al. (2007). Observations: surface and atmospheric climate change. In *Climate Change 2007: The Physical Science Basis: Contribution of Working Group I to the Fourth Assessment Report of the Intergovernmental Panel on Climate Change* (Eds. S. Solomon, D. Qin, M. Manning, Z. Chen, M. Marquis, K.B. Averyt, M. Tignor & H.L. Miller), Cambridge University Press, Cambridge, GB, pp235–336. Online at *http://eprints.soton.ac.uk/50395/* (as of January 2012).

Trujillo, E., Ramirez, J.A. & Elder, K.J. (2009). Scaling properties and spatial organization of snow depth fields in sub-alpine forest and alpine tundra. *Hydrological Processes* **23**, pp1575–1590.

Twomey, S. (1977). *Introduction to the mathematics of inversion in remote sensing and indirect measurements*, Elsevier Publ., Amsterdam, The Netherlands.

Ulaby F.T., Moore, R.K. & Fung, A.K. (1981). *Microwave Sensing – Active and Passive*, Vol. I. Artech House, Durham, MA.

Ulaby F.T., Moore, R.K. & Fung, A.K. (1986). *Microwave Remote Sensing – Active and Passive*, Vol. III., Artech House, Durham, MA.

UNEP (2007). *Global Outlook for Ice and Snow* (Eds. J. Eamer), UNEP/GRID-Arendal, Norway. ISBN: 978-92-807-2799-9.

Vehviläinen, B., Huttunen, M., & Huttunen, I. (2005). Hydrological forecasting and real time monitoring in Finland: The watershed simulation and forecasting system (WSFS). In *Innovation, Advances and Implementation of Flood Forecasting Technology*, Tromsø, Norway, 17-19 October 2005. ISBN: 1-898485-13-5.

Walsh, J., Anisimov, O., Hagen, J.O., Jakobsson, T., Oerlemans, J., Prowse, T.D., Romanovsky, V., Savelieva, N., Serreze, M., Shiklomanov, A., Shiklomanov, I. & Solomon, S. (2005). *Cryosphere and Hydrology, Arctic Climate Impact Assessment*, Cambridge University Press, Cambridge, GB, pp183–242.

Walter, K.M., Zimov, S.A., Chanton, J.P., Verbyl, D. & Chapin III, F.S. (2006). Methane bubbling from Siberian thaw lakes as a positive feedback to climate warming. *Nature* **443**, pp71–75, doi: 10.1038/nature05040.

Walker, N.P., Partington, K.C., Van Woert, M.L. & Street, T.L.T. (2006). Arctic sea ice type and concentration mapping using passive and active microwave sensors. *IEEE Transactions on Geoscience and Remote Sensing* **44**(12), pp3574–3584.

Wang, X. & Key, J. (2005). Arctic surface, cloud, and radiation properties based on the AVHRR Polar Pathfinder data set. Part I: Spatial and temporal characteristics. *Journal of Climate* **18**(14), pp2558–2574.

Wang, Z. & Zeng, X. (2010). Evaluation of snow albedo in land models for weather and climate studies. *Journal of Applied Meteorology and Climatology* **49**(3), pp363–380.

Warren, S.G., Rigor, I.G., Untersteiner, N., Radionov, V., Bryazgin, N., Aleksandrov, Y. & Colony, R. (1999). Snow depth on Arctic sea ice. *Journal of Climate* **12**, pp1814–1829.

WCRP (2009). The World Climate Research Programme Implementation Plan 2010-2015. WMO/TD-No. 1503.

Weinman, J.A., Marzano, F.S., Plant, W.J., Mugnai, A. & Pierdicca, N. (2009). Rainfall observation from X-band, space-borne, synthetic aperture radar. *Natural Hazards and Earth System Sciences* **9**(1), pp77–84.

Willmes, S., Bareiss, J., Haas, C. & Nicolaus, M. (2006). The importance of diurnal processes for the seasonal cycle of sea-ice microwave brightness temperatures during summer in the Weddell Sea. *Annals of Glaciology* **44**, pp297–302.

Willmes, S., Haas, C. & Nicolaus, M. (2011). High radar-backscatter regions on Antarctic sea ice and their relation to sea-ice and snow properties and meteorological conditions. *International Journal of Remote Sensing* **32**, pp3697–3984.

Yueh, S.H. & Kwok, R. (1998). Arctic sea ice extent and melt onset from NSCAT observations. *Geophysical Research Letters* **25**(23), pp4369–4372.

ZAMG (2011). Austrian Weather Service. Online at *http://www.zamg.ac.at/incaanalyse/* (as of January 2012).

Zhang, T., Barry, R.G., Knowles, K., Ling, F. & Armstrong, R.L. (2003). *Distribution of seasonally and perennially frozen ground in the Northern Hemisphere. Permafrost* (Eds. M. Philips, S. Springman & L.U. Arenson), Swets & Zeitlinger, Lisse, The Netherlands, ISBN: 90 5809 582 7.

Zhang, T. (2005). Influence of the seasonal snow cover on the ground thermal regime: An overview. *Reviews of Geophysics* **43**, RG4002, doi: 10.1029/2004RG000157.

Zwally, H.J., Li, J., Brenner, A., Beckley, M., Cornejo, H., DiMarzio, J., Giovinetto, M., Neumann, T., et al. (2001). Greenland ice sheet mass balance: distribution of increased mass loss with climate warming; 2003-07 versus 1992-2002. *Journal of Glaciology* **57**(201), pp88–102.

Zwally, H.J. & Giovinetto, M.B. (2011). Overview and assessment of Antarctic ice-sheet mass balance estimates: 1992–2009. *Surveys in Geophysics* **32**, pp351–376. doi: 10.1007/s10712-011-9123-5.

# → ACRONYMS

# Acronyms

| | |
|---|---|
| **AATSR** | Advanced Along-Track Scanning Radiometer (Envisat) |
| **ACIA** | Arctic Climate Impact Assessment |
| **ACF** | Active antenna Front-end |
| **ADM-Aeolus** | Atmospheric Dynamics Mission (ESA) |
| **ADM** | Antenna Deployment Mechanism |
| **AFE** | Antenna electric Front-End |
| **AIS** | Antarctic Ice Sheet |
| **AIT** | Assembly, Integration & Testing |
| **AKE** | Absolute Knowledge Error |
| **AMIP** | Atmospheric Model Intercomparison Project |
| **AMSR** | Advanced Microwave Scanning Radiometer |
| **AOCS** | Attitude and Orbit Control System |
| **AOES** | Advanced Operations & Engineering Services |
| **AOGCM** | Atmosphere-Ocean General Circulation Model |
| **AOMIP** | Arctic Ocean Model Intercomparison Project |
| **APE** | Absolute Pointing Error |
| **APP-x** | Advanced Polar Pathfinder |
| **ASAR** | Advanced Synthetic Aperture Radar (Envisat) |
| **ASCAT** | Advanced Scatterometer (MetOp) |
| **ASIC** | Application Specific Integrated Circuit |
| **ASTER** | Advanced Spaceborne Thermal Emission and Reflection Radiometer |
| **AVHRR** | Advanced Very High Resolution Radiometer |
| **AWS** | Automatic Weather Stations |
| **BAQ** | Block Adaptive Quantizer |
| **CCIN** | Canadian Cryospheric Information Network |
| **CDR** | Critical Design Review |
| **CEOS** | Committee on Earth Observation Satellites |
| **CF** | Cover Fraction |
| **CFRP** | Carbon Fibre Reinforced Plastic |
| **CH4** | Methane |
| **CID** | Canadian Ice Database |
| **CliC** | Climate and Cryosphere |
| **CLIMo** | Canadian Lake Ice Model |
| **CLIVAR** | Climate Variability and Predictability |
| **CLPX** | Cold Land Process Experiment |
| **CMC** | Canadian Meteorological Center |
| **CMIS** | Conical Microwave Imager/Sounder |
| **COM** | Commissioning |
| **CoReH$_2$O** | Cold Regions Hydrology high-resolution observatory |
| **CZT** | Chirp Z-Transform |
| **dB** | Decibel |

| | |
|---|---|
| **DCG** | Digital Chirp Generator |
| **DGE** | Digital Equipment |
| **DEM** | Digital Elevation Model |
| **DUE** | Data User Element |
| **E2ES** | End-to-End Simulator |
| **EarthCARE** | Earth, Clouds, Aerosols and Radiation Explorer |
| **ECMWF** | European Centre for Medium-range Weather Forecasts |
| **ECV** | Essential Climate Variable |
| **ED** | Echo Digitiser |
| **EECMS** | Earth Explorer Mission Control System |
| **EFM** | Electrical and Functional Model |
| **EGOS** | ESA Ground Operations System |
| **EM** | Engineering Model |
| **EMS** | Estrack Management and Scheduling system |
| **ENKF** | Ensemble Kalman Filter |
| **ENL** | Equivalent Number of Looks |
| **ENVEO** | Environmental Earth Observation |
| **Envisat** | Environmental satellite |
| **EOL** | End Of Life |
| **EOP** | Early Operations Phase |
| **EPC** | Electronics Power Conditioner |
| **EPS** | Electrical Power Subsystem |
| **ERA-40** | European Re-Analysis |
| **ERS-1,-2** | European Remote Sensing satellite -1,-2 |
| **ESA** | European Space Agency |
| **ESAC** | Earth Science Advisory Committee |
| **ESOC** | ESA's European Space Operations Centre |
| **ESTEC** | ESA's European Space Research and Technology Centre |
| **FDIR** | Failure Detection Isolation and Recovery |
| **FG** | Frequency Generator |
| **FOCC** | Flight Operations Control Centre |
| **FM** | Frequency Modulated |
| **FMI** | Finnish Meteorological Institute |
| **FOS** | Flight Operations Segment |
| **FPGA** | Field Programmatic Gate Array |
| **GCM** | Global Circulation Model |
| **GCOS** | Global Climate Observing System |
| **GCOM** | Global Change Observation Mission |
| **GCW** | Global Cryosphere Watch |
| **GEM** | Global Environmental Multiscale |
| **GEO** | Group on Earth Observations |
| **GEOSS** | Global Earth Observation System of Systems |
| **GEWEX** | Global Energy and Water cycle Experiment |
| **GLIMS** | Global Land Ice Measurements from Space |
| **GLRID** | Global Lake and River Ice phenology Database |

| | |
|---|---|
| GMES | Global Monitoring for Environment and Security |
| GNSS | Global Navigation Satellite System |
| GOCE | Gravity field and steady-state Ocean Circulation Explorer |
| GPM | Global Precipitation Measurement |
| GTC | Geo-coded Terrain Corrected |
| GWI | Gamma Wave Instrument |
| HDRM | Hold-Down and Release Mechanism |
| HH | Horizontal Polarisation transmitted–Horizontal Polarisation received |
| HKTM | House Keeping and Telemetry |
| HPA | High Power Amplifier |
| HRU | Hydrologic Response Unit |
| HYPE | Hydrological Predictions for the Environment |
| ICSU | International Council for Science |
| ICU | Instrument Control Unit |
| I/F | Interface |
| IF | Intermediate Frequency |
| IGOS | Integrated Global Observing Strategy |
| IMS | Interactive Mapping System |
| IPPC | Intergovernmental Panel on Climate Change |
| IPY | International Polar Year |
| IRF | Impulse Response Function |
| ISRO | Indian Space Research Organisation |
| JAXA | Japan Aerospace Exploration Agency |
| JPL | Jet Propulsion Laboratory |
| LAM | Limited Area Model |
| LEOP | Launch and Early Orbit Phase |
| LIAG | Lake Ice Analysis Group |
| LNA | Low Noise Amplifier |
| LOS | Line Of Sight |
| LTDN | Local Time of Descending Node |
| MAG | Mission Advisory Group |
| MAS | Mission Automation System |
| MCS | Mission Control System |
| MFA | Multi-Feed Array |
| MIS | Microwave Imager/Sounder |
| MLI | Multilayer Insulation |
| MODIS | Moderate resolution imaging spectroradiometer |
| MPPT | Maximum Power Point Tracking |
| MPS | Mission Planning System |
| NESZ | Noise Equivalent Sigma Zero |
| NH | Northern Hemisphere |
| NASA | National Aeronautics and Space Administration |
| NOAA | National Oceanic and Atmospheric Administration |
| NPOESS | National Polar-orbiting Operational Satellite System |
| NRCS | Normalised Radar Cross Section |
| NSA | National Snow Analyses |
| NSIDC | National Snow and Ice Data Center |
| NWP | Numerical Weather Prediction |

| | |
|---|---|
| OBC | On-Board Computer |
| OBSW | Onboard Software |
| OMT | Ortho-Mode Transducers |
| OSS | Observing System Simulator |
| PAF | Passive Antenna Front-end |
| PCDU | Power Control and Distribution Unit |
| PDAS | Payload Data Acquisition Station |
| PDGS | Payload Data Ground Segment |
| PDHT | Payload Data Handling and Transmission |
| PDR | Preliminary Design Review |
| PFM | Proto Flight Model |
| PILPS | Project for Intercomparison of Land-surface Parameterization Schemes |
| PLM | Payload Module |
| POLSCAT | Polarimetric Ku-band Scatterometer |
| PREMIER | Process Exploration through Measuerments of Infrared and millimetre-wave Emitted Radiation |
| PRF | Pulse Repetition Frequency |
| PSLR | Peak Side Lobe Ratio |
| PUS | Packet Utilisation Services |
| PVT | Position Velocity Time |
| QUICKSCAT | Quick Scatterometer |
| RACE | Radar Central Electronics |
| RCA | Rossby Centre Atmospheric |
| RCM | Regional Climate Model |
| RCS | Radar Cross Section |
| RCT | Reaction Control Thrusters |
| RE | Radar Electronics |
| RF | Radio Frequency |
| RFE | Radio Frequency Equipment |
| RIU | Remote Interface Unit |
| RMS | Root Mean Square |
| RMSD | Root Mean Square Difference |
| RPE | Relative Pointing Error |
| RSS | Root Square Sum |
| Rx | Receive |
| SADM | Solar Array Deployment Mechanism |
| SAR | Synthetic Aperture Radar |
| SD | Snow Depth |
| SE | Snow Extent |
| SLC | Single Look Complex |
| SM | Structural Model |
| SLE | Sea Level Equivalent |
| SMAP | Soil Moisture Active and Passive mission |
| SMHI | Swedish Meteorological and Hydrological Institute |
| SMOS | Soil Moisture and Ocean Salinity mission |
| SNODAS | Snow Data Assimilation System |
| SNOTEL | Snowpack telemetry |
| SnowMIP | Snow Model Intercomparison Project |
| SPECAN | Spectral analysis |
| SRR | System Requirements Review |
| sRT | Semi-empirical Radiative Transfer |
| SSG | Synthetic Scene Generator |
| SSM/I | Special Sensor Microwave Imager |
| SSMM | Solid State Mass Memory |

| | |
|---|---|
| **SSO** | Sun-Synchronous Orbit |
| **SVM** | Service Module |
| **SVAT** | Soil-Vegetation-Atmosphere Transfer |
| **SWE** | Snow Water Equivalent |
| **SYNOP** | Surface synoptic observation |
| **TAR** | Total Ambiguity Ratio |
| **TT&C** | Telemetry, Tracking & Command |
| **TRL** | Technology Readiness Level |
| **TRMM** | Tropical Rainfall Measuring Mission |
| **TWT** | Travelling Wave Tube |
| **Tx** | Transmit |
| **UNEP** | United Nations Environment Programme |
| **UNESCO** | United Nations Educational, Scientific and Cultural Organization |
| **UNFCCC** | United Nations Framework Convention on Climate Change |
| **US** | United States |
| **USO** | Ultra-Stable Oscillator |
| **USDA** | United States Department of Agriculture |
| **UTC** | Coordinated Universal Time |
| **UTM** | Universal Transverse Mercator |
| **VIC** | Variable Infiltration Capacity |
| **VH** | Vertically polarised transmit signal, horizontally polarised receive signal |
| **VV** | Vertically polarised transmit signal, vertically polarised receive signal |
| **W** | Watts (Unit) |
| **WG** | Waveform Generator |
| **WCRP** | World Climate Research Programme |
| **WMO** | World Meteorological Organization |
| **WSFS** | Watershed Simulation and Forecasting System |
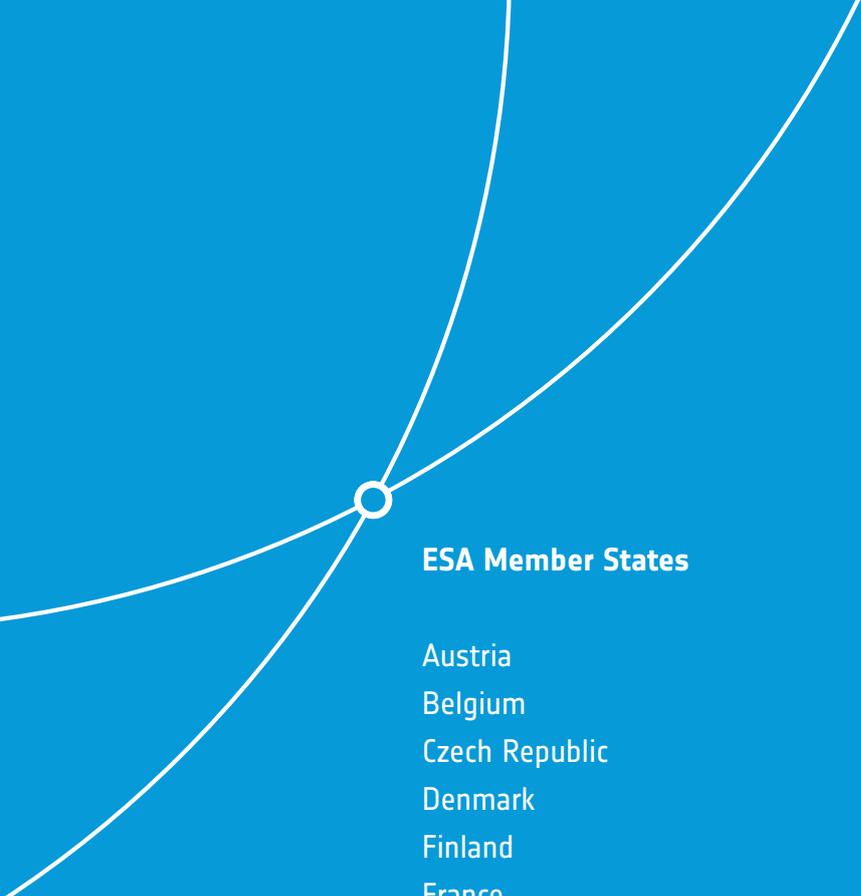
## ESA Member States

Austria
Belgium
Czech Republic
Denmark
Finland
France
Germany
Greece
Ireland
Italy
Luxembourg
Netherlands
Norway
Portugal
Romania
Spain
Sweden
Switzerland
United Kingdom